GENERAL ATOMIC

GA-A14180
UC-77

HTGR FUELS AND CORE DEVELOPMENT PROGRAM

QUARTERLY PROGRESS REPORT FOR THE PERIOD ENDING NOVEMBER 30, 1976

Prepared under
Contract EY-76-C-03-0167
Project Agreement No. 17
for the San Francisco Operations Office
U.S. Energy Research and Development Administration

DATE PUBLISHED: DECEMBER 27, 1976

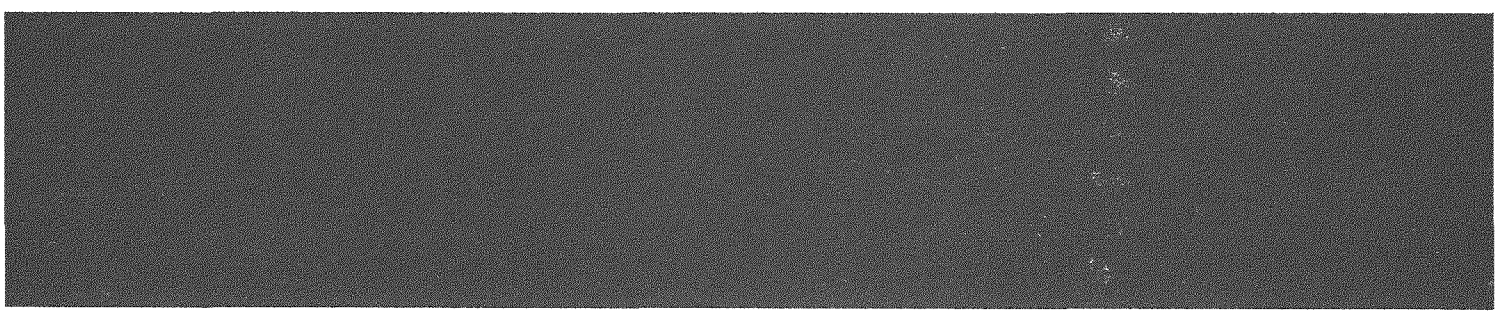

Printed in the United States of America
Available from
National Technical Information Service
U.S. Department of Commerce
5285 Port Royal Road
Springfield, Virginia 22161
Price: Printed Copy $8.00; Microfiche $3.00

DISCLAIMER

GENERAL ATOMIC

A14180
UC-77

HTGR FUELS AND CORE DEVELOPMENT PROGRAM

QUARTERLY PROGRESS REPORT FOR THE PERIOD ENDING NOVEMBER 30, 1976

Prepared under
Contract EY-76-C-03-0167
Project Agreement No. 17
for the San Francisco Operations Office
U.S. Energy Research and Development Administration

GENERAL ATOMIC PROJECT 3224 DATE PUBLISHED: DECEMBER 27, 1976

QUARTERLY REPORT SERIES

GA-4072-December, 1962, through February, 1963
GA-4350-March, 1963, through May, 1963
GA-4569-June, 1963, through August, 1963
GA-4937-September, 1963, through November, 1963
GA-5104-December, 1963, through February, 1964
GA-5366-March, 1964, through May, 1964
GA-5618-June, 1964, through August, 1964
GA-5866-September, 1964, through November, 1964
GA-6113-December, 1964, through February, 1965
GA-6418-March, 1965, through May, 1965
GA-6671-June, 1965, through August, 1965
GA-6869-September, 1965, through November, 1965
GA-7010-December, 1965, through February, 1966
GA-7181-March, 1966, through May, 1966
GA-7396-June, 1966, through August, 1966
GA-7553-September, 1966, through November, 1966
GA-7801-December, 1966, through February, 1967
GA-7981-March, 1967, through May, 1967
GA-8200-June, 1967, through August, 1967
GA-8356-September, 1967, through November, 1967
GA-8530-December, 1967, through February, 1968
GA-8662-March, 1968, through May, 1968
GA-8860-June, 1968, through August, 1968
GA-9090-September, 1968, through November, 1968
GA-9227-December, 1968, through February, 1969
GA-9372-March, 1969, through May, 1969
GA-9660-June, 1969, through August, 1969
GA-9815-September, 1969, through November, 1969
GA-9944-December, 1969, through February, 1970
GA-10088-March, 1970, through May, 1970
GA-10288-June, 1970, through August, 1970
GA-10399-September, 1970, through November, 1970
GA-10501-December, 1970, through February, 1971
GA-10661-March, 1971, through May, 1971
Gulf-GA-A10784-June, 1971, through August, 1971
Gulf-GA-A10930-September, 1971, through November, 1971
Gulf-GA-A10999-December, 1971, through February, 1972
Gulf-GA-A12150-March, 1972, through May, 1972
Gulf-GA-A12222-June, 1972, through August, 1972
Gulf-GA-A12422-September, 1972, through November, 1972
Gulf-GA-A12515-December, 1972, through February, 1973
Gulf-GA-12599-March, 1973, through May, 1973
Gulf-GA-A12725-June, 1973, through August, 1973
Gulf-GA-A12818-September, 1973, through November, 1973
GA-A12916-December, 1973, through February, 1974
GA-A13030-March, 1974, through May, 1974
GA-A13126-June, 1974, through August, 1974
GA-A13253-September, 1974, through November, 1974
GA-A13353-December, 1974, through February, 1975
GA-A13444-March, 1975, through May, 1975
GA-A13592-June, 1975, through August, 1975
GA-A13737-September, 1975, through November, 1975
GA-A13804-December, 1975, through February, 1976
GA-A13941-March, 1976, through May, 1976
GA-A14046-June, 1976, through August, 1976

ABSTRACT

This publication continues the quarterly report series on the HTGR Fuels and Core Development Program. The Program covers items of the base technology of the High-Temperature Gas-Cooled Reactor (HTGR) system. The development of the HTGR system will, in part, meet the greater national objective of more effective and efficient utilization of our national resources. The work reported here includes studies of reactions between core materials and coolant impurities, basic fission product transport mechanisms, core graphite development and testing, the development and testing of recyclable fuel systems, and physics and fuel management studies. Materials studies include irradiation capsule tests of both fuel and graphite. Experimental procedures and results are discussed and, where appropriate, the data are presented in tables, graphs, and photographs. More detailed descriptions of experimental work are presented in topical reports; these are listed at the end of the report.

INTRODUCTION

This report covers the work performed by the General Atomic Company under U.S. Energy Research and Development Administration Contract EY-76-C-03-0167, Project Agreement No. 17. This Project Agreement calls for support of basic technology associated with the fuels and core of the gas-cooled, nuclear power reactor systems. The program is based on the concept of the High-Temperature Gas-Cooled Reactor (HTGR) developed by the General Atomic Company.

Characteristics of advanced large HTGR designs include:

1. A single-phase gas coolant allowing generation of high-temperature, high-pressure steam with consequent high-efficiency energy conversion and low thermal discharge.

2. A prestressed concrete reactor vessel (PCRV) offering advantages in field construction, primary system integrity, and stressed member inspectability.

3. Graphite core material assuring high-temperature structural strength, large temperature safety margins, and good neutron economy.

4. Thorium fuel cycle leading to U-233 fuel which allows good utilization of nuclear resources and minimum demands on separative work.

These basic features are incorporated into the 330-MW(e) prototype Fort St. Vrain reactor which is currently undergoing prestartup testing.

CONTENTS

FIGURES

FIGURES (continued)

FIGURES (continued)

TABLES

TABLES (continued)

4. HTGR FISSION PRODUCT MECHANISMS
189a NO. 00549

TASK 100: FISSION PRODUCT TRANSPORT

The following reports under Task 100 represent analysis of experimental work performed in FY-76 and the transition quarter (prior to FY-77). There is no funding in FY-77 for experimental work under this Task.

Subtask 110: Fission Gas Release

In Fig. 4-1 of the previous quarterly report (Ref. 4-1), the datum at n = 0.2, T = ∿600 K should have been represented by a solid symbol; i.e., this datum was obtained at P = 2.84 MPa.

Subtask 130: Sorption of Fission Product Metals on Matrix Material

Vapor Pressure of Cesium Sorbed on Irradiated Fuel Rod Matrix Material

Introduction and Summary. The vapor pressures of cesium sorbed on irradiated fuel rod matrix material have been measured using a mass spectrometric method. The fuel rod matrix material (M-205) was irradiated in capsule HB-2 at 500° to 600°C to a fluence of 3 to 4 x 10^{25} n/m^2. The resulting isotherms do not differ significantly from isotherms obtained for unirradiated matrix material. It is concluded that irradiation of fuel rod matrix material does not significantly alter the sorption behavior of cesium, at least up to a fluence of 4 x 10^{25} n/m^2.

Experimental. In the mass spectrometric method, which has been previously described (Refs. 4-2 through 4-4), a sample of the matrix material is prepared with sorbed metal. The matrix material particles are in the size

range 44 to 74 μm. The sample is placed in a molybdenum Knudsen cell and maintained at a series of temperatures while the effusion of metal vapor from the cell is monitored with the mass spectrometer. The vapor and sorbed concentrations of the metal are determined from a knowledge of the initial and final quantities of sorbate and the time profile of the effusing metal. However, in the present experiments, the final concentration of sorbate (cesium sorbed on matrix material) could not be determined because of a Th impurity. The Th impurity, which was activated during irradiation of the matrix material, interfered with the measurement of the small quantity of cesium remaining in the matrix material at the end of the experiment. To circumvent this difficulty, the Knudsen cell constant, which depends on the difference in the initial and final sorbate concentrations, was independently determined by measuring cesium vaporization from an H-327 graphite sample in the same Knudsen cell as used for the matrix material experiment. With the aid of this constant, the final sorbed cesium concentration on the matrix material was determined.

The fuel rod matrix material sample (M-205) is a petroleum-pitch-based material containing about 70 wt % pitch and 30 wt % graphite filler. The LHTGR reference matrix material contains about 60 wt % pitch and 40 wt % graphite filler. A more detailed comparison of the matrix materials is given in Ref. 4-5.

Results and Discussion. The measured heats of vaporization, the sorbate concentrations, and the nominal temperature range for each run are given in Table 4-1. The vapor pressure data are presented in Table 4-2 and shown in Fig. 4-1.

The vapor pressure data of Table 4-2 which are enclosed within the solid line are those corresponding roughly to the nominal temperature range of the measurements; the remaining vapor pressure data are extrapolated values. The dashed lines of Table 4-2 separate the concentration regions in which the isotherm behavior is expected to differ. For concentrations above the upper dashed line, the Freundlich isotherm is expected to dominate. A fit of the data corresponding to these concentrations with the

TABLE 4-1
HEAT OF ADSORPTION FOR CESIUM ON IRRADIATED FUEL
ROD MATRIX MATERIAL (M-205)

Cs Concentration (g Cs/kg matrix)	ΔH (kJ/mol)	Nominal Temperature Range (K)
46.14	184 $\pm$ 7	600-800
46.05	187 $\pm$ 13	750-850
45.96	199 $\pm$ 3	800-950
40.60	185 $\pm$ 6	900-1000
28.29	190 $\pm$ 5	900-1050
22.20	187 $\pm$ 4	900-1050
14.61	223 $\pm$ 5	950-1100
9.05	233 $\pm$ 3	1000-1150
6.10	247 $\pm$ 4	1000-1150
4.35	270 $\pm$ 7	1000-1200
3.07	279 $\pm$ 1	1050-1250
2.15	284 $\pm$ 2	1050-1300
1.36	285 $\pm$ 3	1100-1300
0.84	296 $\pm$ 2	1100-1350
0.57	303 $\pm$ 2	1150-1400
0.35	301 $\pm$ 6	1200-1400

TABLE 4-2
DATA FOR CESIUM SORPTION ON IRRADIATED FUEL ROD MATRIX MATERIAL (M-205)[a]

Conc., C' $\left(\frac{\text{g Cs}}{\text{kg carbon}}\right)$	Conc., C[b] $\left(\frac{\text{mmol Cs}}{\text{kg carbon}}\right)$	ln C[c]	ln P(Pa)[c]						
			700°C	800°C	900°C	1000°C	1100°C	1200°C	1300°C
14.61	109.8	4.699	-3.06	-0.492	1.64	3.43	4.97	6.29	7.44
9.049	68.04	4.220	-4.38	-1.71	0.513	2.40	3.98	5.37	6.59
6.104	45.89	3.826	-5.85	-3.02	-0.643	1.35	3.06	4.51	5.80
4.354	32.74	3.489	-7.62	-4.51	-1.93	0.251	2.11	3.73	5.11
3.074	23.11	3.140	-7.88	-5.80	-3.13	-0.884	1.04	2.69	4.15
2.150	16.17	2.783	-10.36	-7.09	-4.40	-2.10	-0.144	1.55	3.18
1.360	10.23	2.325	-11.54	-8.24	-5.53	-3.25	-1.28	0.415	1.89
0.8401	6.317	1.843	-13.03	-9.63	-6.79	-4.40	-2.37	-0.606	0.932
0.5710	4.293	1.457	-14.21	-10.73	-7.83	-5.39	-3.32	-1.51	-0.0647
0.3502	2.633	0.9682	-15.31	-11.86	-8.98	-6.54	-4.47	-2.69	-1.12

[a] Data enclosed in solid line are within the nominal temperature range of the measurements; the remaining data were derived from extrapolations. The dashed lines separate the concentration regions in which the isotherm behavior is expected to differ.

[b] $C = 1000C'/133$.

[c] ln represents logarithm to the base e.

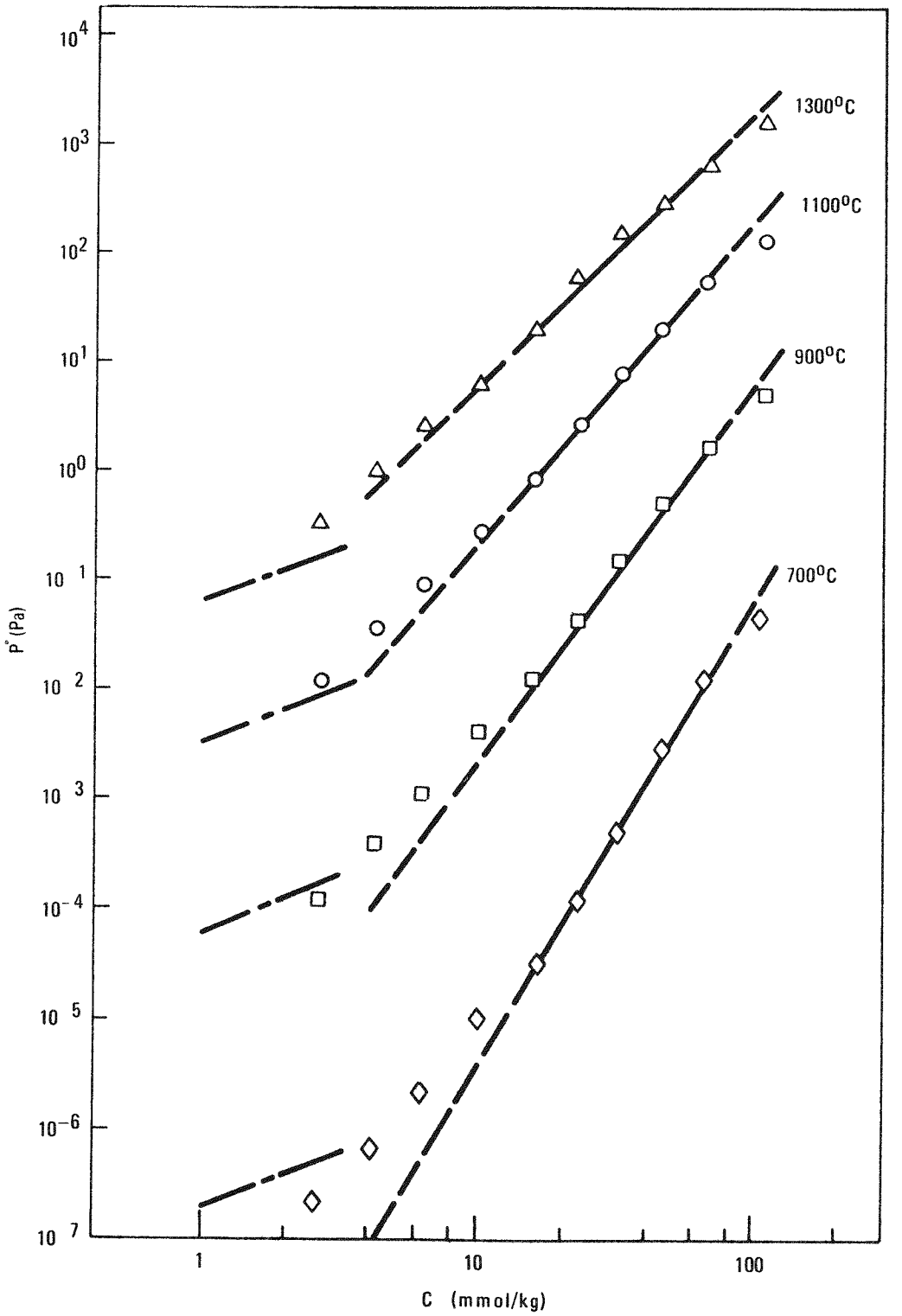

Fig. 4-1. Sorption isotherms for cesium on fuel rod matrix material (M-205)

Freundlich isotherm is shown in Fig. 4-1 by the solid lines. Extrapolation of these fits to lower concentrations indicates that the experimental data deviate from the Freundlich isotherm in the manner expected for a transition to the Henrian isotherm.

On the basis of previous isotherms for cesium sorption on unirradiated fuel rod matrix material (M-205) (Ref. 4-5), the data of Table 4-2 below the lower dashed line would be expected to lie in the Henrian isotherm region. However, the experimental data do not extend to sufficiently low concentrations to conclusively establish a transition to the Henrian isotherm. Therefore, to extend the sorption data to the lower concentrations required in reactor calculations of fission product release, the Henrian isotherms found in the case of cesium sorption on unirradiated fuel rod matrix material (Ref. 4-5) are applied to the case of the irradiated fuel rod matrix material. These (Henrian) isotherms are indicated by the short dash-dot lines in Fig. 4-1 at concentrations below about 3 mmol/kg. As is evident from Fig. 4-1, this approximation will be conservatively high with respect to the vapor pressure of cesium in the Henrian region and consequently also conservative with respect to release of cesium from the core of the HTGR.

The data of Table 4-2 have been fitted to the expressions

$$\ln P_F = (A + B/T) + (D + E/T) \ln C \qquad (4\text{-}1)$$

and

$$\ln P_H = (A + B/T) + [(D - 1) + E/T] \ln C_t + \ln C \quad , \qquad (4\text{-}2)$$

where P = total vapor pressure of cesium, Pa,

P_F = vapor pressure in the Freundlich region,

P_H = vapor pressure in the Henrian region,

ln = logarithm to base e,

C = concentration, mmol Cs/kg carbon,

C_t = transition concentration,

T = temperature, K,

A,B,D,E = constants.

The values of the constants were found to be: A = 25.45, B = -46,275, D = -0.213, and E = 4309. The transition concentration is represented by the expression

$$C_t = a\left[1 + e^{b(T-T_o)}\right]^{-1} \quad , \tag{4-3}$$

where a, b, and T_o are constants with a = 8.5 mmol/kg, b = 0.0055, and T_o = 1350 K.

In Fig. 4-2, the isotherms for cesium sorption on irradiated and unirradiated fuel rod matrix material are compared. The solid curves represent the isotherms for irradiated matrix material and the dashed curves isotherms for unirradiated matrix material. Each isotherm shown is the sum of contributions from the Henrian and Freundlich representations (Eqs. 4-1 and 4-2). For the isotherm at 1100°C representing unirradiated matrix material, the shaded area corresponds to the uncertainty band at the 95% confidence level. By inspection, it can be seen that the isotherms for the irradiated and unirradiated fuel rod matrix materials do not differ significantly. Also, the uncertainty band is essentially the same for the isotherms at 700°, 900°, and 1300°C as at 1100°C. Consequently, it can be concluded that the irradiation of fuel rod matrix material does not significantly alter the sorption behavior of cesium, at least up to a fluence of 4×10^{25} n/m^2.

Subtask 140: Diffusion of Fission Product Metals in Graphite

Diffusion of Cesium in Graphite

Introduction and Summary. Cesium transport through H-451 graphite, which is the reference graphite for the large HTGR, has been studied using a permeation method. The purpose of this work was to gain a better understanding of cesium transport in graphite and to reduce the uncertainty of data relating to cesium diffusivity in graphite. The AIPA study (Ref. 4-6) found that uncertainty in cesium diffusivity in graphite was the largest contributor to the uncertainty in cesium release predictions.

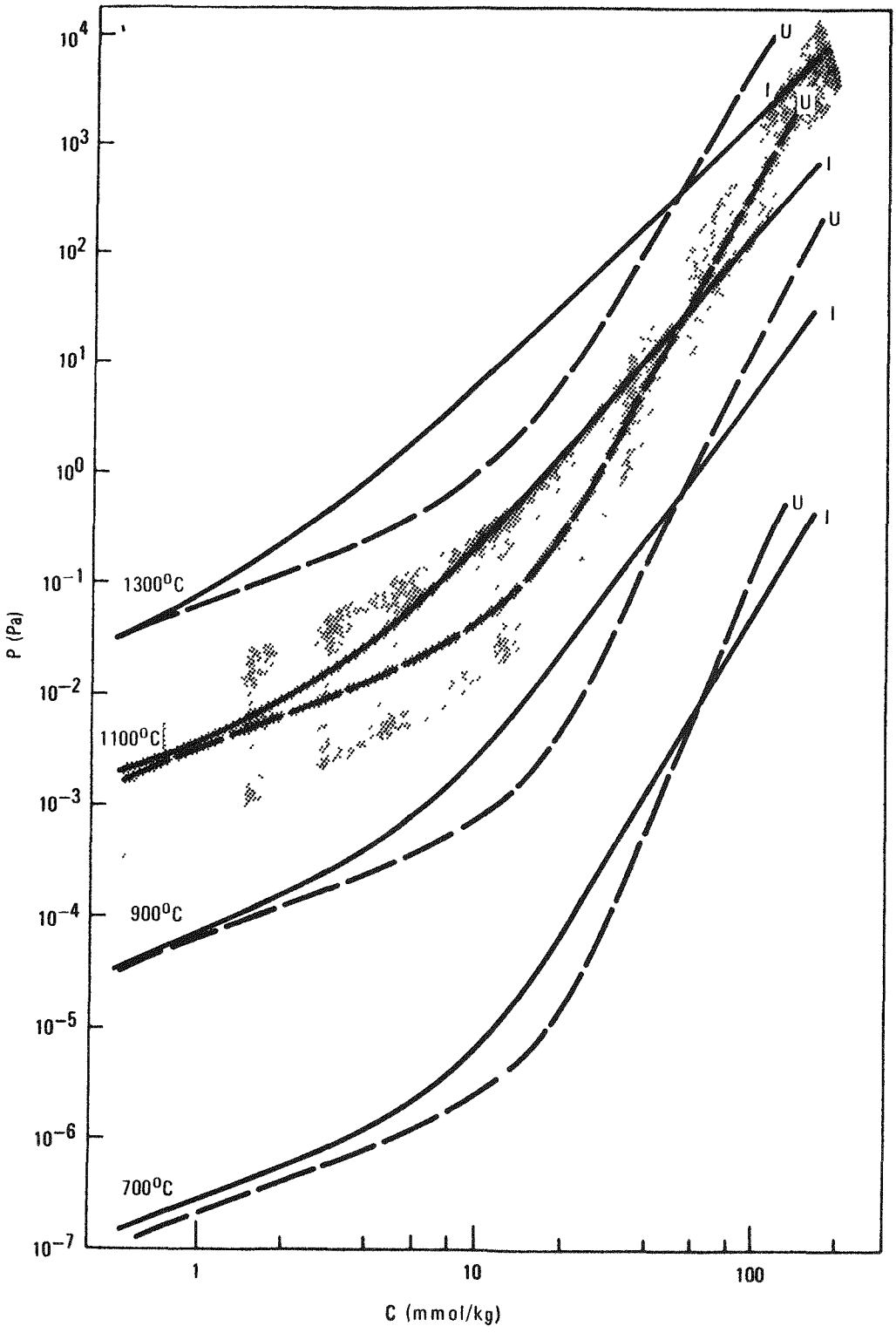

Fig. 4-2. Comparison of sorption isotherms for cesium on irradiated (I) and unirradiated (U) fuel rod matrix material (M-205)

The permeation experiments were discontinued at the end of the transition period (end of September 1976) due to lack of funds. The following report is the first part of a final report covering the results of this work.

In summary of the following report, results show that the "sterile" technique was successful in reducing the extent of the "burst effect" of permeation. An H-451 graphite sample was subjected to a number of anneals ranging from 40 minutes to 6 hours. Analysis of the resulting data, taking the "burst effect" into account, yielded a permeation coefficient of 2.1×10^{-12} m^2/s, in accord with previous values. Experiments on cesium takeup by H-451 graphite yielded a D' value of 1.7×10^{-7} s^{-1} at 1388 K and an activation energy of 184 kJ/mol (44 kcal/mole) for bulk loading of the graphite. Other experiments confirmed that charloaded graphite is ten times more sorptive than H-451 graphite.

Cesium Permeation in H-451 Graphite. The apparatus and procedure developed for measuring the permeation of cesium through graphite have been described in previous reports (Refs. 4-1 and 4-7). The basic method uses highly sorptive, charloaded graphite as the source and sink in measuring the transport of cesium across a barrier sleeve of the graphite to be studied. The source is a small rod that is completely enclosed in the sleeve, which is closed with tightly fitting plugs. This in turn is enclosed in the cylindrical sink, the ends of which are also tightly closed with caps. Thus, cesium has to travel through the graphite sleeve to reach the sink. These parts are illustrated in Fig. 4-2 of Ref. 4-7. A "sterile" technique was developed for protecting all parts from air or moisture throughout the series of experiments after an initial bake-out.

Before this "sterile" technique was developed, the time lag for cesium to penetrate the graphite sleeve was immeasurably short. This was thought to be due to the acceleration of cesium transport through graphite by traces of oxidizing gases, such as would be evolved upon heating of samples exposed to air. It seemed therefore to be of interest to measure the time

lag to determine the effectiveness of the "sterile" technique. Accordingly, one of the sources used previously (Hb) was subjected to a number of 40-minute anneals with a fresh sleeve. Once a constant rate of permeation was established, the system was subjected to additional anneals of 2 and 6 hours. A fresh sink was used in each anneal; the experiments were conducted at 1138 K.

The results are given in Table 4-3 and plotted as cumulative transport (i.e., sink activity/source activity) versus cumulative time in Fig. 4-3. It can be seen that a time lag is present, but the points lie reasonably on two straight lines instead of a single one as would be expected. Clearly the amount of permeation is disproportionately large during the 40-minute anneal times. This has been observed previously and was attributed tentatively to imperfect sinks (Ref. 4-1). This explanation is clearly not applicable here. The necessary conclusion seems to be that the "sterile" technique used is not sufficient to prevent residual traces of impurities which produce an initial "burst effect" of permeation of the order of 3×10^{-2}% once the sleeve has been loaded to the steady-state condition. (The quantity 3×10^{-2}% was derived from the difference in the slopes of the two lines in Fig. 4-3.) By subtracting this quantity for each anneal, the points shown in Fig. 4-4 are obtained. These points define a good straight line and an intercept of about 1.8 hours. This may be a slight overestimate [because the two first anneals give negative permeations (see Table 4-3) which are neglected] but should be closer to reality than the 1.2-hour intercept obtained before correction.

The diffusion coefficient obtained from the intercept is about 5×10^{-10} m^2/s, whereas that obtained from the slope of the line in Fig. 4-4 is 2.1×10^{-12} m^2/s.* As mentioned in the previous quarterly report (Ref. 4-1), the difference in these two values is in the direction expected when

*In calculating these two diffusion coefficient values, Eq. 4-4 and 4-5 of Ref. 4-1 were utilized. Both values were assumed to be diffusion coefficients, although the value 2×10^{-12} m^2/s is more correctly a permeation coefficient and the 5×10^{-10} m^2/s a retention coefficient.

TABLE 4-3
CESIUM PERMEATION THROUGH H-451 GRAPHITE AT 1138 K[(a)]

Anneal Time (hours)	Cumulative Anneal Time (hours)	Sink Activity (μCi)	Observed		Corrected	
			Sink/Source x 10^4	Sink/Source Cumulative x 10^4	Sink/Source x 10^4	Sink/Source Cumulative x 10^4
2/3	0.67	0.0106	1.43	1.43	-1.57	-1.54
2/3	1.33	0.0291	3.93	5.36	0.93	-0.64
2/3	2.0	0.0430	5.81	11.2	2.81	2.18
2/3	2.67	0.0536	7.24	18.4	4.24	6.42
2/3	3.33	0.0578	7.81	26.2	4.81	11.23
2/3	4.00	0.0542	7.32	33.6	4.32	15.6
2/3	4.67	0.0503	6.84	40.4	3.84	19.4
2/3	5.33	0.0706	9.54	49.9	6.54	25.9
2	7.33	0.124	16.8	66.7	13.8	39.7
2	9.3	0.119	16.1	82.9	13.1	52.9
6	15.3	0.292	39.5	122	36.5	89.4
6	21.3	0.301	40.7	171	37.7	135

(a) Source activity was 74 μCi.

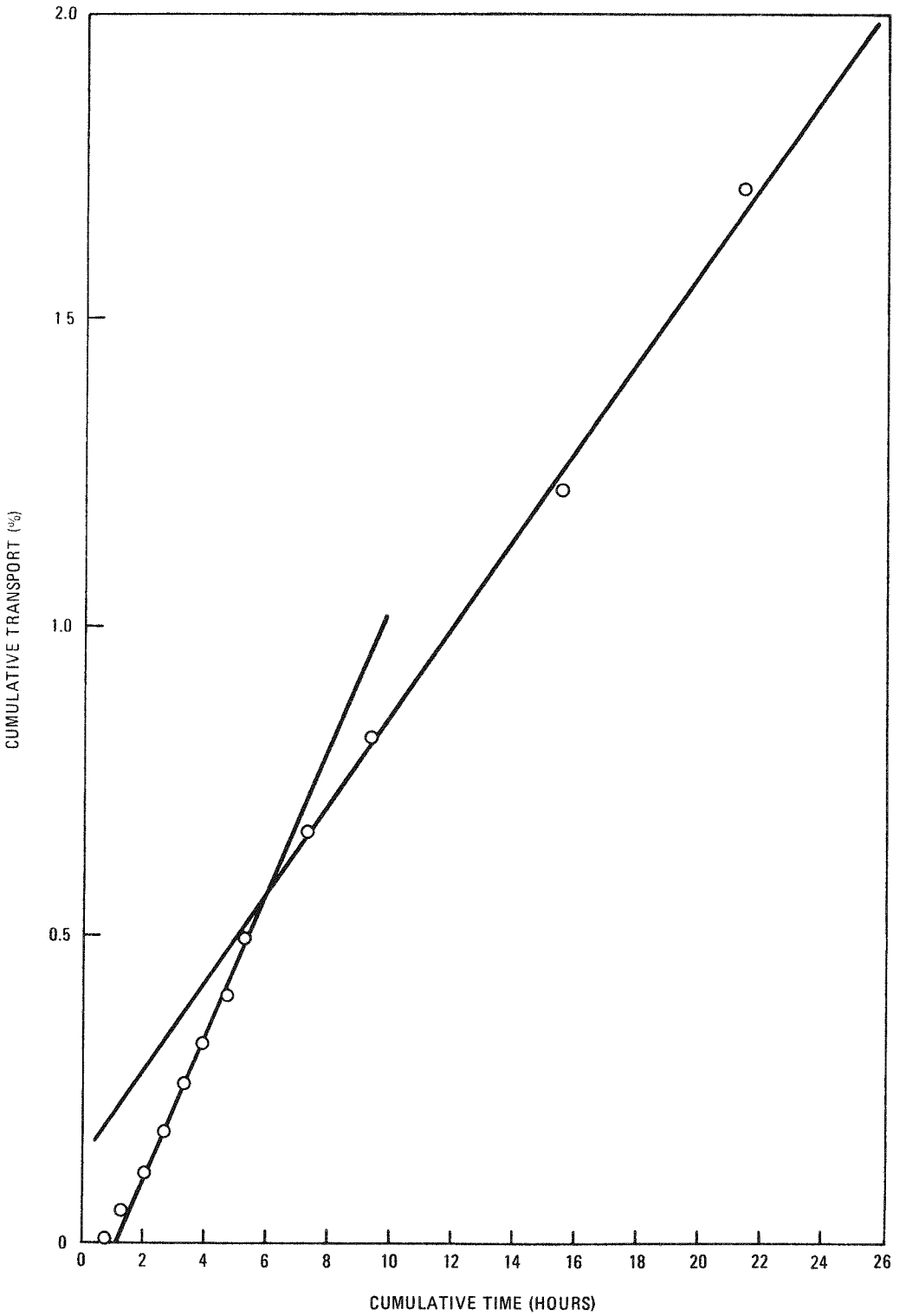

Fig. 4-3. Uncorrected cumulative transport versus cumulative time for permeation anneals using source Hb at 1138 K

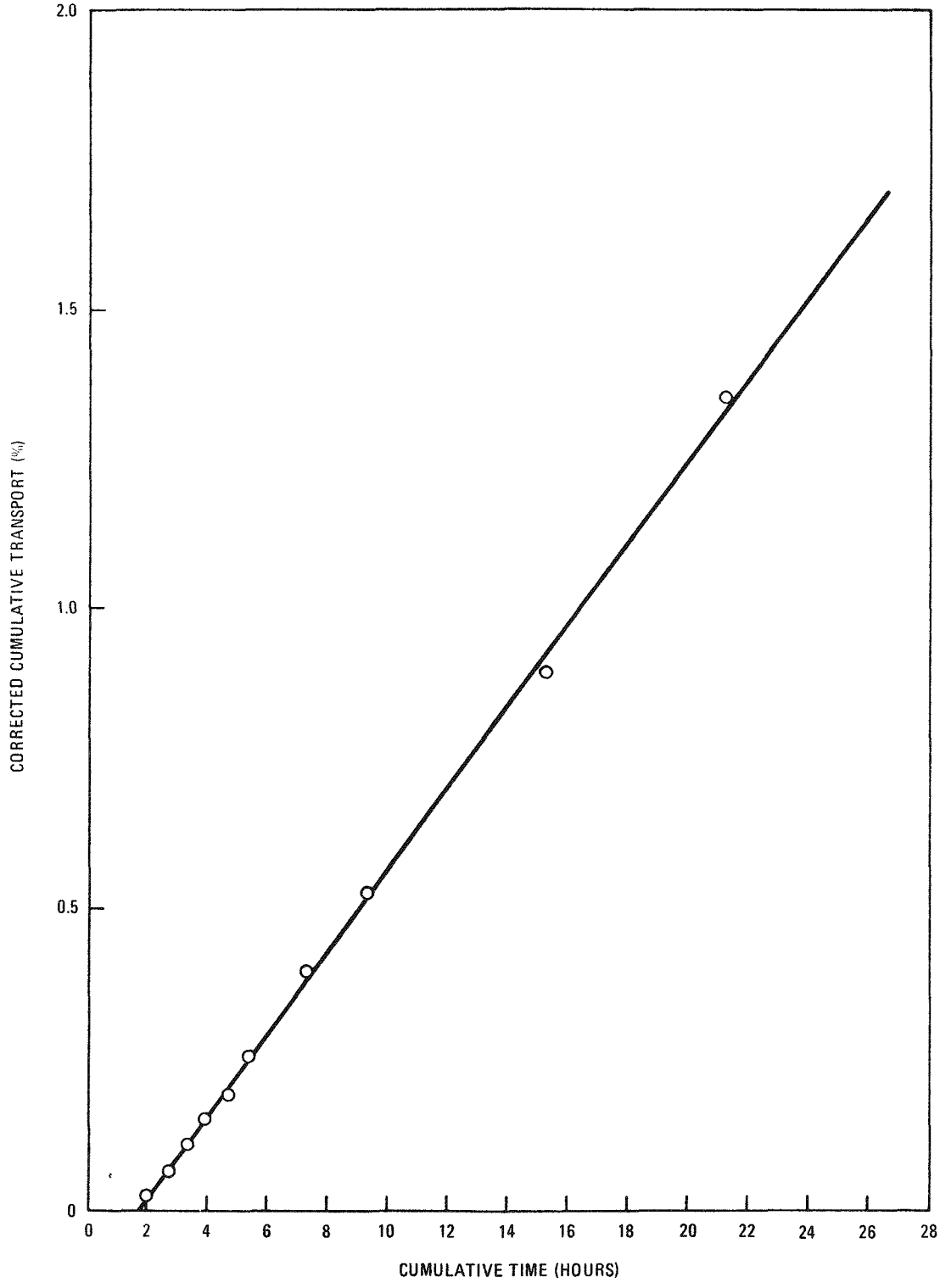

Fig. 4-4. Corrected cumulative transport versus cumulative time for permeation anneals using source Hb at 1138 K

only a small part of the graphite cross section participates in the transport. It can be noted that the permeation coefficient 2 x 10^{-12} m^2/s obtained for this sample of graphite is within the range of 1.6 to 3.6 x 10^{-12} m^2/s found for four samples previously (Ref. 4-1).

The "burst effect" found in these experiments is sufficiently small to be within experimental error for the 2 or 6 hour experiments. The line through these experiments in Fig. 4-3 gives a diffusion coefficient less than 3% higher than found above.

Cesium Takeup by Graphite. A previous report (Ref. 4-8) mentioned some early experiments concerning the rate at which cesium is taken up by graphite. The experiments involved two steps. In the first step a small piece of graphite to be studied in the form of a rod (having the same dimensions as the source in the standard permeation experiment) was annealed within a niobium crucible with a large source of charloaded graphite (having the form of the sleeve of the permeation experiments). In this way the total uptake could be measured as a function of time and temperature. The second step involved depletion of the graphite thus loaded by annealing it for a short time at low temperature (2 hours at 1138 K) in the presence of virgin charloaded graphite (again in the form of sleeve and plugs of the permeation experiments). In this way an easily removable, surface sorbed portion of the cesium could be measured whereas the remainder, which was much more difficult to remove, was formed by bulk-sorbed cesium.

These experiments were initiated before the importance of the "sterile" technique excluding air and moisture was appreciated and gave variable results which were difficult to interpret but pointed to a very long time of equilibration and high activation energy, making it clearly a different process from permeation. The experiments were then resumed using the "sterile" technique but difficulty was encountered with leakage of cesium during long anneals at high temperature, which could not be overcome in the time available. Nevertheless, some results can be reported.

In these last experiments the graphite rod was broken into two halves so that two values were obtained in each anneal. The results are given in Table 4-4. The depleted values, which correspond to the bulk-sorbed cesium, are plotted in Fig. 4-5. In analyzing the results (i.e., in obtaining the percent equilibrium values), the assumption has been made that the charloaded graphite is ten times more sorptive than the H-451 graphite (see below). As can be seen from Fig. 4-5, the results are compatible within the experimental uncertainty with the standard loading curve (solid curve) for a sphere. This means that substantially higher sorptivity ratios are not possible because then the samples would have reached, or come close to, equilibrium, which is certainly not the case. Substantially lower ratios are in principle possible on the basis of these experiments alone but are precluded by the structure of charloaded graphite and by other equilibration experiments (see below).

Analysis of the cesium takeup data yields a D' value of 1.7×10^{-7} s^{-1} at 1388 K, where $D' = D/a^2$, D = the diffusion coefficient, and a = radius of the graphite crystallites (assumed to be spheroid). (See Ref. 4-1 for method of treating data to derive D' value.)

Figure 4-5 shows that it takes about 50 hours at 1388 K to reach the half saturation point and that to come within a few percent of equilibrium requires close to a thousand hours at that temperature. The process is much slower at lower temperatures. Assuming that loading at each temperature is proportional to the square root of time from the very beginning (which is the case for loading of a sphere), the individual points obtained at the other temperatures permit the construction of an Arrhenius plot (Fig. 4-6) which turns out very linear and indicates an activation energy of 184 kJ/mol (44 kcal/mole), which is appreciably higher than the value of about 145 kJ/mol obtained previously for permeation (see Ref. 4-1). It should be noted, however, that the assumption that the initial loading rate is proportional to the square root of time over more than an order of magnitude may well be in error because surface irregularities and very small particles are likely to give a higher initial rate. This would make the lower temperature (lower loading) points higher and thus would lower the

TABLE 4-4
LOADING AND DEPLETION OF H-451 GRAPHITE

Temp (K)	Time (hours)	Sample No.	Percent of Equilibrium[a]		Difference
			After Loading	After Depletion	
1138	16	20A	5.4	0.92	4.5
		20B	5.9	1.05	4.85
1283	16	21A	14.0	8.5	5.5
		21B	13.4	8.95	4.4
1388	16	22A[b]	40.2	33.2	7.0
		22B	38.9	33.4	5.6
1388	4	23A	19.7	15.2	4.5
		23B	18.5	13.2	5.3
1388	48	22A[b]	63.7	58.7[c]	5[d]
		24A	52.2	47.2[c]	5[d]

[a] The percent values given assume that the equilibrium sorptivity of charloaded graphite is 10 times that of H-451; they represent 100 x 10(a/w)/(A/W), where a and w are the activity and weight of the sample and A and W are the corresponding quantities for the charloaded graphite source.

[b] Note that sample 22A has a total anneal time of 64 hours.

[c] Value not measured but calculated from assumed difference.

[d] Assumed on the basis of measured differences.

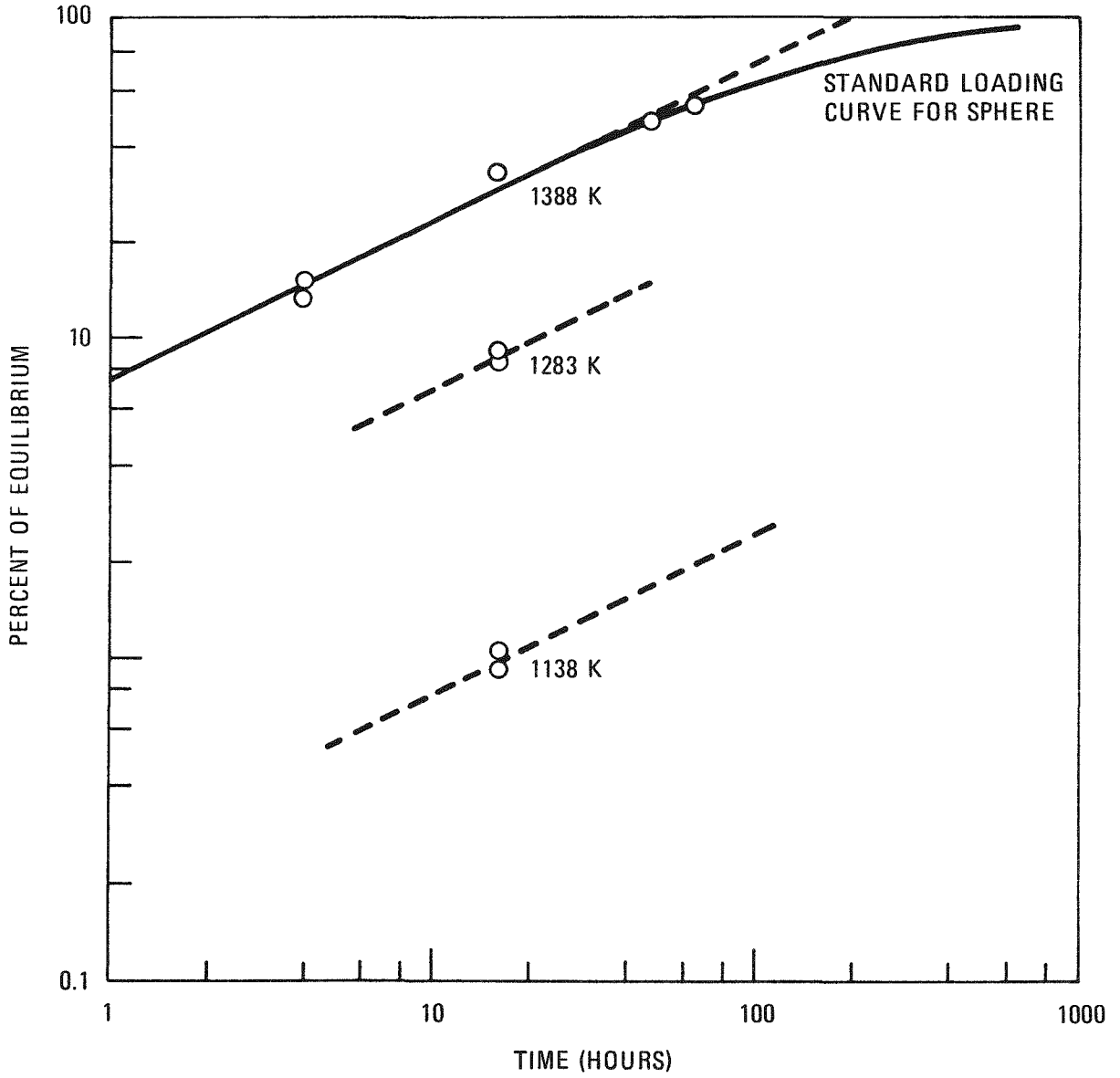

Fig. 4-5. Cesium takeup by H-451 graphite

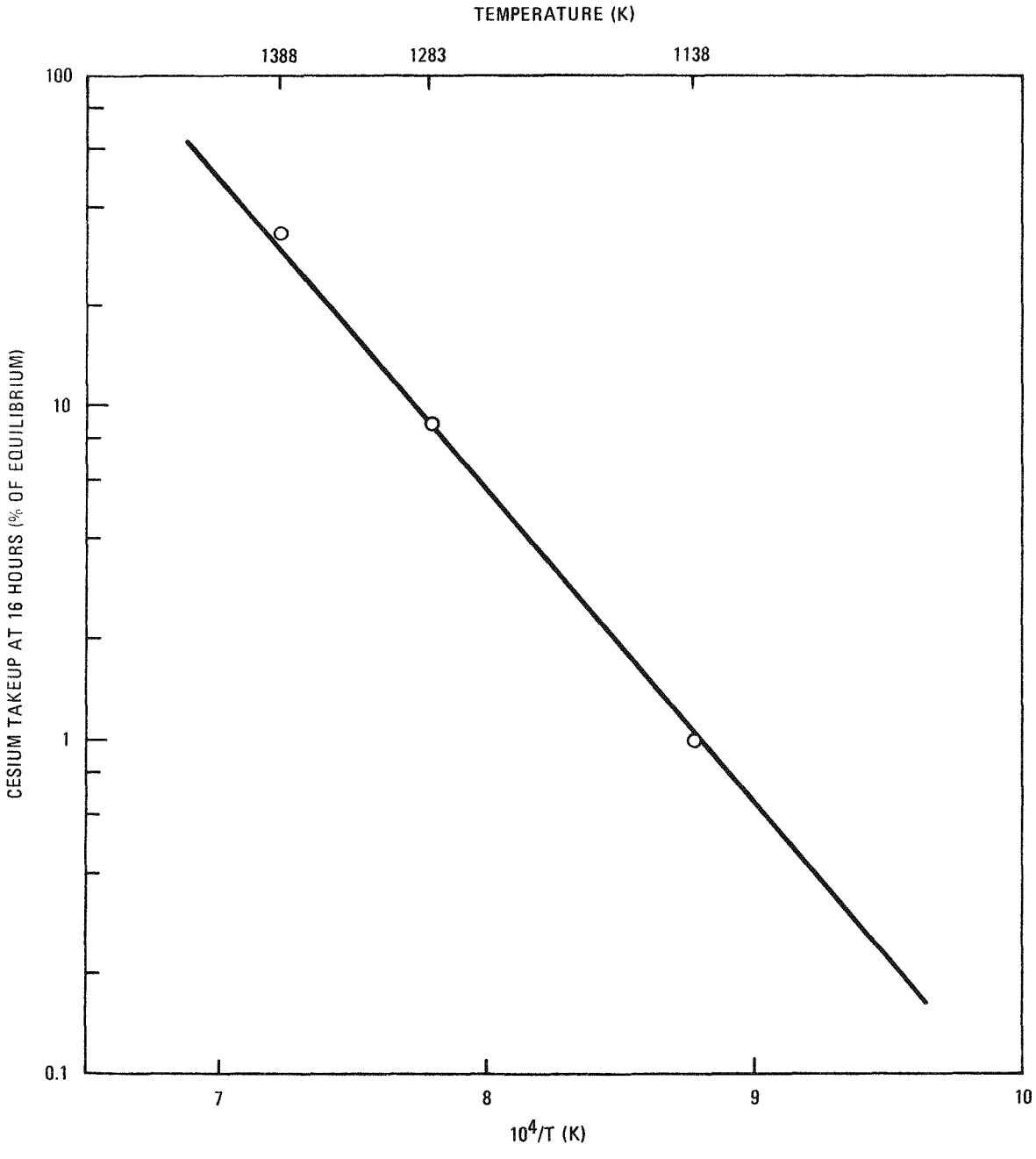

Fig. 4-6. Arrhenius plot of cesium takeup by H-451 graphite at 16 hours

activation energy. Hence, the value given (184 kJ/mol) is probably lower than the value which corresponds to takeup by the large particles. Since takeup of the bulk-sorbed cesium is likely to involve movement within the solid graphite structure rather than movement on pore surfaces as in permeation, it is not surprising that the activation energy is higher for the takeup process than for the permeation process.

Sorptivity Ratio for Charloaded and H-451 Graphites. The values for the relative sorptivity of charloaded graphite and H-451 graphite were derived from experiments performed several years ago in which a cesium source was annealed with charloaded graphite and H-327 graphite for one or two 8-hour periods at 1470 K, and the sorptivity ratio was found to be ten. Other experiments showed that the difference in sorptivity between H-327 and H-451 was negligible.

Results of these experiments indicate that the time alloted (8 to 16 hours) was not sufficient to approach equilibrium very closely; nevertheless, it would have been adequate to exceed 50% of the equilibrium value for H-451 (or H-327) graphite and probably somewhat closer for charloaded graphite. Hence the results probably were quite representative of the equilibrium condition and, if anything, tended to overestimate the sorptivity. Thus it seems that the ratio of ten used in the cesium takeup experiments (see above) and in calculating the permeation coefficients (see Ref. 4-1) is accurate to better than 30% and perhaps on the high side, and so are the permeation coefficients themselves.

TASK 200: FISSION PRODUCT TRANSPORT CODES

Subtask 210: Code Development

Effect of Gas Phase Diffusion on Calculated Fission Gas Release

In the previous quarterly report (Ref. 4-1), it was established that gas phase diffusion is involved in the release of fission product gases from HTGR fuel material. This means that the helium pressure in an HTGR

system has an effect on fission gas release. This is a significant finding because the extent of fission gas release in HTGR systems, which operate at high pressure, is generally calculated (predicted) on the basis of fission gas release data measured at low pressure (for example, in the TRIGA test facility at General Atomic).

On the basis of data given in Ref. 4-9, an analysis was performed to determine how taking gas phase diffusion into account would affect the calculated fractional release of Kr-85m (the reference fission gas nuclide) for an HTGR system. (Fort St. Vrain was the reactor system used.) The results show that including gas phase diffusion in the calculations would reduce the calculated release of Kr-85m by factors of about 5 and 1.5 at low and high reactor power levels, respectively. It is clear, therefore that including the gas phase diffusion effect in reactor calculations would have a significant impact on predicted fission gas release.

As described in Ref. 4-1, evidence for the contribution of gas phase diffusion was obtained from (1) an analysis of fission gas release data obtained from reactor, capsule, and loop (high pressure) tests and TRIGA (low pressure) tests* and (2) TRIGA tests designed specifically to determine the contribution of gas phase diffusion. This evidence is hardly adequate for taking gas phase diffusion into account in reactor calculations. The reactor, capsule, and loop data have a large associated uncertainty and the TRIGA tests were conducted at low pressures over a narrow pressure range.

It is concluded that gas phase diffusion is an important consideration in reactor calculations and that existing data on gas phase diffusion are inadequate and need to be verified and quantified. Accordingly, additional experiments on gas phase diffusion are planned. These experiments will be conducted over the full range of pressures of interest.

*TRIGA tests consist of fission gas release measurements performed in a King furnace facility mounted in a TRIGA reactor at General Atomic.

FIPER Code Development

Two new features were recently added to FIPERQ, which is the reference code for calculating the release of fission product metals from HTGR fuel elements. The first is an automatic calculation of the "ϕ factor" or "partition coefficient" at material interfaces. Previously ϕ was input as a constant; now it is calculated as a function of concentration and temperature. The model is based on the assumption of a vapor pressure equilibrium in the interface gap.

The second feature is a calculation of the removal by transverse flow or a purge gas stream. This model is also based on a vapor pressure equilibrium. The effect of the removal is introduced by subtracting a concentration and flow dependent term from the fission product source.

Both of these new features introduce a nonlinearity into the calculation. This was taken care of by setting a logical flag and invoking the existing iteration capability of FIPERQ. The method was successfully tested in a sample problem.

Subsequent practical applications have disclosed some serious numerical problems in the method. The iterations do not always converge, and negative concentrations are observed. Preliminary investigations indicate that this is a result of an oversimplified iteration logic, and that a more sophisticated formulation will be required to solve this nonlinear problem.

Subtask 220: Code Validation

Analyses of two in-pile loops, the Commissariat a l'Energie Atomique (CEA) Saclay Spitfire loop (SSL-1) and Cadarache Pegase loop (CPL) tests, are being performed to permit comparisons of predicted and observed fission product release. Study of the behavior of cesium isotopes has been emphasized in the SSL-1 test (Refs. 4-10, 4-11). Final predictions of cesium release are being formulated and parametric studies are being carried out

to quantify the associated uncertainties. Work on the CPL-2 test includes characterization of both fission gases and fission metals (Refs. 4-10, 4-12). Analyses of the observed cesium profiles in the fuel rod - coolant hole graphite web are currently in progress. These profiles will be fit with the FIPERQ code as one step in the "validation" phase of the study. In addition, final calculations of temperatures and helium mass flows in the heat exchanger of CPL-2/1 are nearing completion.

TASK 300: FISSION PRODUCT DATA ANALYSIS

A review has begun of release rate data used in accident calculations relating to plant siting. The release rate data pertain to the release of fission products from fuel particles.

TASK 400: TRITIUM TRANSPORT

This task is not funded for FY-77.

TASK 500: PLATEOUT AND LIFTOFF

This task is not funded for FY-77.

TASK 600: COOLANT IMPURITY/CORE MATERIAL INTERACTION

Subtask 610: Reaction of Coolant Impurities with Fuel Material

Rate of Hydrolysis of Exposed Fuel Carbide

Summary and Conclusions. The effect of helium pressure on the apparent rate of hydrolysis of ThC_2 in graphite crucibles was determined at 573 K, utilizing pressures from 0.2 to 2.5 MPa (2 to 25 atm). The objective of this work was to quantitatively determine the overall reaction rate of the fuel hydrolysis reaction as a function of helium pressure for comparison with theoretical predictions. The data are needed for use in predicting the consequences of a steam in-leakage accident, where hydrolysis

of some of the exposed carbide fuel material is postulated to occur. The results of this study agree with the theoretical prediction that the rate of hydrolysis of ThC_2 fuel in graphite crucibles is inversely proportional to the total helium pressure and is therefore controlled by mass transport of water vapor through graphite.

Introduction. The mechanism of hydrolysis of exposed carbide fuel in HTGR fuel elements comprises two distinct steps: (1) transport of water vapor through the graphite and (2) chemical reaction. The chemical reaction is given by the equation:

$$ThC_2 + H_2O = ThO_2 + H_2O + CH_4 + H_2 + \text{other hydrocarbons} \qquad (4\text{-}4)$$

The yield of the gaseous products depends on experimental conditions, particularly temperature. At constant temperature, however, the yield of gaseous products H_2 and CH_4 was found to be relatively constant; therefore, monitoring the effluent process stream for H_2 and CH_4 was used as a measure of reaction rate.

The rate of chemical reaction is known to be very fast (Refs. 4-13, 4-14); therefore, the overall rate is predicted to be controlled by mass transport, due to transverse flow and/or diffusion. At reactor shutdown conditions, where the core pressure drop is low, transverse flow may be neglected, and the mass transport of water vapor through graphite to the reactive exposed carbide will be by Fickian diffusion as given by:

$$J = AD_{eff}\, dC/d\ell \quad , \qquad (4\text{-}5)$$

where J is the flux of water molecules through the graphite (mol/s), A is the diffusion area (m^2), ℓ is the diffusion length or web thickness (m), C is the water vapor concentration (mol/m^3), and D_{eff} is the effective diffusion coefficient for water vapor in the graphite (m^2/s). D_{eff} is given by:

$$D_{eff} = mD^{o}_{1,2} \frac{P_o}{P_T} \quad , \tag{4-6}$$

where m is a geometry correction term relating ordinary gas phase diffusion, $D^{o}_{1,2}$, to that in graphite, P_T is the total gas pressure (Pa), and $D^{o}_{1,2}$ is defined as the diffusion coefficient for H_2O in He at a standard pressure, P_o, which is 0.1 MPa (1 atm). $D^{o}_{1,2}$ can be calculated by the formula (Ref. 4-15):

$$D^{o}_{1,2} = 1.06 \times 10^{-8} T^{1.58}$$

$$(= 2.4 \times 10^{-4} \text{ m}^2/\text{s at } 573 \text{ K}) \tag{4-7}$$

If virtually all the water vapor that diffuses in reacts rapidly with the exposed carbide, then $dC/d\ell$ can be assumed to be equal to the concentration of water in the coolant channel divided by ℓ, and Eq. 4-5 and 4-6 can be combined to give:

$$J = \frac{mD^{o}_{1,2} A P_{H_2O}}{RT\ell} \frac{P_o}{P_T} \quad . \tag{4-8}$$

Thus at constant T and P_{H_2O}, the flux of water vapor is predicted to be inversely proportional to total pressure.

Previous studies (Ref. 4-16) showed that the number of water molecules reacting in Eq. 4-4 is nominally 2.6 times that of ThC_2. Accordingly, in the experiments described here, J is taken to be equal to 2.6 times the initial steady-state reaction rate of the ThC_2 which is obtained from measurements of H_2 and CH_4 production rate (see below). The procedure for this measurement is given in the next section.

Apparatus and Procedure. The reaction rate studies were carried out in a high-pressure double-chamber furnace (Fig. 4-7), capable of maintaining temperatures up to 1223 K at helium pressures up to 5 MPa (50 atm).

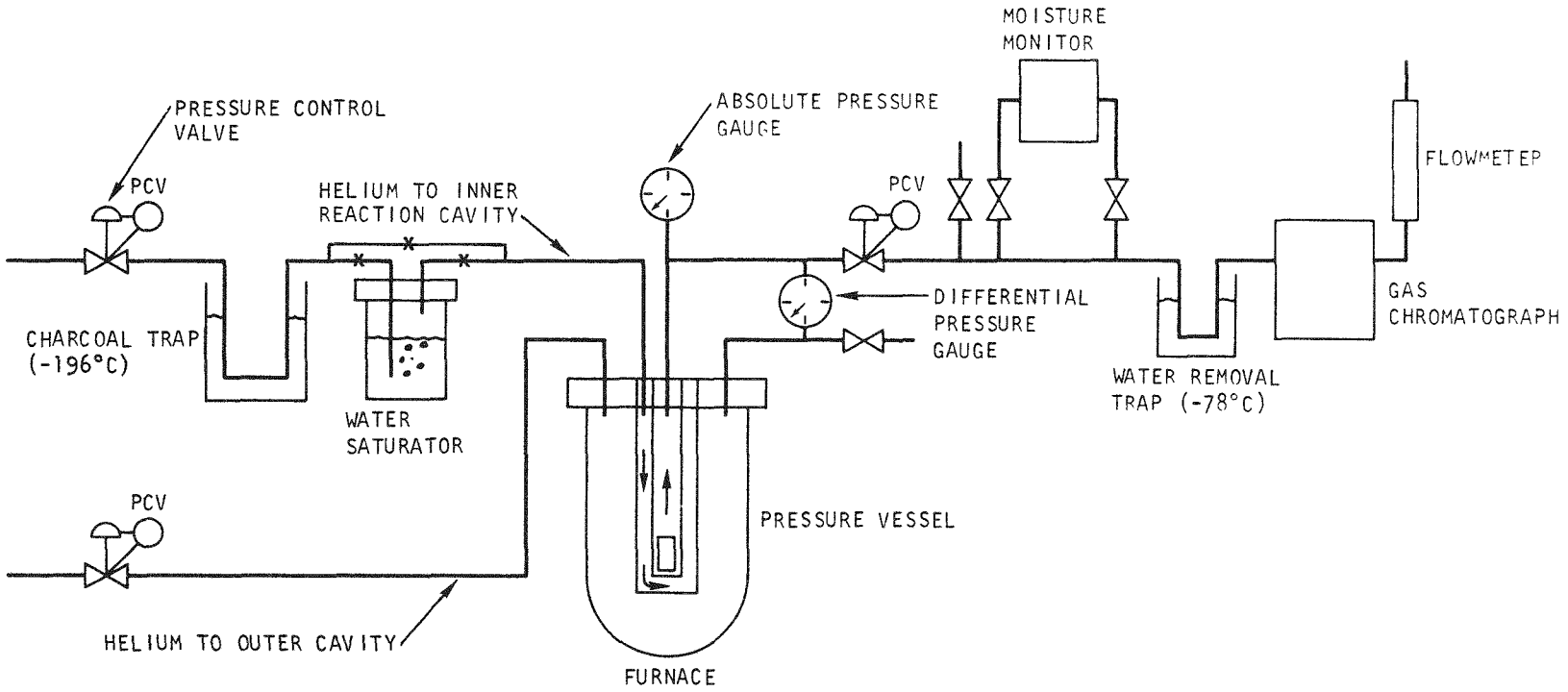

Fig. 4-7. High-pressure apparatus for thorium carbide hydrolysis studies

The inner and outer chambers were separated by a closed tube of Inconel 625, a material characterized by high strength and low oxidation at high temperatures. The inner chamber contained the test sample and was so designed that the incoming high-pressure helium-steam mixture was first heated and then passed upward over the graphite crucible. The outer chamber contained a resistance heater with suitable insulation and was independently pressurized with helium to maintain a near-zero pressure gradient across the Inconel chamber wall. The pressure within the furnace and any pressure differential existing between the inner and outer chambers were continuously monitored with absolute and differential pressure gauges, respectively.

Prior to entering the inner chamber of the furnace, the high-pressure helium was passed through a charcoal trap maintained at 77 K to remove traces of oxygen. The helium was then saturated with water vapor at controlled temperatures in a high-pressure saturator. After exiting from the furnace, the gas pressure was reduced and the low-pressure gas mixture was passed through a cold trap maintained at 195 K to remove the excess water vapor. Samples of the dry gas were automatically introduced into a Varian trace gas analyzer every 15 minutes. The chromatogram peak areas were automatically integrated with a Spectraphysics Minigrater.

The test samples were mixtures of bare ThC_2 fertile fuel kernels approximately 500 μm in diameter and graphite shim particles homogeneously mixed with a small amount of graphite glue (Dylon grade GC) and pressed into graphite crucibles. The test samples were then high fired at 2073 K for 6 hours to form fuel rods containing only ThC_2 and carbon. The ThC_2 loading was 0.1 Mg/m^3, which approximates a fuel rod having 13% failed fertile particles. The graphite crucible design is shown in Fig. 4-8. The crucibles were machined from either H-327, H-451, or ATJ graphite. They were especially designed with a thick bottom and a long threaded top with machined mating surfaces to ensure that transport of water vapor was primarily through the crucible walls.

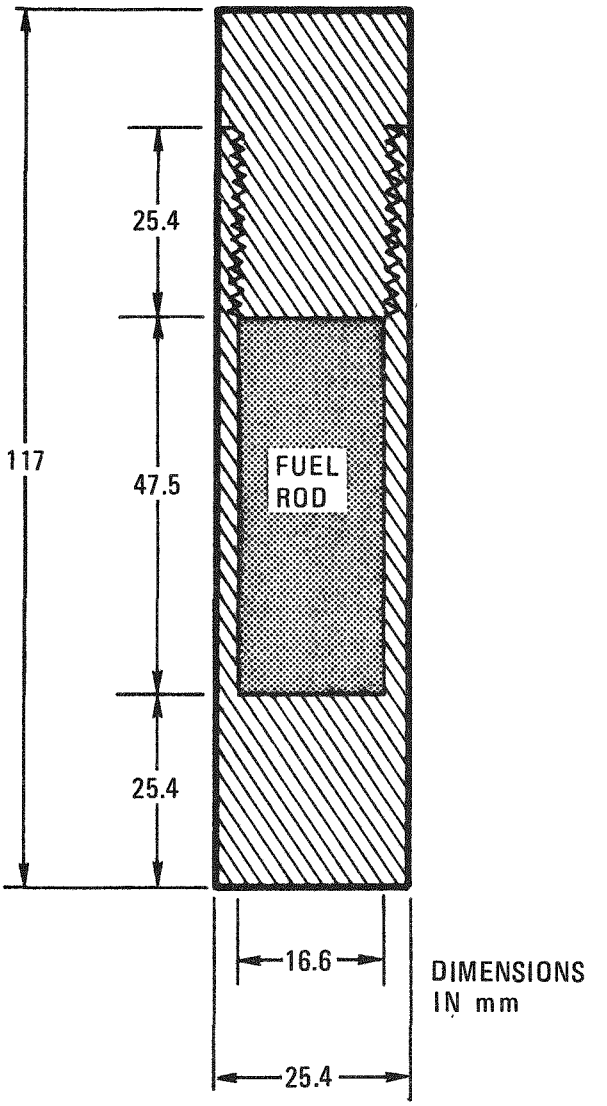

Fig. 4-8. Graphite crucible used in ThC_2 hydrolysis tests

The test procedure was to quickly transfer a fuel rod/crucible sample from the anneal furnace to the inner chamber of the pressure rig and to immediately evacuate the system. The furnace was then back filled with purified He to the desired pressure and flow was established at 1.8×10^{-5} m^3 (STP)/s (1.1 liter/minute). The furnace was then brought to the test temperature (573 K) and the effluent process gas was continuously monitored with the Varian trace gas analyzer to obtain background impurity concentrations. After test conditions had stabilized, the water saturator was valved in to start the test run.

At this point, one of two procedures was utilized: (1) variable He pressure or (2) constant He pressure. In the variable pressure method, using a water vapor pressure of 2.6 KPa (0.026 atm), the overall rate of reaction was slow enough to permit the use of several different helium pressures in a single run. That is, after the gaseous reaction products stabilized at a given He pressure, the pressure was adjusted to a new value and a new steady-state reaction rate was obtained. In a given run, several different pressures could be investigated before the hydrolysis rate was affected by depletion of the ThC_2. J was taken to be 2.6 times the rate of H_2 evolution. Previous work has shown that the number of moles H_2O reacted per mole ThC_2 is nominally 2.6 (see above), and it has been experimentally shown by the constant pressure runs that the total moles H_2 evolved at 573 K is roughly equal to the moles of ThC_2 in the sample (see Table 4-5).

The constant pressure method utilized a higher water vapor pressure [18 KPa (0.18 atm)] and operated at a single He pressure until all hydrogen and methane evolution had ceased.

At the conclusion of each run the total H_2 or CH_4 formed was obtained by integrating the concentration versus time data. The reaction rate was then converted to the fraction reacted per second at various times by dividing the amount of H_2 or CH_4 produced (moles/second) by the total moles obtained in the run. J was calculated by multiplying the rate (fraction/second) by 2.6 times the number of moles of ThC_2 in the samples.

TABLE 4-5
SUMMARY OF RESULTS OF HYDROLYSIS OF ThC_2 IN GRAPHITE CRUCIBLES
(Temperature = 573 K; He flow = 1.8×10^{-5} m^3(STP)/s; Th loading = 0.1 Mg/m^3(g/cm^3), ~3.5 mmol, total)

Run No.	Graphite Type	A ($\times 10^{-4}$ m^2)	ℓ ($\times 10^{-3}$ m)	P_{H_2O} (kPa)	P_{He} (MPa)	Total Gas Products Observed		n_{H_2} (a)	n_{CH_4} (b)
						H_2 (mmol)	CH_4 (μmol)		
4	H-451	33.5	0.508	2.63	Variable	ND (b)	ND	1.01	0.86
5	H-451	33.5	0.508	2.63	Variable	ND	ND	1.06	0.88
6	H-451	33.5	0.508	18.2	1.15	2.9	40		
7	H-451	33.5	0.508	18.2	0.79	2.7	48	0.86	1.03
8	H-451	33.5	0.508	18.2	0.44	2.9	52		
9	H-451	33.5	0.508	18.2	0.20	4.4	58		
10	ATJ	31.2	0.445	18.2	0.51	3.7	58	1.0	0.86
11	ATJ	31.2	0.445	18.2	1.46	2.9	58		
12	H-327	33.5	0.438	18.2	0.47	2.5	52	0.8	1.03
13	H-327	33.5	0.438	18.2	1.67	3.7	52		
						3.2 avg	52.3 avg	0.95 avg	0.93 avg

(a) n is the "order" or pressure dependence derived from the slope of plots of log rate versus log P_{He}; see Fig. 4-13.

(b) ND = not determined.

Experimental Results. The conditions and results of all the tests are given in Table 4-5.

Figure 4-9 is a plot of the concentrations of H_2 and CH_4 versus time for run 6, which was operated at a constant P_T [1.14 MPa (11.3 atm)]. During this run the water saturator was intentionally turned off for 920 minutes, demonstrating that the product gases were indeed evolved during hydrolysis of the ThC_2 sample and not from some other source. Figure 4-9 shows that hydrogen evolution during carbide hydrolysis at elevated temperatures far exceeds CH_4 formation. Also, the data listed in Table 4-5 show that the total moles H_2 produced is roughly equal to the moles of ThC_2 in the sample, which is 1/2.6 the theoretical yield. This suggested that a large fraction of the product gases remained sorbed in the sample or graphite. In fact, when some of the crucibles were heated above 573 K at the conclusion of the hydrolysis runs, large quantities of H_2 and CH_4 were desorbed from the samples, indicating rather strong sorption of these species of 573 K.

Plots of the fraction H_2 evolved for runs 6, 7, 8, and 9 are given in Fig. 4-10. It is seen that through about 50% of the reaction, the reaction rates are all quite linear with time. For analysis of the effect of pressure, only the initial reaction rates were used. Figure 4-11 is a plot of the fraction of H_2 versus the fraction of CH_4 evolved for four separate experiments at different He pressures. This plot shows that the ratio of H_2 to CH_4 was independent of the total pressure and that when all the H_2 had evolved, the CH_4 production ceased.

Figure 4-12 is a plot of log H_2 evolution (μmol/s) versus log total pressure for the H-451 crucible using both the variable pressure and constant pressure methods. The slopes of the lines thus obtained in the H_2 plot in Fig. 4-12 are all nearly one, indicating agreement with the theoretical prediction. The rate is inversely proportional to total pressure. Also of interest is the fact that the absolute reaction rates of the two methods are very nearly linear with water concentration. The flux of water vapor, J, for three different graphite crucibles using the constant pressure method is

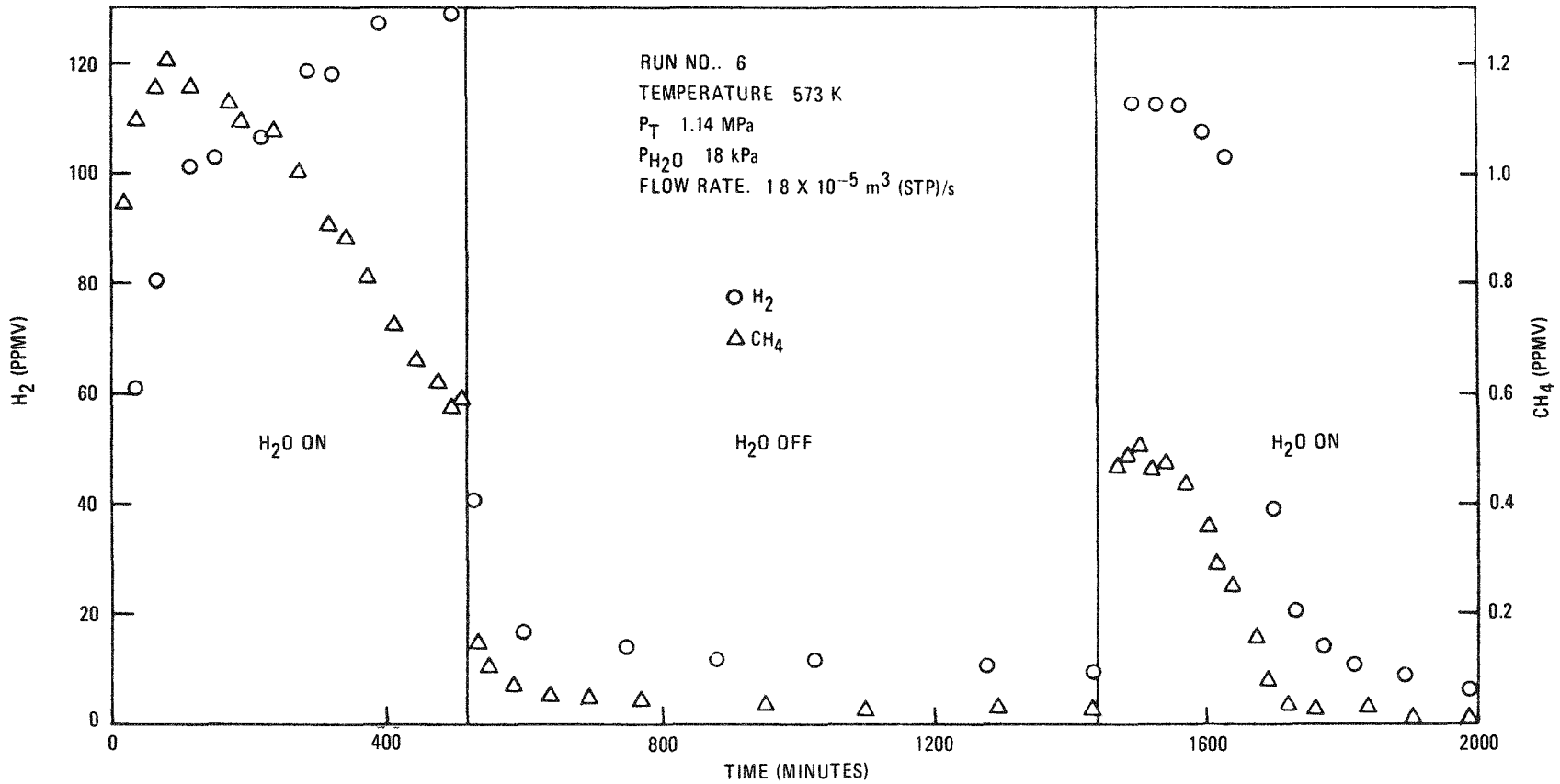

Fig. 4-9. Methane and hydrogen evolution versus time during hydrolysis of ThC_2

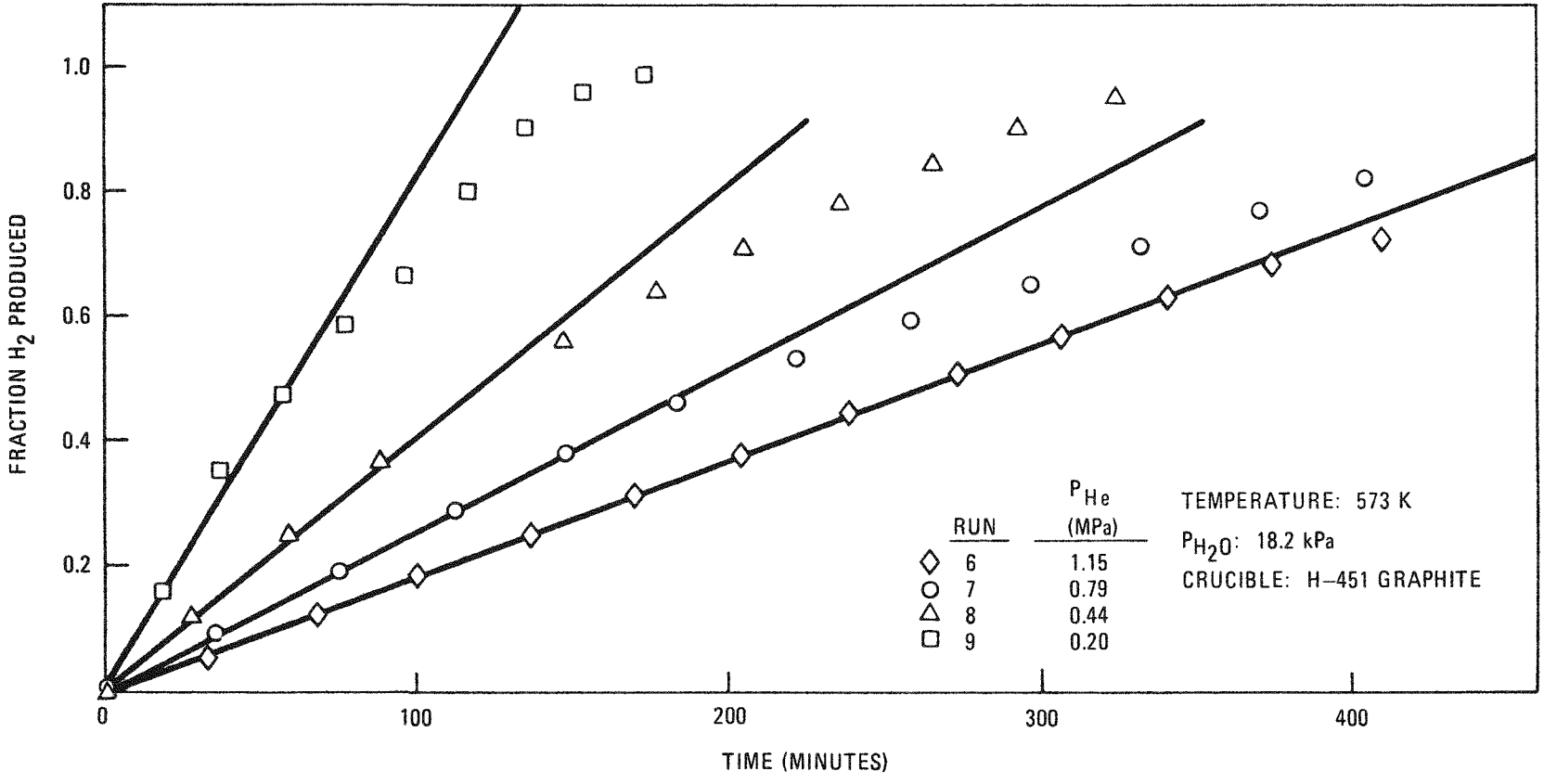

Fig. 4-10. Effect of pressure and time on hydrogen evolution during hydrolysis of ThC_2

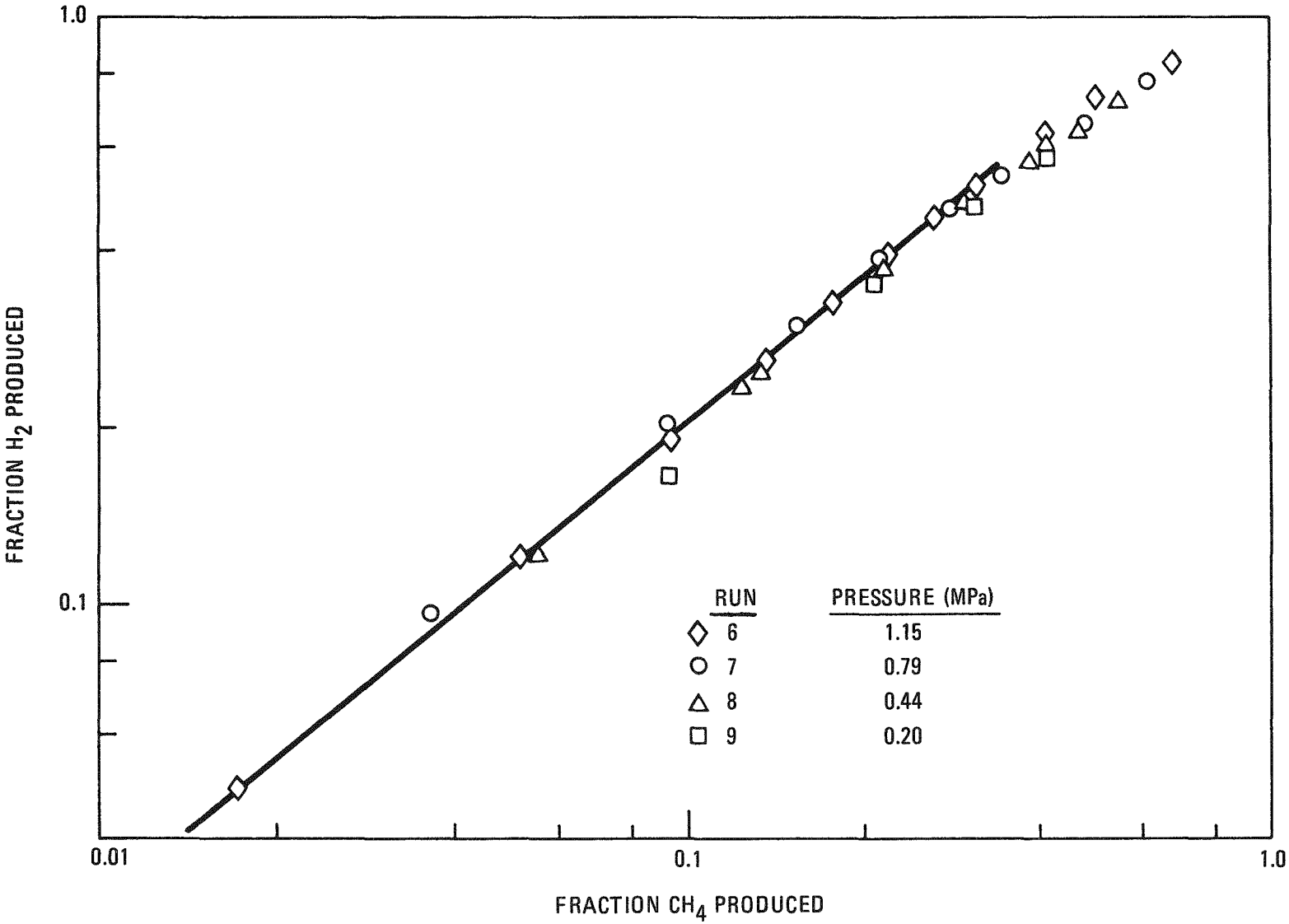

Fig. 4-11. Relation between fraction H_2 produced and fraction CH_4 produced during hydrolysis of ThC_2 in H-451 graphite crucible

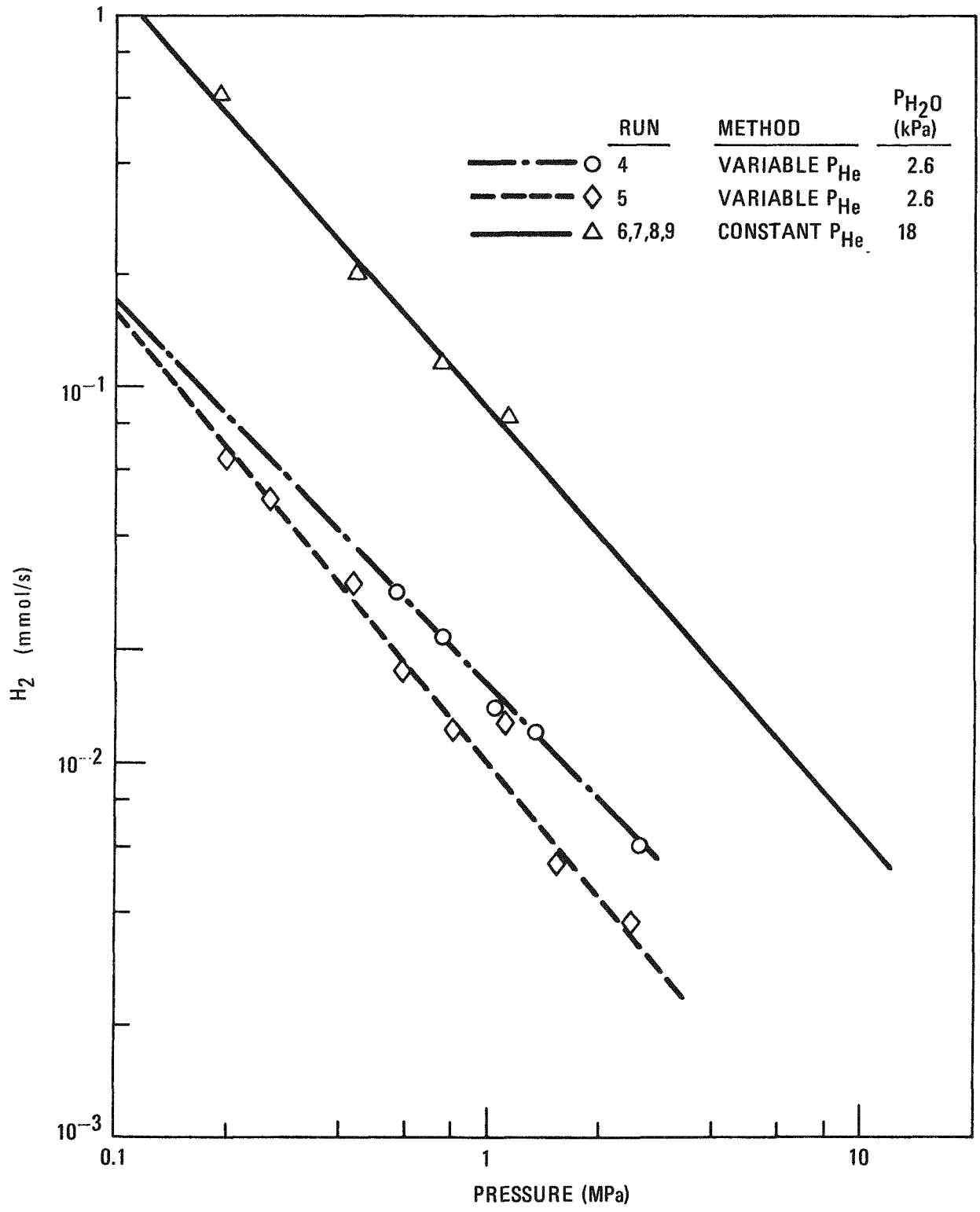

Fig. 4-12. Effect of total pressure on rate of hydrolysis of ThC_2 in H-451 graphite

shown in Fig. 4-13. These data show that all three graphite types demonstrate the predicted linear dependence of J on P_T. Also, the apparent diffusivities of the graphites are within a factor of two of each other, which is well within the normal variability for a given grade.

Effective diffusion coefficients, D_{eff}, for all the test runs are plotted versus reciprocal pressure, P_T, in Fig. 4-14. From these data and using Eq. 4-6, average geometry factors, m, were calculated (Table 4-6).

TABLE 4-6
m VALUES DERIVED FROM ThC_2 HYDROLYSIS TESTS

Graphite	m
H-451	0.004
H-327	0.007
ATJ	0.009

The values of m in Table 4-6 and D_{eff} in Fig. 4-14 are somewhat uncertain because they are directly proportional to the value of the molar ratio of water reacting with ThC_2. This molar ratio, taken to be 2.6 in this study, is uncertain and, therefore, the values of m (or D_{eff}) should be confirmed with further studies.

TASK 700: PLANNING AND COORDINATION

Efforts under this task are continuing.

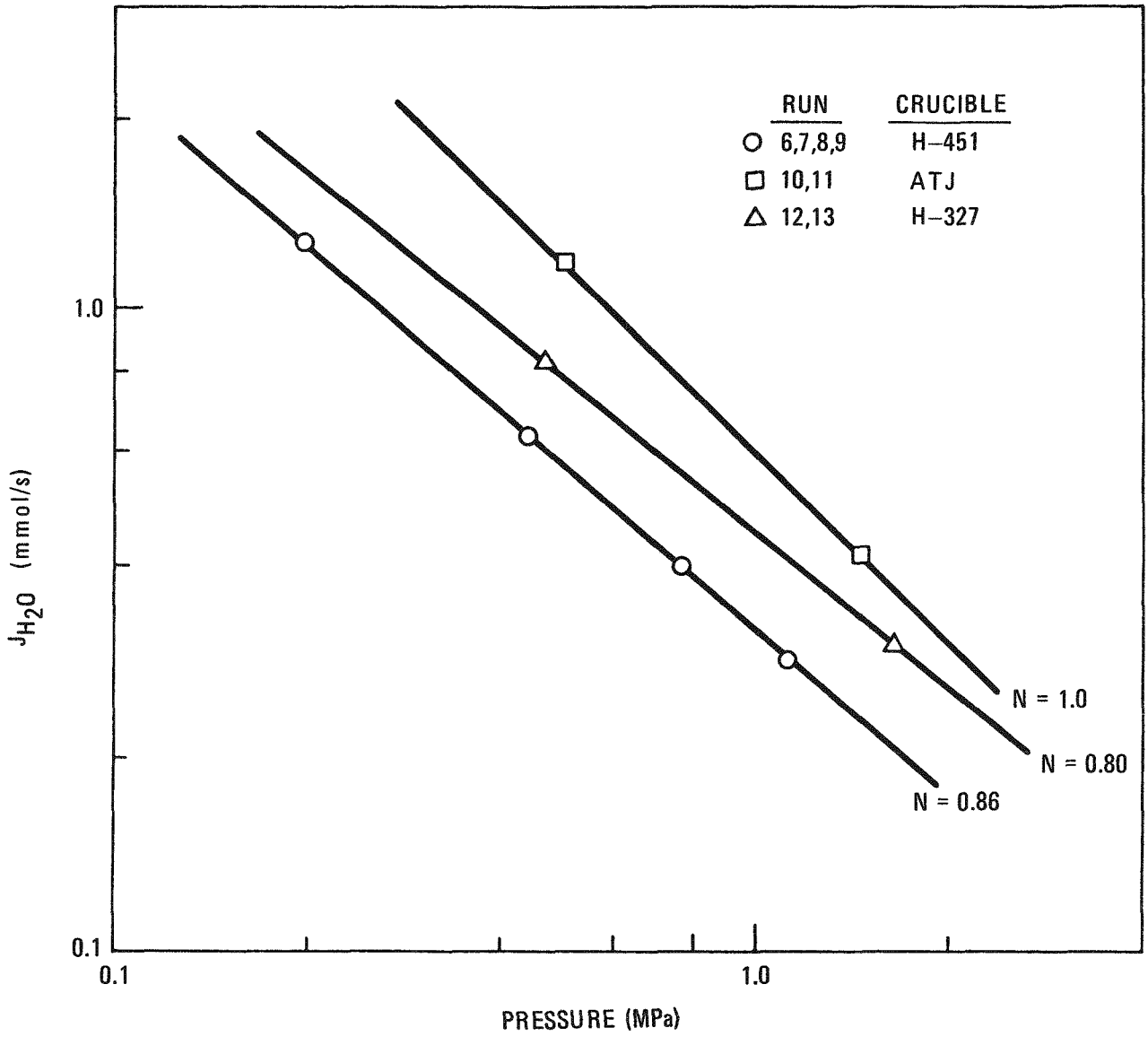

Fig. 4-13. Effect of total pressure on flux of water, J

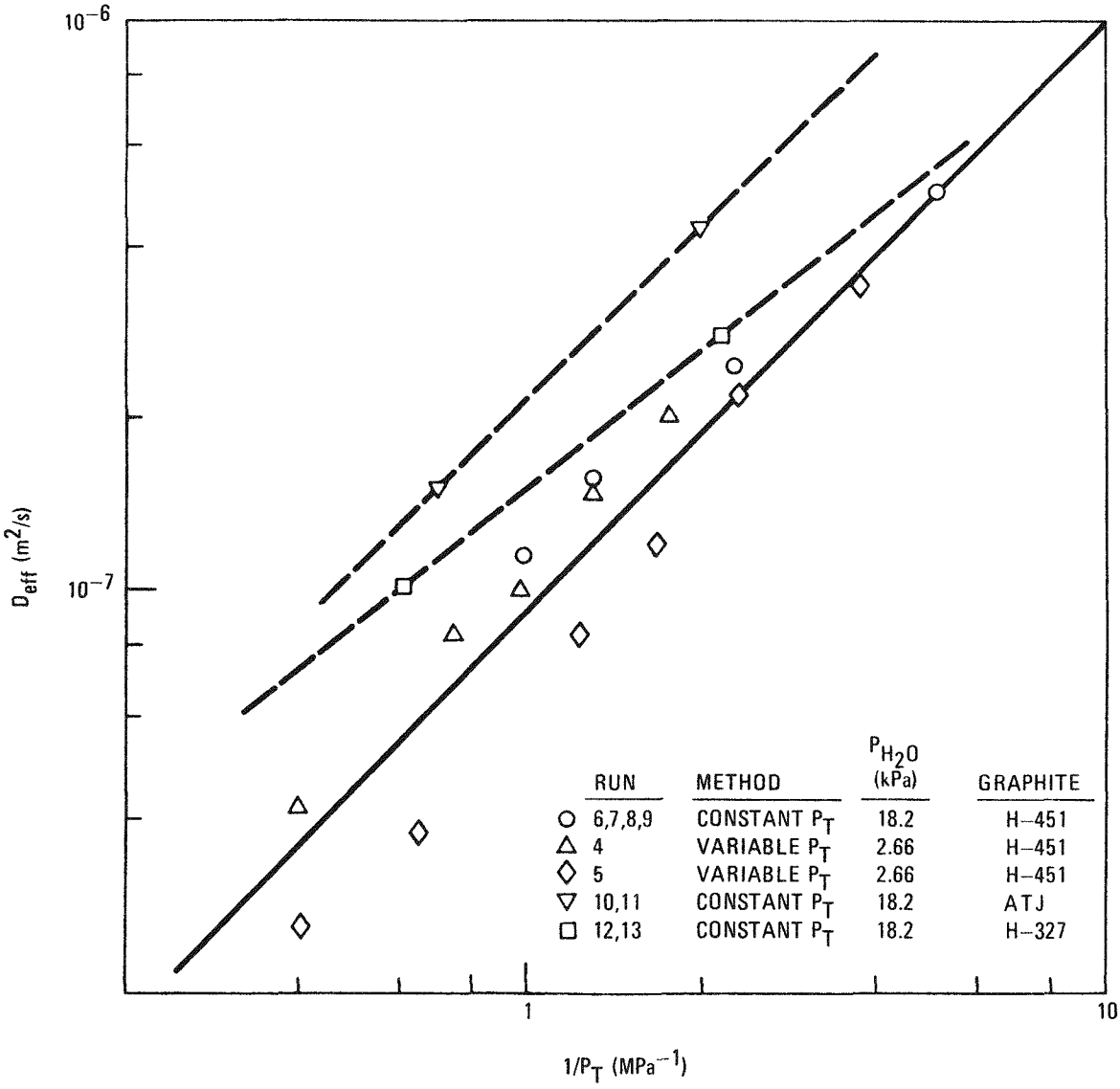

Fig. 4-14. Effect of total pressure on effective diffusion coefficient

TASK 900: FORT ST. VRAIN CHEMISTRY SURVEILLANCE

Subtask 940: Fort St. Vrain Coolant Impurity Surveillance

Evaluation of HTGR Coolant Core Interactions Using Fort St. Vrain Startup Data*

Summary. The measured gas compositions in the coolant of the Fort St. Vrain HTGR during the initial rise to 27% power have been compared with predicted compositions using the Graphite Oxidation Program (GOP). Although changes in the code are clearly needed for a close correlation with actual compositions, a general agreement has been achieved. Evaluation of the data is complicated at present by outgassing of the core components and the fact that the hydrogen getter portion of the purification system was not operative. In spite of these complications, the data suggest that radiolytic reactions are occurring and, at the low temperatures studied to date, appreciably affect the gas composition. The GOP analyses clearly overestimate the effect of irradiation as shown in the comparison with actual startup data at 19.5 and 27% of full power. Adjustment will be made in the input data to achieve better agreement. It is anticipated that more conclusive results will be achievable from future tests where more of the uncertainties will be eliminated.

Introduction. Successful operation of a HTGR requires that the reactions of the coolant gas with the core components be almost eliminated. Thus, very high purity helium is used for the coolant in direct contact with the graphite fuel blocks. In spite of great care, very low levels of reactive impurities are expected during normal operation, with much higher concentration possible during abnormal or accident conditions. To enable reactor designers to set realistic helium purity standards, estimates must be made of the rates of reactions expected. Considerable kinetic data have been collected over the past decade in an attempt to accurately predict the

*This work was performed by G. L. Tingey and W. C. Morgan (Battelle Pacific Northwest Laboratory) under a subcontract.

coolant chemistry of the HTGR system. The task presently is to verify, and modify where necessary, the codes used for these predictions. The startup tests of the Fort St. Vrain HTGR provide a unique opportunity to test the validity of these codes. The current tests are particularly suited for this verification because the water levels are sufficiently high to yield measurable reaction rates, and the lower power tests are conducted at low enough temperatures to enable evaluation of irradiation-induced reactions without interference from thermal reactions.

In this study, the measured gas compositions are compared with those calculated using the GOP code (Refs. 4-17, 4-18). These comparisons are then used to evaluate the validity of the reaction parameters used in the GOP code. Revisions are made where necessary to improve the accuracy of the code.

In this report, measured gas compositions up to 27% of full power are compared with calculations. The conclusions from these evaluations, although preliminary, give some insight into the importance of irradiation-induced reactions in the HTGR system.

Description of Model. Because of the complicated nature of the coolant chemistry of the reactor system, it is virtually impossible to predict the effect of impurity gases in a helium-cooled reactor without the aid of a mathematical model. Several computer codes to evaluate the coolant chemistry have been developed in the U.S. and in Europe. In this study, data from the initial rise to power of the Fort St. Vrain HTGR were evaluated using the GOP code, which treats the system in a fairly simple fashion, but which attempts to include most of the anticipated chemical reactions including the irradiation-induced reactions. An earlier version of this code and the model on which the code is based were described previously (Refs. 4-17, 4-18).

The current version of this code (GOP-3) considers ten reactions, including four thermally induced reactions and six radiolytic reactions.

The kinetic rate expressions and rate constants used in the code for the thermal reactions are depicted in Table 4-7. The rate constants for the gas-solid reactions are for the chemically controlled rates.

It is, therefore, necessary to account for diffusion in and out of the pores of the graphite. This is done in the GOP code by calculating an "equivalent depth of oxidation" and by solving the Bessel functions for diffusion from the interior of a hollow cylinder to obtain the volume integral reaction rates.

The radiolytic reactions along with their yields (G values) are listed in Table 4-8. The kinetic rate expression for these reactions is of the general form

$$R^* = EF_p F_c G T^{1/2} e^{-A/RT} \quad , \tag{4-9}$$

where E = energy transferred to the gas molecules,

F_p = a partition function to account for distribution of active species to the various paths,

F_c = a factor which accounts for the efficiency of energy transfer from helium to the reactive gases at low concentrations,

G = radiolytic yield of the reaction in units of reactions per unit of energy adsorbed in the gas,

T = gas temperature,

A = activation energy for the reaction.

Although some of the G values for the radiolytic rates have experimental bases, the other parameters, i.e., distribution of active species and efficiency of energy transfer, are merely estimates based on scientific judgment. Thus, to establish the validity of the calculations, experimental evaluation of these parameters is badly needed. The analysis of the Fort St. Vrain data is one attempt to obtain experimental data for such an evaluation.

TABLE 4-7
KINETIC RATE EXPRESSIONS

Reaction	Rate Expression	Kinetic Constants[(a)]	Reference
$C + H_2O \rightarrow CO + H_2$	$\frac{d[-C]}{dt} = \frac{k_1 P_{H_2O}}{1 + k_2 P_{H_2}^{0.75} + k_3 P_{H_2O}}$	$k_1 = 0.513\ e^{-40,900/RT}\ Pa^{-1} s^{-1}$ $k_2 = 2.92 \times 10^{-6}\ e^{+28,600/RT}\ Pa^{-0.75}$ $k_3 = 5.24 \times 10^{-7}\ e^{+27,500/RT}\ Pa^{-1}$	4-15
$C + CO_2 \rightarrow 2CO$	$\frac{d[-C]}{dt} = \frac{k_1 P_{CO_2}}{1 + k_2 P_{CO} + k_3 P_{CO_2}}$	$k_1 = 16.7\ e^{-66,800/RT}\ Pa^{-1} s^{-1}$ $k_2 = 1.13 \times 10^{-9}\ e^{+29,500/RT}\ Pa^{-1}$ $k_3 = 2.63 \times 10^{-5}\ Pa^{-1}$	4-19
$CO + H_2O \rightarrow CO_2 + H_2$	$\frac{d[-CO]}{dt} = \frac{k_1 P_{CO}^{1/2} P_{H_2O}}{\left(1 + k_2 P_{H_2O}\right)^{1/2}}$	$k_1 = 2.52 \times 10^{11}\ e^{-65,500/RT}\ \ell^{1/2} mol^{-1/2} s^{-1}$ $k_2 = 2.18 \times 10^{3}\ \ell\ mol^{-1}$	4-20
$CO_2 + H_2 \rightarrow H_2O + CO$	$\frac{d[-CO_2]}{dt} = k_1 P_{CO_2} P_{H_2}^{1/2} + k_2 P_{CO_2} P_{H_2}^{1/3}$	$k_1 = 1.2 \times 10^{13}\ e^{-78,000/RT}\ \ell^{1/2} mol^{-1/2} s^{-1}$ $k_2 = 7.6 \times 10^{4}\ e^{-39,200/RT}\ \ell^{1/3} mol^{-1/3} s^{-1}$	4-21

[(a)] Activation energies are given in cal/mol, and R = 1.987 cal deg^{-1} mol^{-1}; to convert calories to joules, multiply by 4.18 and use R = 8.314 joule deg^{-1} mol^{-1}. Other units are Pascal (Pa), liter (ℓ), mole (mol), and second (s).

TABLE 4-8
RADIOLYTIC REACTIONS CONSIDERED IN GOP-3

Reaction	Yield[a] (reactions/100 eV)	Activation Energy (cal)	Reference
$C + 2H_2O \rightarrow CO_2 + 2H_2$	0.9	--	4-22
$C + CO_2 \rightarrow 2CO$	0.675	--	4-23
$2CO \rightarrow C + CO_2$	1.0	--	(b)
$CO + H_2O \rightarrow CO_2 + H_2$	0.179	200	4-24
$H_2 + CO_2 \rightarrow CO + H_2O$	0.757	215	4-24
$C + 2H_2 \rightarrow CH_4$	1.0	--	(b)

[a] Radiolytic yields are normally given in G values, which are the yields in units of molecules formed or removed per 100 eV (or 16 aJ) of absorbed energy.

[b] Assumed yield.

Integration of the rate of change in gas composition with distance along the flow channel is accomplished by use of the Runge-Kutta method to obtain starting data required by the predictor-corrector procedure at the inlet to the flow channel and repeated use of Milne's predictor formula to obtain integral solutions at subsequent points along the channel. Provisions for input variations in temperature and radiation dose rate with position, as well as variations of flow rate and flow fraction for different regions of the core, allow considerable flexibility in modeling the operating reactor.

Data on the temperature and power distributions, flow velocities, and flow fractions for each of the 37 fuel regions of the Fort St. Vrain reactor at three different times during the planned startup testing were obtained from GA. These data were reduced to 5 or 6 equivalent regions. For many of the calculations, satisfactory accuracy could be obtained when the 5 or 6 equivalent regions were further reduced to a single region to represent the entire reactor core. With the single-region representation, 1 hour of reactor operation at full power requires only 25 seconds of computer time on the Control Data Corporation CDC-7600 computer system.

Results. Initial startup tests in the Fort St. Vrain reactor were conducted in April and May 1975. During these tests the power was limited to 2% of full power. Although the data were very limited, and to some extent uncertain, valuable information was obtained which was compared (Ref. 4-24) with calculated gas compositions.

Startup tests were again resumed in July 1976 and operation continued until early August. During these tests the reactor was operated at various power levels up to 27% of full power. Gas compositions were analyzed by gas chromatography sensitive to concentrations of less than 0.1 ppm. Table 4-9 lists the results of the analysis at five power levels. These levels were chosen because the power was held relatively constant for a period long enough to have a reasonable chance of nearing the steady-state gas compositions. Table 4-9 also shows calculated gas compositions for conditions comparable to those of the tests. Since moisture input is probably

TABLE 4-9
MEASURED AND CALCULATED GAS COMPOSITIONS FOR FORT ST. VRAIN STARTUP CONDITIONS

	2% Power		7.5% Power		11.4% Power		19.5% Power		27% Power	
	GOP	Measured 7/15 to 7/20	GOP	Measured 7/11 to 7/15	GOP	Measured 7/24 to 7/27	GOP	Measured 7/30	GOP	Measured 8/1 to 8/2
H_2O, ppm	20	30	16	50	33	34	102	100	90	80
CO, ppm	0.02	0.2	0.8	1	3.7	1.5	25	2	32	3
CO_2, ppm	1.7	0.7	4.9	3	13.3	2.5	56	6	60	7
H_2, ppm	14	22	7.6	25	18.4	33	65	80	61	30
CH_4, ppm	1.0	0.3	1.5	1.2	6.0	2	35	3.5	45	3
H_2/H_2O	0.7	0.73	0.5	0.5	0.56	1	0.64	0.8	0.67	0.38
H_2/CH_4	14	73	5	21	3.1	16.5	1.9	23	1.4	10
CO/CO_2	0.01	0.3	0.16	0.33	0.28	0.6	0.45	0.33	0.53	0.43
Outlet temp, °C	240	240	330	330	390	390	450	450	500	500
H_2O leak rate, kg/hour	0.018	-	0.018	-	0.018	-	0.18	-	0.18	-
$\frac{H_2 \text{ purification rate}}{H_2O \text{ purification rate}}$	0.1	∿0	1	∿0	1	∿0	1	∿0	1	1

due mostly to outgassing of the core components at an unknown rate, the inleakage rates have been adjusted to yield a moisture level approximately that observed in the tests. The measured impurity gas concentrations are quite variable, and thus the values listed in Table 4-9 are best estimates of the steady-state composition. The ratio of purification flow to total flow was also varied during the testing period but was monitored. Therefore, the measured purification factors were used for the calculations.

The hydrogen purification system was not functioning properly during the testing period with the exception of the last 2 days of the 27% power runs; therefore, one parameter which should be adjusted is the hydrogen purification factor. This has been tested at the 2% power level and yields an improved fit with the measured values, but this parameter has not yet been considered at other power levels.

Discussion. The comparison of the data in Table 4-9 shows the extent of agreement of the calculated gas compositions with the measured ones. The extent of agreement is best indicated by comparing calculated and measured gas product ratios. Obviously the agreement is not as close as desired, but many meaningful observations appear to be possible. It should be recognized that the model treats a system where the only source of impurity is from leakage from outside the core. During the early stages of startup this is certainly not true, since gases are being desorbed from the core components. It could be argued that the gas compositions are entirely dictated by outgassing rates and it is indeed true that the product ratios fall within the widely varying product ratios reported from outgassing of various grades of graphite. However, the almost steady source of gases observed at constant temperature is not consistent with the exponentially decreasing rate observed in outgassing studies. In addition, outgassing should be very slow or nonexistent when the temperature is decreased during the course of the test below the maximum temperature to which the core has been exposed. For these reasons the tendency is to reject the theory that the gases observed are solely a result of outgassing. Rather it appears that chemical reactions are occurring between the graphite and the water

vapor or other reactive gases. Also reactions are expected to occur between the gaseous components in the coolant.

GOP estimates predict that thermally induced reactions make an almost insignificant contribution to the reactions at the temperatures of interest (up to 500°C). Therefore, radiolytic processes appear to be controlling the system.

The gas product ratios are reasonably close to predicted values in most cases. The gas composition data at 19.5 and 27% power, however, clearly show that the code is overestimating the rate of the radiolytic process. Changes will, therefore, be made in the code to bring the prediction closer to the measured values. Studies are currently under way to evaluate the functions which are most likely to be causing this error.

Future tests are expected to resolve some of the problems in interpertation of the data because outgassing should continue to decrease and the purification system will be operative for hydrogen removal. The true success of this program is to be measured by improving the ability to more accurately predict gas compositions in the HTGR. Some progress toward this goal is already being made.

REFERENCES

4-1. "HTGR Fuels and Core Development Program Quarterly Progress Report for the Period Ending August 31, 1976," ERDA Report GA-A14046, General Atomic Company, September 24, 1976.

4-2. "HTGR Base Program Quarterly Progress Report for the Period Ending August 31, 1970," USAEC Report GA-10288, Gulf General Atomic, September 30, 1970.

4-3. "HTGR Base Program Quarterly Progress Report for the Period Ending May 30, 1969," USAEC Report GA-9372, Gulf General Atomic, June 27, 1969.

4-4. "HTGR Base Program Quarterly Progress Report for the Period Ending February 28, 1967," USAEC Report GA-7801, General Atomic, Division of General Dynamics, April 20, 1967.

4-5. Myers, B. F., and W. E. Bell, "Cesium Transport Data for HTGR Systems," ERDA Report GA-A13990, General Atomic Company, to be published.

4-6. "HTGR Accident Initiation and Progression Analysis Status Report - Volume V. AIPA Fission Product Source Terms," ERDA Report GA-A13617, General Atomic Company, February 1976.

4-7. "HTGR Fuels and Core Development Program Quarterly Progress Report for the Period Ending May 31, 1975," ERDA Report GA-A13444, General Atomic Company, June 30, 1975.

4-8. "HTGR Fuels and Core Development Program Quarterly Progress Report for the Period Ending February 28, 1975," ERDA Report GA-A13353, General Atomic Company, March 31, 1975.

4-9. Myers, B. F., et al., "The Behavior of Fission Product Gases in HTGR Fuel Material," ERDA Report GA-A13723, General Atomic Company, to be published.

4-10. "HTGR Fuels and Core Development Program Quarterly Progress Report for the Period Ending August 31, 1975," ERDA Report GA-A13592, General Atomic Company, September 30, 1975.

4-11. "HTGR Fuels and Core Development Program Quarterly Progress Report for the Period Ending February 29, 1976," ERDA Report GA-A13804, General Atomic Company, March 31, 1976.

4-12. "HTGR Fuels and Core Development Program Quarterly Progress Report for the Period Ending May 31, 1976," ERDA Report GA-A13941, General Atomic Company, June 30, 1976.

4-13. Burnette, R. D., "The Hydrolysis of Uranium and Thorium Carbides," USAEC Informal Report GAMD-9670 (Rev.), Gulf General Atomic, October 1, 1969.

4-14. Engle, G. B., W. V. Goeddel, and C. S. Luby, "Reaction Rate Studies of Thorium-Uranium Dicarbides in Moist Air," Am. Ceram. Soc. J. 45 (3), 136 (1962).

4-15. Peroomian, M. B., A. W. Barsell, and J. C. Saeger, "OXIDE-3: A Computer Code for Analysis of HTGR Steam or Air Ingress Accidents," General Atomic Report GA-A12493 (GA-LTR-7), January 15, 1974.

4-16. Fuel Design Data Manual, Issue B, General Atomic unpublished data, December 17, 1975.

4-17. Giberson, R. D., and C. A. Oster, "Computer Calculation of Reactor Graphite Oxidation," Battelle Pacific Northwest Laboratory Report BNWL-331, April 1967.

4-18. Giberson, R. C., and G. L. Tingey, "Reactions of Gaseous Impurities in a High-Temperature Gas-Cooled Reactor," Battelle Pacific Northwest Laboratory Report BNWL-974, December 1968.

4-19. Giberson, R. C., "Rate Constants for the Reaction of Carbon Dioxide and Water Vapor with KC Graphite," Battelle Pacific Northwest Laboratory Report BNWL-CC-1381, October 1967.

4-20. Graven, W. M., and F. J. Long, J. Am. Chem. Soc. 76, 2602, 6421 (1954).

4-21. Tingey, G. L., J. Phys. Chem. 70, 1406 (1966).

4-22. Woodley, R. E., "The Radiolytic Reaction of Graphite with Water Vapor," Battelle Pacific Northwest Laboratory Report BNWL-SA-1804, April 1968.

4-23. Tingey, G. L., R. G. Giberson, and E. D. Jenson, Chem. Eng. Prog., Symp. Ser. 66 (104), 73 (1970).

4-24. Turcotte, R. P., and G. L. Tingey, "Radiolysis of Helium Diluted Mixtures of Carbon Monoxide and Water Vapor," Battelle Pacific Northwest Laboratory Report BNWL-1664, June 1972.

4-24. Tingey, G. L., and W. C. Morgan, "Radiolytic Reactions in the Coolant of Helium-Cooled Reactors," in Transactions of the Symposium on Gas-Cooled Reactors with Emphasis on Advanced Systems, Vol. 1, International Atomic Energy Agency, Vienna, 1976, pp. 309-317.

9. HTGR FUEL DEVELOPMENT AND ENGINEERING

189a NO. 00551

TASK 100: FUEL PRODUCT SPECIFICATION

Work continued on the Fuel Product Specification support document. The BISO ThO_2 portion of the document was drafted and prepared for review at ORNL.

TASK 200: ACCELERATED IRRADIATION TESTING

Subtask 210: Fresh Fuel Qualification

Summary and Conclusions

Irradiation of capsule P13V was completed on November 11, 1976. The capsule reached a peak exposure of 9×10^{25} n/m^2 $(E > 29\ fJ)_{HTGR}$, and the end-of-life Kr-85m fission gas release was $<10^{-4}$ for all cells. The post-irradiation examination (PIE) on capsule P13V is scheduled to begin in the GA Hot Cell during the first quarter of FY-78.

The PIE of capsule P13T was started in the GA Hot Cell on September 10, 1976. The capsule has been disassembled, and the following PIE items have been completed:

1. Fuel rod removal from graphite bodies.
2. Visual examination.
3. Dimensional measurements on graphite bodies and fuel rods.
4. Gamma scanning and fission gas release.

The PIE is scheduled for completion by January 1977, with a final report to be issued by March 1978.

Capsule P13V

Capsule P13V is a constant temperature and thermal cycle qualification test of WAR TRISO and ThO_2 BISO cured-in-place fuel. Irradiation of this capsule was started on March 2, 1976 and was completed on November 11, 1976 when the experiment reached its peak design exposure of 9×10^{25} n/m^2 $(E > 29\ fJ)_{HTGR}$.

Following the GETR shutdown on November 11, 1976, the P13V capsule was discharged from the reactor on November 13, 1976. Neutron radiographs of the capsule have been planned prior to its shipment to the GA Hot Cell. The PIE on P13V is currently scheduled to begin during the first quarter of FY-78.

Cells 4, 5, and 6 reached design temperature only 50 to 75% of the time. During these periods, the temperature averaged 50° to 100°C below design for cells 5 and 6 and 100° to 200°C below design for cell 4. The low-temperature operation of these cells was caused by frequent GETR shutdown, which resulted in generally low control rod bank positions. The low rod bank position caused the flux seen by P13V to be generally skewed from design conditions toward the bottom of the core.

Sufficient W/Re thermocouple decalibration data were internally generated from P13V so that a set of new decalibration factors could be derived. In late October these data, when averaged with the decalibration factors established for P13R and P13S, were used to modify the control temperature set point for each of the P13V cells. As a result of this analysis, it appeared that during periods in which the GETR rod bank was greater than 25 in., cell 5 of P13V was operated at near 1500°C rather than the specified 1375°C temperature. The operating set point for cell 5 was therefore changed from 1375° to 1500°C on October 22, 1976 so that this cell would continue to operate at the control temperature set point specified originally in the P13V Irradiation Test Plan.

Flow tests run during a recent GETR shutdown indicated that cell 3 and the thermocouple cell had developed secondary-to-primary containment leaks. Cells 1, 2, and 4 had previously exhibited these same leaks. In addition, a special argon tracer gas test on all of the P13V cells indicated that cells 5 and 6 also contained these leaks. This problem will be investigated through the neutron radiographs planned for P13V and during the postirradiation examination of this capsule.

Recent (October 3, 1976) steady-state operating conditions for P13V are shown in Table 9-1 and in Figs. 9-1 through 9-8.*

Thermal analysis work on P13V was continued during the quarter. All of the TAC2D computer models were completed for each cell and beginning-of-life temperature matching was begun. Preliminary results indicated general agreement within 10 to 15% between calculated and corrected thermocouple temperatures. Efforts are under way to correct the calculated power in each cell to account for the difference.

Capsule P13T

Introduction. Capsule P13T is the ninth in a GA series of LHTGR fuel irradiation tests conducted under the HTGR Fuels and Core Development Program. P13T is a large-diameter capsule containing two cells. Cell 1 is a qualification test of reference fresh fuel [TRISO UC_2 (VSM) and BISO ThO_2 particles] irradiated at 1300°C. Cell 2 is an evaluation test of reference fresh fuel and recycle fissile fuel [TRISO UC_xO_y (WAR) particles] irradiated at 1100°C. The capsule was inserted in the ORR reactor in May 1975. The capsule was discharged from the core on July 6, 1976 after being irradiated to a peak fast fluence of 8.8×10^{25} n/m^2 $(E > 29\ fJ)_{HTGR}$. A detailed description of the capsule is given in Ref. 9-1.

The detailed PIE plan for P13T (Ref. 9-2) was reviewed, comments on the plan were resolved, and the plan was formally issued during the quarter.

*Figures appear at the end of Section 9.

TABLE 9-1
CURRENT[a] STEADY-STATE P13V OPERATING CONDITIONS

Cell No.	Control Temperature (°C)		Cell Contents	Fast Fluence (x 10^{25} n/m^2) (E > 29 fJ)$_{HTGR}$	R/B Kr-85m x 10^{-5}
	Design	Decalibrated[b]			
1	1250	1186	WAR UC_2 TRISO/ ThO_2 BISO	5.8	0.4
2	1150 (860)	TC failed 946	WAR UC_2 TRISO/ ThO_2 BISO	7.9	0.4
3	1250 (1175)	TC failed 1208	ThO_2 BISO only	7.8	5.0
4	1250	1084	Unbonded reference VSM UC_2 TRISO/ ThO_2 BISO particles	7.4	1.0
5	1375	1406	WAR UC_2 TRISO/ ThO_2 BISO	5.7	2.0
6	1250	1265	WAR UC_2 TRISO only	3.7	1.0
	Rod bank = 27.7 in.				

[a] October 3, 1976.

[b] Decalibration factors based on P13R and P13S data.

The GA P13T PIE cognizant engineer observed the P13T lead pipe cutoff and shipping preparations at ORNL from August 23 to 25. The cuts and packaging were done without difficulty. Neutron radiographs of P13T were not taken at ORNL because all of the equipment needed to seal the experiment within the ORR neutron radiograph facility was not available when needed. In addition, it was desired to start the PIE of P13T in early September at the GA Hot Cell. The capsule left ORNL via motor freight transport on August 27, 1976 and arrived at the GA Hot Cell on September 8, 1976.

Capsule Disassembly. The PIE of P13T was started on September 10, 1976. All four graphite crucibles were removed from the metal containments without difficulty. Removal of dosimeters and thermocouples from crucible 1 was difficult. This may be attributed to the following:

1. Crucible 1 experienced the most bow of the four crucibles.

2. Impure secondary containment gas was used for a short period after the secondary-to-primary containment leak in cell 1 was discovered during capsule operation.

Some evidence of apparent diffusion bonding between niobium dosimeter containments was observed in crucibles 1 and 2. The new concept of placing dosimeters in alumina vials within sealed niobium tubes appears to have been quite successful and an improvement over the dosimetry containment used in previous capsules.

The primary-to-secondary containment leak that was observed in cell 1 during the operation of the capsule was found to have been caused by leaks around two thermocouple penetrations through the bottom head of the cell 1 primary containment.

Fission gas release characteristics were then determined on each of the four crucibles utilizing the TRIGA irradiation facility at GA. The results of the PIE fission gas release analysis for each of the loaded crucibles are shown in Table 9-2, along with end-of-life in-pile R/B values

TABLE 9-2
TRIGA RELEASE RESULTS FOR P13T CRUCIBLES

Crucible No.	Cell No.	TRIGA Kr-85m R/B	EOL In-Pile Kr-85m R/B
1	1	1.3×10^{-4} [a]	1.6×10^{-5}
2	2	1.3×10^{-5}	Cell 2:
3	2	8.0×10^{-6}	2.8×10^{-6}
4	2	2.6×10^{-6}	

[a] Crucible irradiated in TRIGA at room temperature; R/B value shown corrected to 1100°C.

for each cell of P13T. Because of a heater tube failure, crucible 1 was irradiated in TRIGA at room temperature and corrected to 1100°C. Because this results in a large correction, the R/B for four fuel rods from crucible 1 were run in TRIGA at both room temperature and 1100°C to establish the R/B relationship between these temperatures for capsule P13T.

All of the fuel rods were pushed out of crucibles 1, 2, and 4 and two fuel rods were removed from crucible 3 without difficulty using the unloading mechanism shown in Fig. 9-9. The force necessary to begin the fuel stack movement in each fuel hole is shown in Table 9-3. Note that the higher forces are apparently associated with Great Lakes Carbon Corporation H-451 graphite.

Fuel Rod Visual Examination. General irradiation performance of fuel rods after irradiation was assessed by visual examination. The examination was conducted using an in-cell Bausch and Lomb stereomicroscope with a magnification range of 4 to 30X and a camera attachment for photography. The criteria used during the visual examination for judging fuel rod integrity are that fuel rods remain intact and experience negligible debonding. In addition, the visual examination serves to characterize the following:

1. Surface striations and fuel particle damage attributed to unloading cured-in-place irradiated fuel rods.

2. Fuel particle damage attributed to irradiation.

The general irradiation performance of all P13T fuel rods was good to excellent. Figure 9-10 is a photomicrograph of fuel rods unloaded from body 1, column B. The surface appearance of these rods is excellent and representative of most P13T fuel rods. Two rods (2B1 and 2B2) exhibited surface striations, which were attributed to unloading damage.

A significant percent of failed OPyC layers was observed in fuel rods tested in body 1, i.e., values ranging from 1.1 to 27.7%. Generally it was

TABLE 9-3
FORCE NECESSARY TO BEGIN FUEL STACK MOVEMENT
IN EACH FUEL HOLE OF CAPSULE P13T

Crucible No.	Hole	Nominal Fuel Rod Diameter (mm)	Nominal Fuel Stack Length (mm)	Graphite Type	Force Necessary to Begin Fuel Stack Movement (Newtons)
1	A	15.8	182.8	H-451	667
1	B	15.8	182.8	H-451	534
1	C	15.8	182.8	H-451	489
2	A	15.8	100.1	TS-1240	44
2	B	15.8	100.1	TS-1240	22
2	C	15.8	100.1	TS-1240	22
3	B[(a)]	15.8	100.1	H-451	356
4	A	15.8	121.9	TS-1240	<22
4	B	15.8	121.9	TS-1240	53
4	C	15.8	121.9	TS-1240	22

[(a)]The remaining two fuel holes in crucible 3 were not unloaded as this body is planned to be used for postirradiation annealing thermal stability experiments under another ERDA program.

impossible to discriminate at ∿30X if failures were fissile, fertile, or inert particles. The results of the visual examination are summarized in Table 9-4.

Irradiation-Induced Dimensional Changes in P13T Fuel Rods. All P13T fuel rods were carbonized in-place in the graphite fuel bodies. The rods were fired with Grafoil disks ∿0.13 mm thick by 15.8 mm in diameter separating all fuel-rod/graphite and fuel-rod/fuel-rod interfaces. The Grafoil spacers prevented intimate bonding during carbonization; however, portions of the disks, and in some instances intact disks, remained adhered to the rod during preirradiation and postirradiation length measurements.

Preirradiated fuel rod dimensional measurements were made on historical quality control rods which were carbonized in graphite bodies and removed. These rods were comparable to the actual irradiated rods and provided a statistical base for defining the dimensional limits of rods carbonized in-place. One axial and one diametral measurement were made on each rod using calibrated micrometers. The tolerance on any individual measurement was ±0.013 mm. Table 9-5 presents statistical limits on the diametral and axial measurements for preirradiated fuel rods.

Postirradiation fuel rod dimensional measurements were performed using a calibrated dial gauge micrometer that could be interpreted to ±0.013 mm. Two axial measurements rotated 90° to one another were taken on each fuel rod. Six diametral measurements were made at randomly selected 0° and 90° orientations. Table 9-6 summarizes axial and diametral irradiation-induced strains in P13T fuel rods. The table defines statistical bounds at the 95% confidence level for mean axial and radial strains. The bounds establish limits based on the uncertainty of the preirradiated dimensional measurements.

Graphite Crucible Dimensional Measurements. Extensive measurements were made on the graphite fuel bodies from P13T. The dimensional change data for P13T graphite crucibles for axes both parallel and perpendicular to the extrusion axis are presented in Table 9-7. Greater dimensional

TABLE 9-4
STEREO VISUAL EXAMINATION OF P13T FUEL RODS

Capsule Ident.[a]	Fuel Rod Designation 7161-008-	Capsule Design Irradiation Conditions[b]		Maximum Force Required To Remove Fuel Column From Graphite Body (Newtons)	Macroscopic Visual Examination at 20X Magnification				
					Observed Surface Striations Attributed to Unloading	Failed OPyC Layers Within Surface Striations	Failed OPyC Layers Attributed to Performance		Upper 95% Confidence Bound on Failure (%)
		Temp. (°C)	Fast Fluence ($\times 10^{25}$ n/m^2) ($E > 29$ fJ)$_{HTGR}$				Total No. of Particles Observed on Surface	Failed OPyC Layers (%)	
1-1A1	01-9	1300	4.7	667	None	NA[c]	350	10.3	14.0
1-1A2	04-3	1300	5.8	667	↓	↓	175	1.1	4.0
1-1A3	07-9	1300	7.3	667	↓	↓	168	6.0	11.5
1-1A4	10-6	1300	8.4	667	↓	↓	700	6.1	8.0
1-1B1	02-10	1300	4.7	534	↓	↓	350	10.6	15.0
1-1B2	05-20	1300	5.8	534	↓	↓	350	18.0	23.0
1-1B3	08-11	1300	7.3	534	↓	↓	700	14.7	16.0
1-1B4	11-7	1300	8.4	534	↓	↓	350	3.7	5.5
1-1C1	03-12	1300	4.7	890	↓	↓	350	27.7	30.0
1-1C2	06-2	1300	5.8	890	↓	↓	350	12.6	17.0
1-1C3	09-12	1300	7.3	890	↓	↓	700	9.6	12.0
1-1C4	12-1	1300	8.4	890	↓	↓	700	18.0	19.0
2-2A1	13-2	1100	9.0	44	↓	↓	290	0	2.0
2-2A2	16-12	1100	8.8	44	↓	↓	↓	0	2.0
2-2B1	14-5	1100	9.0	22	Yes	19	↓	0	2.0
2-2B2	17-14	1100	8.8	22	Yes	21	↓	2.7	5.5
2-2C1	15-3	1100	9.0	22	None	NA	↓	0	2.0
2-2C2	18-4	1100	8.8	22	↓	↓	↓	0	2.0
2-3B1	20-11	1100	7.9	356	↓	↓	290	0.3	2.0
2-3B2	23-4	1100	7.0	356	↓	↓	583	9.3	11.0
2-4A1	25-6	1100	5.7	<22	↓	↓	175	0	4.0
2-4A2	28-6	1100	4.8	<22	↓	↓	↓	0	4.0
2-4A3	31-7	1100	3.9	<22	↓	↓	↓	0.6	3.5
2-4A4	34-7	1100	3.1	<22	↓	↓	↓	0	4.0
2-4B1	26-12	1100	5.7	53	↓	↓	↓	0	4.0
2-4B2	29-2	1100	4.8	53	↓	↓	↓	2.8	7.5
2-4B3	32-15	1100	3.9	53	↓	↓	↓	0	4.0
2-4B4	35-3	1100	3.1	53	↓	↓	↓	0	4.0
2-4C1	27-4	1100	5.7	22	↓	↓	↓	0	4.0
2-4C2	30-1	1100	4.8	22	↓	↓	↓	0	4.0
2-4C3	33-9	1100	3.9	22	↓	↓	↓	0	4.0
2-4C4	37-8	1100	3.1	22	↓	↓	↓	0	4.0

[a] The first digit is the cell number, the second digit is the graphite body number, the letter refers to the axial hole, and the last digit refers to the axial stacking sequence in the hole.

[b] Final thermal and dosimetry analysis not completed.

[c] Not applicable.

TABLE 9-5
PREIRRADIATED DIMENSIONS OF P13T
FUEL RODS CARBONIZED IN GRAPHITE BODIES

Mean Diametral Measurement, μ_o (mm)	Mean Axial Measurement, μ_A (mm)	Standard Deviation (mm)	Number of Measurements	Statistical Bounds[(a)] on Measurements
15.80	--	0.02	36	$15.74 \leq \mu_o \leq 15.86$
--	30.52	0.24	18	$29.77 \leq \mu_A \leq 30.78$
--	50.07	0.26	12	$49.22 \leq \mu_A \leq 50.92$
--	61.13	0.16	6	$60.48 \leq \mu_A \leq 61.78$

[(a)] Statistical bounds defined such that no more than 1% of the measurements will be beyond limits at the 95% confidence level.

TABLE 9-6
IRRADIATION-INDUCED DIMENSIONAL CHANGE IN P13T FUEL RODS

Capsule Ident.[a]	Fuel Rod Designation 7161-008-	Capsule Design Irradiation Conditions[b]		Irradiation-Induced Strain						
				Diametral Strain, $\Delta D/D \times 100$					Axial Strain, $\Delta L/L \times 100$	
		Temp. (°C)	Fast Fluence ($\times 10^{25}$ n/m^2) ($E > 29$ fJ)$_{HTGR}$	Top of Rod	Middle of Rod	Bottom of Rod	Mean μ_D[c]	Upper Lower Bounds on Mean[d]	Mean μ_A[e]	Upper and Lower Bounds on Mean[d]
1-1A1	01-9	1300	4.7	-2.22	-2.03	-1.90	-2.02	$-1.65 \geq \mu_D \geq -2.40$	-3.41	$-0.97 \geq \mu_A \geq -4.22$
1-1A2	04-3		5.8	-1.71	-1.90	-1.52	-1.71	$-1.33 \geq \mu_D \geq -2.08$	-3.41	$-0.97 \geq \mu_A \geq -4.22$
1-1A3	07-9		7.3	-1.14	-1.52	-1.52	-1.71	$-1.02 \geq \mu_D \geq -1.77$	-2.03	$-0.98 \geq \mu_A \geq -3.06$
1-1A4	10-6		8.4	-1.58	-1.46	-1.14	-1.71	$-1.02 \geq \mu_D \geq -1.77$	-1.36	$-0.31 \geq \mu_A \geq -2.64$
1-1B1	02-10		4.7	-2.09	-2.22	-2.53	-2.28	$-1.91 \geq \mu_D \geq -2.65$	-0.56	$-1.07 \leq \mu_A \leq 1.95$
1-1B2	05-20		5.8	-1.65	-1.71	-1.77	-1.71	$-1.33 \geq \mu_D \geq -2.08$	-4.46	$-5.06 \geq \mu_A \geq -2.05$
1-1B3	08-11		7.3	-1.33	-1.46	-1.65	-1.46	$-1.08 \geq \mu_D \geq -1.83$	-1.95	$-2.98 \leq \mu_A \leq -0.90$
1-1B4	11-7		8.4	-1.71	-1.33	-1.14	-1.39	$-1.02 \geq \mu_D \geq -1.77$	-0.57	$-1.62 \leq \mu_A \leq 0.50$
1-1C1	03-12		4.7	-2.22	-2.22	-2.41	-2.28	$-1.91 \geq \mu_D \geq -2.65$	-1.97	$-2.79 \leq \mu_A \leq 0.49$
1-1C2	06-2		5.8	-2.15	-2.09	-1.90	-2.03	$-1.65 \geq \mu_D \geq -2.40$	-1.87	$-2.69 \leq \mu_A \leq 0.59$
1-1C3	09-12		7.3	-0.95	-1.14	-1.46	-1.20	$-0.83 \geq \mu_D \geq -1.58$	-0.95	$-1.99 \leq \mu_A \leq 0.11$
1-1C4	12-1		8.4	-0.70	-0.95	-1.20	-0.95	$-0.57 \geq \mu_D \geq -1.32$	-1.44	$-2.48 \leq \mu_A \leq -0.39$
2-2A1	13-2	1100	9.0	-1.52	-1.46	-1.33	-1.46	$-1.08 \geq \mu_D \geq -1.83$	-0.62	$-2.27 \leq \mu_A \leq 1.09$
2-2A2	16-12		8.8	-1.90	-1.65	-1.52	-1.71	$-1.33 \geq \mu_D \geq -2.08$	-0.68	$-2.33 \leq \mu_A \leq 1.03$
2-2B1	14-5		9.0	-0.82	-0.89	-1.14	-0.95	$-0.57 \geq \mu_D \geq -1.32$	-0.88	$-2.53 \leq \mu_A \leq 0.83$
2-2B2	17-14		8.8	-1.20	-1.27	-1.14	-1.20	$-0.83 \geq \mu_D \geq -1.58$	-0.68	$-2.33 \leq \mu_A \leq 1.03$
2-2C1	15-3		9.0	-1.77	-1.65	-1.39	-1.58	$-1.21 \geq \mu_D \geq -1.95$	-0.78	$-2.43 \leq \mu_A \leq 0.93$
2-2C2	18-4		8.8	-1.65	-1.71	-1.58	-1.65	$-1.27 \geq \mu_D \geq -2.02$	-0.26	$-1.94 \leq \mu_A \leq 1.46$
2-3B1	20-11	1100	7.9	-1.20	-1.46	-1.27	-1.33	$-0.95 \geq \mu_D \geq -1.70$	-0.62	$-2.27 \leq \mu_A \leq 1.09$
2-3B2	23-4		7.0	-2.53	-2.22	-1.90	-2.22	$-1.84 \geq \mu_D \geq -2.59$	-1.38	$-3.02 \leq \mu_A \leq 0.32$
2-4A1	25-6	1100	5.7	-2.28	-2.22	-2.09	-2.22	$-1.84 \geq \mu_D \geq -2.59$	-0.46	$-1.30 \leq \mu_A \leq 2.04$
2-4A2	28-6		4.8	-1.96	-1.84	-2.03	-1.96	$-1.59 \geq \mu_D \geq -2.33$	-0.79	$-1.62 \leq \mu_A \leq 1.70$
2-4A3	31-7		3.9	-2.41	-2.28	-2.28	-2.34	$-1.97 \geq \mu_D \geq -2.71$	-2.20	$-3.02 \leq \mu_A \leq 0.25$
2-4A4	34-7		3.1	-2.34	-2.72	-2.53	-2.53	$-2.16 \geq \mu_D \geq -2.90$	-1.97	$-2.79 \leq \mu_A \leq 0.49$
2-4B1	26-12		5.7	-2.28	-2.15	-2.09	-2.15	$-1.78 \geq \mu_D \geq -2.52$	-1.21	$-2.04 \leq \mu_A \leq 1.26$
2-4B2	29-2		4.8	-2.66	-2.53	-2.34	-2.53	$-2.16 \geq \mu_D \geq -2.90$	-3.87	$-4.68 \leq \mu_A \leq -1.46$
2-4B3	32-15		3.9	-2.47	-2.47	-2.28	-2.41	$-2.03 \geq \mu_D \geq -2.77$	-0.39	$-1.23 \leq \mu_A \leq 2.10$
2-4B4	35-3		3.1	-2.97	-3.29	-3.29	-3.16	$-2.79 \geq \mu_D \geq -3.53$	-4.19	$-5.00 \leq \mu_A \leq 2.77$
2-4C1	27-4		5.7	-2.28	-2.34	-2.15	-2.28	$-1.91 \geq \mu_D \geq -2.65$	-0.46	$-1.30 \leq \mu_A \leq 2.04$
2-4C2	30-1		4.8	-2.15	-2.22	-2.03	-2.15	$-1.78 \geq \mu_D \geq -2.52$	-0.72	$-1.56 \leq \mu_A \leq 1.75$
2-4C3	33-9		3.9	-1.96	-1.90	-2.09	-1.96	$-1.59 \geq \mu_D \geq -2.33$	-1.80	$-2.63 \leq \mu_A \leq 0.66$
2-4C4	36-8		3.1	-2.47	-2.28	-2.09	-2.28	$-1.91 \geq \mu_D \geq -2.65$	-2.13	$-2.95 \leq \mu_A \leq 0.66$

[a] The first digit is the cell number, the second digit is the graphite body number, the letter refers to the axial hole, and the last digit refers to the axial stacking sequence in the hole.

[b] Final thermal and dosimetry analysis not completed.

[c] Mean of top, middle, and bottom diametral strains.

[d] Based on a 95% confidence statement that no more than 1% of the measurements will be outside stated bounds.

[e] Based on two axial measurements taken at right angles.

TABLE 9-7
GRAPHITE DIMENSIONAL CHANGE DATA FOR P13T CRUCIBLES

Crucible No.	Graphite Type	Avg. Orig. Dimension (cm)	Avg. Lifetime Irrad. Temp. (°C)	Design Fast Fluence (x 10^{25} n/m^2) (E > 29 fJ) HTGR			ΔD/D (% Change)					
							Top		Middle		Bottom	
				Top	Middle	Bottom	0°	90°	0°	90°	0°	90°
Diametral Change (Perpendicular to Extrusion Axis)												
1	H-451	6.040	1070			3.7					-0.70	-0.71
		6.114		8.7	7.2		-0.78	-0.74	-0.88	-0.98		
2	TS-1240	6.152	890	8.4	8.8	8.9	-0.48	-0.40	-0.44	-0.41	-0.61	-0.38
3	H-451	6.101	890	6.4	7.4	8.2	-0.87	-0.84	-1.12	-1.10	-1.29	-1.25
4	TS-1240	6.139	820		4.3	6.0			-0.20	-0.24	-0.19	-0.32
				3.5			-0.08	-0.05				

							ΔL/L (% Change)			
Length Change (Parallel to Extrusion Axis)										
							0°	90°	180°	270°
1	H-451	20.069	1070	8.7	7.2	3.7	-2.78	-2.41	-1.92	-2.26
2	TS-1240	11.697	890	8.4	8.8	8.9	-0.99	-0.93	-0.94	-1.02
3	H-451	11.697	890	6.4	7.4	8.2	-1.40	-1.44	-1.53	-1.41
4	TS-1240	13.721	820	3.5	4.3	6.0	-0.22	-0.25	-0.26	-0.24

change per unit fast fluence was noted for H-451 graphite than for TS-1240 graphite, as had been expected.

Bowing measurements were also taken on all four P13T fuel crucibles; the bowing data are presented in Table 9-8. Note that H-451 graphite exhibits more bowing per unit fast fluence than TS-1240. The most bowing was indicated in crucible 1. This may explain why the dosimeters and thermocouples from this crucible were difficult to remove.

Other Work Accomplished on the PIE of P13T. In addition to the results discussed above, the tasks listed below have been accomplished during this quarter on the PIE of P13T. These data, while taken, have not yet been analyzed.

1. All of the fuel rods have been gamma scanned.

2. All of the empty graphite crucibles have been gamma scanned.

3. Gamma scanning of the secondary containment was accomplished.

4. All of the secondary (piggyback) samples have been removed from the four fuel bodies.

5. Once the fuel rods were removed the internal diameters of all fuel rod holes contained in each crucible were measured.

6. Individual R/B measurements were made on each fuel rod (30) removed from P13T. These measurements were made at the GA TRIGA irradiation facility.

7. All of the dosimetry wires (27) were removed from their containment and transferred to Analytical Chemistry for analysis.

8. Coefficient of thermal expansion measurements have been started on P13T fuel rods.

TABLE 9-8
BOWING MEASUREMENTS TAKEN ON P13T GRAPHITE CRUCIBLES
DURING THE POSTIRRADIATION EXAMINATION

Crucible No.	Cell No.	Graphite Type	Avg. Orig. Length (cm)	Body Midlength Design Fast Fluence (x 10^{25} n/m^2) (E > 29 fJ)$_{HTGR}$	Avg. Lifetime Irrad. Temp.[a] (°C)	Peripheral Angle (degrees)	Maximum Observed Bow[b] (mm)
1	1	H-451	20.069	7.2	1070	0	0.65
						90	0.39
						180	0.70
						270	0.40
2	2	TS-1240	11.697	8.8	890	0	0.06
						90	0.10
						180	0.08
						270	0.03
3	2	H-451	11.697	7.4	890	0	0.24
						90	0.21
						180	0.22
						270	0.22
4	2	TS-1240	13.721	4.3	820	0	0.02
						90	0.09
						180	0.14
						270	0.11

[a] The fluence and temperature values shown have been estimated and are subject to revision following completion of the P13T dosimetry and thermal analyses.

[b] Defined as the absolute magnitude of the maximum difference between the high and low points along the length of the crucible.

9. Fuel rod metallography has been started on P13T fuel rods.

10. Thermal analysis of the day-to-day irradiation history of P13T has begun.

TASK 300: INTEGRAL FUEL SYSTEM TESTING

Subtask 320: FSV Fuel Test Elements

Preparation for fuel manufacture for FTE-3 through FTE-8 continued.

TASK 400: OUT-OF-PILE PARTICLE TESTING AND EVALUATION

Subtask 430: Isothermal Postirradiation Heating

Summary and Conclusions

Fuel coating behavior and fission product release have been studied during postirradiation isothermal heating of TRISO UC_2 and TRISO $UC_{4.3}O_{1.3}$ fuel particles. The conclusions drawn are summarized as follows:

1. Pressure vessel failure of TRISO UC_2 fuels having a representative range of fission densities is low (3 failures in 180 particles) at temperatures in the range 1600° to 2000°C. The dominant failure mechanism during isothermal heating in this temperature range is SiC - lanthanide fission product reactions.

2. TRISO coating behavior and fission product release fractions are functions of time, temperature, and fission density. Release occurs more rapidly as temperature and fission density are increased. For any constant set of conditions, lanthanide fission product release occurs first followed by Cs and then Kr-85 release, suggesting that individual models could be developed to describe the release of each fission product. All fission products were eventually released by migration through the SiC layer and an intact OPyC layer.

3. Comparison of experimental release data with LHTGR fuel performance predictions showed the fuel performance models to be conservative when applied under conditions like those predicted for a hypothetical loss of forced cooling (LOFC) core heatup event.

4. Comparison of low-burnup (22.9% FIMA) TRISO $UC_{4.3}O_{1.3}$ and TRISO UC_2 behavior showed that the performance of the uranium oxycarbide and UC_2 fuel particles will be similar when heated in the absence of a thermal gradient to temperatures greater than 1600°C. Arguments were also presented which suggest that higher burnup uranium oxycarbide fuels will perform better than UC_2 at temperatures above 1600°C.

Introduction

A lengthy series of experiments has been initiated to provide data describing LHTGR fuel particle performance under conditions predicted for the hypothetical LOFC core heatup events that must be treated during reactor safety studies. The test series will eventually include samples of TRISO UC_2 and TRISO WAR-derived uranium oxycarbide (UC_xO_y) fissile fuel and TRISO and BISO coated ThO_2 fertile fuel.

Core performance analyses show that fuel temperatures during a core heatup event would increase from near normal operating temperatures to temperatures in excess of 2000°C in a matter of hours and that thermal gradients would be near-zero (isothermal). Studies of fuel performance during such an event will begin with postirradiation isothermal heating of unbonded particles at constant temperatures to define the effects of time at temperature on particle coating behavior and fission product release. These tests will be followed by tests to show the impact of the temperature ramps predicted for various core heatup events on the behavior of unbonded particles and, eventually, on irradiated fuel rods containing mixtures of fissile and fertile fuel particles.

This report summarizes the results of the initial tests of irradiated TRISO UC_2 and TRISO $UC_{4.3}O_{1.3}$ fuel particles. The tests were done by postirradiation isothermal heating at temperatures of 1600°, 1800°, or 2000°C. Fuel coating and fission product release data are discussed in terms of kernel type and the concentration of fission products within the SiC layers of the fuels tested.

Description of the Experiment

The purpose of thse tests was to provide an initial description of particle coating failure and fission product release from TRISO fissile fuels during postirradiation isothermal heating at 1600°, 1800°, or 2000°C. Release of Eu-154, Ce-144, Cs-137, and Kr-85 was monitored as a function of time at temperature. The tests were performed at constant temperature to provide data on the kinetics of coating failure and fission product release that can be used to predict performance under the varying temperature conditions projected for a hypothetical core heatup.

The properties of the test samples used are summarized in Table 9-9. The three UC_2 samples were from the same initial coating batch. The three samples were isolated from the original coating batch and irradiated in various tests to evaluate the impact of fission density on irradiation-induced pressure vessel failure. These UC_2 samples provided an ideal source of material for higher temperature, postirradiation isothermal heating studies designed to show the impact of fission density on coating failure and fission product release during a core heatup event. Fission density is a key parameter since it is proportional to the concentration of fission products within a given particle, and the primary mechanism for failure under the conditions studied is SiC - fission product reactions.

The properties of the UC_2 particles are similar to the properties specified for LHTGR fissile fuel (Ref. 9-3). Selected properties of the reference UC_2 particle are given in Table 9-9 for comparison with the test samples. To demonstrate the wide range of fission densities studied in

TABLE 9-9
DESCRIPTION OF FUEL PARTICLES USED IN POSTIRRADIATION ISOTHERMAL HEATING TESTS

Data Retrieval Number	Type	Diameter (μm)	Burnup (% FIMA)	Irradiation Test	Fission Density (f_{SiC})[a]	Burnup in LHTGR Fuel Needed to Achieve f_{SiC}[b] (% FIMA)
4161-01-030	UC_2	203	22.9	FTE-14	0.6×10^{21}	32
4161-01-034-2	UC_2	176	60.2	P13P	1.2×10^{21}	63
4161-01-032-02	UC_2	133	60.6	P13P	1.9×10^{21}	100
Reference HTGR	UC_2	200	78.0[c]	--	1.6×10^{21}	78
OR 1694	$UC_{4.0}O_{1.3}$	314	22.9	FTE-14	0.5×10^{21}	27

[a] f_{SiC} = fission per cubic centimeter inside the SiC layer.
[b] Assume a 200-μm-diameter kernel, 100-μm-thick buffer, and 30-μm-thick IPyC layer.
[c] Peak LHTGR fissile kernel burnup.

this test series, the kernel burnups needed in reference UC_2 fuel to obtain the fission densities of the test samples are also shown in Table 9-9.

One TRISO coated WAR uranium oxycarbide sample ($UC_{4.3}O_{1.3}$) was included in this test series. TRISO coated UC_xO_y fuel is being evaluated as potential reference LHTGR fresh fuel for a number of reasons, including an increased resistance to SiC - fission product attack during normal reactor operation (Refs. 9-4 through 9-6). The WAR sample was included in these tests to provide the initial comparison between TRISO UC_2 and TRISO UC_xO_y behavior in the isothermal environment postulated for a core heatup event. The properties of this WAR sample are similar to those being considered for reference LHTGR fresh fissile fuel.

All particles were carefully characterized prior to postirradiation heating to ensure that they had not failed during irradiation. Visual examinations and contact x-radiography were utilized as macroscopic evidence of survival. Gamma-ray spectrometry was also used to ensure that fission product inventories were consistent with inventories expected for intact fuel.

After particle characterization, 20 particles of each sample were loaded into small graphite crucibles for heating at 1600°, 1800°, or 2000°C. The loaded crucibles were then gamma counted to define the fission product content of each test sample prior to heating. These gamma-counting data yielded Cs-137, Ce-144, Ru-106, and Zr-95 inventories. Initial inventories of Kr-85 and Eu-154 were estimated from the Ru-106 inventories for each individual sample.

The postirradiation heating tests were conducted in resistance-heated graphite tube (King) furnaces. Provisions were made for insertion of four Ta containment tubes into each end of the King furnaces. Three of the tubes at each end were available for test samples; the fourth was used to optically monitor test temperatures. The heating configuration is shown schematically in Fig. 9-11. In this series no more than four samples were tested at any one time. The test samples and the temperature control

sample were placed in each Ta tube so that operating temperatures of the test samples were within ±10°C of the temperature control sample. Removable, water-cooled, Cu-coated, stainless steel cold fingers were then inserted into each sample tube. The cold fingers were positioned so that sample operating temperatures were not depressed relative to the temperature control sample.

Metallic fission products released during heating of the test samples (Cs-137 and Eu-154) were collected on the copper-plated portion of the cold fingers. The cold fingers were removed periodically. The Cu coating and any trapped metallic fission products were stripped from the cold fingers and analyzed quantitatively by gamma-ray spectroscopy. Release of gaseous Kr-85 was monitored by periodically purging the atmosphere within the Ta tubes through a liquid nitrogen cold trap and then gamma counting the trap to analyse for Kr-85.

Release of Eu-154, Cs-137, and Kr-85 was monitored without interrupting the tests. Cerium release could only be measured when the tests were interrupted, since Ce released from the particles was trapped in the graphite sample holders. Cerium release was therefore measured by gamma counting the coated particle samples and graphite holders separately during test interruptions.

After completing the tests, individual particles from all samples were gamma counted to define Cs-137 and Ce-144 inventories. Selected samples were then prepared for hot cell metallographic and electron microprobe examination at Oak Ridge National Laboratory (ORNL) to define fission product distributions that resulted from isothermal heating.

Results

Fission Product Release. Fission product release measurements showed, with one exception, a period of very low release (<1%) followed by slow release of the fission products being evaluated. The one exception occurred during 1800°C heating of the UC_2 sample having a fission density

of 1.9×10^{21} f_{SiC}. In this case visual examination and fission product release measurements confirmed that 3 of 20 particles burst shortly after reaching 1800°C. This was the only example of pressure vessel failure encountered in these tests. Considering that 60 UC_2 particles having this very high fission density and a total of 180 UC_2 particles having a representative range of fission densities were heated at 1600° to 2000°C, the probability of TRISO fissile fuel pressure vessel failure during a LOFC core heatup is low (<2%).

With the exception of these three particles, fission product release occurred by diffusion through intact outer PyC layers only after SiC fission product reactions rendered the SiC layer ineffective as an absolute barrier to fission product release. A precise, quantitative description of the release of individual fission products during isothermal heating must therefore include the effects of time, temperature, and fission density on SiC - fission product interactions followed by diffusive release of the fission products through any remaining coating layers. It will be shown later, however, that the LHTGR performance models now used to predict TRISO UC_2 behavior are conservative relative to the observed fission product release data.

A typical plot of fission product release versus time is shown in Fig. 9-12. The data are for an 1800°C anneal of a TRISO UC_2 sample having a fission density of 1.2×10^{21} f_{SiC}. In all cases, Eu-154 and Ce-144 releases were more rapid than Cs-137 release, which was more rapid than Kr-85 release. The Eu and Ce release fractions were similar in each instance where a direct comparison could be made, suggesting that lanthanide fission product - SiC reactions are responsible for the reduced resistance of the SiC layer to fission product release. This is consistent with results from studies of SiC - fission product reactions that occur in the presence of a thermal gradient (Refs. 9-4, 9-5). The long times before Kr-85 release was detected imply that release of short-lived gaseous species would be very low at temperatures as high as 2000°C.

All particles heated were gamma counted before and after heating to define the impact of isothermal heating on the fission product contents of individual fuel particles. The effect of heating for 905 hours at 1800°C on Cs/Ru and Ce/Ru activity ratios of the 20 particles having a fission density of 1.2×10^{21} f_{SiC} is shown in Fig. 9-13. Ruthenium was used as a standard since it is not released from TRISO UC_2 fuel with failed coatings. Thirty percent of the particles lost nearly all their Ce, while 70% of the particles lost a portion of their Ce. Thirty percent of the particles also lost nearly all their Cs, while 70% lost no Cs. There was a 1 to 1 correspondence between particles releasing all their Ce and all their Cs. This coupled with the lack of Cs release from particles having partial Ce loss suggests that Cs release does not occur in TRISO UC_2 fuel until 100% of the lanthanide fission products has been released. The data in Fig. 9-13 also show that the fission product loss detected in these tests was from individual particles rather than uniform release from all particles.

The impact of fission density on fuel performance during isothermal heating is illustrated in Fig. 9-14, which shows Cs-137 release as a function of time at 1800°C for the three samples of TRISO UC_2 tested. The conclusion that the time to some value for fractional release (i.e., 20%) increases with decreasing fission density is applicable to all fission products evaluated at each test temperature. Note in this case that fuel having a fission density about equal to that expected for 1-year fuel did not release significant amounts of Cs until after 2400 hours at 1800°C.

The only results which were in partial disagreement with those described above occurred during testing at 1600°C. This test was interrupted after 1030 hours at temperature by a loss of power. As a result the samples cooled rapidly from 1600°C to room temperature. After about 1000 hours at temperature, the UC_2 sample having a fission density of 1.9×10^{21} f_{SiC} had released 38% of its Eu-154 inventory and 6% of its Cs inventory. The other three samples showed less than 3% release of any individual fission product.

When testing was resumed, rapid fission product release was observed. An example is shown in Fig. 9-15 for the TRISO UC_2 sample having a fission density of 1.2×10^{21} f_{SiC}. The increment of fission product release noted after resuming the test increased with the fission density of the individual samples. The rate of release was also higher than observed for tests conducted at higher temperatures. These observations suggest that the failure and release modes were different for these samples than for those tested at higher temperatures. One hypothesis is that the SiC coatings which had been weakened by SiC - fission product attack cracked due to the thermal shock experienced during rapid cool-down. This is supported by metallographic evidence showing considerable fission product SiC attack in the high fission density samples and little attack in the low fission density samples. Because of this apparent change in behavior after the rapid cool-down, data from the 1600°C test will not be used for times greater than 1030 hours.

Metallographic and Electron Microprobe Evaluation. A number of samples were selected for metallographic and electron microprobe examination at ORNL after heating. The metallographic examinations showed qualitatively that the degree of detectable fission product - SiC attack increased with the observed fission product release. An extreme example is shown in Fig. 9-16, which shows photomicrographs of a particle having a fission density of 1.2×10^{21} f_{SiC} after heating for 165 hours at 2000°C. This particle released its complete inventory of Eu-154 and Ce-144, but little or no Cs-137 and Kr-85. The photomicrographs illustrate three general observations. The first is that SiC attack is uniform around the inner surface of the SiC layer. This was expected since, in the absence of a thermal gradient, there is no driving force for concentration of the reacting fission products to any local region of the SiC-IPyC interface. Secondly, although the fission products clearly penetrated the SiC layer, the areas of obvious penetration seem to be filled with a new phase. Electron microprobe examinations showed that no metallic species were correlated with this new phase, which suggests that it is primarily C. The third observation is that the OPyC layer remained intact. This explains why gaseous release (Kr-85) lagged behind metallic fission product release.

These observations will be utilized later in discussions of the kinetics of Cs release.

The electron microprobe results were consistent with expectations based on the behavior of TRISO UC_2 fuels in a thermal gradient. The observations for several key species are summarized as follows:

1. Those lanthanide fission products released from the kernels were uniformly distributed throughout the buffer or IPyC layers. In cases where lanthanide release occurred during heating, lanthanides were detected only in the kernels, implying that once SiC failure occurs, lanthanide release is controlled by release from the UC_2 kernel.

2. Cesium and Ba were not detected in the UC_2 kernels. The majority of the Cs and Ba was uniformly distributed throughout the buffer layer with smaller quantities detected in the IPyC layer. Lanthanide release had no impact on the Cs or Ba distributions before detectable Cs release occurred.

3. Some Si redistribution to the IPyC layer and kernels was noted.

4. Chlorine was detected in nearly all particles examined. No clear correlation between Cl and other species was noted.

Electron microprobe results for the TRISO $UC_{4.3}O_{1.3}$ were also consistent with expected results. All of the Cs and Ba was released from the kernels and found in the buffer layer. Although the Cs and Ba concentrations were uniform in the circumferential direction, the concentrations decreased with distance away from the kernel. No lanthanide fission products were detected in the buffer or IPyC layers of intact samples (heated at 1600°C) or samples from which metallic fission products were lost during heating at 2000°C. However, fewer lanthanide fission products were in the kernels from the samples heated at 2000°C than in those which survived the 1600°C

treatment. Silicon and Cl observations were the same as for the UC_2 samples.

Discussion of Results. The discussion of results is directed toward four principal areas. The first is a comparison between the results of these tests and predictions made using performance models for LHTGR TRISO UC_2 fuel and shows that the LHTGR models conservatively predict performance during a core heatup event. Secondly, the isothermal heating data are compared with data describing TRISO UC_2 fuel performance in a thermal gradient to relate fuel performance under normal operating conditions to performance during a hypothetical core heatup event. The third area of discussion provides an evaluation of the kinetics of Cs release, suggesting that even after lanthanide fission products penetrate the SiC, the SiC layer is a more effective barrier to Cs release than the PyC layers of a TRISO coating. The final treatment includes a comparison of TRISO UC_2 and TRISO $UC_{4.3}O_{1.3}$ data, showing that for low burnup fuel the UC_2 and uranium oxycarbide show similar performance when heated isothermally to temperatures above 1600°C. This observation is in conflict with considerable in-pile (Ref. 9-6) and out-of-pile (Ref. 9-5) experience that shows uranium oxycarbide performance to be better than UC_2 performance under thermal gradients at temperatures less than 1700°C.

Comparison of Isothermal Heating Data and LHTGR Fuel Performance Models. Detailed models used to predict the performance of LHTGR TRISO UC_2 and BISO ThO_2 fuels are provided in Ref. 9-7. Control of fuel performance in the temperature ranges studied here is assumed in Ref. 9-7 to change from pressure vessel failure to failure by SiC - fission product reactions as temperatures increase through a critical value defined as T_{crit}. Values for T_{crit} (°C) are

$$T_{crit} = -3.45(BU) + 1869$$

for kernel burnups (BU) exceeding 20% FIMA or

$$T_{crit} = 1800°C$$

for burnups less than 20% FIMA. Failure is assumed to occur instantaneously and to increase linearly with temperature from the pressure vessel value at T_{crit} to 100% at 2000°C. A new increment of failure is assumed in the unfailed fuel each time T_{crit} is exceeded and after each 100 hours that the fuel operates continuously above T_{crit}.

The UC_2 samples tested in this series had been irradiated to burnups of about 23 or 60% FIMA (Table 9-9). The two samples irradiated to 60% FIMA, however, had different fission densities (1.2×10^{21} and 1.9×10^{21} f_{SiC}) and the test results (Fig. 9-14) showed conclusively that fuel performance was a function of fission density rather than kernel burnup. The burnups used for LHTGR fuel performance predictions were therefore adjusted so that the fission densities for the predictions equaled the fission densities of the test samples. The equivalent LHTGR burnups are given in Table 9-9.

Comparisons of observed Eu-154, Cs-137, and Kr-85 release fractions and predicted failure fractions are given in Figs. 9-17, 9-18, and 9-19 for UC_2 samples having fission densities of 1.9×10^{21} f_{SiC}, 1.2×10^{21} f_{SiC}, and 0.6×10^{21} f_{SiC}, respectively. The only data not shown are for the 1600°C test of the 0.6×10^{21} f_{SiC} sample. The predicted failure fraction for this sample was approximately 1×10^{-4}. Observed release fractions during this test were 1×10^{-2} for Eu-154 and 4×10^{-4} for Kr-85 after 1000 hours at temperature. The observed Cs-137 release fraction of 6×10^{-3} occurred nearly instantaneously and was attributed to a combination of Cs contamination from companion irradiation samples and uncertainties in the low Cs release fractions.

As a group, the experimental data show the basis for earlier statements that lanthanide release precedes Cs release which precedes Kr-85 release and that release at any temperature increases more rapidly with time as fission density increases. In one case (Fig. 9-18c), a very low value for Cs release is shown before Eu release was detected. This is attributed to a combination of Cs contamination from companion irradiation

samples and uncertainties in Cs measurements for low release as discussed above.

The data also show that separate performance models must be provided for different groups of fission products to accurately predict coating performance and fission product release. The most important conclusion to be drawn from the comparisons, however, is that the LHTGR fuel performance models (Ref. 9-7) conservatively treat the behavior of TRISO UC_2 fuels during an isothermal core heatup. This justifies use of the models to predict TRISO UC_2 performance during analyses designed to study the impact of hypothetical accident conditions on fuel and fission product behavior.

Comparison of Isothermal and Thermal Gradient Data. A series of postirradiation thermal gradient heating tests, designed to study SiC - fission product reactions in TRISO UC_2 fuel under conditions expected during normal reactor operation, was recently completed. Preliminary data are summarized in Ref. 9-4. Final data will be summarized in Ref. 9-5. These tests showed that lanthanide fission products concentrate on the cool side and react with the SiC layer of TRISO UC_2 fuel in a temperature gradient and that reaction rates are independent of fission density. The tests also provided a kinetics expression for estimating the reduction in SiC thickness caused by SiC fission product reactions as a function of time and temperature. The data also suggested that in a thermal gradient, lanthanide release may begin after penetration of about 50% of the available SiC thickness.

A comparison of the time to 50% Eu-154 release determined from the isothermal heating tests and the predicted time to 50% lanthanide fission product release in a thermal gradient is shown as a function of temperature in Fig. 9-20. The predictions assumed that the time to 50% lanthanide release during thermal gradient heating corresponds to the time to a 50% reduction in SiC thickness due to SiC - fission product reactions. The average SiC thickness for the samples heated in the isothermal tests was 26 μm. The data show that TRISO UC_2 performance in an isothermal environment will be the same as, or better than, performance in a thermal gradient.

The fact that the isothermal data from samples having the highest fission density (1.9×10^{21} f_{SiC}) are consistent with predictions made using the thermal gradient data suggests the rate of reaction for this high fission density sample is not controlled by the concentration reactants. This also implies that the lifetime of the lower fission density samples is a function of the concentration of available reactants.

Analysis of Cs Release Data. Fission product release results presented in Fig. 9-13 showed that Cs release from individual TRISO UC_2 particles does not begin during isothermal heating until nearly 100% lanthanide fission product release has occurred. This suggests that Cs release begins only after the SiC layer has been rendered ineffective as a barrier to metallic fission product release. The rate of Cs release could therefore be controlled by Cs diffusion through the PyC layers of the TRISO coatings.

This hypothesis was tested by comparing experimental values for Cs release with Cs release values predicted using the COPAR code (Ref. 9-8). COPAR is used to predict diffusive release from multilayered coated particles as a function of diffusion within and release from the kernel and the equilibrium concentrations and diffusivities of the species of interest in the various coating layers. COPAR calculations were done at 1600°, 1800°, and 2000°C. The three key sets of input data included the initial Cs distribution, partition factors, and Cs diffusivity. Based on the electron microprobe data, all of the Cs was assumed to be in the buffer layer at the start of the tests. Partition factors (ϕ) are the ratios of the equilibrium Cs concentration in the i and i+1 layers ($\phi_{i/i+1}$). One set of calculations (Type I) was done assuming that equilibrium concentrations in the buffer, IPyC, SiC, and OPyC layers were equal (ϕ=1), while Cs diffusivities in the SiC (DCs_{SiC}) were varied from values equal to the Cs diffusivity in PyC (DCs_{PyC}) to 10^{-3} times DCs_{PyC}. A second set of calculations (Type II) was done assuming equal values for Cs diffusivity in the PyC and SiC layers. These calculations were prompted by the metallographic and microprobe results which suggested that porosity introduced in the SiC layer by escaping lanthanide fission products was filled with carbon. To account

for the small volume fraction of these carbon-filled pores, partition factors at the IPyC-SiC interface were varied from 1 to 10^3. Nominal values for DCs_{PyC} (Ref. 9-9) were used at each temperature. Examples of the input data used for 1800°C calculations are included in Table 9-10. A comparison of Type I and II calculations showed that results assuming $DCs_{SiC} = \gamma\ DCs_{PyC}$ at ϕ values of 1 were the same as results assuming $DCs_{SiC} = DCs_{PyC}$ for IPyC-SiC partition factors of $1/\gamma$. The results are therefore discussed in terms of calculations assuming $DCs_{SiC} = DCs_{PyC}$ and variable values for PyC-SiC partition factors.

Since it was shown that experimental Cs release values represented release from individual particles, the experimental Cs release data were normalized to the fraction of particles releasing Cs for comparison with the COPAR calculations. A comparison of COPAR and experimental Cs loss results is shown in Fig. 9-21 for the 1.2×10^{21} f_{SiC} sample during 1800°C isothermal heating. When Cs release is controlled only by diffusion, the time to detectable Cs release (delay time) is a function of the Cs diffusivity through the coating layers. Delay times predicted for the Cs diffusivities used in this study were on the order of hours or less. In the example shown in Fig. 9-21, the time to detectable Cs release was approximately 400 hours, which is the time required for SiC - lanthanide fission product reactions to render the SiC layer ineffective as an absolute barrier to metallic fission product release. This comparison between COPAR calculations and experimental data suggests that after the SiC layer is penetrated by lanthanide fission products during isothermal heating, it remains two to three orders of magnitude more effective as a barrier to Cs release than the PyC layers. This same conclusion was drawn for all samples heated at 1800° and 2000°C. Careful examination of the forms of the COPAR and experimental release curves shows, however, that the COPAR calculations as done do not yet accurately predict the release of Cs as a function of time. A possible source of the discrepancy is the assumption of no holdup in the buffer layer. The effect of input assumptions relative to the buffer layer will be examined by additional COPAR calculations.

TABLE 9-10
KEY INPUT PARAMETERS FOR TYPE I[(a)] AND TYPE II[(b)]
COPAR CALCULATIONS AT 1800°C

Calculation Type	Particle Region	Dimensions (μm)	Initial Cs Concentration	Position Factor[(c)]	Cs Diffusivity (cm^2/s)
I	Kernel	176[(d)]	0	10^{-4}	4.9×10^{-9}
	Buffer	87[(e)]	1	1.0	4.9×10^{-3}
	IPyC	28[(e)]	0	1.0	4.9×10^{-9}
	SiC	25[(e)]	0	1.0	$\alpha(4.9 \times 10^{-9})$[(f)]
	OPyC	34[(e)]	0		4.9×10^{-9}
II	Kernel	176[(d)]	0	10^{-4}	4.9×10^{-9}
	Buffer	87[(e)]	1	1.0	4.9×10^{-3}
	IPyC	28[(e)]	0	[(g)]	4.9×10^{-9}
	SiC	25[(e)]	0	ϕ^{-1}	4.9×10^{-9}
	OPyC	34[(e)]	0	ϕ	4.9×10^{-9}

[(a)] Type I calculations evaluated the impact of assumed values for Cs diffusivity in SiC in calculated Cs release.

[(b)] Type II calculations evaluated the impact of SiC-PyC partition factors on calculated Cs release.

[(c)] Partition factor = ratio of Cs concentrations in the i and i+1 coating layers.

[(d)] Diameter.

[(e)] Thickness.

[(f)] Values for α ranged from 1 to 10^{-3}.

[(g)] Values for ϕ ranged from 1 to 10^{3}.

Comparison of COPAR and experimental release results at 1600°C showed the kinetics of Cs release to be similar to calculated values if the PyC layers were assumed to control release. This confirmed earlier suspicions that the mode of failure and fission product release in these samples differed from the higher temperature failure modes.

Comparison of Low Fission Density TRISO UC_2 and TRISO $UC_{4.3}O_{1.3}$ Performance. A direct comparison of the performance of low fission density TRISO UC_2 and TRISO WAR-derived $UC_{4.3}O_{1.3}$ is also possible from the data generated in these tests. Release fractions for Eu-154 and Cs-137 are shown in Figs. 9-22 and 9-23, respectively, for isothermal tests run on both particle types at 1800° and 2000°C. There is no significant difference in the data for the two particle types. A similar statement can be made about the 1600°C results, although the fission product release data were too low to be significant (<3% for any individual species). This leads to a preliminary conclusion that the TRISO uranium oxycarbide and TRISO UC_2 will show similar behavior when subjected to heating conditions like those predicted for a hypothetical core heatup event. This conclusion must, however, be tested by studying the behavior of higher fission density TRISO UC_xO_y samples.

The relative behaviors of higher fission density TRISO UC_2 and UC_xO_y fuels can be surmised from a combination of thermal gradient test results and the results presented here. The isothermal heating results showed that fission product release occurred earlier from high fission density TRISO UC_2 fuel than from low fission density fuel. This was related to the fact that more fission products are available for SiC fission product reactions in the high fission density UC_2 fuel. Thermal gradient tests have already shown that fewer lanthanide fission products are released from high fission density TRISO $UC_{4.3}O_{1.3}$ fuel than from high fission density TRISO UC_2 fuel (Refs. 9-4, 9-5). This implies that as fission densities increase, the performance of TRISO UC_xO_y fuel heated under isothermal conditions will improve relative to TRISO UC_2 fuel. This reasoning leads to the conclusion that the current LHTGR fuel performance models (Ref. 9-7) will be even more conservative if applied to TRISO UC_xO_y behavior than they were shown to be for TRISO UC_2 behavior.

TASK 500: FUEL ROD TEST AND EVALUATION

The work reported here was performed in FY-76. This task is not funded in FY-77.

Summary

Thermal expansivity was measured on HTGR fuel rods tested in the P13Q irradiation experiment. Six fuel rods irradiated in capsule P13Q to fast neutron fluences ranging from 4.2 to 9.4 x 10^{25} n/m^2 $(E > 29\ fJ)_{HTGR}$ at temperatures of 1130 to 1435 K were tested in a thermal expansion measurement unit designed for hot cell use. Unirradiated, historical companions to the P13Q rods were tested out-of-cell in an identical device.

The mean coefficient of thermal expansion between room temperature and 1073 K $[\bar{\alpha}_{(300-1073)}]$ ranged from 4.5 to 5.05 x 10^{-6} K^{-1} with a mean of 4.86 x 10^{-6} K^{-1} for the unirradiated specimens. For irradiated specimens, $\bar{\alpha}_{(300-1073)}$ varied from 3.17 to 3.58 x 10^{-6} K^{-1} with a mean of 3.44 x 10^{-6} K^{-1}.

Within the sample tested, $\bar{\alpha}_{(300-1073)}$ was independent of the relative fractions of fuel or inert particle types, fuel rod fabrication technique, and rod curing environment. The thermal expansivity $[\bar{\alpha}_{(300-1073)}]$ decreased by approximately 30% with neutron irradiation independent of total neutron fluence or irradiation temperature.

Description of Tests

HTGR development fuel rods from the P13Q experiment were selected for testing because of the variety of fuel and inert particle types and fabrication techniques used in the fuel rods (Ref. 9-10). The P13Q experiment exposed the fuel rods to moderate to high neutron

fluences over a range of irradiation temperatures (Ref. 9-11). The fuel rods measured in this effort are described in Table 9-11. The rods tested were approximately 5.38 cm (2.12 in.) long and 1.58 cm (0.62 in.) in diameter.

Two identical devices were built to measure the thermal expansion of fuel rods. The design of the units incorporated a quartz dilatometer made specifically for 1.58-cm-diameter (0.62 in.) rods. Figure 9-24 is a schematic of the units. Basically, the design consisted of a quartz push-rod dilatometer [(1) and (2)] mounted on a brass water-cooled base (9) which butted against one end of a quartz enclosure (3) inserted into a clamshell furnace (4). The quartz push rod (1) pushed an Inconel rod (5) at the cold junction which was attached to the core of an LVDT (6), which translated movement of the core into voltage output. The specimen temperature was continuously measured by a Pt-Rh thermocouple (7), which touched the bottom of the specimen. The thermocouple was compensated at the cold junction brass support (8). Instrument and power connections were made by quick connects to a remote control station. The specimen was protected during tests by inert gas purged into the quartz enclosure.

As reported earlier (Ref. 9-12), heating rate control is critical to this design; therefore, a programmer and SCR control (10) were used to generate slow, steady, and repeatable heating curves. The heating program was determined by minimizing the difference between the furnace temperature [thermocouple (11)] and the specimen temperature [thermocouple (7)]. The heating program used resulted in a ΔT between furnace and sample of 10 K at 675 K, 4 K at 875 K, and 1 K at 1175 K.

Both units were calibrated using the same heating program with tungsten and graphite standards. During the early stages of calibration, the decision was made to place quartz discs at each end of the fuel rods to provide a flat, hard surface for dilatometer contact.

TABLE 9-11
THERMAL EXPANSIVITY SPECIMENS - P13Q FUEL RODS

Rod Location	Average Irrad. Temp. (K)	Total Neutron Fluence (10^{25} n/m^2) (E > 29 fJ)$_{HTGR}$	Volume Fraction Particle Loadings (%)				Fabrication[a]	Curing[b]
			Fertile	Fissile	Inert BISO	Inert TRISO		
G1-1B	1435	9.4	2	6	19	12	I	C
G1-2A	1380	9.0	2	7	17	9	C	P
G2-1A	1180	7.2	2	10	13	8	C	C
G3-1B	1155	5.6	3	15	8	8	C	C
G3-2B	1155	5.6	3	15	8	8	C	C[c]
G3-3A	1130	4.2	-[d]	-	-	-	I	C

[a] Fabrication symbols: I = injection molded, C = admix compaction

[b] Curing symbols: C = cured-in-place, P = packed bed.

[c] Fired at 1773 K.

[d] Thermocouple rod; relative volume fraction unknown.

Subsequently, all calibrations included quartz discs at both ends of the axial specimens. No quartz discs were used for radial measurements. The tungsten standard used was a cylinder 5.16 cm (2.03 in.) long by 1.27 cm (0.50 in.) in diameter, arc cast and polished, and 99.97% pure. The two graphite standards were machined from 2020 graphite, one cylinder 5.11 cm (2.01 in.) long by 1.59 cm (0.62 in.) in diameter cut along the grain and an identical cylinder cut perpendicular to the grain.

The thermal expansion of the tungsten specimen was taken from established literature values (Ref. 9-13) and confirmed by comparison to an NBS traceable platinum standard. The graphite standards were calibrated to the tungsten standard. Both units were calibrated using tungsten and graphite standards in the axial [5.15 cm (2.03 in.) gage length] configuration. Calibration of the radial [1.58 cm (0.62 in.) gage length] configuration was done using the graphite standards. In each calibration run the standards and quartz discs (for axial configuration only) were deliberately inserted in the dilatometer as randomly as possible so that calibration variance included the variance of insertion and alignment of specimens.

The standard deviation measured for the calibration tests was 2% of the mean LVDT output between 300 and 1075 K. Therefore, the reported results are considered to be accurate within ±5%.

Results

Twelve fuel rods were tested: six irradiated rods and six unirradiadiated companion rods. Of the six rod types tested, five exhibited essentially identical thermal expansivity. The rod type in position G2-1A differed from the other types in both irradiated and unirradiated states. The data are given in Table 9-12.

TABLE 9-12
THERMAL EXPANSIVITY OF HTGR FUEL RODS - P13Q EXPERIMENT

Rod Type	$\bar{\alpha}_{(298-1073)}$ (10^{-6} K^{-1})		$\Delta\bar{\alpha}$ (%)	$\bar{\alpha}_{(298-773)}$ (10^{-6} K^{-1})		$\Delta\bar{\alpha}$ (%)
	Unirrad.	Irrad.		Unirrad.	Irrad.	
G1-1B	5.05	3.42	-32	4.60	2.98	-35
G1-2A	4.87	3.44	-29	4.48	3.04	-32
G2-1A	4.50	3.17	-30	3.95	2.46	-38
G3-1B	5.06	3.54	-30	4.63	2.96	-36
G3-2B	4.75	3.58	-25	4.31	2.85	-34
G3-3A	4.95	3.51	-29	4.44	2.89	-35
Mean	4.86	3.44	-29	4.40	2.86	-35
Std. dev.	0.21	0.15	2.3	0.25	0.21	2

The mean coefficient of thermal expansion between room temperature and 1073 K [$\bar{\alpha}_{(300-1073)}$] was measured to be 4.86 x 10^{-6} K^{-1} for all unirradiated rods and 4.94 x 10^{-6} K^{-1} for the five consistent rod types. The coefficient of variance (standard deviation/mean value) was 4% for all rods and 3% for the five most consistent rod types. $\bar{\alpha}_{(300-1073)}$ for the irradiated rods averaged 3.44 x 10^{-6} K^{-1} for all rods with a coefficient of variance of 4%. Excluding rod type G2-1A, the mean was 3.50 x 10^{-6} K^{-1}, with a coefficient of variance of 2%.

The thermal expansivity expressed as $\bar{\alpha}_{(300-1073)}$ decreased an average of 29% for all rods irradiated in P13Q. Typical preirradiation and postirradiation curves of thermal expansion versus temperature are given in Fig. 9-25.

Discussion

The thermal expansivity values measured on the fuel rod specimens were nearly identical regardless of the fuel rod tested. Rod type G2-1A differed from the other rods somewhat, but no explanation for that difference is readily available. Other rods tested included the same particle types and packing fractions, the same fabrication techniques, and the same curing environment as rod G2-1A. Indeed variation of the above parameters apparently had no effect on fuel rod thermal expansivity based on the results reported above. In addition, neutron irradiation reduced thermal expansivity by about 30% regardless of the total fast neutron fluence or the irradiation temperature. Any fluence or irradiation temperature dependency is not obvious in this experiment, possibly because of the narrow irradiation temperature range and moderate to high fluences.

Three other variables which may be significant were not available for test in this experiment. Relative shim particle volume is most likely to have an effect on thermal expansivity. The matrix composition and fuel kernel fabrication process may also exert some influence on fuel rod thermal expansivity. However, P13Q was a test of fuel at about average HTGR reactor fuel temperatures and peak fast neutron fluences. The fuel rods tested represented nominal fuel types in an HTGR.

Within the limits of the P13Q experiment, the thermal expansivity of representative HTGR fuel rods irradiated to peak fast neutron fluence at average reactor fuel temperatures has been determined. The mean values reported for all six rods have been used to generate the design curves of Fig. 9-25.

REFERENCES

9-1. Young, C.A., and D.P. Harmon, "Preirradiation Report of Fuel Materials for P13T Capsule Irradiation," ERDA Report GA-A13343, General Atomic Company, April 1976.

9-2. Scheffel, W.J., "Capsule P13T Postirradiation Examination Plan," General Atomic unpublished data, October 14, 1976.

9-3. "HTGR Fuel Product Specification," General Atomic unpublished data, January 1976.

9-4. "HTGR Fuels and Core Development Program Quarterly Progress Report for the Period Ending February 29, 1976," ERDA Report GA-A13804, General Atomic Company, March 31, 1976, pp. 9-13 to 9-48.

9-5. Smith, C.L., "Fission Product - SiC Reactions in Irradiated LHTGR TRISO Fissile Fuel," General Atomic Report, to be published.

9-6. Homan, F.J., et al., "Stoichiometric Effects on Performance of HTGR Fuels from the U-C-O System," to be published in J. Nucl. Tech.

9-7. Smith, C.L., "Fuel Particle Behavior Under Normal and Transient Conditions," USAEC Report GA-A12971 (GA-LTR-15), General Atomic Company, October 1, 1974.

9-8. Smith, P.D., and R.G. Steinke, "Release of Metallic Fission Products from Multilayered Coated Particles: Part I, Theory," to be published in J. Nucl. Tech.

9-9. "HTGR Accident Initiation and Progression Analysis Status Report, Volume V, AIPA Fission Product Source Terms," ERDA Report GA-A13617, General Atomic Company, February 1976.

9-10. Smith, C.L., "Preirradiation Report - Fuel Materials for Irradiation P13Q," ERDA Report GA-A13265, General Atomic Company, June 13, 1975.

9-11. Young, C.A., "P13Q Postirradiation Report," ERDA Report GA-A14174, General Atomic Company, to be published.

9-12. "HTGR Fuels and Core Development Program Quarterly Progress Report for the Period Ending May 31, 1976," ERDA Report GA-A13941, General Atomic Company, June 30, 1976.

9-13. Touloukian, Y.S., et al., Thermophysical Properties of Matter, Volume 12, Thermal Expansion, Thermophysical Properties Research Center (TPRC) Data Series, Purdue University, IFI/Plenum, New York, 1975.

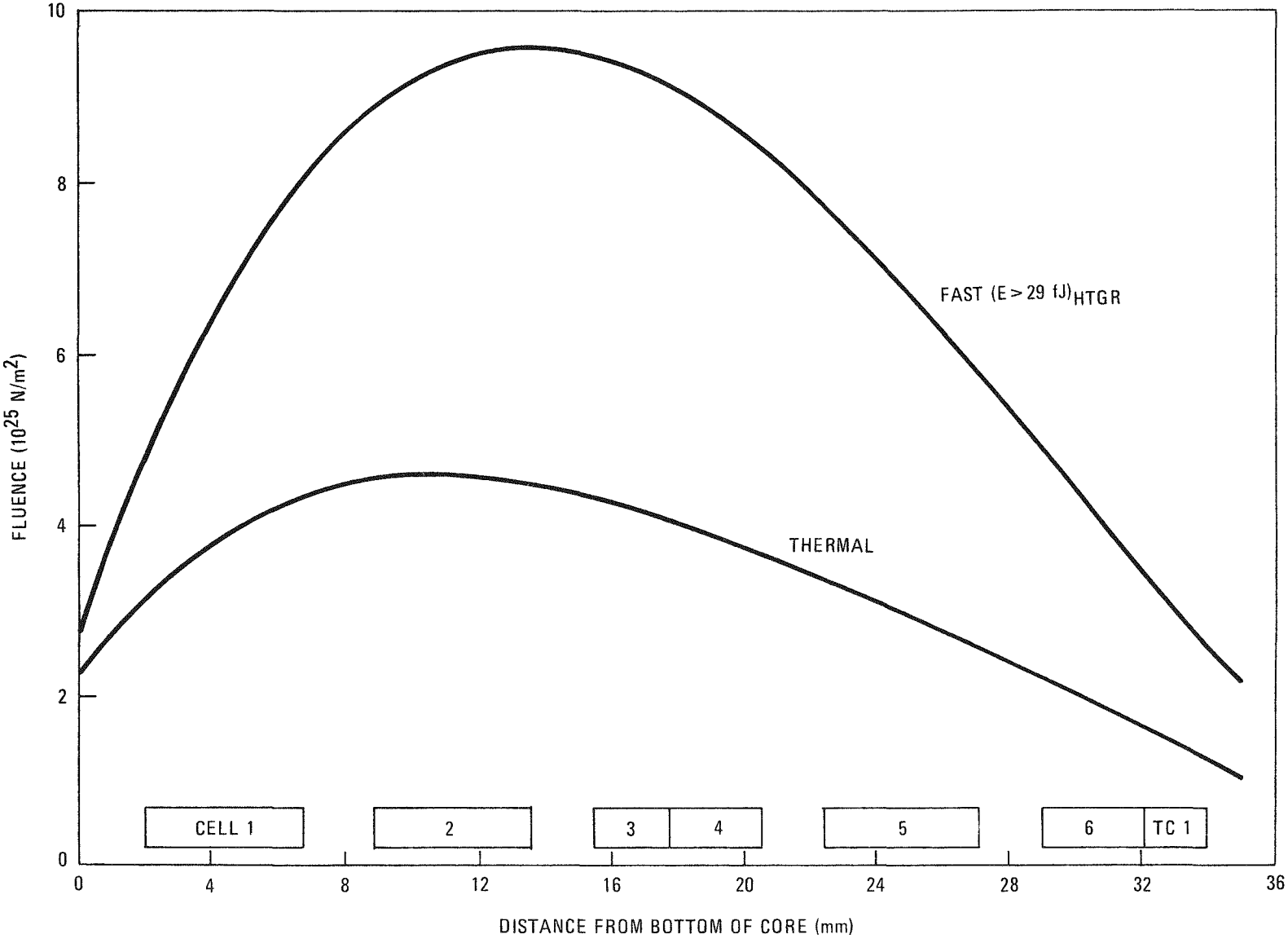

Fig. 9-1. Design fast and thermal fluences to November 5, 1976 for capsule P13V

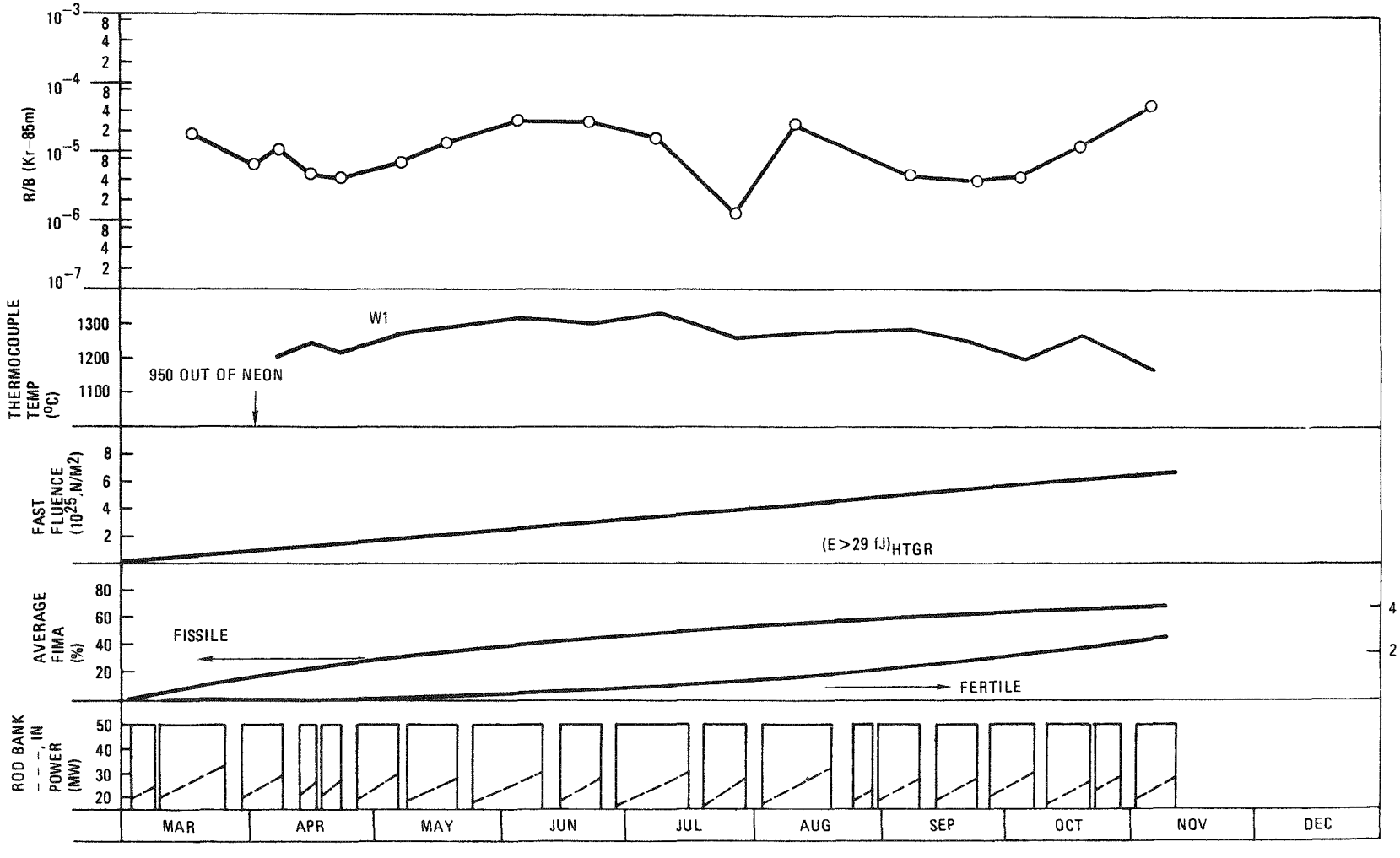

Fig. 9-2. Operation history for P13V cell 1 (WAR UC_2 TRISO/ThO_2 BISO) steady-state operation to November 5, 1976

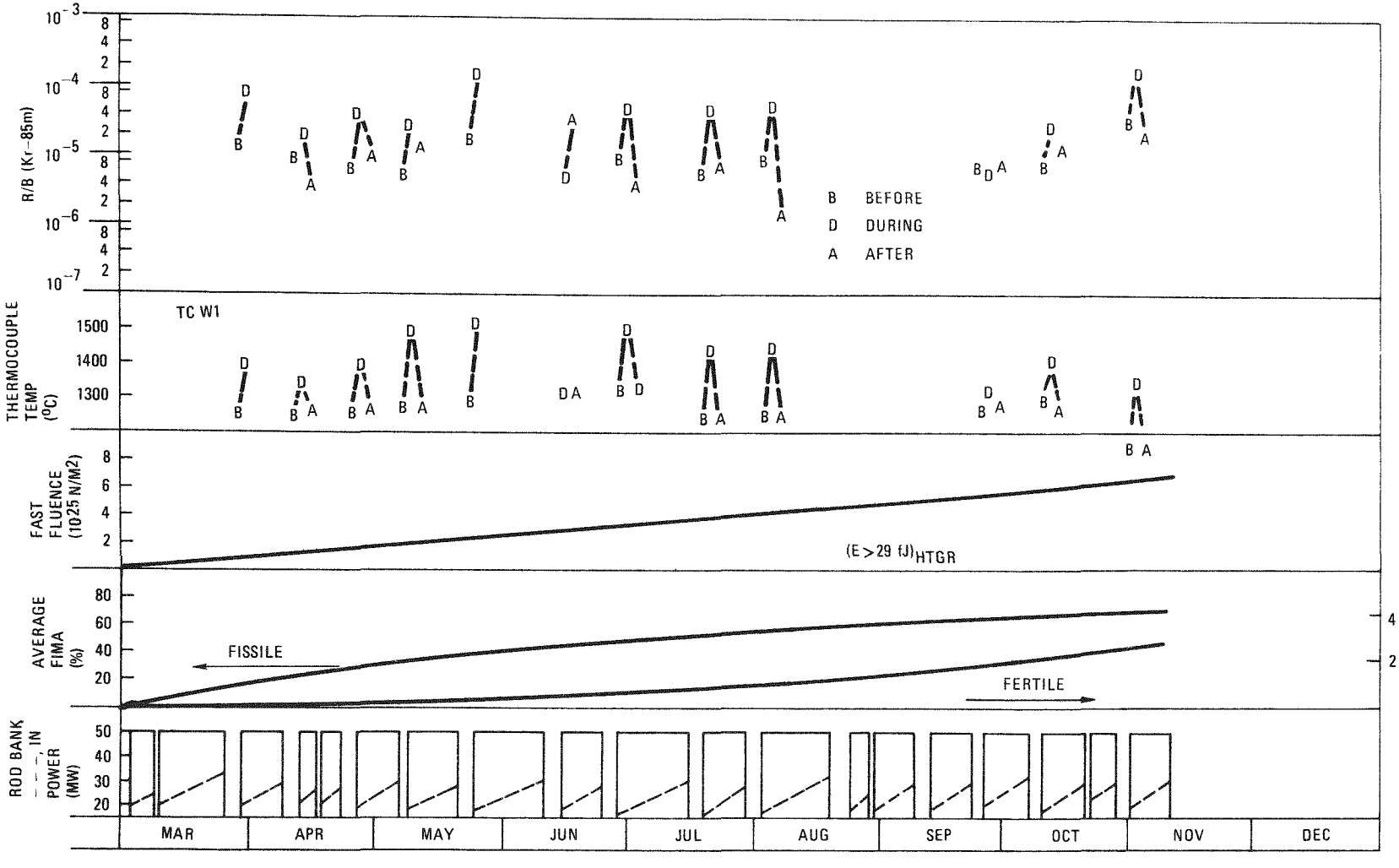

Fig. 9-3. Operation history for P13V cell 1 (WAR UC_2 TRISO/ThO_2 BISO) thermal cycled to November 5, 1976

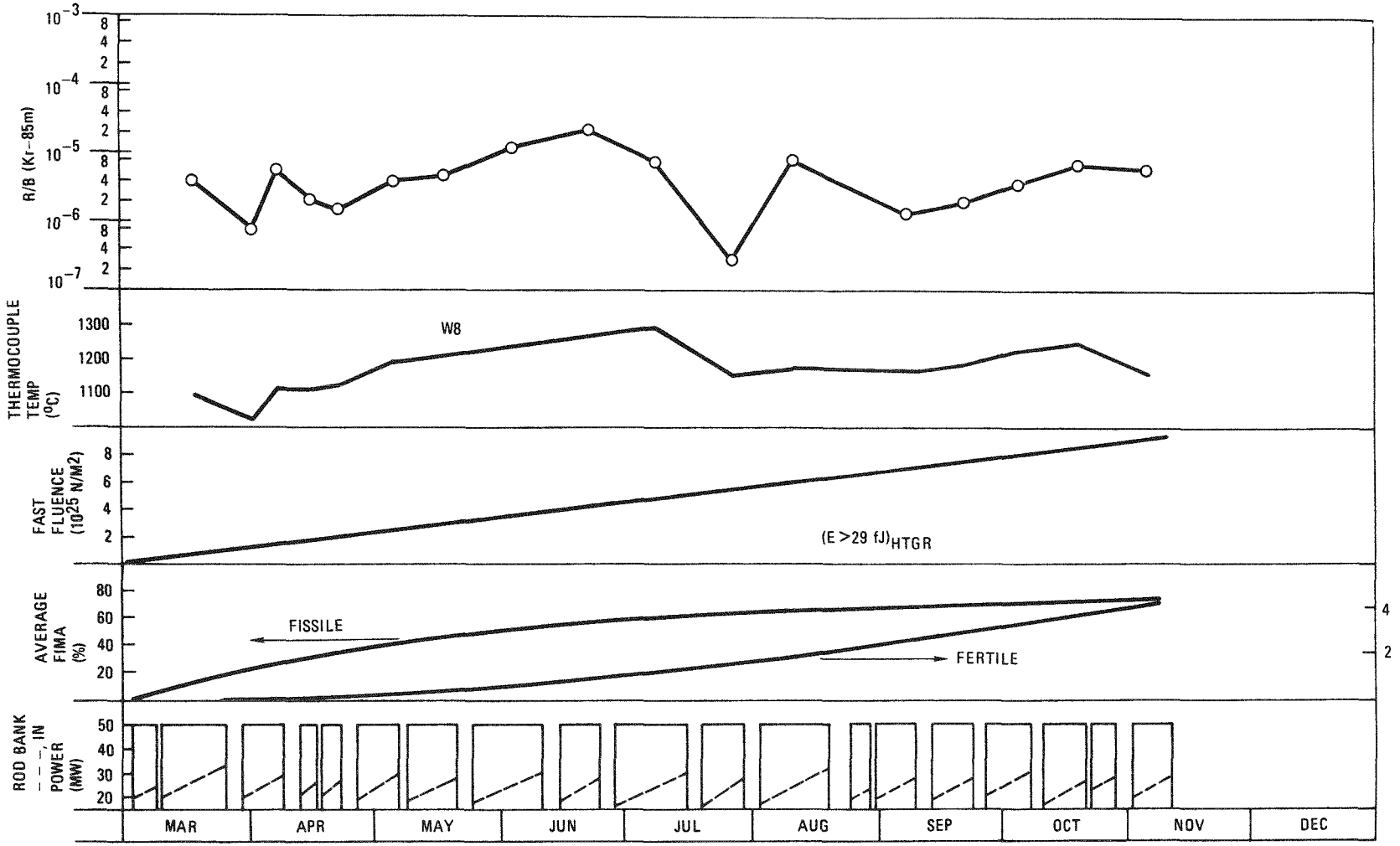

Fig. 9-4. Operation history for P13V cell 2 (WAR UC_2 TRISO/ThO_2 BISO) to November 5, 1976

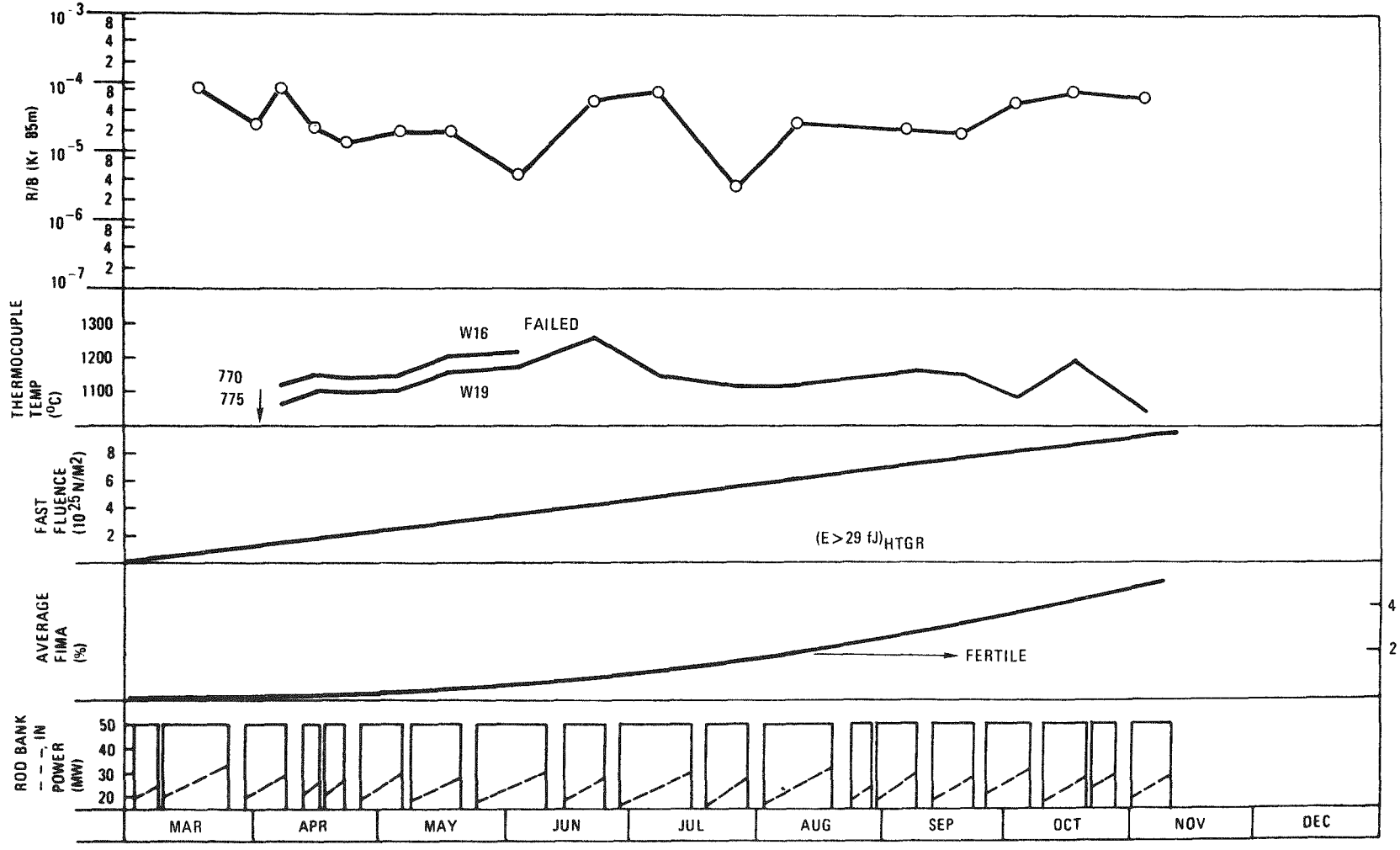

Fig. 9-5. Operation history for P13V cell 3 (ThO_2 BISO only) to November 5, 1976

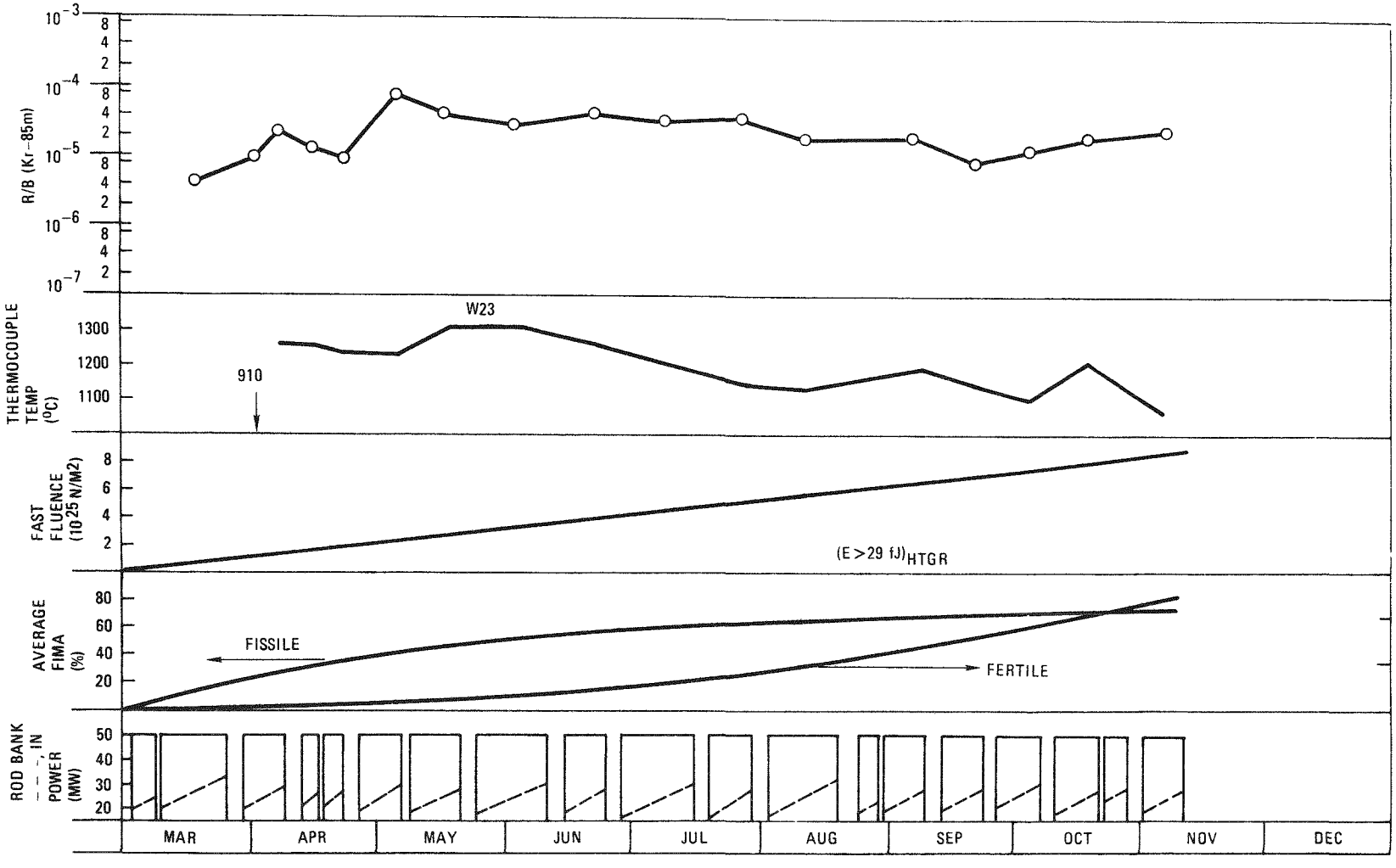

Fig. 9-6. Operation history for P13V cell 4 (VSM UC_2 TRISO/ThO_2 BISO) to November 5, 1976

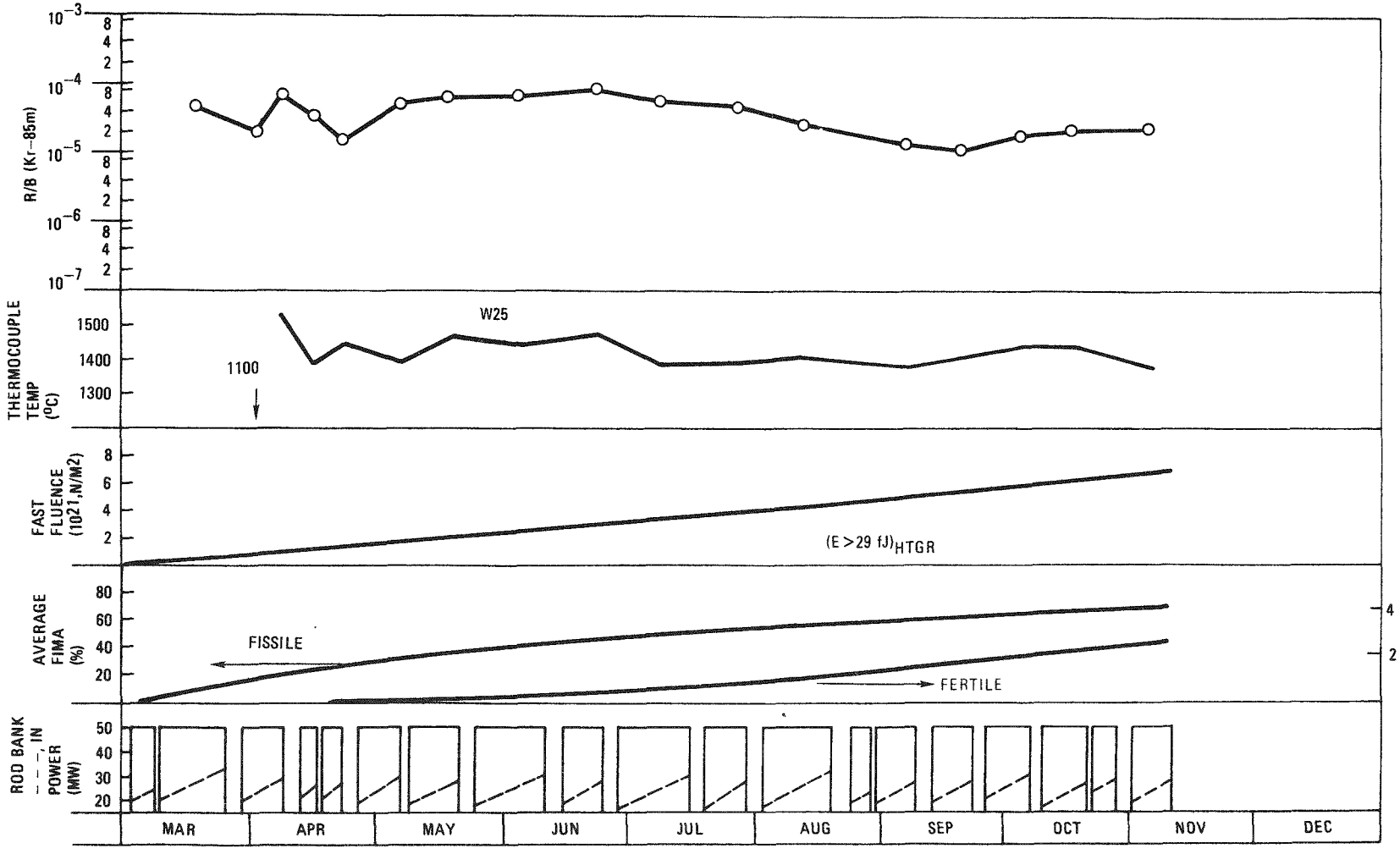

Fig. 9-7. Operation history for P13V cell 5 (WAR UC_2 TRISO/ThO_2 BISO) to November 5, 1976

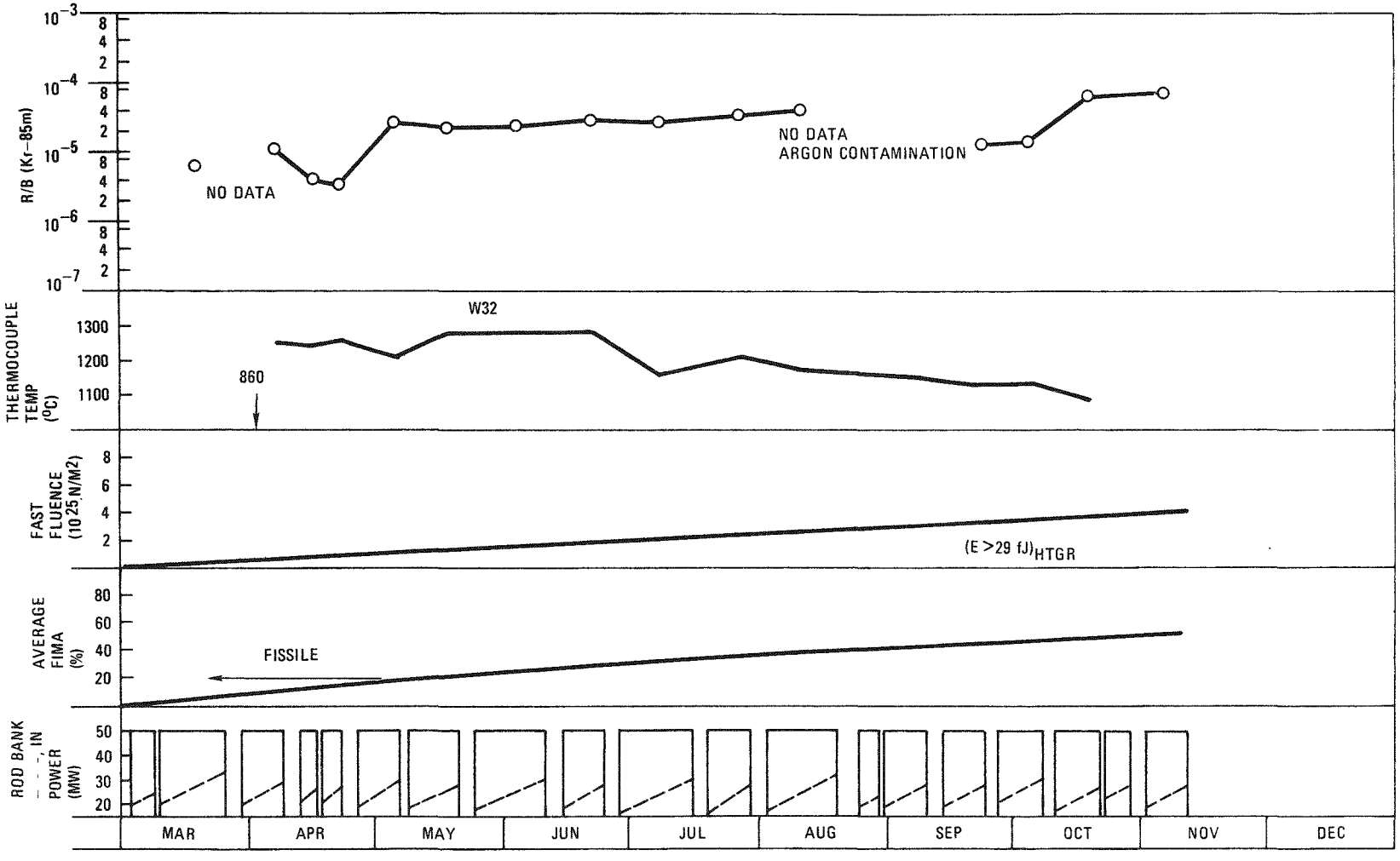

Fig. 9-8. Operation history for P13V cell 6 (WAR UC_2 TRISO only) to November 5, 1976

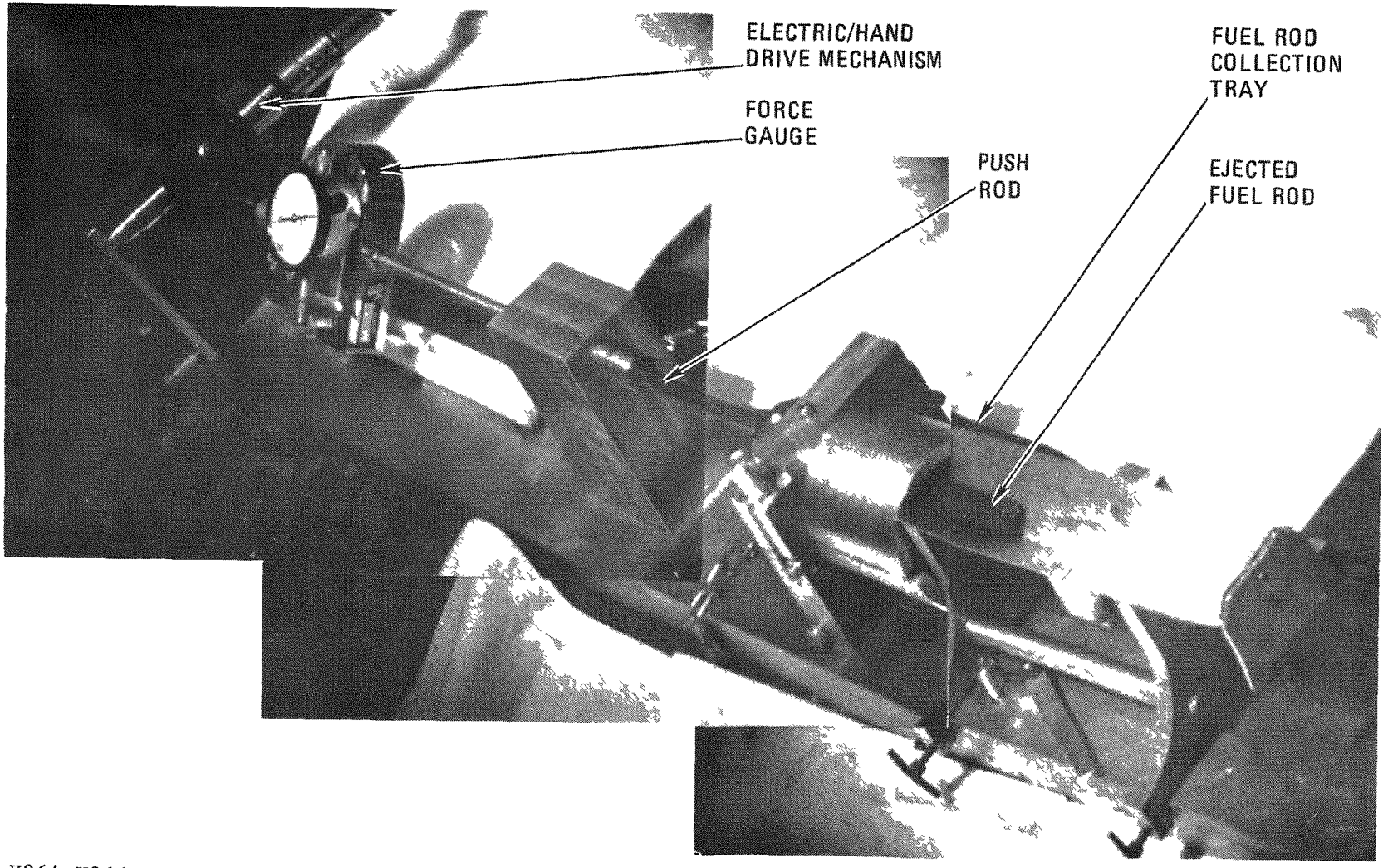

Fig. 9-9. Mechanism used to push fuel rod stacks out of P13T graphite crucible (crucible 2, column A)

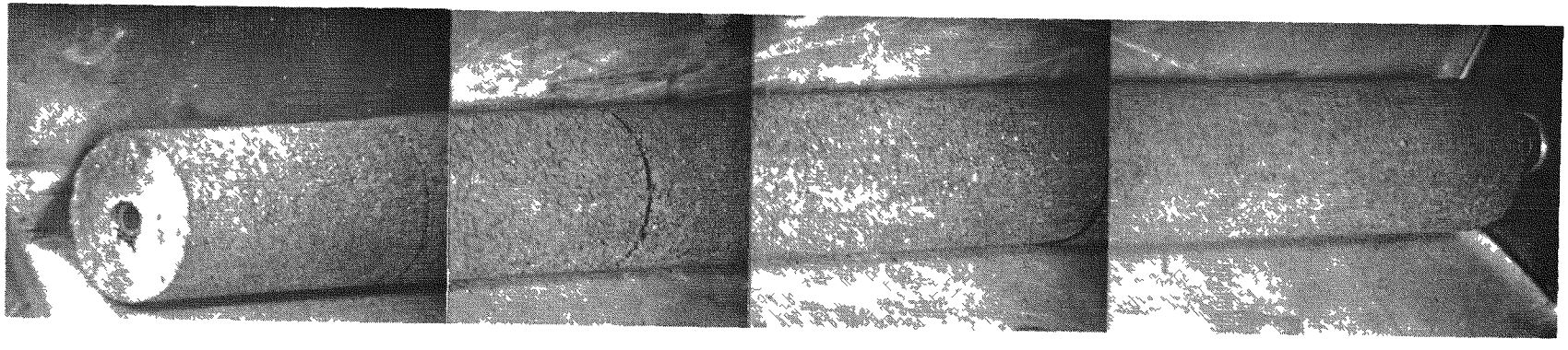

K2109-K2112

Fig. 9-10. As-ejected P13T fuel rod stack (crucible 1, column B)

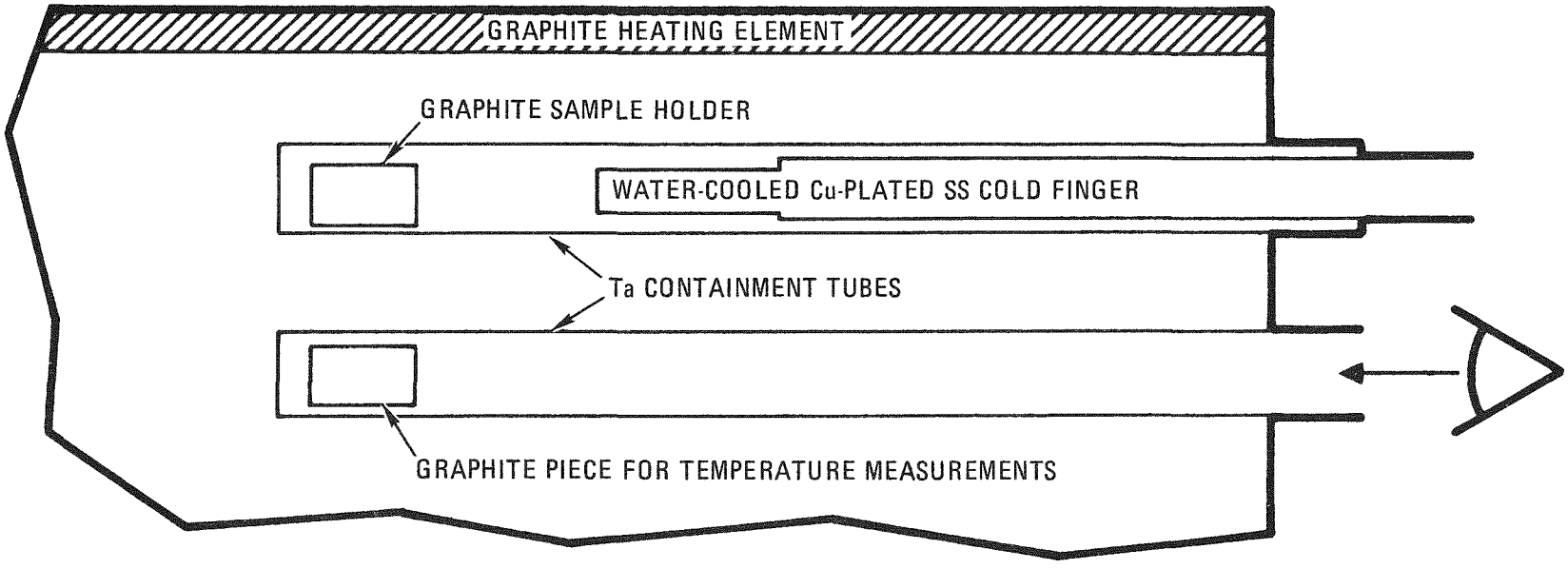

Fig. 9-11. Schematic diagram showing configuration for isothermal heating studies

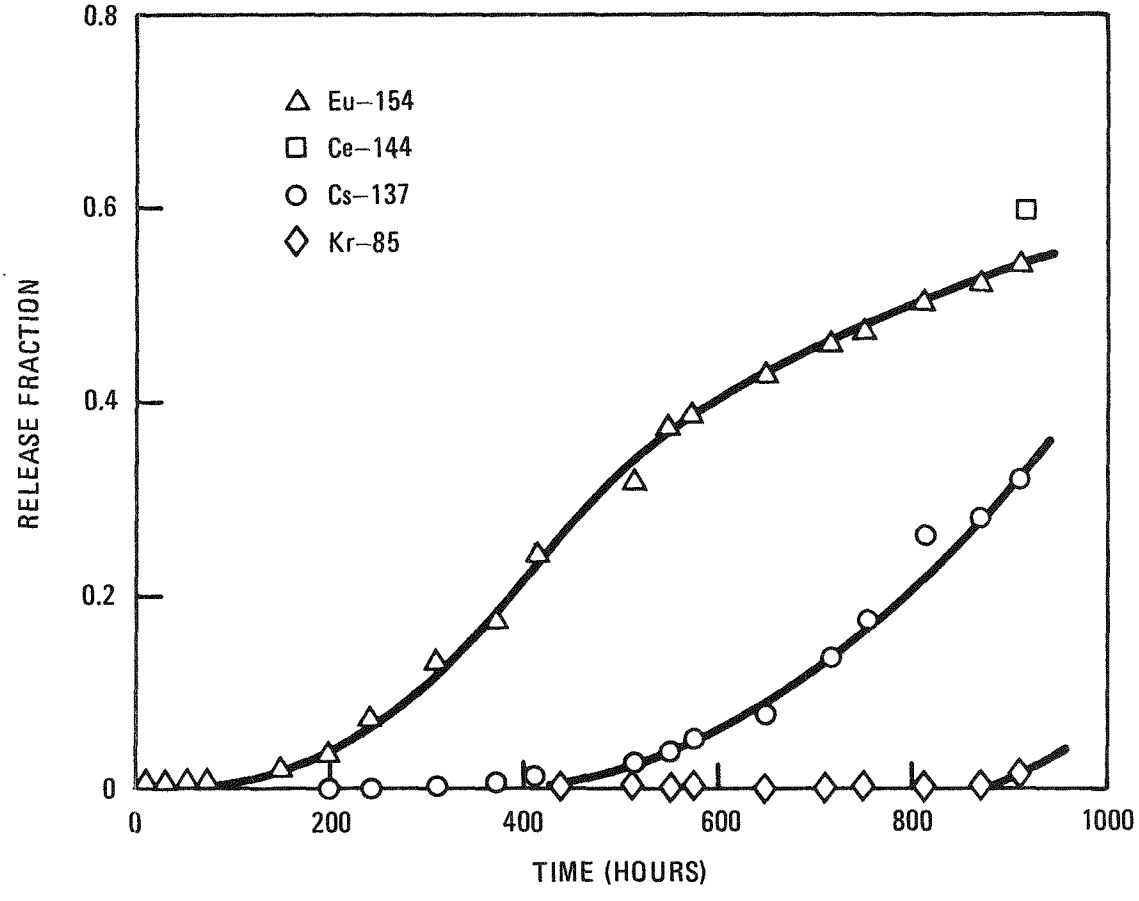

Fig. 9-12. Fission product release as a function of time at 1800°C for irradiated TRISO UC_2 fuel having a fission density of 1.2 x 10^{21} fissions/cm^3 inside the SiC layer

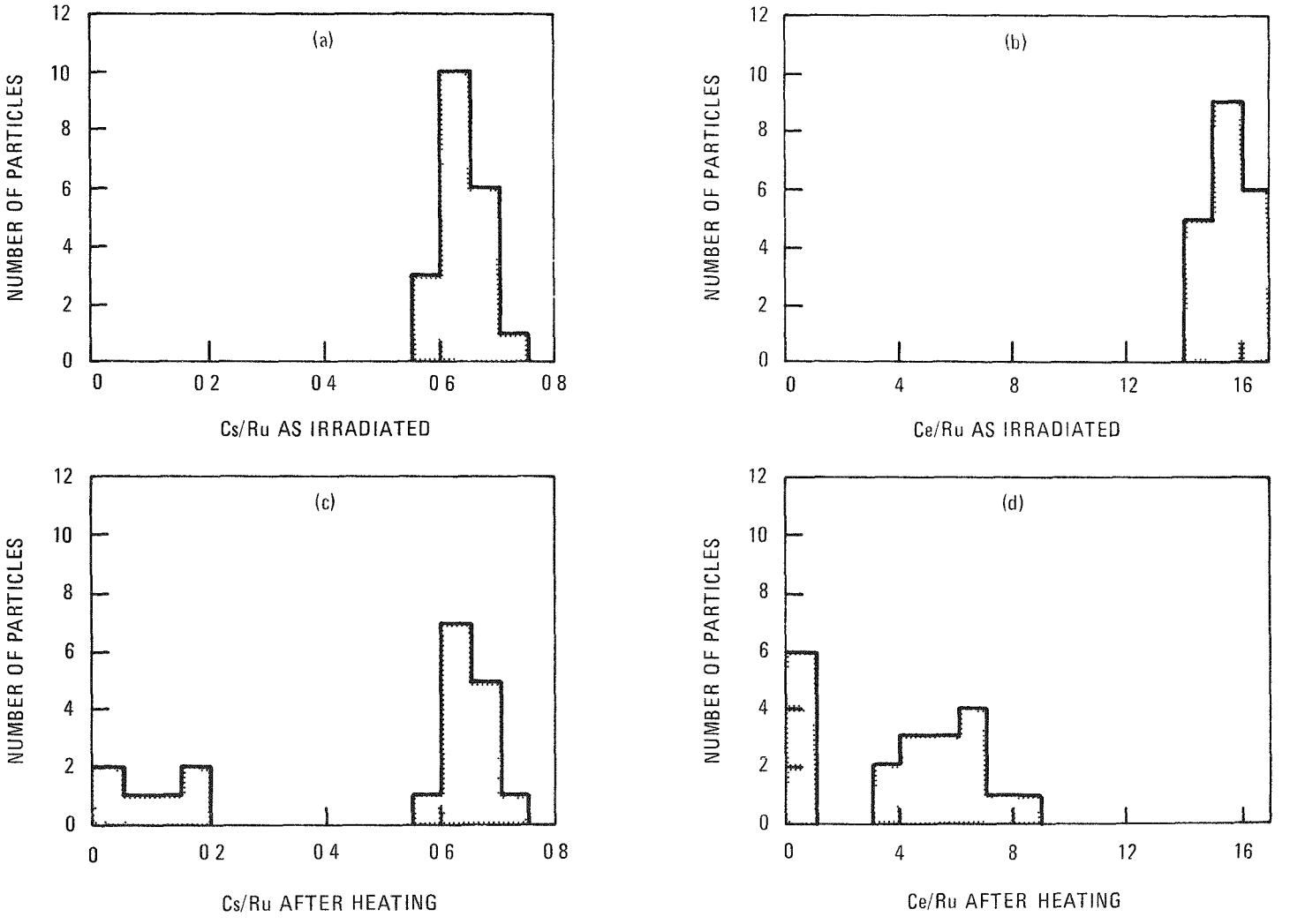

Fig. 9-13. Comparison of Cs/Ru (a,c) and Ce/Ru (b,d) activity ratios for TRISO UC_2 fuel having a fission density of 1.2×10^{21} f_{SiC} as irradiated and after isothermal heating for 905 hours at 1800°C

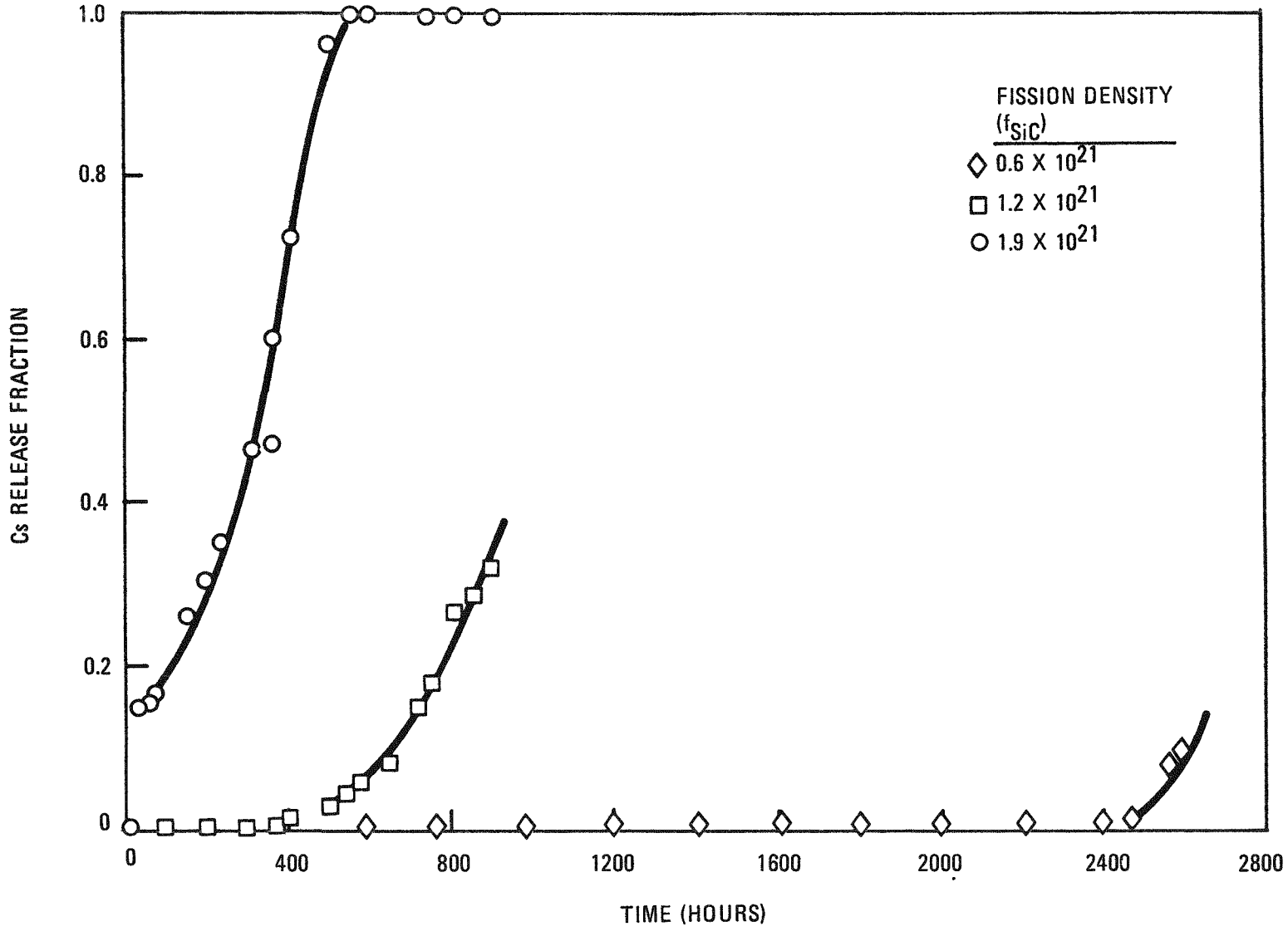

Fig. 9-14. Effect of fission density on Cs-137 release from irradiated TRISO UC_2 fuel particles as a function of time at 1800°C

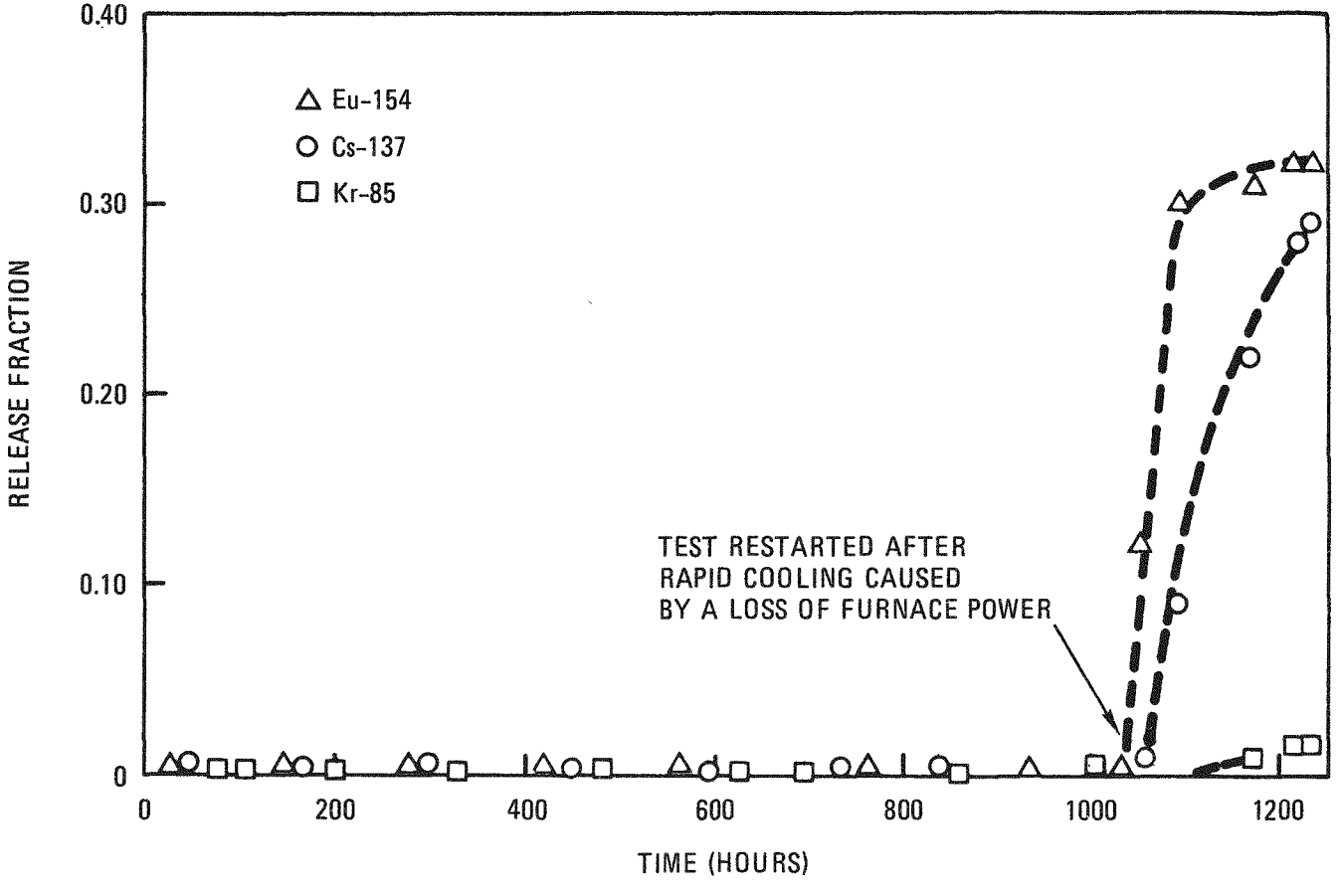

Fig. 9-15. Fission product release versus time measured at 1600°C from a TRISO UC_2 sample having a fission density of 1.2×10^{21} f_{SiC}. The test was cooled rapidly to room temperature after 1030 hours because of a power loss.

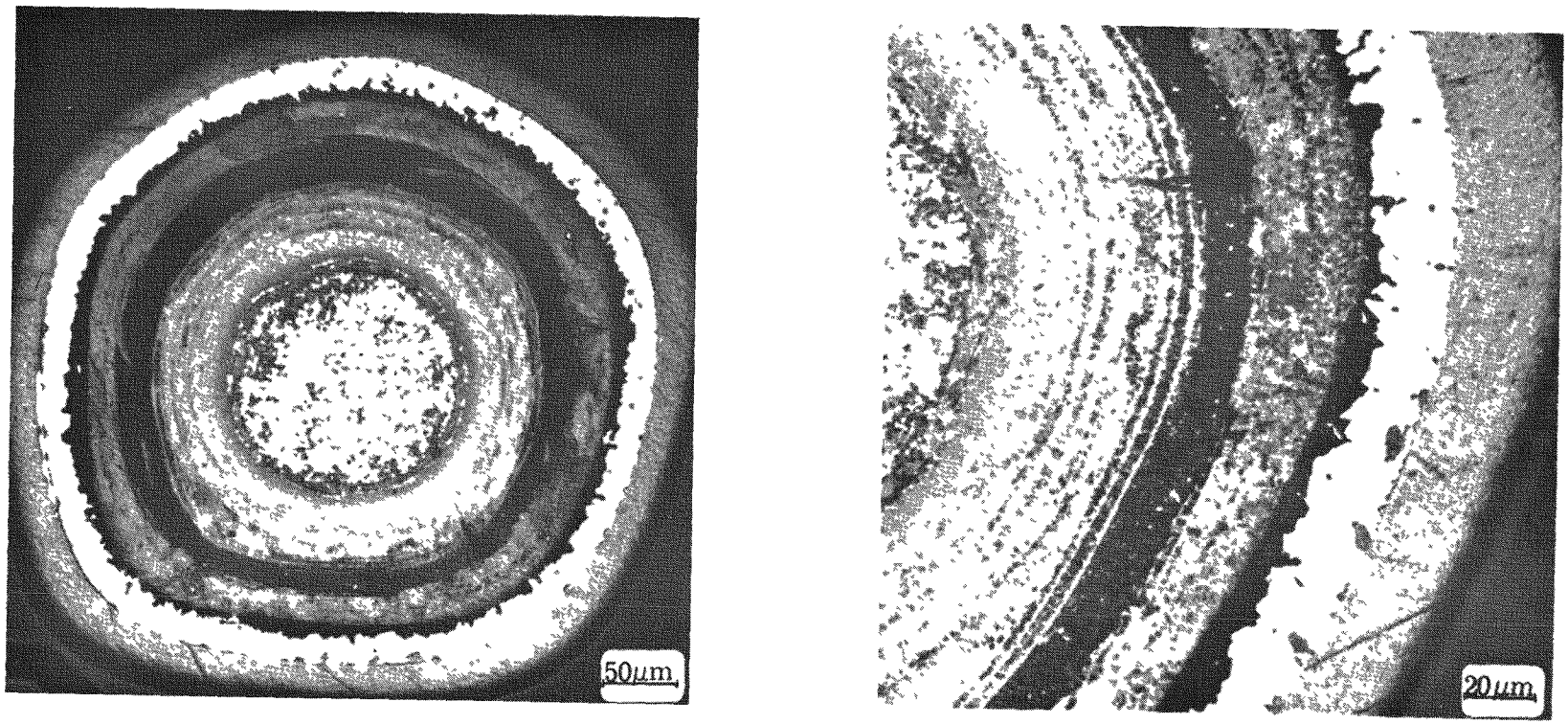

Fig. 9-16. Fission product - SiC attack observed in irradiated TRISO UC_2 having a fission density of 1.2×10^{21} f_{SiC} after isothermal heating for 165 hours at 2000°C

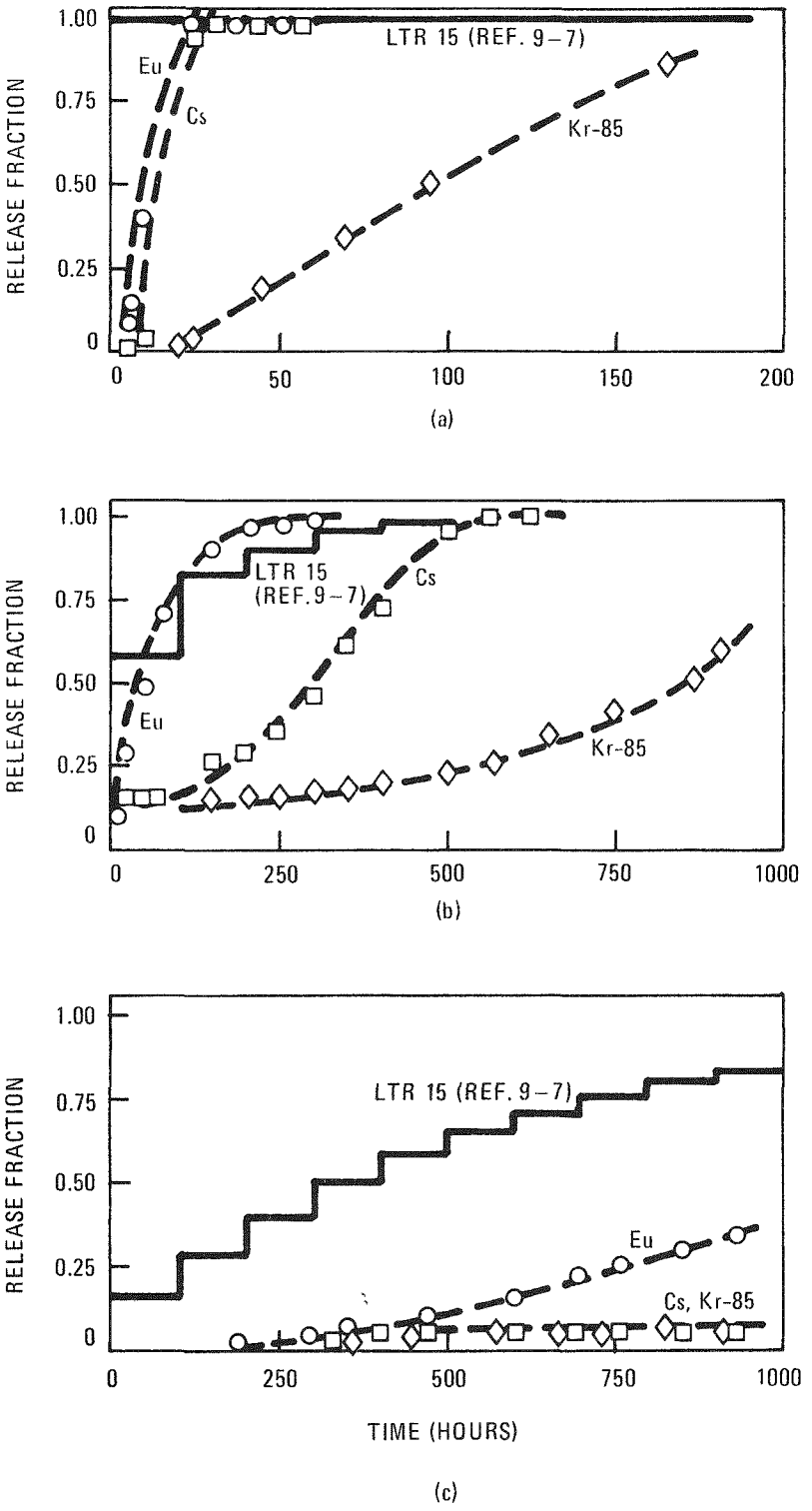

Fig. 9-17. Comparison of failure predictions made using LHTGR fuel performance models and observed fission product release as a function of time at 2000°C (a), 1800°C (b), and 1600°C (c) for a TRISO UC_2 sample having a fission density of $1.9 \times 10^{21} f_{SiC}$

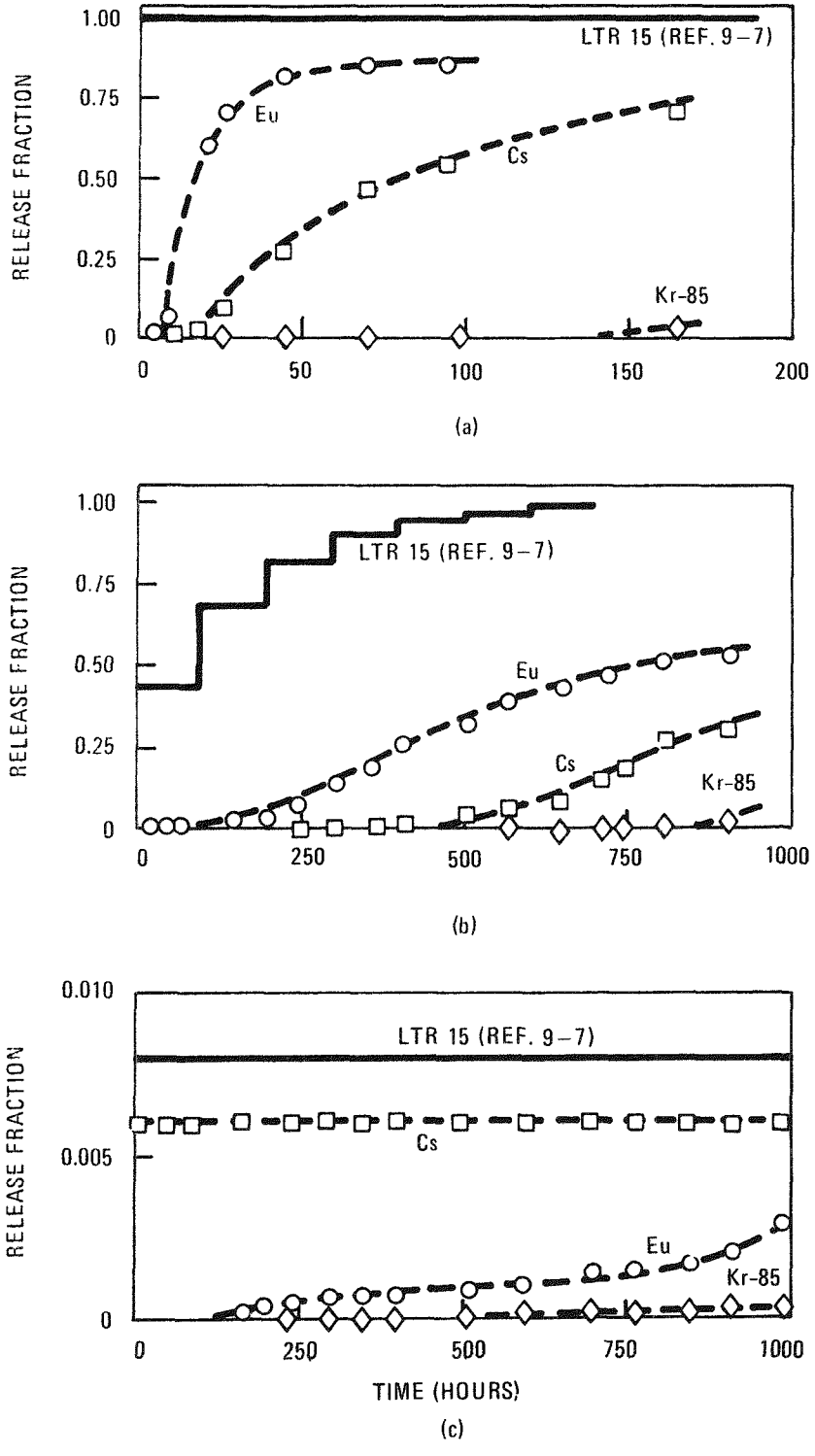

Fig. 9-18. Comparison of failure predictions made using LHTGR fuel performance models and observed fission product release as a function of time at 2000°C (a), 1800°C (b), and 1600°C (c) for a TRISO UC_2 sample having a fission density of 1.2×10^{21} f_{SiC}

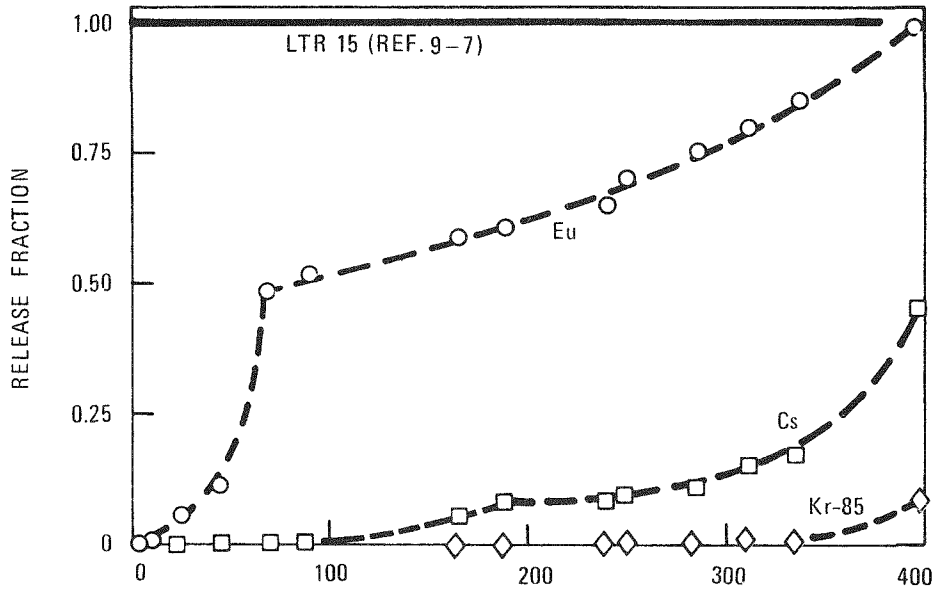

(a)

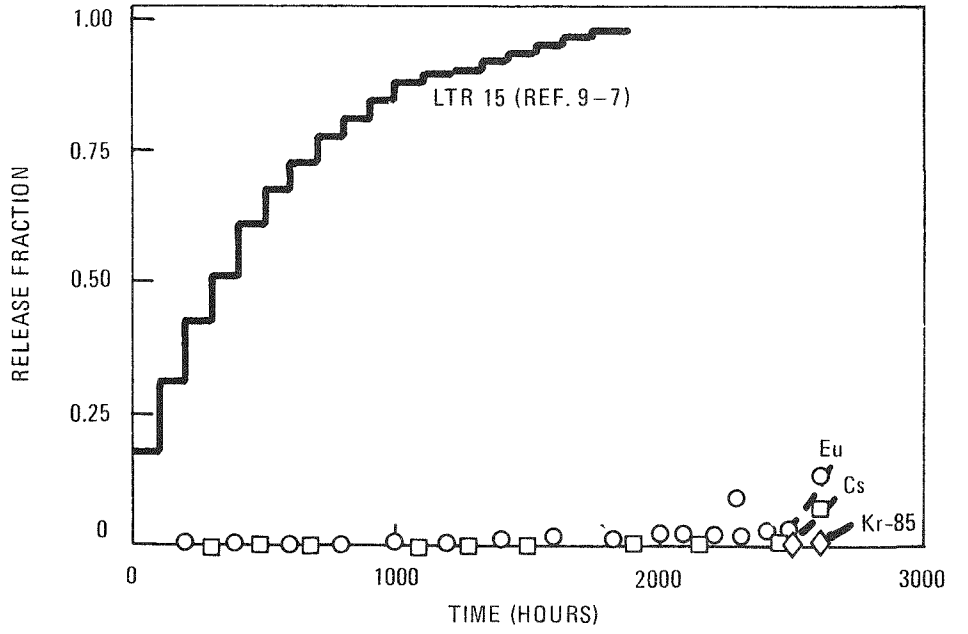

(b)

Fig. 9-19. Comparison of failure predictions made using LHTGR fuel performance models and observed fission product release as a function of time at 2000°C (a) and 1800°C (b) for a TRISO UC_2 sample having a fission density of 0.6×10^{21} f_{SiC}

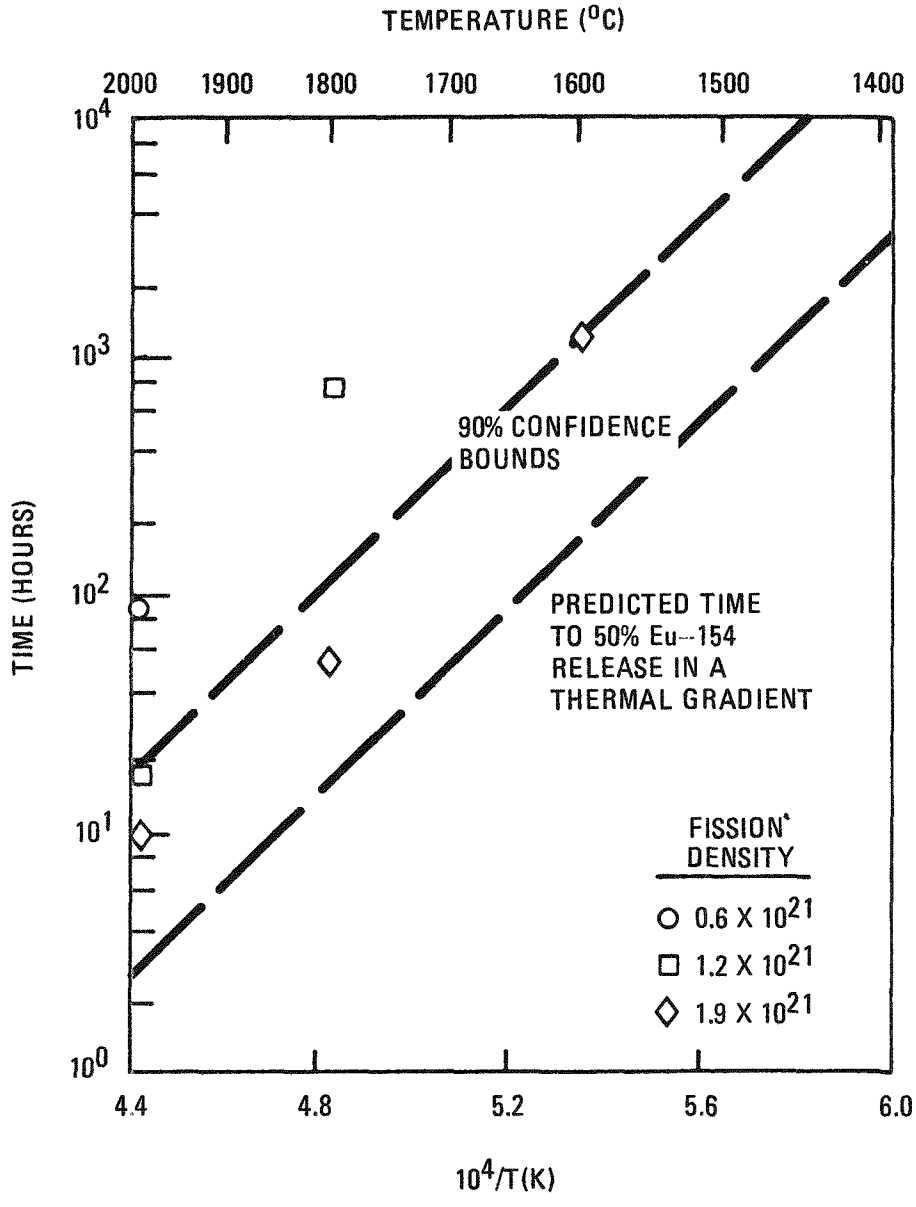

Fig. 9-20. Comparison of the predicted time to 50% lanthanide fission product release from irradiated TRISO UC_2 fuel in a thermal gradient and the observed time to 50% Eu release during isothermal heating

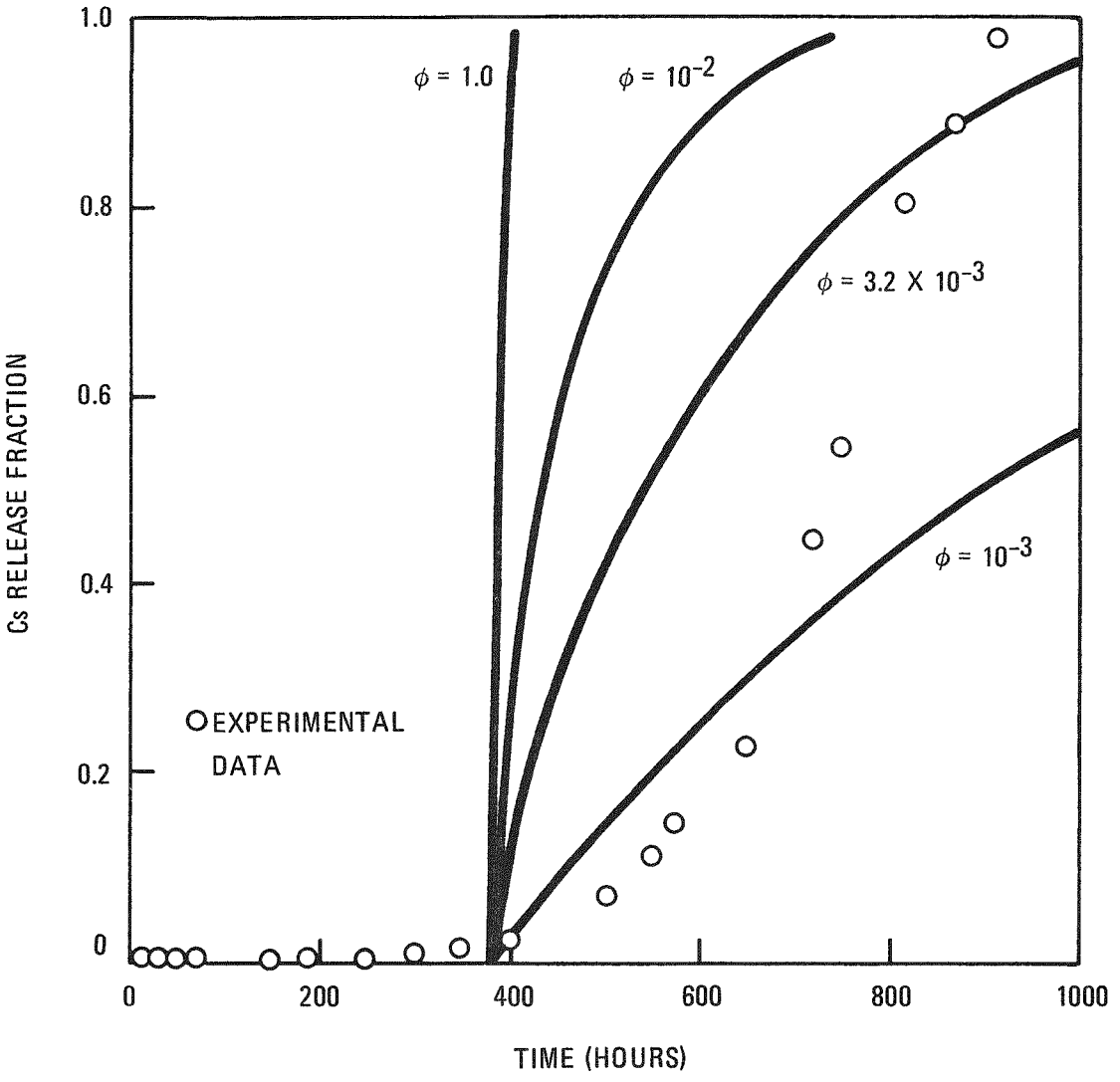

Fig. 9-21. Comparison of experimental Cs release data measured during an 1800°C isothermal anneal of a TRISO UC_2 sample having a fission density of 1.2 x 10^{21} f_{SiC} and COPAR calculations assuming DCs_{SiC} = DCs_{PyC} and partition factors (ϕ) between the IPyC and SiC layers of 1.0, 10^{-2}, 3.2 x 10^{-3}, and 10^{-3}

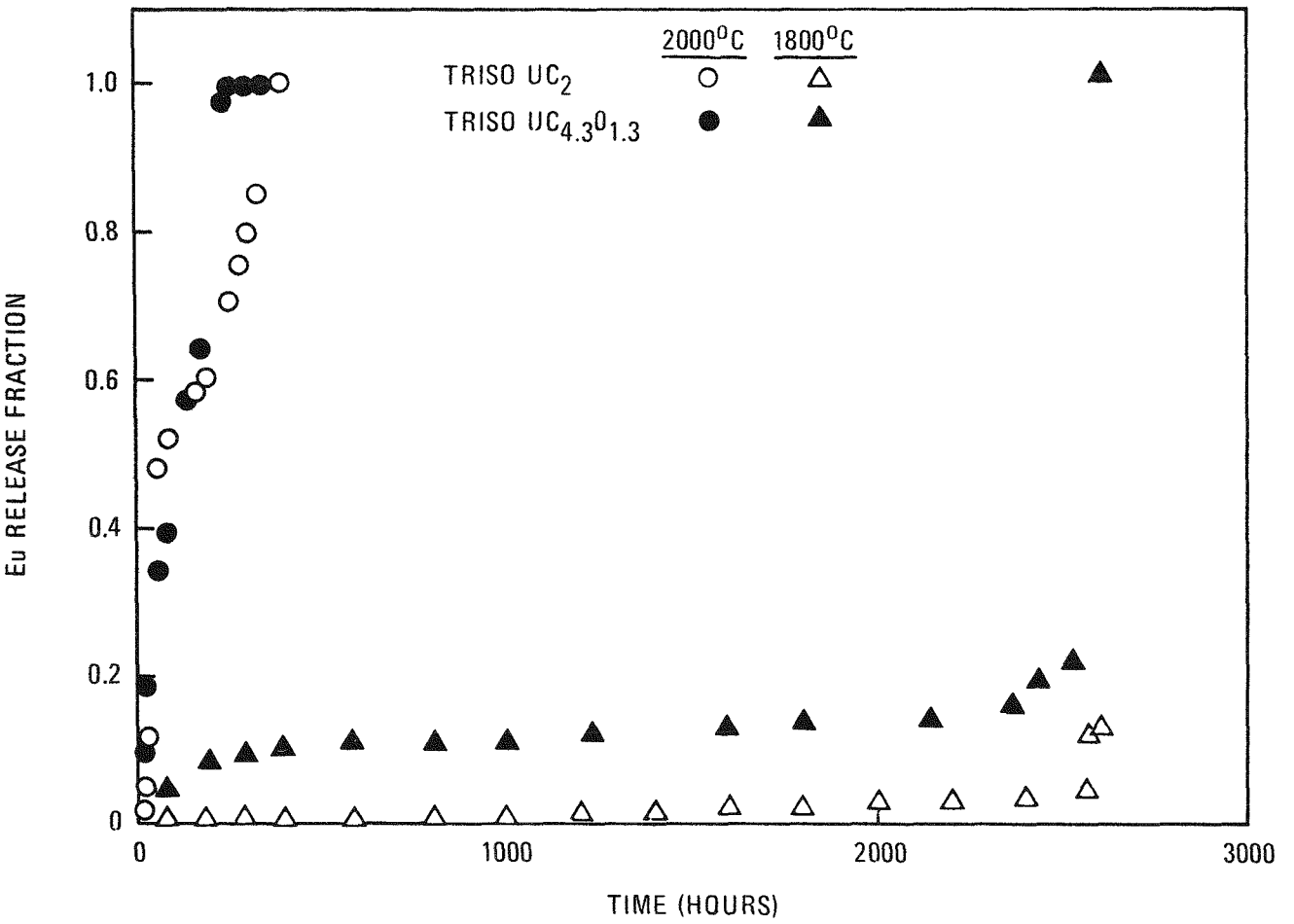

Fig. 9-22. Comparison of Eu-154 release fractions as a function of time during isothermal heating of TRISO UC_2 having a fission density of 0.6×10^{21} f_{SiC} and TRISO $UC_{4.3}O_{1.3}$ having a fission density of 0.5×10^{21} f_{SiC}

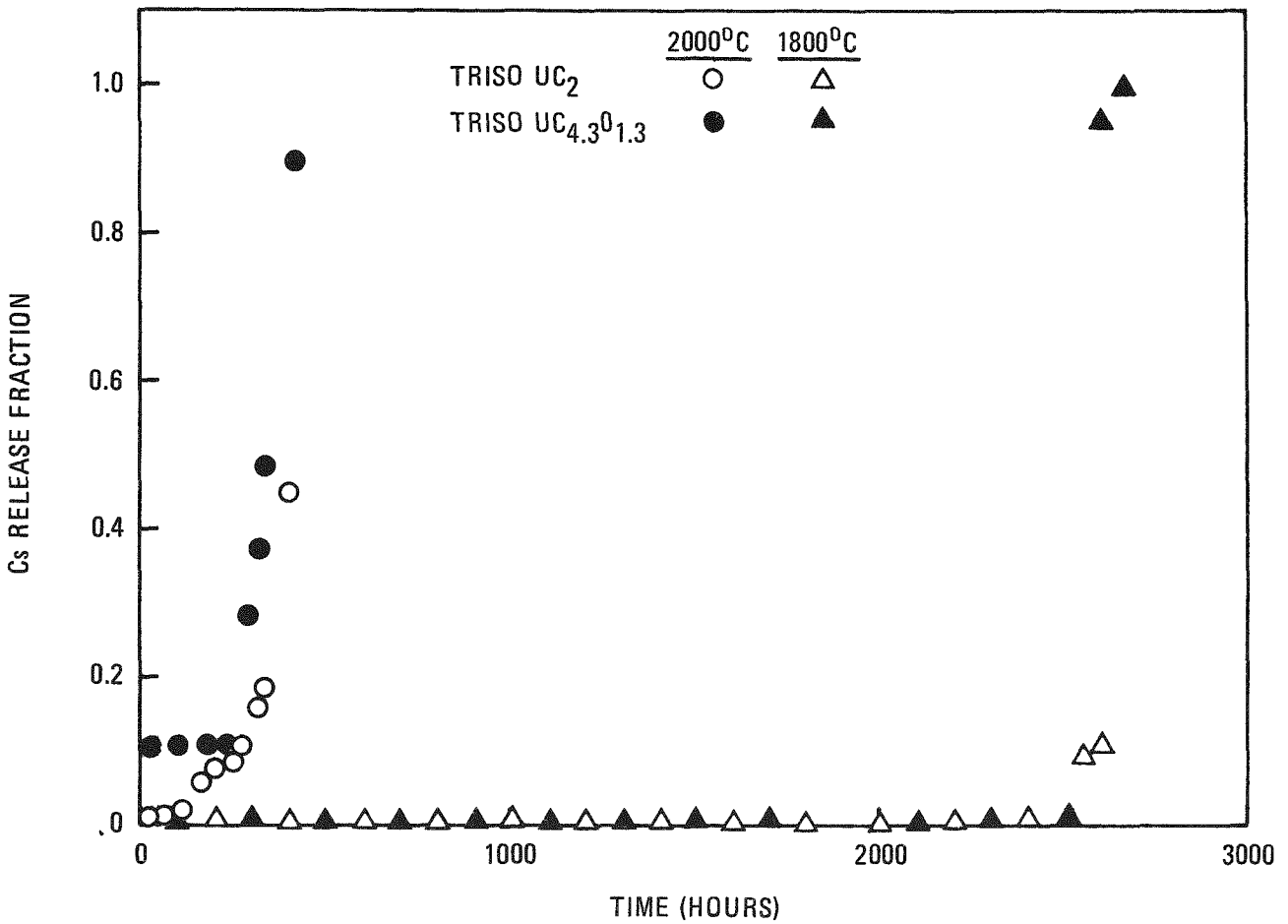

Fig. 9-23. Comparison of Cs-137 release fractions as a function of time during isothermal heating of TRISO UC_2 having a fission density of 0.6×10^{21} f_{SiC} and TRISO $UC_{4.3}O_{1.3}$ having a fission density of 0.5×10^{21} f_{SiC}

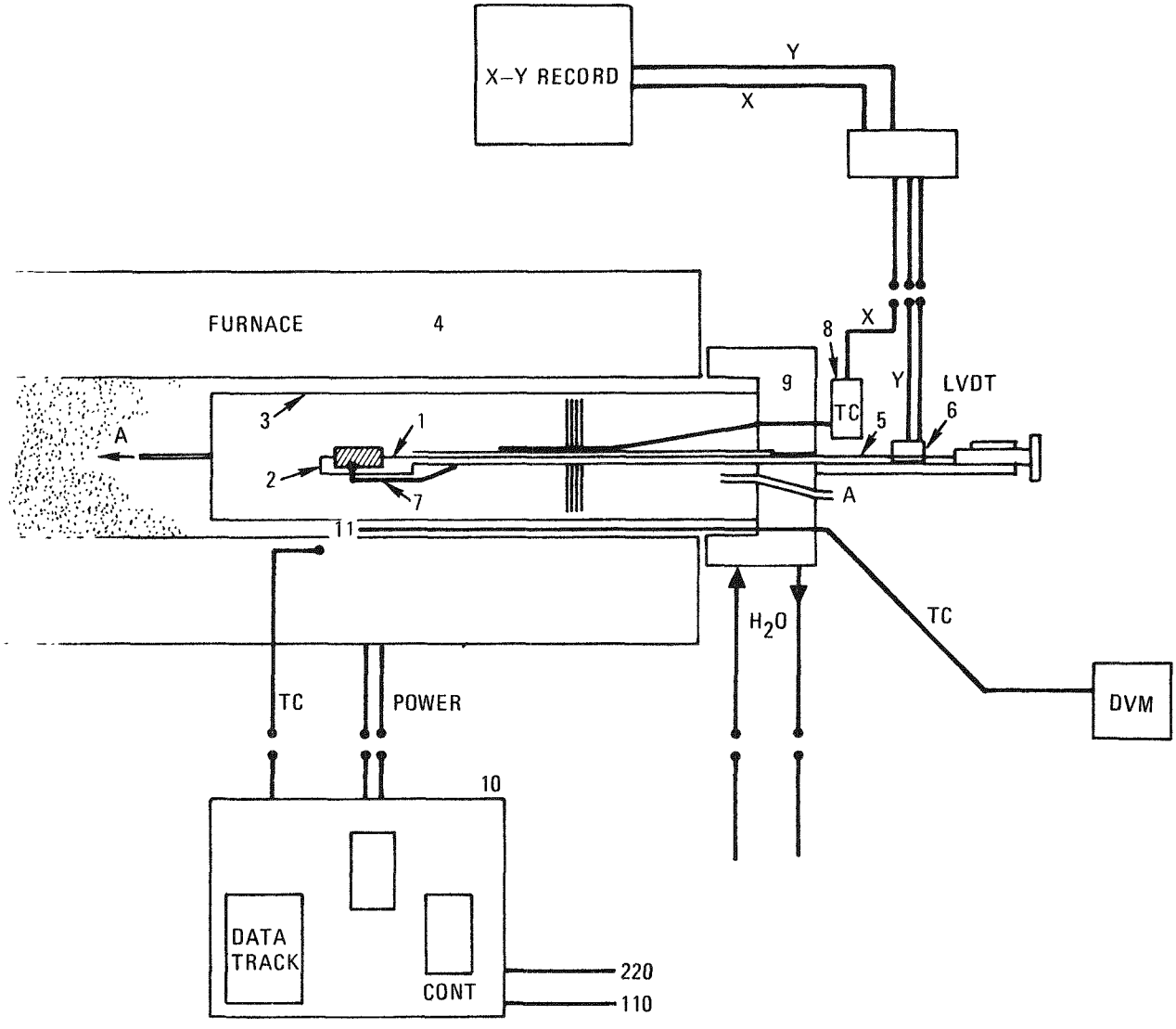

Fig. 9-24. Schematic of thermal expansivity test device

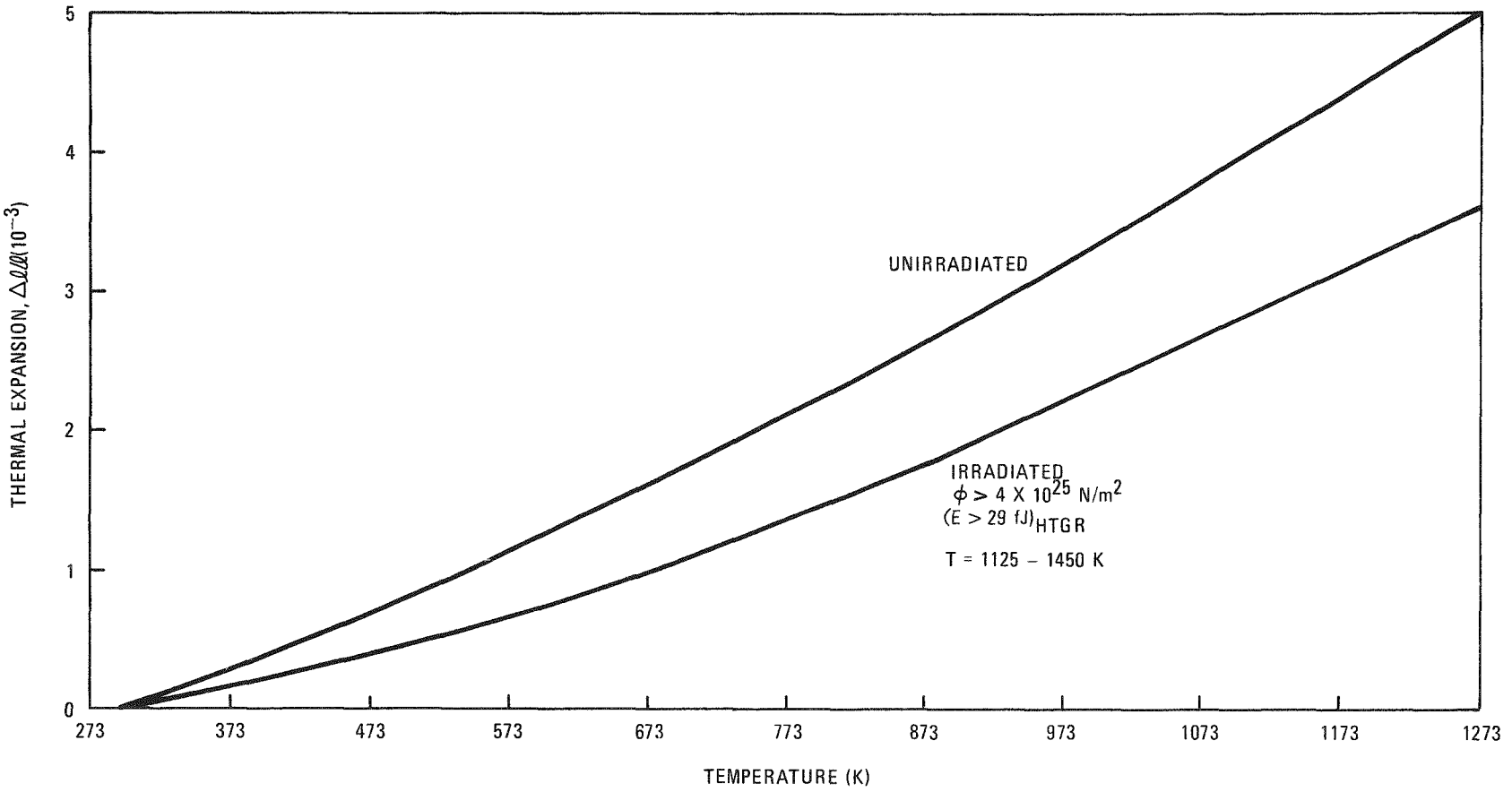

Fig. 9-25. Axial thermal expansion of HTGR fuel rods in P13Q experiment

11. GRAPHITE DEVELOPMENT
189a NO. 00552

Characterization and irradiation of graphites for replaceable fuel and reflector elements, core support components, and permanent side reflectors are under way. The work includes irradiation, characterization, mechanics of strength, fatigue behavior, writing of standards, structural integrity of fuel blocks, and oxidation studies. Development of control materials is also included, but no work is funded during FY-77.

TASK 100: FABRICATION AND OPERATION OF IRRADIATION CAPSULES

Capsule OG-5

Work on capsule OG-5 has been suspended due to the shutdown of the Oak Ridge Reactor during FY-77. Design documents, drawings, and completed hardware have been stored pending resolution of the resumption of ORR operations. Assuming the ORR operates in FY-78, capsule OG-5 will be completed and assembled for shipment to the ORR for an early FY-78 insertion.

TASK 200: GRAPHITE SPECIMEN PREPARATION AND PROPERTY MEASUREMENTS FOR CAPSULE IRRADIATION

Capsule OG-3: Thermal Expansivity

Postirradiation work on capsule OG-3 was completed with the measurements of the thermal expansivity of control specimens of H-451 graphite (lot 426) and SO818 graphite. The measurements were used to compute the irradiation-induced changes in thermal expansivity (measured between ambient temperature and 773 K) in specimens of these two grades irradiated in capsules OG-1 through OG-3 to a variety of fluences and temperatures. The results are summarized in Tables 11-1 and 11-2.*

*Tables appear at the end of Section 11.

The data in Tables 11-1 and 11-2, together with data on thermal expansivity changes in graphites H-429 and TS-1240 tabulated in the previous quarterly report (Ref. 11-1), are plotted as a function of neutron fluence and irradiation temperature in Fig. 11-1. At the lower irradiation temperatures (865 to 1045 K), the thermal expansivity first increases by 5 to 10% and then slowly decreases. At higher irradiation temperatures, the thermal expansivity decreases by as much as 50% of its preirradiation value, with the decrease most marked at the highest irradiation temperatures. Data for all the near-isotropic graphites fall into the same band regardless of orientation and log location, with the exception of grade H-429 (small-diameter prototype of H-451); the irradiation-induced changes in thermal expansivity for H-429 were lower than those for the other graphites.

For convenience in design calculations, the data for irradiation-induced fractional changes in thermal expansivity, $\Delta\alpha/\alpha$, for H-451, TS-1240, and S0818 graphites were fit to the following polynomial:

$$\Delta\alpha/\alpha = (0.27830 - 4.2734 \times 10^{-4}T + 1.7815 \times 10^{-7}T^2)\Phi - 2.0664 \times 10^{-2}\Phi^2 + 1.3601 \times 10^{-3}\Phi^3 \quad ,$$

where T is the irradiation temperature (°C) and Φ is the neutron fluence $[10^{25}\ n/m^2\ (E > 29\ fJ)_{HTGR}]$. Curves calculated from the polynomial are included in Fig. 11-1. The curves are similar to the empirical design curves currently in use.

A topical report on irradiation experiment OG-3 is in preparation.

TASK 300: CHARACTERIZATION OF CANDIDATE GRAPHITES FOR PROPERTIES AND PURITY

Replaceable Fuel and Reflector Elements

Characterization work on preproduction lots of graphite H-451 has been completed. Work on Union Carbide Corporation (UCC) grade TS-1240 and AirCo

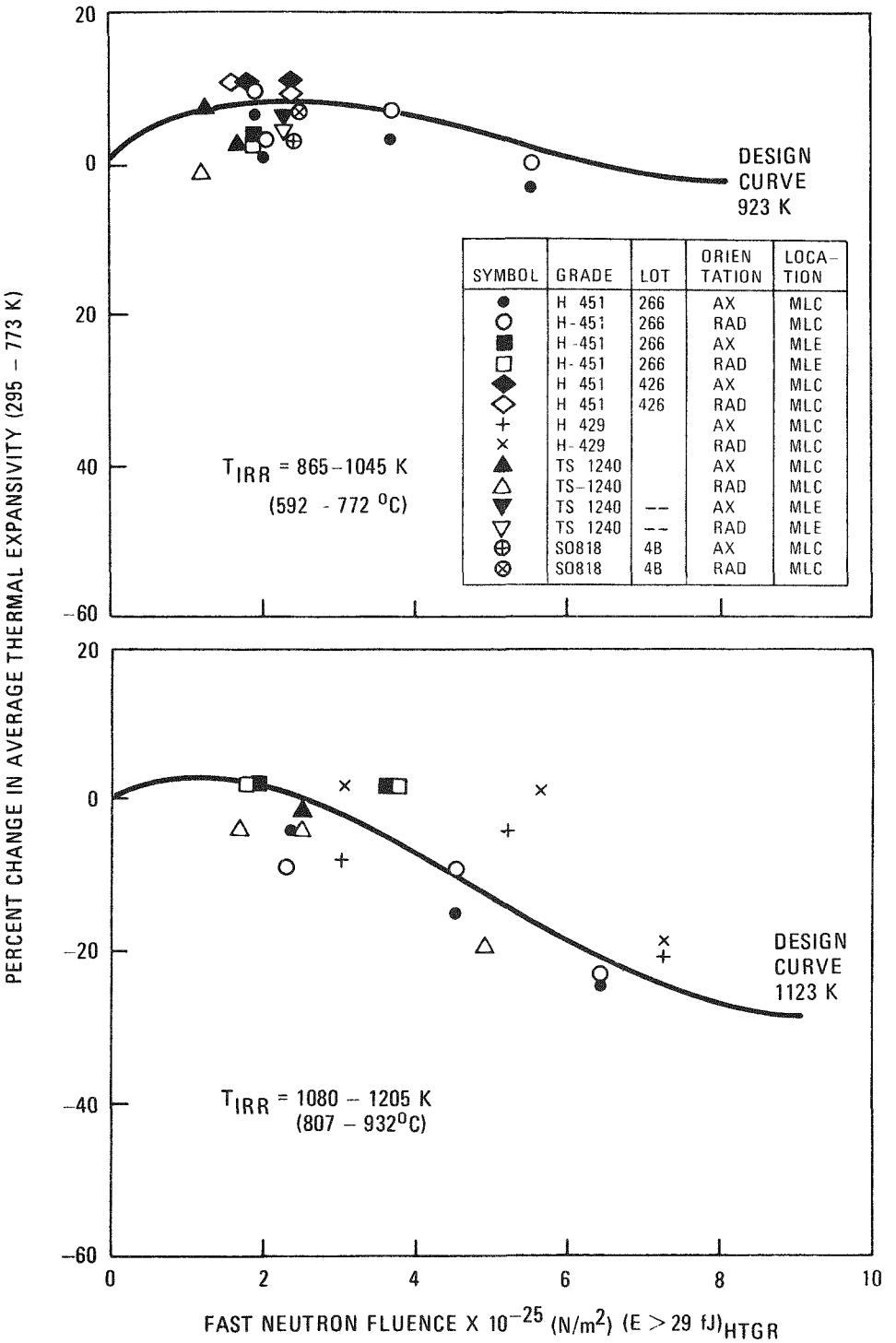

Fig. 11-1. Percent change in thermal expansivity (295-773 K) of near-isotropic graphites as a function of fast neutron fluence: (a) irradiation temperature 865-1205 K

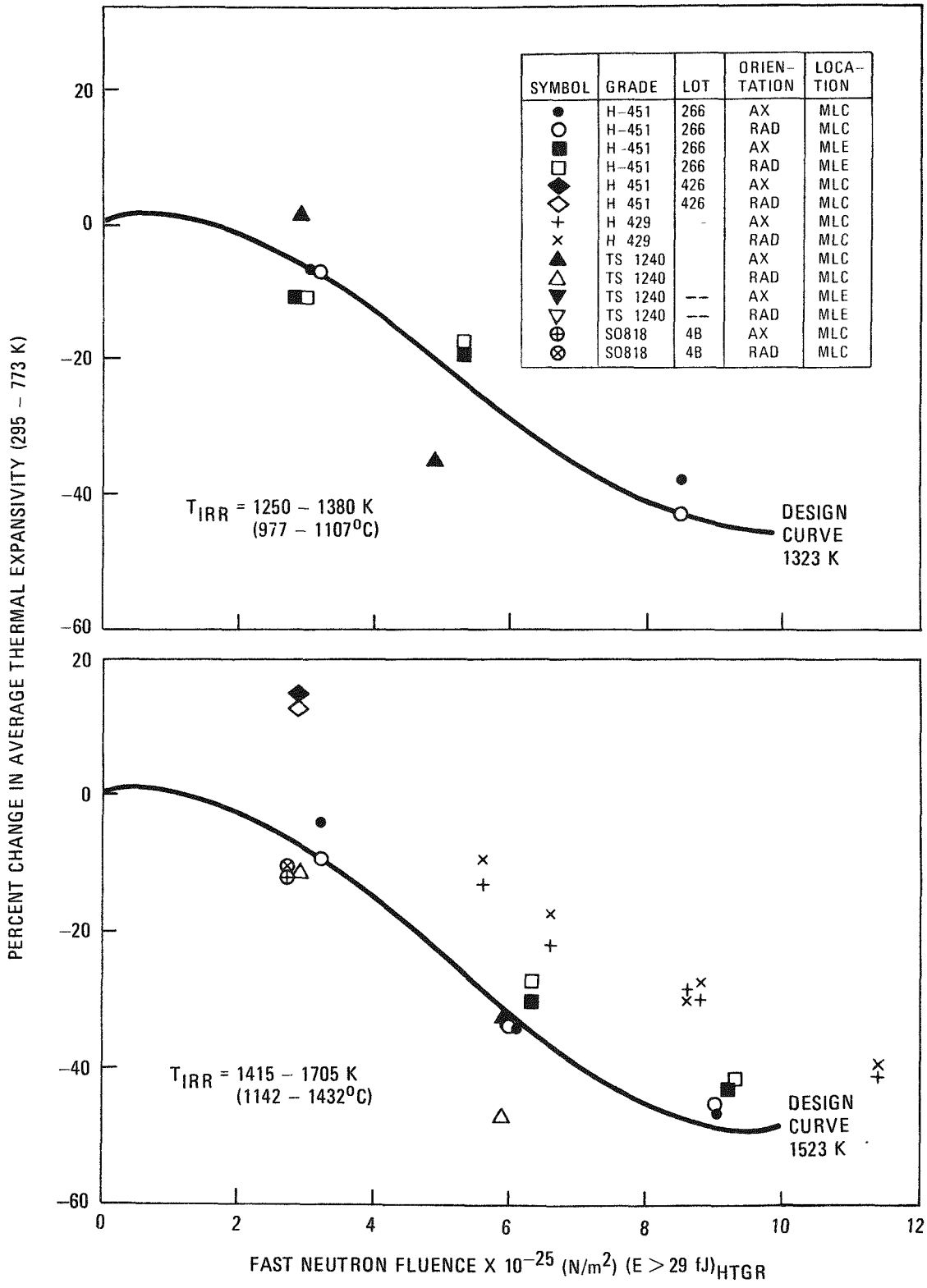

Fig. 11-1. Percent change in thermal expansivity (295-773 K) of near-isotropic graphites as a function of fast neutron fluence: (b) irradiation temperature 1250-1705 K

Speer (AS) grade S0818 has been suspended. Current work is concentrated on production logs of H-451 manufactured for Fort St. Vrain fuel element reloads. Approximately 350 logs were processed through the bake state during FY-76.

H-451 Production Logs

One hundred of the 350 logs were processed through graphitization and delivered to General Atomic for experimental purposes. Approximately 250 logs remain in storage in the bake state at the GLCC Morganton plant. These logs will be completed and utilized for future FSV fuel element reload segments. Thirty-four logs from this production order were procured for experimental work on Task 11. Eight of the logs were resold to ORNL and four to Brookhaven National Laboratory (BNL) for experimental work. Approximately 45 of the logs were purchased by GA-ORNL for reprocessing studies. Six logs were purchased by GA for fuel processing studies and an additional 14 for fuel test element work. The following work is planned under Task 11 on the H-451 production logs:

1. Characterization of four logs for properties and purity.

2. Tensile strength measurements on specimens taken from each of the 100 logs.

The tensile specimens were taken at the approximate midlength center (MLC) of each log (axial) and from an end slab (radial). Data will be compiled to determine the mean and minimum tensile strength at the weakest location (MLC) of each log.

In conjunction with testing the strength of the 100 production logs, a round-robin test program is under way with GLCC to assure that tensile and flexural test procedures give equivalent results. A log of H-451 was sampled and the specimens divided randomly; one portion is being tested by GLCC and a second portion by GA. Results are expected for the next quarterly report.

S0818 Preproduction Graphite

Thermal conductivity values for S0818 graphite are given in Table 11-3. This completes the preliminary characterization of S0818.

Side Reflector Graphite

GLCC's grade HLM is under investigation as a candidate graphite for side reflector blocks. Grade HLM is an extruded graphite 1.14 m in diameter by 1.83 m long. A half log was purchased for characterization.

A summary of the mean values of tensile, flexural, and compressive strengths of HLM is given in Table 11-4. Complete data sets are presented in Tables 11-5 through 11-7. Thermal conductivity data are presented in Table 11-8. In general the axial strength of HLM is highest at the outer edge of the log and there is a gradient across the diameter from the edge to the center. This pattern was less pronounced in the radial specimens. The tensile strength values ranged from 6.8 to 13.8 MPa, flexural strength from 13.8 to 20.8 MPa, and compressive strength from 35.3 to 44.7 MPa.

Core Support Floor Graphites

UCC's grade PGX is under investigation as a candidate graphite for core support floor blocks. Grade PGX is a molded graphite 1.14 m in diameter by 1.83 m long. A full log was purchased for characterization.

A summary of the mean values of tensile and compressive strengths of PGX is given in Table 11-9. Complete data sets are presented in Tables 11-10 and 11-11. The tensile values of PGX range from 8.1 to 11.4 MPa and the compressive strength from 38.3 to 45.7 MPa. The strengths in the radial direction were slightly lower than those for the axial direction. There was a gradient from end to end in the log, but not along the radius.

Core Support Post and Seat Graphites

Stackpole Carbon's (SC) grade 2020 and GLCC's grade H-440 are candidate materials for core support post and seat components. Grades 2020 and H-440 are fine-grained isostatically molded graphites. Grade 2020 is manufactured as logs 254 mm in diameter by 1828 mm long, and grade H-440 is manufactured as a preproduction log with a cross section of 330 mm by 330 mm and a length of 1828 mm. Production logs of H-440 will be 254 mm in diameter by 2108 mm long.

Grade 2020 is being characterized first. A summary of the mean values of tensile, flexural, and compressive strengths of 2020 is given in Table 11-12. Complete data sets are presented in Tables 11-13 through 11-15. Thermal conductivity data are given in Table 11-16. Grade 2020 is uniform in strength along the radius, but the longitudinal center had a higher strength than the ends. The tensile strengths range from 14.1 to 18.9 MPa, the flexural strengths from 25.0 to 27.4 MPa, and the compressive strengths from 78.5 to 78.6 MPa.

TASK 400: FRACTURE MECHANICS (FORMERLY STATISTICAL STRENGTH STUDIES)

No work funded under this subtask in FY-77.

TASK 500: FATIGUE BEHAVIOR OF GRAPHITE

Ambient temperature uniaxial fatigue tests are being conducted on PGX graphite. The test procedures and methods of data analysis were described in an earlier quarterly progress report (Ref. 11-2).

Three series of tests were completed during the current reporting period. Forty fatigue tests were completed on radial specimens with a 1:1 tension-compression loading cycle (R = -1). The second series consisted of 34 baseline tensile tests on axial specimens mounted in the fatigue machine. The third series consisted of 48 fatigue tests on axial specimens

with a tension-zero-tension loading cycle (R = 0). The results of the tests are given in Tables 11-17 through 11-19.

S-N curves for the two sets of fatigue data, plotted in log-log coordinates, are shown in Figs. 11-2 and 11-3. The lower population tolerance limits calculated by statistical analysis are included in the figures. As expected, the endurance limits for radial specimens tested with a stress ratio; R, of -1 are lower than the equivalent endurance limits for R = 0 [reported in the previous quarterly (Ref. 11-1)]. For 50% survival to 100,000 cycles, the endurance limits for R = -1 and R = 0 were 74 and 85%, respectively, of the mean tensile strength. Endurance limits for the axial specimens tested with R = 0 were slightly lower than the corresponding limits in radial specimens. A final series of tests on radial specimens with R = -1 is in progress. These tests will complete the planned fatigue tests on PGX graphite.

TASK 600: RDT AND ASTM GRAPHITE STANDARDS

This section concerns the writing of RDT graphite standards for HTGR graphite component materials. These standards are funded as a subtask under Task 11 work. ASTM standard work on nuclear graphite will be monitored and progress will be reported. The ASTM work is by industry concensus and as such is not a part of the Task 11 scope.

RDT STANDARDS

Fuel Element and Replaceable Reflector Graphites

The final draft (No. 5) of E6-1 is under review by ERDA.

Permanent Side Reflector Graphites

The first draft is being written.

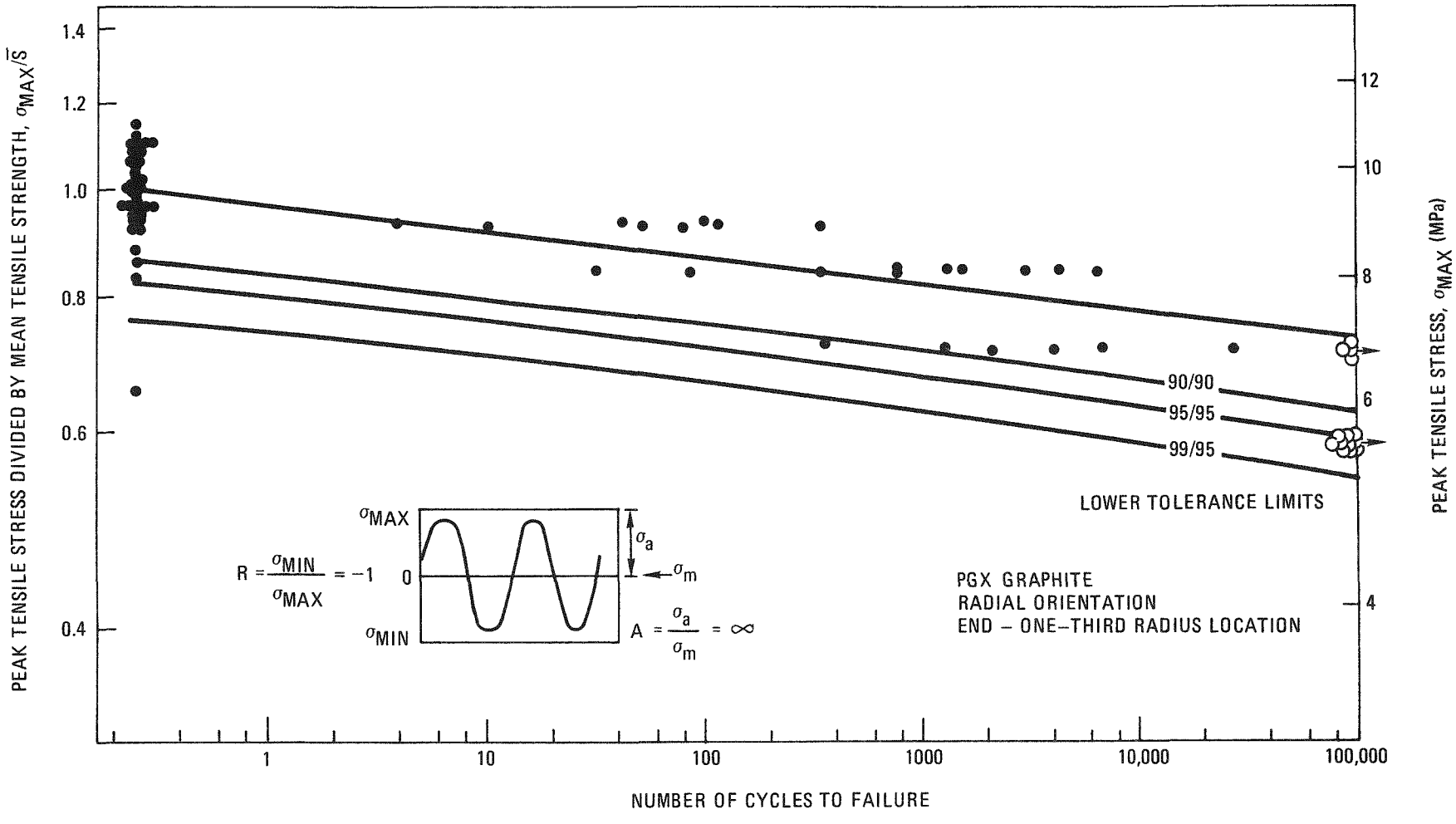

Fig. 11-2. Fatigue test data for PGX graphite, radial orientation, end - one-third radius location, in air at ambient temperature. Log-log plot of normalized maximum stress versus number of cycles to failure with stress ratio R = -1. Lower x/y tolerance limits represent the limits above which at least x% of the points fall, with y% confidence. Open circles represent runouts.

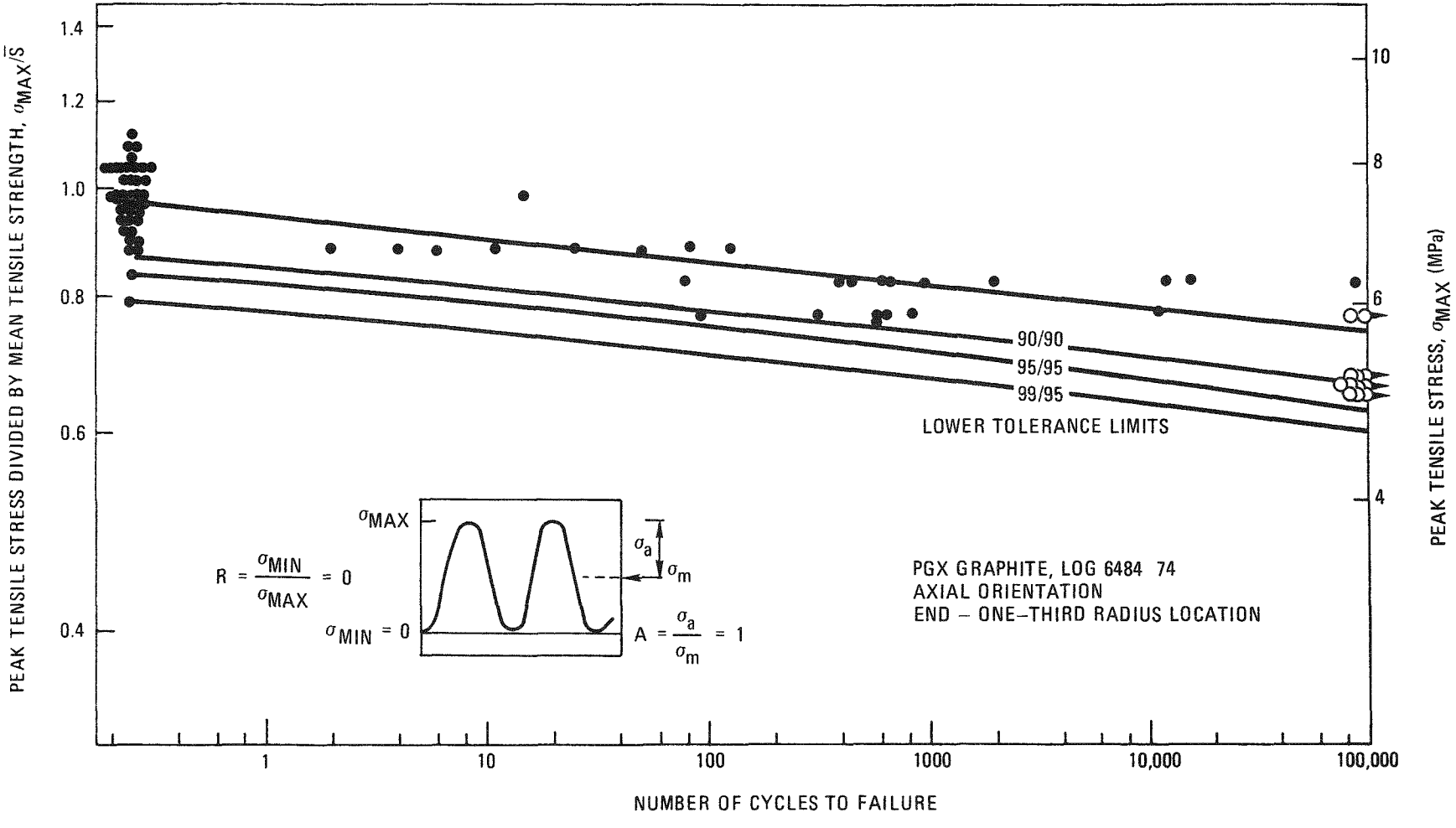

Fig. 11-3. Fatigue test data for PGX graphite, axial orientation, end - one-third radius location, in air at ambient temperature. Log-log plot of normalized maximum stress versus number of cycles to failure with stress ratio R = 0. Lower s/y tolerance limits represent the limits above which at least x% of the points fall, with y% confidence. Open circles represent runouts.

Core Support Floor Block Graphites

The first draft is being written.

Core Support Post and Seat Graphites

The first draft is being written.

TASK 700: IRRADIATION-INDUCED CREEP IN GRAPHITE

This work is funded at ORNL.

TASK 800: STRUCTURAL INTEGRITY OF GRAPHITE BLOCKS

Residual Stress Analysis

Residual stress calculations were performed for FTE-3, -5, and -6. In addition, stresses were recalculated for the eight-hole teledial element FTE-4 and the six-hole teledial element FTE-14. Previous results for FTE-4 and FTE-14 were reported in Ref. 11-1. The recalculations were made to correct errors in the physical property data that had been used in the earlier calculations. The results of the calculations were compared with preliminary experimental results obtained during the examination of the test element bodies in the hot cell.

Analyses of FTE-3, -4, -5, -6, and -14

Residual stresses were calculated for FTE-3, -5, and -6 in the same manner as discussed previously in Ref. 11-1. During the analysis, an error was found in the treatment of thermal expansivity for H-327 graphite by the GTEPC program (Ref. 11-3). It was also discovered that the test element bodies had been machined from the outside portion of the H-327 graphite log. As a result, the elastic modulus is believed to be better represented by the midlength edge values (12.41 GPa in the axial direction and 4.826 GPa in the radial direction) than by the average of midlength edge and

midlength center used previously. Both of these corrections were made in calculating stresses in FTE-3, -5, and -6 and were also incorporated in recalculations for FTE-4 and -14.

A brief summary of the end-of-life (EOL) fluence, maximum and minimum temperatures, and stresses is given in Table 11-20. The maximum and minimum temperatures and stresses occurred at the same locations for each test element. These are illustrated in Fig. 11-4 and listed in Table 11-20. Because of the notch, the stress computed at location 359 by the linear elastic and infinitesimal displacement model is not likely to be reliable. This is expected to have a negligible effect on stresses in the remainder of the test element.

Comparison of Analytical and Experimental Results

In order to verify the residual stress calculations, long specimens were cut into strips and disks were slit along a radius. Measurements of the changes in dimensions following cutting were compared with predictions based on the calculated stresses at EOL.

The axial stress distributions were used in conjunction with beam theory to estimate the bow of strips (Fig. 11-5). In computing the deformation of disks after a slit cut, the GTEPC finite element program was used. A half-disk model was constructed, and the hoop stresses adjacent to the surface of the slit were converted to nodal forces and applied in the reverse direction to the model to compute the relative displacement after cutting. As an example, the change of maximum principal stresses after the cutting of a FTE-3 disk is presented in Fig. 11-6.

Analytical and experimental results are presented in Table 11-21. The in-plane stress calculations appear in better agreement with the preliminary experimental measurements than the axial stress calculations. The reasons for the differences between the analytical and experimental results are currently under investigation. Possible explanations include errors in

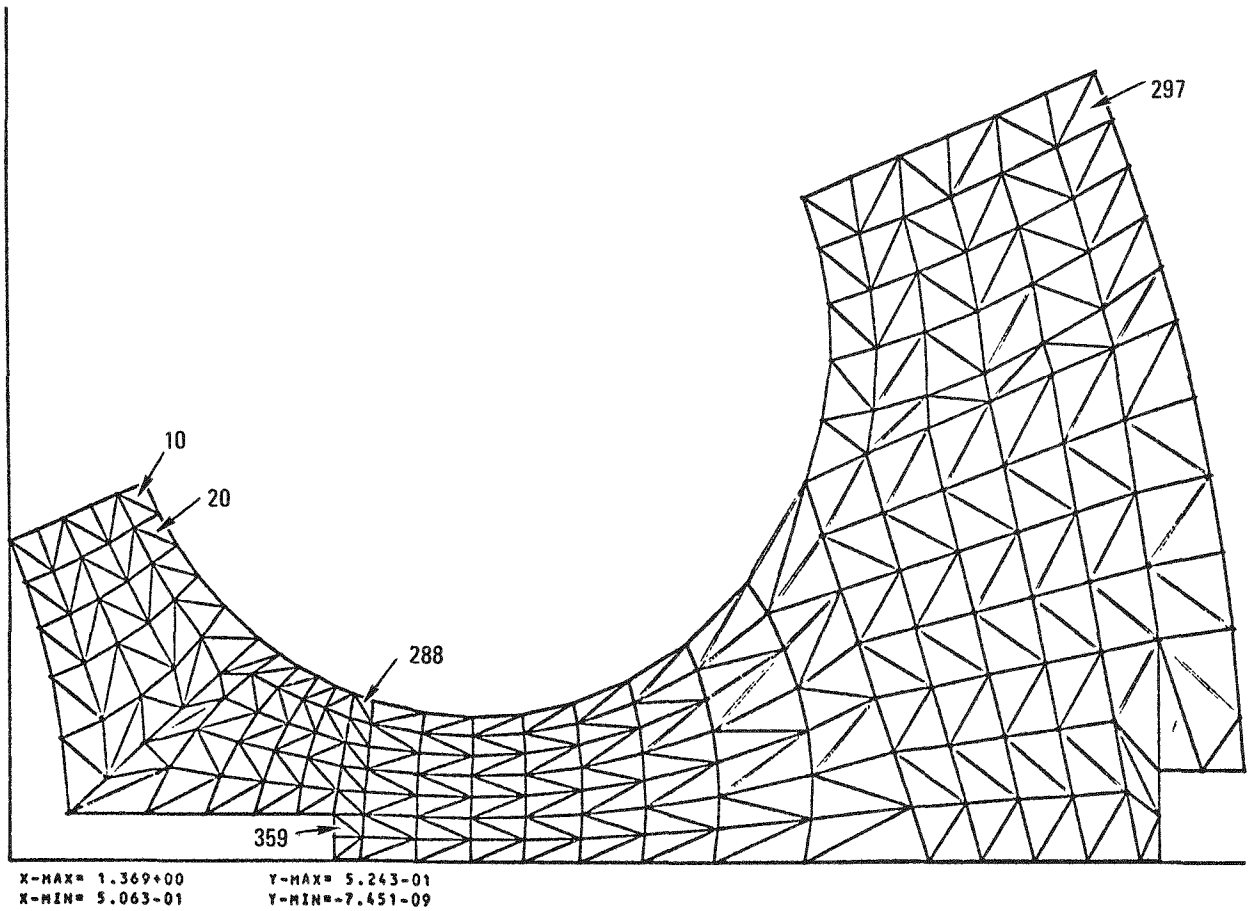

Fig. 11-4. Location of maximum and minimum temperatures and stresses

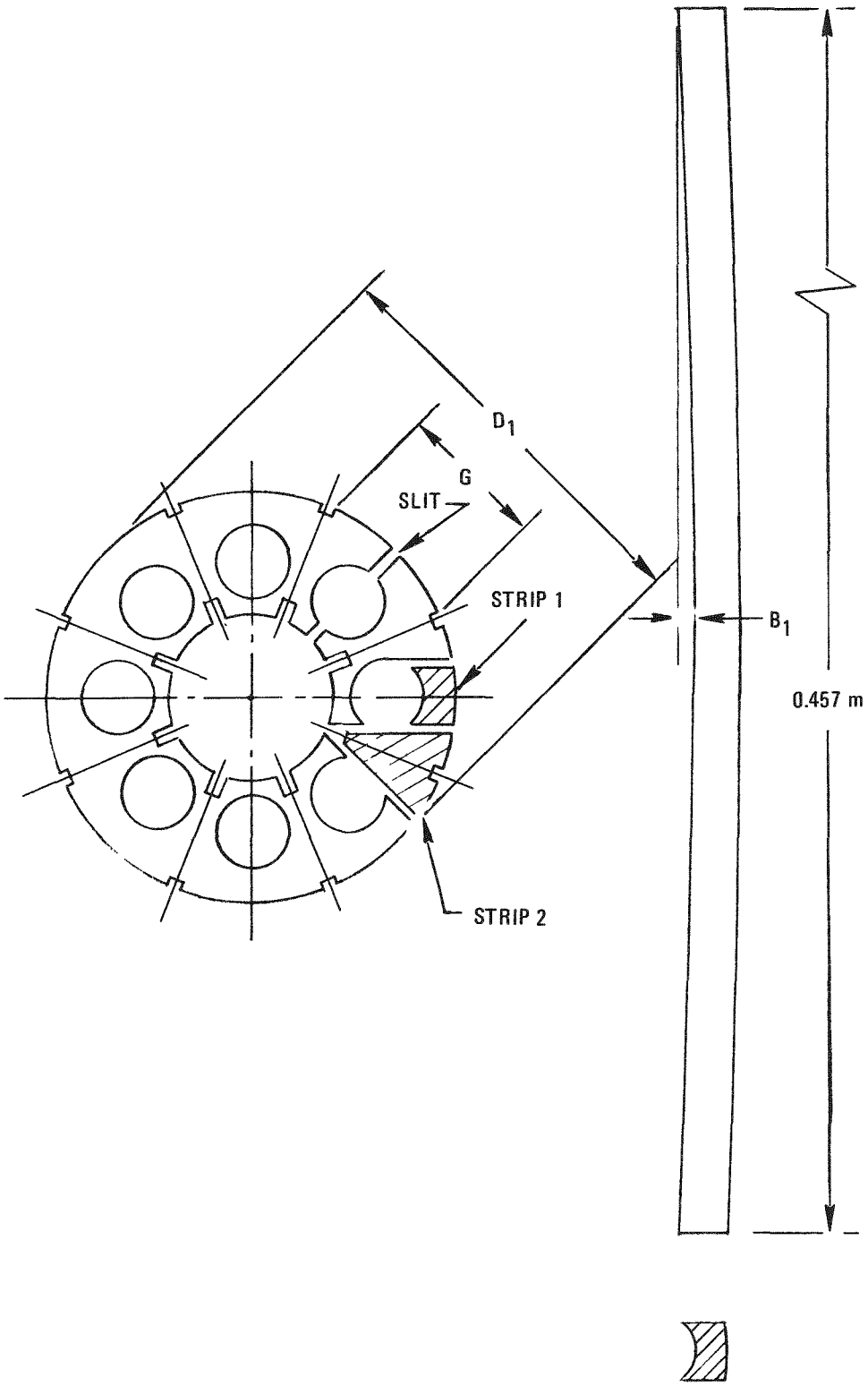

Fig. 11-5. Measurements of strips and slit rings

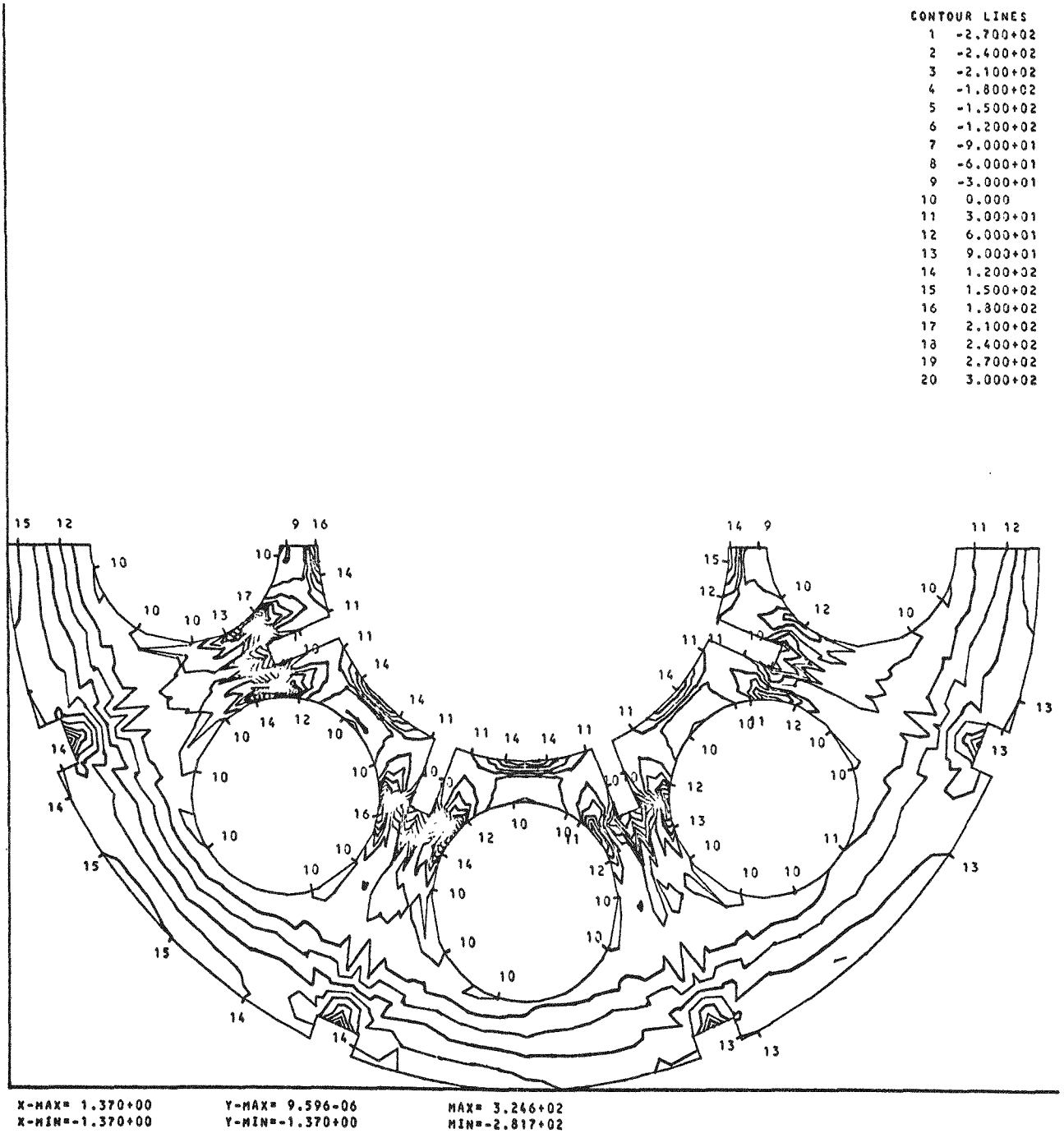

Fig. 11-6. Change of maximum principal stresses after the cutting of FTE-3 disk at axial position 5

the material data (thermal expansion properties in particular), or the analytical method, and perturbations in the measured bow due to the strip-cutting technique.

TASK 900: CONTROL MATERIALS DEVELOPMENT

No work funded under this subtask in FY-77.

TASK 1000: GRAPHITE OXIDATION STUDIES

The HTGR Fuels and Core Development Program work on graphite oxidation, previously reported under Task 4, 189a No. SU001, will be reported under this task of 189a No. 00552 in FY-77.

Scope of Work

Graphite oxidation studies comprise two major efforts: (1) characterization studies, in which rates of reaction and the effect of oxidation on mechanical properties of candidate graphites are determined and (2) tests where specific model assumptions or theoretical predictions are tested or validated. The objective of the characterization work is to supply statistically relevant rate and strength data as input to computer codes for calculation of the effect of steam ingress in the reactor. The objectives of the validation tests are to verify code assumptions, models, and theoretical predictions and to reduce uncertainties in the results of the code calculations.

Characterization Studies

The characterization work will eventually include all candidate graphites. During FY-77 only GLCC grade H-451, a replaceable fuel and reflector element candidate, and SC 2020, a core support post candidate, will be studied.

Oxidation Rate Measurements

The reaction rate measurements include parametric studies of graphite oxidation for determining rate constants in the Langmuir-Hinshelwood equation, which is the basic equation used in the OXIDE-3 computer code (Ref. 11-4). The parameters being studied are: water and H_2 concentration, temperature, degree of burnup, and sample configuration. The initial portion of the first phase of this work, concerning grade H-451 graphite, has been reported previously (Ref. 11-1). In Ref. 11-1 it was shown that the Langmuir-Hinshelwood equation is not valid over the wide range of water concentration which could occur in the reactor [5 Pa to 0.1 MPa H_2O (50 μatm to 1 atm)]. It was discovered that a distinct change in the rate constants occurred at about 300 Pa H_2O. The most reliable and accurate data were obtained at water vapor pressures above 300 Pa, and so rate constants in the high concentration range were reported. At present, rate constant determinations are being measured in the low-pressure range (<300 Pa H_2O). This work is scheduled for completion in June 1977. Two sets of reaction rate constants for water vapor concentrations may be recommended, one in the range 10 to 300 Pa and another in the range 300 to 3000 Pa. Stackpole's grade 2020 graphite will be studied next.

Effect of Oxidation on Mechanical Properties

The goal of this effort is to determine the mechanical properties, ultimate tensile strength, modulus, and strain at fracture, and in some cases ultimate compressive strength, as a function of uniform burnoff. Large numbers of cylindrical graphite tensile specimens are being oxidized under conditions which achieve a uniform oxidation profile. After predetermined burnoffs (percent weight loss), the samples are tested to fracture. The mechanical property data thus obtained are compared with nonoxidized control specimens to determine the changes caused by oxidation. The first phase of this work on H-451 graphite was reported in Ref. 11-5. Reference 11-5 also presents data for burnoffs of up to 20% at 1173 K and up to 2% at 1073 K and details on sampling and test procedures. The

samples oxidized at 1073 K will ultimately be taken to higher burnoffs. Stackpole's grade 2020 will be studied next.

Validation Tests

A test is being planned to determine the mechanical properties of graphite with a nonuniform oxidation profile. Oxidized slabs of replaceable fuel and reflector element (grade H-451) and core support post (grade 2020) graphites will be cut into bar specimens and tested in four-point bending. Their strength will be compared with predictions based on their oxidation profile. A test plan for this experiment is being written. Design and construction of the test apparatus will be initiated upon completion of the test plan.

REFERENCES

11-1. "HTGR Fuels and Core Development Program Quarterly Progress Report for the Period Ending August 31, 1976," ERDA Report GA-A14046, General Atomic Company, September 24, 1976.

11-2. "HTGR Fuels and Core Development Program Quarterly Progress Report for the Period Ending May 31, 1976," ERDA Report GA-A13941, General Atomic Company, June 30, 1976.

11-3. Tzung, F. K., "GTEPC-2D, A Computer Program for Two-Dimensional Graphite Thermal-Elastic-Plastic-Creep Analysis, User's Manual," General Atomic Report GA-A13532, January 31, 1976.

11-4. Peroomian, M. B., A. W. Barsell, and J. C. Sayer, "OXIDE-3: A Computer Code for Analysis of HTGR Steam or Air Ingress Accidents," General Atomic Report GA-A12493, January 15, 1974.

11-5. "HTGR Fuels and Core Development Program Quarterly Progress Report for the Period Ending February 29, 1976," ERDA Report GA-A13804, General Atomic Company, March 31, 1976.

TABLE 11-1
SUMMARY OF IRRADIATION-INDUCED CHANGES IN THERMAL EXPANSIVITY OF H-451 GRAPHITE IRRADIATED IN CAPSULES OG-1, OG-2, AND OG-3

Lot	Log No.	Orientation	Location in Log	Mean Irradiation Temperature (K)	Fluence x 10^{-25} (n/m^2) $(E>29\ fJ)_{HTGR}$	Average Percent Change in CTE (295-773 K)
266	5651-28	Axial	Midlength center	915	2.0	+1
				935	3.7	+3
				935	5.5	-3
				1045	1.9	+6
				1195	2.3	-4
				1205	4.5	-15
				1170	6.4	-24
				1270	8.5	-38
				1335	3.0	-7
				1665	3.2	-4
				1660	6.1	-34
				1660	9.0	-47
			Midlength edge	1045	1.9	+4
				1125	1.9	+2
				1110	3.6	+2
				1255	2.8	-11
				1260	5.3	-20
				1480	6.3	-30
				1515	9.2	-43

TABLE 11-1 (continued)

Lot	Log No.	Orientation	Location in Log	Mean Irradiation Temperature (K)	Fluence x 10^{-25} (n/m^2) $(E>29\ fJ)_{HTGR}$	Average Percent Change in CTE (295-773 K)
266	5651-28	Radial	Midlength center	915	2.0	+3
				935	3.7	+7
				935	5.5	0
				1045	1.9	+9
				1195	2.3	-9
				1205	4.5	-9
				1170	6.4	-23
				1270	8.5	-43
				1335	3.0	-7
				1665	3.2	-9
				1660	6.1	-34
				1660	9.0	-46
			Midlength edge	1045	1.9	+2
				1125	1.9	+2
				1110	3.6	+2
				1255	2.8	-11
				1260	5.3	-18
				1480	6.3	-27
				1515	9.3	-41
426	6484-34	Axial	Midlength center	970	1.8	+10
				1040	2.4	+11
				1655	2.9	+15
		Radial	Midlength center	970	1.8	+10
				1010	2.4	+9
				1655	2.9	+13

TABLE 11-2
SUMMARY OF IRRADIATION-INDUCED CHANGES IN THERMAL EXPANSIVITY OF SO818 GRAPHITE IRRADIATED IN CAPSULE OG-3

Lot	Log No.	Orientation	Location in Log	Mean Irradiation Temperature (K)	Fluence x 10^{-25} (n/m^2) $(E>29\ fJ)_{HTGR}$	Average Percent Change in CTE (295-773 K)
4B	6484-22	Axial	Midlength	1040	2.4	+3
			center	1655	2.9	-12
		Radial	Midlength	1010	2.4	+7
			center	1655	2.9	-11

TABLE 11-3

THERMAL CONDUCTIVITY OF SO818 GRAPHITE

LOT NUMBER: 4B LOG NUMBER: 6484-22

ORIENTATION	LOCATION	SPECIMEN NUMBER	THERMAL CONDUCTIVITY (W/M-K) AT: 295K (22C)	473K (200C)	673K (400C)	873K (600C)	1073K (800C)
AXIAL	MLC	3AL51D	124.6	104.3	84.2	67.7	59.2
		3AL51E	122.7	100.4	81.3	66.8	58.7
		3AL55D	125.7	102.9	83.8	69.7	59.7
		3AL55E	125.6	109.3	90.7	73.6	66.9
		3BL02D	113.6	98.9	78.6	65.9	59.1
		3BL02E	108.6	98.4	78.1	65.5	58.7
		3BL06A	113.9	101.6	78.2	66.0	57.1
		3BL06B	115.6	111.0	88.5	74.6	65.1
		MEAN:	118.8	103.3	82.9	68.7	60.6
		STD. DEV:	6.6	4.6	4.8	3.6	3.5

TABLE 11-4
MEAN STRENGTH VALUES OF GRADE HLM GRAPHITE (LOT 367, LOG 6484-78)
(MPa)

Axial						Radial					
Slab 1			Slab 6			Slab 1			Slab 6		
EC	EM	EE	MLC	MLM	MLE	EC	EM	EE	MLC	MLM	MLE
Tensile											
7.8 ±2.1	9.4 ±1.0	13.8 ±1.2	6.8 ±1.0	9.3 ±2.2	13.3 ±1.8	11.9 ±1.8	12.0 ±0.7	11.9 ±1.1	9.9 ±1.3	10.6 ±1.7	12.4 ±0.8
Flexural											
16.3 ±1.9	16.9 ±1.9	20.8 ±1.5	13.8 ±2.6	18.0 ±1.7	20.8 ±1.4	17.9 ±1.7	17.7 ±1.6	16.6 ±1.4	17.5 ±2.1	17.4 ±1.7	17.9 ±1.3
Compressive											
38.1 ±0.9	35.0 ±1.5	39.8 ±1.5	35.3 ±2.2	35.4 ±3.2	41.1 ±1.8	43.0 ±1.1	41.0 ±1.8	41.6 ±2.4	40.5 ±1.6	42.6 ±1.5	44.7 ±1.0

TABLE 11-5

TENSILE PROPERTIES OF HLM GRAPHITE

LOT NO. 367 SPEC. DIA. 12.8 MM
LOG NO. 6484-78 SPEC. LENGTH 71. MM
LOG DENSITY = MG/M**3

SPECIMEN NUMBER	ORIENTATION	LOCATION	DENSITY (MG/M**3)	YOUNGS MODULUS (GPA)	PERMANENT SET (PCT)	FRACTURE STRAIN (PCT)	TENSILE STRENGTH (MPA)
1AC-E-10A	AX	EC	1.784	7.0	.020	.161	9.1
-12A	AX	EC	1.788	6.7	.018	.175	9.6
-22A	AX	EC	1.795				8.9
-24A	AX	EC	1.768	7.0	.016	.156	9.1
06A	AX	EC					7.2
08A	AX	EC					9.6
10B	AX	EC					9.8
12B	AX	EC					9.2
18A	AX	EC					6.5
20B	AX	EC					5.1
22B	AX	EC					8.6
24B	AX	EC					6.1
1BC-E-106B	AX	EC	1.780				5.0
108B	AX	EC	1.784				3.4
94B	AX	EC	1.787				4.3
96B	AX	EC	1.785				7.9
102A	AX	EC					10.2
104B	AX	EC					3.6
106A	AX	EC					9.3
1BCE-108A	AX	EC					8.6
90A	AX	EC					7.7
92B	AX	EC					9.7
94A	AX	EC					9.1
96A	AX	EC					8.5
	MEAN		1.784	6.9 (1.00 MPSI)	.018	.164	7.8 (1124. PSI)
	STD. DEV.		.008	.1 (.02 MPSI)	.002	.010	2.1 (304. PSI)

TABLE 11-5 (Continued)

TENSILE PROPERTIES OF HLM GRAPHITE

LOT NO. 367 SPEC. DIA. 12.8 MM
LOG NO. 6484-78 SPEC. LENGTH 71. MM
LOG DENSITY -- MG/M**3

SPECIMEN NUMBER	ORIENTATION	LOCATION	DENSITY (MG/M**3)	YOUNGS MODULUS (GPA)	PERMANENT SET (PCT)	FRACTURE STRAIN (PCT)	TENSILE STRENGTH (MPA)
1ACE- 31	RAD	EC	1.772	6.7	.023	.268	12.5
27	RAD	EC	1.773	6.5	.021	.251	12.2
11	RAD	EC	1.777	6.3	.021	.291	13.3
07	RAD	EC	1.770	6.4	.023	.299	13.8
05	RAD	EC					13.2
09	RAD	EC					14.3
23	RAD	EC					13.7
25	RAD	EC					12.7
29	RAD	EC					12.5
1BCE-113	RAD	EC	1.788	6.5	.015	.190	9.9
117	RAD	EC	1.785				12.3
133	RAD	EC	1.784	7.1	.030	.214	10.4
137	RAD	EC	1.786	6.5	.014	.160	8.7
1BCE-111	RAD	EC					12.3
115	RAD	EC					7.5
119	RAD	EC					10.5
131	RAD	EC					12.8
135	RAD	EC					11.7
139	RAD	EC					11.6
MEAN			1.780	6.6 (.95 MPSI)	.021	.239	11.9 (1724.PSI)
STD. DEV.			.007	.3 (.04 MPSI)	.005	.053	1.8 (254.PSI)

TABLE 11-5 (Continued)

TENSILE PROPERTIES OF HLM GRAPHITE

LOT NO. 367 SPEC. DIA. 12.8 MM
LOG NO. 6484-78 SPEC. LENGTH 71. MM
LOG DENSITY -- MG/M**3

SPECIMEN NUMBER	ORIENTATION	LOCATION	DENSITY (MG/M**3)	YOUNGS MODULUS (GPA)	PERMANENT SET (PCT)	FRACTURE STRAIN (PCT)	TENSILE STRENGTH (MPA)
1AYE- 30B	AX	EM	1.769				9.6
34A	AX	EM	1.778	6.7	.017	.162	9.0
46B	AX	EM	1.771	7.3	.015	.128	8.2
54A	AX	EM	1.785	6.5	.020	.161	8.5
30A	AX	EM					8.9
34B	AX	EM					9.6
42A	AX	EM					9.6
42B	AX	EM					8.8
46A	AX	EM					8.6
54B	AX	EM					8.2
1BYE-114B	AX	EM	1.782	6.8	.020	.200	10.3
118A	AX	EM	1.779	7.4	.019	.176	9.6
130B	AX	EM	1.761	6.9	.021	.201	10.3
1BYE-138A	AX	EM	1.767	7.1	.015	.190	10.6
114A	AX	EM					9.1
118B	AX	EM					9.1
126A	AX	EM					8.2
126B	AX	EM					9.4
130A	AX	EM					11.4
138B	AX	EM					11.4
MEAN			1.774	7.0 (1.01 MPSI)	.018	.174	9.4 (1367.PSI)
STD. DEV.			.008	.3 (.05 MPSI)	.002	.026	1.0 (140.PSI)

TABLE 11-5 (Continued)

TENSILE PROPERTIES OF HLM GRAPHITE

LOT NO. 367 SPEC. DIA. 12.8 MM
LOG NO. 6484-78 SPEC. LENGTH 71. MM
LOG DENSITY -- MG/M**3

SPECIMEN NUMBER	ORIENTATION	LOCATION	DENSITY (MG/M**3)	YOUNGS MODULUS (GPA)	PERMANENT SET (PCT)	FRACTURE STRAIN (PCT)	TENSILE STRENGTH (MPA)
1AYE- 45	RAD	EM	1.772	6.7	.020	.278	12.1
49	RAD	EM	1.772	6.3	.030	.304	12.7
53	RAD	EM	1.775	6.3	.026	.251	11.8
67	RAD	EM	1.773	6.3	.024	.276	12.6
43	RAD	EM					10.7
47	RAD	EM					10.5
51	RAD	EM					12.7
61	RAD	EM					12.4
65	RAD	EM					12.7
69	RAD	EM					12.0
1BYE-153	RAD	EM	1.783	6.1	.026	.264	12.0
157	RAD	EM	1.787	6.2	.025	.249	11.7
1BYE-171	RAD	EM	1.766	6.0	.024	.270	12.6
175	RAD	EM	1.766	5.9	.029	.274	11.8
151	RAD	EM					12.9
155	RAD	EM					13.1
159	RAD	EM					12.7
169	RAD	EM					12.0
173	RAD	EM					11.0
177	RAD	EM					11.4
	MEAN		1.774	6.2 (.90 MPSI)	.025	.271	12.0 (1745.PSI)
	STD. DEV.		.007	.2 (.03 MPSI)	.003	.017	.7 (106.PSI)

TABLE 11-5 (Continued)

TENSILE PROPERTIES OF HLM GRAPHITE

LOT NO. 367 SPEC. DIA. 12.8 MM
LOG NO. 6484-78 SPEC. LENGTH 71. MM
LOG DENSITY -- MG/M**3

SPECIMEN NUMBER	ORIENTATION	LOCATION	DENSITY (MG/M**3)	YOUNGS MODULUS (GPA)	PERMANENT SET (PCT)	FRACTURE STRAIN (PCT)	TENSILE STRENGTH (MPA)
1AEE- 60B	AX	EE	1.769	7.6	.019	.253	14.2
64A	AX	EE	1.770	7.3	.015	.265	14.5
76B	AX	EE	1.757	7.4	.015	.220	12.8
84A	AX	EE	1.771	6.3	.021	.214	10.3
60A	AX	EE					14.6
64B	AX	EE					14.3
72A	AX	EE					13.7
72B	AX	EE					13.4
76A	AX	EE					12.4
84B	AX	EE					11.5
1BEE-144B	AX	EE	1.787				13.6
148A	AX	EE	1.778	7.7	.022	.282	15.0
160B	AX	EE	1.767	7.7	.019	.276	15.1
168A	AX	EE	1.772	7.9	.015	.241	13.9
144A	AX	EE					14.9
148B	AX	EE					14.8
156A	AX	EE					14.7
156B	AX	EE					14.7
160A	AX	EE					14.1
168B	AX	EE					14.1
MEAN			1.772	7.4 (1.08 MPSI)	.018	.251	13.8 (2006.PSI)
STD. DEV.			.009	.6 (.08 MPSI)	.003	.025	1.2 (178.PSI)

TABLE 11-5 (Continued)

TENSILE PROPERTIES OF HLM GRAPHITE

LOT NO. 367 SPEC. DIA. 12.8 MM
LOG NO. 6484-78 SPEC. LENGTH 71. MM
LOG DENSITY -- MG/M**3

SPECIMEN NUMBER	ORIENTATION	LOCATION	DENSITY (MG/M**3)	YOUNGS MODULUS (GPA)	PERMANENT SET (PCT)	FRACTURE STRAIN (PCT)	TENSILE STRENGTH (MPA)
1AEE- 85	RAD	EE	1.768	6.7	.031	.293	11.9
81	RAD	EE	1.770	5.5	.029	.319	12.5
99	RAD	EE	1.765	5.6	.039	.209	8.9
103	RAD	EF	1.768	5.8	.025	.224	10.0
79	RAD	EE					12.6
83	RAD	EE					11.4
87	RAD	EE					13.4
97	RAD	EF					12.0
101	RAD	EE					12.7
1AEE-105	RAD	EE					13.1
1BEE-189	RAD	EE	1.785	5.9	.034	.285	11.9
193	RAD	EE	1.783				11.8
207	RAD	EE	1.766	5.6	.039	.293	11.6
211	RAD	EE	1.765	5.6	.035	.294	11.7
187	RAD	EE					12.3
191	RAD	EE					10.6
195	RAD	EE					12.9
205	RAD	EF					11.7
209	RAD	EF					12.8
213	RAD	EE					12.2
	MEAN		1.771	5.8 (.85 MPSI)	.033	.274	11.9 (1724.PSI)
	STD. DEV.		.008	.4 (.06 MPSI)	.005	.041	1.1 (155.PSI)

TABLE 11-5 (Continued)

TENSILE PROPERTIES OF HLM GRAPHITE

LOT NO. 367 SPEC. DIA. 12.8 MM
LOG NO. 6484-78 SPEC. LENGTH 71. MM
LOG DENSITY -- MG/M**3

SPECIMEN NUMBER	ORIENTATION	LOCATION	DENSITY (MG/M**3)	YOUNGS MODULUS (GPA)	PERMANENT SET (PCT)	FRACTURE STRAIN (PCT)	TENSILE STRENGTH (MPA)
6ACM	10B AX	MLC	1.791	7.3	.019	.119	7.0
	12A AX	MLC	1.794				4.4
	22A AX	MLC	1.803	6.7	.025	.134	7.2
	24A AX	MLC	1.799	6.2	.022	.156	8.2
	10A AX	MLC					8.6
	08B AX	MLC					5.8
	06B AX	MLC					8.9
	12A AX	MLC					6.2
6ACM*	18A AX	MLC					6.7
	20A AX	MLC					6.0
	22B AX	MLC					6.6
	24B AX	MLC					7.5
6BCM*	94B AX	MLC	1.787				6.5
	96A AX	MLC	1.795	6.2	.021	.136	6.9
	98A AX	MLC	1.805	6.3	.025	.150	7.7
	106B AX	MLC	1.795				6.2
	92A AX	MLC					5.9
	94A AX	MLC					6.9
	96B AX	MLC					7.5
	98B AX	MLC					6.8
	104B AX	MLC					6.1
	106A AX	MLC					6.5
	MEAN		1.796	6.5 (.95 MPSI)	.022	.139	6.8 (989.PSI)
	STD. DEV.		.006	.5 (.07 MPSI)	.003	.015	1.0 (145.PSI)

TABLE 11-5 (Continued)

TENSILE PROPERTIES OF HLM GRAPHITE

LOT NO. 367 SPEC. DIA. 12.6 MM
LOG NO. 6484-78 SPEC. LENGTH 71. MM
LOG DENSITY -- MG/M**3

SPECIMEN NUMBER	ORIENTATION	LOCATION	DENSITY (MG/M**3)	YOUNGS MODULUS (GPA)	PERMANENT SET (PCT)	FRACTURE STRAIN (PCT)	TENSILE STRENGTH (MPA)
6ACM	07	RAD	MLC	1.800	6.6	.026	.171	8.9
	11	RAD	MLC	1.796	6.7	.024	.244	11.9
	25	RAD	MLC	1.798	7.1	.029	.190	9.7
	29	RAD	MLC	1.797	6.7	.025	.141	7.7
	05	RAD	MLC					11.7
6ACM	09	RAD	MLC					8.2
	13	RAD	MLC					10.8
	23	RAD	MLC					8.3
	27	RAD	MLC					10.3
	31	RAD	MLC					7.0
6BCM	115	RAD	MLC	1.790	6.3	.026	.205	10.0
	119	RAD	MLC	1.794	6.4	.027	.243	11.3
	133	RAD	MLC	1.797	6.4	.025	.180	9.1
	137	RAD	MLC	1.798	6.5	.025	.180	9.3
	113	RAD	MLC					10.9
	117	RAD	MLC					10.3
	121	RAD	MLC					11.0
	131	RAD	MLC					9.7
	135	RAD	MLC					11.0
	139	RAD	MLC					10.2
	MEAN			1.796	6.6	.026	.194	9.9
					(.96 MPSI)			(1431.PSI)
	STD. DEV.			.003	.2	.002	.035	1.3
					(.04 MPSI)			(195.PSI)

TABLE 11-5 (Continued)

TENSILE PROPERTIES OF HLM GRAPHITE

LOT NO. 367 SPEC. DIA. 12.8 MM
LOG NO. 6484-78 SPEC. LENGTH 71. MM
LOG DENSITY -- MG/M**3

SPECIMEN NUMBER	ORIENTATION	LOCATION	DENSITY (MG/M**3)	YOUNGS MODULUS (GPA)	PERMANENT SET (PCT)	FRACTURE STRAIN (PCT)	TENSILE STRENGTH (MPA)
6AYM	30B AX	MLM	1.791				
	34A AX	MLM	1.804	6.7	.021	.149	8.3
	46B AX	MLM	1.798				6.0
	52A AX	MLM	1.806				5.4
6AYM	30A AX	MLM					9.2
	34B AX	MLM					10.2
	42A AX	MLM					8.7
	42B AX	MLM					6.6
	46A AX	MLM					13.0
	52B AX	MLM					9.5
6BYM	112B AX	MLM	1.797	6.6	.023	.193	9.8
	116A AX	MLM	1.800	7.6	.027	.166	9.3
	128B AX	MLM	1.792				5.7
	134A AX	MLM	1.795	8.2	.020	.169	10.8
	112A AX	MLM					10.0
	116B AX	MLM					9.0
	124A AX	MLM					12.3
	124B AX	MLM					10.7
	128A AX	MLM					11.6
	134B AX	MLM					11.1
	MEAN		1.798	7.2 (1.05 MPSI)	.023	.169	9.3 (1352. PSI)
	STD. DEV.		.005	.8 (.11 MPSI)	.003	.018	2.2 (316. PSI)

TABLE 11-5 (Continued)

TENSILE PROPERTIES OF HLM GRAPHITE

LOT NO. 367 SPEC. DIA. 12.8 MM
LOG NO. 64R4-78 SPEC. LENGTH 71. MM
LOG DENSITY -- MG/M**3

SPECIMEN NUMBER	ORIENTATION	LOCATION	DENSITY (MG/M**3)	YOUNGS MODULUS (GPA)	PERMANENT SET (PCT)	FRACTURE STRAIN (PCT)	TENSILE STRENGTH (MPA)
6AYM	45	RAD	MLM	1.802	6.8	.029	.200	10.0
	49	RAD	MLM	1.795	6.7	.024	.189	9.9
	63	RAD	MLM	1.800	6.5	.026	.205	10.0
6AYM	67	RAD	MLM	1.800				4.5
	43	RAD	MLM					10.8
	47	RAD	MLM					10.5
	51	RAD	MLM					11.3
	61	RAD	MLM					10.3
	65	RAD	MLM					12.1
	69	RAD	MLM					13.2
6BYM	153	RAD	MLM	1.796	6.1	.025	.268	11.9
	157	RAD	MLM	1.788	5.9	.029	.270	11.7
	171	RAD	MLM	1.797	6.1	.028	.207	9.9
	175	RAD	MLM	1.786	5.6	.028	.272	11.0
	151	RAD	MLM					12.0
	155	RAD	MLM					11.8
	159	RAD	MLM					10.0
	169	RAD	MLM					11.1
	173	RAD	MLM					10.3
	177	RAD	MLM					10.6
		MEAN		1.795	6.2 (.91 MPSI)	.027	.230	10.6 (1542.PSI)
		STD. DEV.		.006	.4 (.06 MPSI)	.002	.038	1.7 (248.PSI)

TABLE 11-5 (Continued)

TENSILE PROPERTIES OF HLM GRAPHITE

LOT NO. 307 SPEC. DIA. 12.8 MM
LOG NO. 6484-78 SPEC. LENGTH 71. MM
LOG DENSITY -- MG/M**3

SPECIMEN NUMBER	ORIENTATION	LOCATION	DENSITY (MG/M**3)	YOUNGS MODULUS (GPA)	PERMANENT SET (PCT)	FRACTURE STRAIN (PCT)	TENSILE STRENGTH (MPA)
6AEM	60B	AX	MLE	1.793	7.7	.016	.233	13.5
	64A	AX	MLE	1.786	8.8	.015	.254	16.2
6AEM	76B	AX	MLE	1.794	7.5	.016	.184	10.8
	84A	AX	MLE	1.802	7.6	.020	.188	10.7
	60A	AX	MLE					14.3
	64B	AX	MLE					14.9
	72A	AX	MLE					12.7
	72B	AX	MLE					14.4
	76A	AX	MLE					8.2
	84B	AX	MLE					12.5
6AEM	142B	AX	MLE	1.794	7.0	.021	.263	13.7
	146A	AX	MLE	1.792	7.6	.020	.244	13.4
	158B	AX	MLE	1.794	7.8	.020	.247	14.1
	164A	AX	MLE	1.794	7.8	.020	.242	14.0
	142A	AX	MLE					14.6
	146B	AX	MLE					14.1
	154A	AX	MLE					14.7
	154B	AX	MLE					12.8
	158A	AX	MLE					13.3
	164B	AX	MLE					12.2
	MEAN			1.794	7.7 (1.12 MPSI)	.018	.232	13.3 (1922.PSI)
	STD. DEV.			.004	.5 (.07 MPSI)	.002	.030	1.8 (257.PSI)

TABLE 11-5 (Continued)

TENSILE PROPERTIES OF HLM GRAPHITE

LOT NO. 367 SPEC. DIA. ****** MM
LOG NO. 6484-78 SPEC. LENGTH 71. MM
LOG DENSITY -- MG/M**3

SPECIMEN NUMBER	ORIENTATION	LOCATION	DENSITY (MG/M**3)	YOUNGS MODULUS (GPA)	PERMANENT SET (PCT)	FRACTURE STRAIN (PCT)	TENSILE STRENGTH (MPA)
6AEM	81	RAD	MLE	1.798	6.4	.013	.279	12.6
	85	RAD	MLE	1.801	6.2	.027	.289	12.6
	99	RAD	MLE	1.800	6.6	.023	.230	11.4
	103	RAD	MLE	1.798	6.2	.022	.214	10.7
	79	RAD	MLE					12.0
	83	RAD	MLE					12.6
	87	RAD	MLE					12.5
	97	RAD	MLE					12.3
	101	RAD	MLE					12.7
	105	RAD	MLE					13.7
6BEM	189	RAD	MLE	1.795	6.1	.029	.270	11.9
	193	RAD	MLE	1.792	5.7	.026	.292	12.0
	207	RAD	MLE	1.785	5.8	.030	.289	11.9
	211	RAD	MLE	1.787	5.9	.029	.300	12.5
	187	RAD	MLE					13.0
	191	RAD	MLE					12.3
	195	RAD	MLE					12.7
	205	RAD	MLE					14.5
	209	RAD	MLE					13.0
6BEM	213	RAD	MLE					11.8
		MEAN		1.794	6.1 (.89 MPSI)	.025	.270	12.4 (1804.PSI)
		STD. DEV.		.006	.3 (.04 MPSI)	.006	.031	.8 (116.PSI)

TABLE 11-6

FLEXURAL PROPERTIES OF HLM GRAPHITE

LOT NO. 367 SPEC. DIA. 6.4 MM
LOG NO. 6484-78 SPEC. LENGTH 51. MM
LOG DENSITY -- MG/M**3

SPECIMEN NUMBER	ORIENTATION	LOCATION	DENSITY (MG/M**3)	MODULUS OF RUPTURE (MPA) (UNCORRECTED)	FLEXURAL STRENGTH (MPA) (CORRECTED)
1A	56A AX	EE		27.2	22.4
	56B AX	EE		24.8	20.9
	58A AX	EE		26.3	21.8
	58B AX	EE		27.9	22.8
	62A AX	EE		24.5	20.7
	62B AX	EE		24.6	20.6
	68A AX	EE		19.1	16.9
	68B AX	EE		21.7	18.6
	70A AX	EE		23.6	20.1
	70B AX	EE		24.1	20.4
1B	128A AX	EE		22.7	19.5
	128B AX	EE		27.9	22.8
	130A AX	EE		26.0	21.6
	130B AX	EE		24.8	20.9
	134A AX	EE		24.8	20.9
	134B AX	EE		21.9	18.9
	140A AX	EE		27.8	22.8
	140B AX	EE		23.9	20.3
	142A AX	EE		25.5	21.3
1B	142B AX	EE		25.4	21.3
	MEAN			24.7 MPA (3584. PSI)	20.8 MPA (3015. PSI)
	STD. DEV.			2.3 MPA (327. PSI)	1.5 MPA (217. PSI)

TABLE 11-6 (Continued)

FLEXURAL PROPERTIES OF HLM GRAPHITE

LOT NO. 367 SPEC. DIA. 6.4 MM
LOG NO. 6484-78 SPEC. LENGTH 51. MM
LOG DENSITY -- MG/M**3

SPECIMEN NUMBER	ORIENTATION	LOCATION	DENSITY (MG/M**3)	MODULUS OF RUPTURE (MPA) (UNCORRECTED)	FLEXURAL STRENGTH (MPA) (CORRECTED)
1A	36A AX	EM		20.7	17.9
	36B AX	EM		21.1	18.1
	38A AX	EM		21.7	18.5
	38B AX	EM		21.7	18.5
	42A AX	EM		20.9	18.0
	42B AX	EM		15.6	14.1
	48A AX	EM		15.3	13.8
	48B AX	EM		17.7	15.7
	50A AX	EM		19.2	16.8
1A	50B AX	EM		17.3	15.4
1B	108A AX	EM		20.9	18.0
	108B AX	EM		19.0	16.7
	110A AX	EM		19.0	16.7
	110B AX	EM		22.1	18.8
	114A AX	EM		16.3	14.6
	114B AX	EM		16.0	14.4
	120A AX	EM		17.6	15.6
	120B AX	EM		20.0	17.4
	122A AX	EM		23.3	19.6
	122B AX	EM		22.1	18.8
	MEAN			19.4 MPA (2811. PSI)	16.9 MPA (2447. PSI)
	STD. DEV.			2.4 MPA (353. PSI)	1.8 MPA (258. PSI)

TABLE 11-6 (Continued)

FLEXURAL PROPERTIES OF HLM GRAPHITE

LOT NO. 367 SPEC. DIA. 6.4 MM
LOG NO. 6484-78 SPEC. LENGTH 51. MM
LOG DENSITY -- MG/M**3

SPECIMEN NUMBER	ORIENTATION	LOCATION	DENSITY (MG/M**3)	MODULUS OF RUPTURE (MPA) (UNCORRECTED)	FLEXURAL STRENGTH (MPA) (CORRECTED)
1A	12A AX	EC		21.8	18.6
	12B AX	EC		19.5	17.0
	10A AX	EC		19.7	17.1
	10B AX	EC		20.0	17.4
	16A AX	EC		16.1	14.4
	16B AX	EC		16.4	14.7
	24A AX	EC		20.4	17.6
	24B AX	EC		18.2	16.0
	26A AX	EC		15.9	14.3
	26B AX	EC		20.9	18.3
	32A AX	EC		19.5	17.0
	32B AX	EC		19.6	17.1
1B	88A AX	EC		19.5	17.0
	88B AX	EC		21.8	18.6
	86A AX	EC		14.2	12.9
	86B AX	EC		15.6	14.0
	80A AX	EC		19.2	16.7
	80B AX	EC		20.1	17.4
	96A AX	EC		21.7	18.5
	96B AX	EC		20.3	17.6
	102A AX	EC		19.3	16.8
	102B AX	EC		11.9	11.0
	104A AX	EC		18.1	16.0
1B	104B AX	EC		16.3	14.6
	MEAN			18.6 MPA (2695. PSI)	16.3 MPA (2358. PSI)
	STD. DEV.			2.5 MPA (368. PSI)	1.9 MPA (279. PSI)

TABLE 11-6 (Continued)

FLEXURAL PROPERTIES OF HLM GRAPHITE

LOT NO. 367 SPEC. DIA. 6.4 MM
LOG NO. 6484-7B SPEC. LENGTH 51. MM
LOG DENSITY -- MG/M**3

SPECIMEN NUMBER	ORIENTATION	LOCATION	DENSITY (MG/M**3)	MODULUS OF RUPTURE (MPA) (UNCORRECTED)	FLEXURAL STRENGTH (MPA) (CORRECTED)
6A	200A AX	MLE		23.4	20.1
	200B AX	MLE		27.9	23.1
	202A AX	MLE		27.5	22.8
	202B AX	MLE		25.0	21.2
	206A AX	MLE		25.3	21.4
	206B AX	MLE		25.1	21.3
	212A AX	MLE		24.5	20.9
	212B AX	MLE		24.1	20.6
	214A AX	MLE		25.9	21.8
	214B AX	MLE		21.8	19.0
6B	270A AX	MLE		22.8	19.7
	270B AX	MLE		23.1	19.9
	272A AX	MLE		28.3	23.3
	272B AX	MLE		24.2	20.7
	276A AX	MLE		21.6	18.9
	276B AX	MLE		24.2	20.7
	280A AX	MLE		24.9	21.2
	280B AX	MLE		27.4	22.7
	278A AX	MLE		22.7	19.6
	278B AX	MLE		20.4	18.0
	MEAN			24.5 MPA (3554. PSI)	20.8 MPA (3022. PSI)
	STD. DEV.			2.2 MPA (313. PSI)	1.4 MPA (210. PSI)

TABLE 11-6 (Continued)

FLEXURAL PROPERTIES OF HLM GRAPHITE

LOT NO. 367 SPEC. DIA. 6.4 MM
LOG NO. 6484-78 SPEC. LENGTH 51. MM
LOG DENSITY -- MG/M**3

SPECIMEN NUMBER		ORIENTATION	LOCATION	DENSITY (MG/M**3)	MODULUS OF RUPTURE (MPA) (UNCORRECTED)	FLEXURAL STRENGTH (MPA) (CORRECTED)
6A	180A	AX	MLM		19.2	16.9
	180B	AX	MLM		23.6	20.0
	182A	AX	MLM		17.6	15.7
	182B	AX	MLM		19.7	17.3
	196A	AX	MLM		21.2	18.4
	196B	AX	MLM		21.0	18.2
	186A	AX	MLM		20.2	17.6
	186B	AX	MLM		18.6	16.4
	192A	AX	MLM		21.4	18.5
	192B	AX	MLM		20.7	18.0
	194A	AX	MLM		16.6	14.9
	194B	AX	MLM		18.3	16.2
6B	250A	AX	MLM		17.5	15.6
	250B	AX	MLM		19.0	16.7
	252A	AX	MLM		20.7	18.0
	252B	AX	MLM		21.2	18.3
	256A	AX	MLM		20.1	17.6
	256B	AX	MLM		24.6	20.6
	262A	AX	MLM		24.7	20.7
	262B	AX	MLM		24.3	20.4
	264A	AX	MLM		25.2	21.0
	264B	AX	MLM		21.2	18.3
	MEAN				20.8 MPA (3012. PSI)	18.0 MPA (2608. PSI)
	STD. DEV.				2.5 MPA (358. PSI)	1.7 MPA (252. PSI)

TABLE 11-6 (Continued)

FLEXURAL PROPERTIES OF HLM GRAPHITE

LOT NO. 367 SPEC. DIA. 6.4 MM
LOG NO. 6484-78 SPEC. LENGTH 51. MM
LOG DENSITY -- MG/M**3

SPECIMEN NUMBER	ORIENTATION	LOCATION	DENSITY (MG/M**3)	MODULUS OF RUPTURE (MPA) (UNCORRECTED)	FLEXURAL STRENGTH (MPA) (CORRECTED)
6A	154A	AX	MLC	18.0	15.8
	154B	AX	MLC	17.8	15.6
	156A	AX	MLC	11.9	11.0
	156B	AX	MLC	14.5	13.0
	160A	AX	MLC	20.1	17.3
	160B	AX	MLC	18.5	16.1
	174A	AX	MLC	12.4	11.4
	174B	AX	MLC	18.9	16.4
	176A	AX	MLC	15.7	14.0
	176B	AX	MLC	8.0	7.6
	168A	AX	MLC	17.1	15.1
	168B	AX	MLC	17.0	15.0
6B	224A	AX	MLC	15.6	14.0
	224B	AX	MLC	15.7	14.0
	226A	AX	MLC	13.2	12.0
	226B	AX	MLC	12.9	11.8
	232A	AX	MLC	19.4	16.7
	232B	AX	MLC	16.8	14.9
	236A	AX	MLC	8.9	8.4
	236B	AX	MLC	19.0	16.5
	238A	AX	MLC	17.6	15.4
	238B	AX	MLC	17.6	15.5
	244A	AX	MLC	15.0	13.5
	244B	AX	MLC	11.5	10.6
	MEAN			15.6 MPA (2256. PSI)	13.8 MPA (2004. PSI)
	STD. DEV.			3.3 MPA (475. PSI)	2.6 MPA (378. PSI)

TABLE 11-6 (Continued)

FLEXURAL PROPERTIES OF HLM GRAPHITE

LOT NO. 367 SPEC. DIA. 6.4 MM
LOG NO. 6484-78 SPEC. LENGTH 51. MM
LOG DENSITY -- MG/M**3

SPECIMEN NUMBER	ORIENTATION	LOCATION	DENSITY (MG/M**3)	MODULUS OF RUPTURE (MPA) (UNCORRECTED)	FLEXURAL STRENGTH (MPA) (CORRECTED)
1A	111 RAD	EE		22.2	18.1
	115 RAD	EF		19.3	16.3
	117 RAD	EE		18.5	15.8
	121 RAD	EF		22.0	18.0
	123 RAD	EF		20.6	17.1
	137 RAD	EE		20.7	17.2
	141 RAD	EE		22.1	18.0
	143 RAD.	EF		19.0	16.1
	147 RAD	EE		18.8	16.0
	149 RAD	EE		20.9	17.3
1B	267 RAD	EF		17.9	15.3
	271 RAD	EF		23.6	18.9
	273 RAD	EE		22.1	18.0
	277 RAD	EE		15.7	13.8
	279 RAD	EE		19.8	16.6
	293 RAD	EE		20.7	17.2
	297 RAD	EF		17.0	14.8
	299 RAD	EF		16.3	14.2
	303 RAD	EE		18.9	16.1
	305 RAD	EF		20.3	16.9
	MEAN			19.8 MPA (2875. PSI)	16.6 MPA (2407. PSI)
	STD. DEV.			2.1 MPA (306. PSI)	1.4 MPA (198. PSI)

TABLE 11-6 (Continued)

FLEXURAL PROPERTIES OF HLM GRAPHITE

LOT NO. 367 SPEC. DIA. 6.4 MM
LOG NO. 6484-7R SPEC. LENGTH 51. MM
LOG DENSITY -- MG/M**3

SPECIMEN NUMBER	ORIENTATION	LOCATION	DENSITY (MG/M**3)	MODULUS OF RUPTURE (MPA) (UNCORRECTED)	FLEXURAL STRENGTH (MPA) (CORRECTED)
1A	59 RAD	EM		19.5	16.6
	63 RAD	EM		23.7	19.3
	65 RAD	EM		25.9	20.5
	69 RAD	EM		25.4	20.2
	71 RAD	EM		23.6	19.2
	85 RAD	EM		21.8	18.2
	89 RAD	EM		23.8	19.3
	91 RAD	EM		18.6	16.0
	95 RAD	EM		20.2	17.1
1A	97 RAD	EM		22.5	18.6
1B	215 RAD	EM		19.8	16.9
	219 RAD	EM		19.3	16.5
	221 RAD	EM		17.3	15.1
	225 RAD	EM		21.1	17.7
	227 RAD	EM		19.4	16.6
	241 RAD	EM		18.0	15.6
	245 RAD	EM		21.8	18.2
	247 RAD	EM		23.1	18.9
	251 RAD	EM		18.9	16.3
	253 RAD	EM		19.4	16.6
	MEAN			21.2 MPA (3070. PSI)	17.7 MPA (2562. PSI)
	STD. DEV.			2.5 MPA (362. PSI)	1.6 MPA (226. PSI)

TABLE 11-6 (Continued)

FLEXURAL PROPERTIES OF HLM GRAPHITE

LOT NO. 367 SPEC. DIA. 6.4 MM
LOG NO. 6484-78 SPEC. LENGTH 51. MM
LOG DENSITY -- MG/M***3

SPECIMEN NUMBER	ORIENTATION	LOCATION	DENSITY (MG/M***3)	MODULUS OF RUPTURE (MPA) (UNCORRECTED)	FLEXURAL STRENGTH (MPA) (CORRECTED)
1A	7 RAD	EC		19.0	16.5
	9 RAD	EC		24.6	20.1
	13 RAD	EC		24.7	20.2
	15 RAD	EC		18.0	15.8
	19 RAD	EC		23.6	19.5
	33 RAD	EC		20.4	17.4
	35 RAD	EC		22.8	19.0
	39 RAD	EC		22.0	18.5
	41 RAD	EC		23.3	19.4
	45 RAD	EC		22.1	18.6
1B	163 RAD	EC		18.2	15.9
	165 RAD	EC		15.4	13.8
	169 RAD	EC		20.7	17.7
	171 RAD	EC		22.2	18.6
	175 RAD	EC		19.2	16.6
	189 RAD	EC		22.6	18.9
	191 RAD	EC		22.6	18.9
	195 RAD	EC		22.6	18.9
	197 RAD	EC		21.7	18.3
	201 RAD	EC		17.3	15.2
	MEAN			21.2 MPA (3068. PSI)	17.9 MPA (2594. PSI)
	STD. DEV.			2.5 MPA (370. PSI)	1.7 MPA (251. PSI)

TABLE 11-6 (Continued)

FLEXURAL PROPERTIES OF HLM GRAPHITE

LOT NO. 367 SPEC. DIA. 6.4 MM
LOG NO. 6484-7A SPEC. LENGTH 51. MM
LOG DENSITY -- MG/M**3

SPECIMEN NUMBER	ORIENTATION	LOCATION	DENSITY (MG/M**3)	MODULUS OF RUPTURE (MPA) (UNCORRECTED)	FLEXURAL STRENGTH (MPA) (CORRECTED)
1A	59 RAD	EM		19.5	16.6
	63 RAD	EM		23.7	19.3
	65 RAD	EM		25.9	20.5
	69 RAD	EM		25.4	20.2
	71 RAD	EM		23.6	19.2
	85 RAD	EM		21.8	18.2
	89 RAD	EM		23.8	19.3
	91 RAD	EM		18.6	16.0
	95 RAD	EM		20.2	17.1
1A	97 RAD	EM		22.5	18.6
1B	215 RAD	EM		19.8	16.9
	219 RAD	EM		19.3	16.5
	221 RAD	EM		17.3	15.1
	225 RAD	EM		21.1	17.7
	227 RAD	EM		19.4	16.6
	241 RAD	EM		18.0	15.6
	245 RAD	EM		21.8	18.2
	247 RAD	EM		23.1	18.9
	251 RAD	EM		18.9	16.3
	253 RAD	EM		19.4	16.6
	MEAN			21.2 MPA (3070. PSI)	17.7 MPA (2562. PSI)
	STD. DEV.			2.5 MPA (362. PSI)	1.6 MPA (226. PSI)

TABLE 11-6 (Continued)

FLEXURAL PROPERTIES OF HLM GRAPHITE

LOT NO. 367 SPEC. DIA. 6.4 MM
LOG NO. 6484-78 SPEC. LENGTH 51. MM
LOG DENSITY -- MG/M**3

SPECIMEN NUMBER	ORIENTATION	LOCATION	DENSITY (MG/M**3)	MODULUS OF RUPTURE (MPA) (UNCORRECTED)	FLEXURAL STRENGTH (MPA) (CORRECTED)
1A	7 RAD	EC		19.0	16.5
	9 RAD	EC		24.6	20.1
	13 RAD	EC		24.7	20.2
	15 RAD	EC		18.0	15.8
	19 RAD	EC		23.6	19.5
	33 RAD	EC		20.4	17.4
	35 RAD	EC		22.8	19.0
	39 RAD	EC		22.0	18.5
	41 RAD	EC		23.3	19.4
	45 RAD	EC		22.1	18.6
1B	163 RAD	EC		18.2	15.9
	165 RAD	EC		15.4	13.8
	169 RAD	EC		20.7	17.7
	171 RAD	EC		22.2	18.6
	175 RAD	EC		19.2	16.6
	189 RAD	EC		22.6	18.9
	191 RAD	EC		22.6	18.9
	195 RAD	EC		22.6	18.9
	197 RAD	EC		21.7	18.3
	201 RAD	EC		17.3	15.2
	MEAN			21.2 MPA (3068. PSI)	17.9 MPA (2594. PSI)
	STD. DEV.			2.5 MPA (370. PSI)	1.7 MPA (251. PSI)

TABLE 11-6 (Continued)

FLEXURAL PROPERTIES OF HLM GRAPHITE

LOT NO. 367 SPEC. DIA. 6.4 MM
LOG NO. 6484-78 SPEC. LENGTH 51. MM
LOG DENSITY -- MG/M**3

SPECIMEN NUMBER	ORIENTATION	LOCATION	DENSITY (MG/M**3)	MODULUS OF RUPTURE (MPA) (UNCORRECTED)	FLEXURAL STRENGTH (MPA) (CORRECTED)
6A	423 RAD	MLE		23.7	19.2
	427 RAD	MLE		20.3	17.1
	429 RAD	MLE		24.0	19.4
	433 RAD	MLE		18.5	16.0
	435 RAD	MLE		24.5	19.7
	449 RAD	MLE		20.8	17.5
	453 RAD	MLE		23.2	18.9
	455 RAD	MLE		23.0	18.8
	459 RAD	MLE		21.7	18.0
	461 RAD	MLE		21.5	17.9
6B	553 RAD	MLE		21.5	17.9
	557 RAD	MLE		18.8	16.2
	559 RAD	MLE		25.9	20.3
	563 RAD	MLE		19.1	16.4
	565 RAD	MLE		22.6	18.6
	579 RAD	MLE		21.0	17.6
	583 RAD	MLE		19.4	16.5
	585 RAD	MLE		20.9	17.5
	589 RAD	MLE		18.7	16.1
	591 RAD	MLE		22.0	18.2
	MEAN			21.6 MPA (3126. PSI)	17.9 MPA (2593. PSI)
	STD. DEV.			2.1 MPA (301. PSI)	1.3 MPA (185. PSI)

TABLE 11-6 (Continued)

FLEXURAL PROPERTIES OF HLM GRAPHITE

LOT NO. 367 SPEC. DIA. 6.4 MM
LOG NO. 6484-78 SPEC. LENGTH 51. MM
LOG DENSITY -- MG/M**3

SPECIMEN NUMBER	ORIENTATION	LOCATION	DENSITY (MG/M**3)	MODULUS OF RUPTURE (MPA) (UNCORRECTED)	FLEXURAL STRENGTH (MPA) (CORRECTED)
6A	371 RAD	MLM		17.2	15.0
	375 RAD	MLM		20.5	17.4
	377 RAD	MLM		23.1	19.0
	381 RAD	MLM		22.1	18.4
	383 RAD	MLM		24.0	19.5
	397 RAD	MLM		15.3	13.7
	401 RAD	MLM		16.5	14.5
	403 RAD	MLM		18.6	16.0
	407 RAD	MLM		21.3	17.9
	409 RAD	MLM		19.3	16.5
6B	501 RAD	MLM		23.3	19.1
	505 RAD	MLM		21.7	18.1
	507 RAD	MLM		19.6	16.8
	511 RAD	MLM		23.1	19.0
	513 RAD	MLM		20.3	17.2
	527 RAD	MLM		17.6	15.3
	531 RAD	MLM		20.9	17.6
	533 RAD	MLM		22.0	18.3
	537 RAD	MLM		23.2	19.1
	539 RAD	MLM		22.5	18.6
	MEAN			20.6 MPA (2989. PSI)	17.4 MPA (2517. PSI)
	STD. DEV.			2.5 MPA (365. PSI)	1.7 MPA (245. PSI)

TABLE 11-6 (Continued)

FLEXURAL PROPERTIES OF HLM GRAPHITE

LOT NO. 367 SPEC. DIA. 6.4 MM
LOG NO. 6484-7A SPEC. LENGTH 51. MM
LOG DENSITY -- MG/M***3

SPECIMEN NUMBER	ORIENTATION	LOCATION	DENSITY (MG/M***3)	MODULUS OF RUPTURE (MPA) (UNCORRECTED)	FLEXURAL STRENGTH (MPA) (CORRECTED)
6A	319 RAD	MLC		24.9	20.3
	321 RAD	MLC		16.7	14.8
	325 RAD	MLC		19.2	16.7
	327 RAD	MLC		15.4	13.8
	331 RAD	MLC		25.6	20.8
	345 RAD	MLC		21.1	18.0
	347 RAD	MLC		22.1	18.6
	351 RAD	MLC		22.7	19.0
	353 RAD	MLC		18.1	15.9
	357 RAD	MLC		19.9	17.2
6B	471 RAD	MLC		21.3	18.1
	473 RAD	MLC		22.7	19.0
	475 RAD	MLC		21.3	18.1
	477 RAD	MLC		23.6	19.6
6H	481 RAD	MLC		18.3	16.0
	483 RAD	MLC		23.7	19.6
	485 RAD	MLC		21.0	17.9
	487 RAD	MLC		16.2	14.4
	489 RAD	MLC		22.3	18.7
	493 RAD	MLC		15.4	13.8
	MEAN			20.6 MPA (2984. PSI)	17.5 MPA (2539. PSI)
	STD. DEV.			3.1 MPA (446. PSI)	2.1 MPA (308. PSI)

TABLE 11-7

COMPRESSIVE PROPERTIES OF HLM GRAPHITE

LOT NO. 367 SPEC. DIA. 12.8 MM
LOG NO. 6484.78 SPEC. LENGTH 25. MM
LOG DENSITY -- MG/M**3

SPECIMEN NUMBER	ORIENTATION	LOCATION	DENSITY (MG/M**3)	YOUNGS MODULUS (GPA)	PERMANENT SET (PCT)	FRACTURE STRAIN (PCT)	COMPR. STRENGTH (MPA)
1AC E 6C	AX	EC		5.3	.200	2.371	37.9
E 8C	AX	EC		4.7	.229	2.532	38.9
E10C	AX	EC		4.9	.210	2.559	38.7
E12C	AX	EC		5.3	.200	2.148	37.4
1BC E102C	AX	EC		5.5	.200	2.201	38.5
E104C	AX	EC		5.3	.200	2.331	38.4
E106C	AX	EC		4.5	.230	2.377	38.7
E108C	AX	EC		5.1	.200	1.965	36.2
MEAN				5.1	.208	2.310	38.1
				(.74 MPSI)			(5524.PSI)
STD. DEV.				.4	.013	.199	.9
				(.05 MPSI)			(133.PSI)
1AC E 9B	RAD	EC		5.8	.180	2.370	44.2
E23B	RAD	EC		6.3	.180	2.327	44.5
E25B	RAD	EC		6.3	.200	2.252	44.1
E29B	RAD	EC		6.2	.190	2.073	42.5
1BC E111B	RAD	EC		6.0	.190	2.048	42.2
E115B	RAD	EC		5.2	.180	2.253	41.9
E119B	RAD	EC		5.7	.220	2.179	42.1
E131B	RAD	EC		5.8	.210	2.288	42.8
MEAN				5.9	.194	2.224	43.0
				(.86 MPSI)			(6241.PSI)
STD. DEV.				.3	.015	.116	1.1
				(.05 MPSI)			(154.PSI)

TABLE 11-7 (Continued)

COMPRESSIVE PROPERTIES OF HLM GRAPHITE

LOT NO. 367 SPEC. DIA. 12.8 MM
LOG NO. 6484-78 SPEC. LENGTH 25. MM
LOG DENSITY -- MG/M**3

SPECIMEN NUMBER	ORIENTATION	LOCATION	DENSITY (MG/M**3)	YOUNGS MODULUS (GPA)	PERMANENT SET (PCT)	FRACTURE STRAIN (PCT)	COMPR. STRENGTH (MPA)
1AY E30C	AX	EM		5.0	.210	1.891	34.6
E34C	AX	EM		5.6	.190	1.735	35.0
E42C	AX	EM		5.1	.180	2.010	36.7
E46C	AX	EM		3.9	.210	2.157	33.6
1BY E114C	AX	EM		5.1	.200	1.852	35.8
E118C	AX	EM		5.7	.180	2.102	37.1
E126C	AX	EM		5.2	.200	1.891	34.5
E130C	AX	EM		4.5	.200	2.015	32.9
	MEAN			5.0	.196	1.957	35.0
				(.73 MPSI)			(5078.PSI)
	STD. DEV.			.6	.012	.140	1.5
				(.08 MPSI)			(212.PSI)
1AY E43B	RAD	EM		6.1	.160	2.234	43.6
E47B	RAD	EM		5.9	.190	2.154	41.7
E51B	RAD	EM		5.5	.200	2.484	42.6
E61B	RAD	EM		6.5	.170	1.770	40.2
1BY E151B	RAD	EM		5.6	.220	2.193	41.1
E155B	RAD	EM		5.5	.210	2.276	41.7
E159B	RAD	EM		5.5	.200	1.986	39.6
E169B	RAD	EM		5.3	.210	1.812	37.7
	MEAN			5.7	.195	2.114	41.0
				(.83 MPSI)			(5951.PSI)
	STD. DEV.			.4	.021	.242	1.8
				(.06 MPSI)			(265.PSI)

TABLE 11-7 (Continued)

COMPRESSIVE PROPERTIES OF HLM GRAPHITE

LOT NO. 367 SPEC. DIA. 12.8 MM
LOG NO. 6484-78 SPEC. LENGTH 25. MM
LOG DENSITY -- MG/M**3

SPECIMEN NUMBER	ORIENTATION	LOCATION	DENSITY (MG/M**3)	YOUNGS MODULUS (GPA)	PERMANENT SET (PCT)	FRACTURE STRAIN (PCT)	COMPR. STRENGTH (MPA)
1AE E60C	AX	EE		6.3	.200	1.735	38.3
E64C	AX	EF		7.2	.180	1.846	41.0
E72C	AX	EF		6.7	.175	1.617	37.7
E76C	AX	EE		6.9	.160	1.543	39.8
1BE E144C	AX	EE		6.5	.180	1.907	40.4
E148C	AX	EF		7.1	.170	1.878	42.3
E156C	AX	EE		6.5	.190	1.931	40.0
E160C	AX	EE		6.7	.170	1.661	39.2
	MEAN			6.7 (.98 MPSI)	.178	1.765	39.8 (5777.PSI)
	STD. DEV.			.3 (.05 MPSI)	.012	.146	1.5 (213.PSI)
1AE E79B	RAD	EE		5.6	.210	2.338	41.6
E83B	RAD	EE		5.2	.190	2.488	41.8
E87B	RAD	EE		5.1	.220	1.801	37.3
E97B	RAD	EE		5.5	.160	1.877	39.1
1BE E187B	RAD	EE		5.4	.200	2.650	44.5
E191B	RAD	EE		5.5	.200	2.471	42.7
E195B	RAD	EE		5.6	.200	2.466	44.2
E205B	RAD	EE		4.6	.200	2.456	41.6
	MEAN			5.3 (.77 MPSI)	.197	2.318	41.6 (6073.PSI)
	STD. DEV.			.3 (.05 MPSI)	.017	.309	2.4 (352.PSI)

TABLE 11-7 (Continued)

COMPRESSIVE PROPERTIES OF HLM GRAPHITE

LOT NO. 367 SPEC. DIA. 12.8 MM
LOG NO. 6484-78 SPEC. LENGTH 25. MM
LOG DENSITY -- MG/M**3

SPECIMEN NUMBER	ORIENTATION	LOCATION	DENSITY (MG/M**3)	YOUNGS MODULUS (GPA)	PERMANENT SET (PCT)	FRACTURE STRAIN (PCT)	COMPR. STRENGTH (MPA)
6AC	M10C	AX	MLC			1.609	35.5
	M 8C	AX	MLC			1.787	33.3
	M12C	AX	MLC	5.4	.180	1.996	37.5
	M16C	AX	MLC	6.3	.080	1.906	38.3
6BC	M92C	AX	MLC	4.7	.200	2.290	37.3
	M94C	AX	MLC	4.7	.200	1.807	34.9
	M96C	AX	MLC	5.7	.040	1.277	33.4
	M98C	AX	MLC	5.0	.189	1.330	32.4
	MEAN			5.3	.148	1.750	35.3
				(.77 MPSI)			(5123.PSI)
	STD. DEV.			.6	.070	.338	2.2
				(.09 MPSI)			(318.PSI)
6AC	M 5B	RAD	MLC	6.4	.180	1.917	41.8
	M 9B	RAD	MLC	5.9	.180	1.898	41.0
	M13B	RAD	MLC	6.4	.150	1.929	41.8
	M23B	RAD	MLC	6.0	.170	1.822	39.9
6BC	M113B	RAD	MLC	5.7	.210	2.230	41.5
	M117B	RAD	MLC	6.1	.170	1.794	39.9
	M121B	RAD	MLC	5.5	.180	2.146	41.0
	M131B	RAD	MLC	5.4	.190	1.735	36.9
	MEAN			5.9	.179	1.934	40.5
				(.86 MPSI)			(5870.PSI)
	STD. DEV.			.4	.017	.171	1.6
				(.05 MPSI)			(235.PSI)

TABLE 11-7 (Continued)

COMPRESSIVE PROPERTIES OF MLM GRAPHITE

LOT NO. 367 SPEC. DIA. 12.8 MM
LOG NO. 6484-78 SPEC. LENGTH 25. MM
LOG DENSITY = MG/M**3

SPECIMEN NUMBER	ORIENTATION	LOCATION	DENSITY (MG/M**3)	YOUNGS MODULUS (GPA)	PERMANENT SET (PCT)	FRACTURE STRAIN (PCT)	COMPR. STRENGTH (MPA)
6AY M30C	AX	MLM		7.3	.160	1.910	40.1
M34C	AX	MLM		5.6	.180	1.347	32.8
M42C	AX	MLM		6.1	.160	1.658	36.7
M46C	AX	MLM		5.2	.180	1.946	37.8
6BY M112C	AX	MLM		4.4	.220	1.486	31.6
M116C	AX	MLM		6.1	.180	1.749	37.2
M124C	AX	MLM		5.3	.190	1.406	32.2
M128C	AX	MLM		5.8	.180	1.469	34.6
MEAN				5.7	.181	1.621	35.4
				(.83 MPSI)			(5130.PSI)
STD. DEV.				.8	.019	.230	3.1
				(.12 MPSI)			(446.PSI)
6AY M43B	RAD	MLM		5.6	.180	2.346	43.2
M47B	RAD	MLM		6.3	.160	2.426	44.4
M51B	RAD	MLM		5.9	.180	2.404	44.5
M61B	RAD	MLM		6.1	.170	1.866	41.9
6BY M151B	RAD	MLM		5.6	.200	2.016	40.5
M155B	RAD	MLM		5.1	.200	2.731	42.8
M159B	RAD	MLM		5.6	.210	2.427	42.6
M169B	RAD	MLM		5.8	.170	1.941	40.8
MEAN				5.8	.184	2.269	42.6
				(.83 MPSI)			(6175.PSI)
STD. DEV.				.4	.018	.298	1.5
				(.06 MPSI)			(216.PSI)

TABLE 11-7 (Continued)

COMPRESSIVE PROPERTIES OF HLM GRAPHITE

LOT NO. 367 SPEC. DIA. 12.8 MM
LOG NO. 6484-78 SPEC. LENGTH 25. MM
LOG DENSITY = MG/M**3

SPECIMEN NUMBER		ORIENTATION	LOCATION	DENSITY (MG/M**3)	YOUNGS MODULUS (GPA)	PERMANENT SET (PCT)	FRACTURE STRAIN (PCT)	COMPR. STRENGTH (MPA)
6AE	M60C	AX	MLE		6.4	.180	2.142	41.3
	M64C	AX	MLE		8.6	.110	1.636	43.6
	M72C	AX	MLE		7.2	.150	1.659	38.8
	M76C	AX	MLE		6.9	.150	1.978	42.4
6BE	M142C	AX	MLE		6.7	.170	2.012	42.1
	M146C	AX	MLE		7.3	.180	2.030	41.9
	M154C	AX	MLE		6.9	.180	1.714	38.6
	M158C	AX	MLE		7.0	.200	1.712	39.9
	MEAN				7.1 (1.03 MPSI)	.165	1.861	41.1 (5958.PSI)
	STD. DEV.				.7 (.10 MPSI)	.028	.200	1.8 (261.PSI)
6AE	M79B	RAD	MLE		5.9	.200	2.711	45.6
	M83B	RAD	MLE		5.8	.200	2.479	44.3
	M87B	RAD	MLE		5.9	.180	2.410	44.7
	M97B	RAD	MLE		6.1	.180	2.380	45.7
6BE	M187B	RAD	MLE		5.6	.180	2.677	45.9
	M191B	RAD	MLE		5.7	.210	2.624	44.5
	M195B	RAD	MLE		6.1	.190	2.218	42.7
	M205B	RAD	MLE		5.8	.220	2.498	44.3
	MEAN				5.9 (.85 MPSI)	.195	2.500	44.7 (6485.PSI)
	STD. DEV.				.2 (.02 MPSI)	.015	.166	1.0 (151.PSI)

TABLE 11-8

THERMAL CONDUCTIVITY OF HLM GRAPHITE

LOT NUMBER: -- LOG NUMBER: 6484-78

ORIENTATION	LOCATION	SPECIMEN NUMBER	THERMAL CONDUCTIVITY (W/M-K) AT: 295K (22C)	473K (200C)	673K (400C)	873K (600C)	1073K (800C)
AXIAL	MLC	M-90A	134.9	113.1	95.3	77.9	66.8
		M-90B	144.2	127.9	104.7	89.6	77.7
		M-90C	104.2	107.2	85.8	70.8	59.4
		M-90D	111.6	119.1	100.2	76.3	62.4
		M-90E	131.4	115.8	95.9	77.6	66.2
		M-90F	123.0	115.6	93.6	77.7	66.6
		M-90G	119.0	101.5	80.6	66.3	56.0
		M-90H	125.2	112.4	89.1	71.0	65.2
		MEAN:	124.2	114.1	93.2	75.9	65.0
		STD. DEV:	12.9	7.8	7.8	7.0	6.4

TABLE 11-9
MEAN STRENGTH VALUES OF GRADE PGX GRAPHITE (LOT 805-3, LOG 6484-112)
(MPa)

Axial									Radial								
Slab 1			Slab 6			Slab 12			Slab 1			Slab 6			Slab 12		
EC	EM	EE	MLC	MLM	MLE	EC	EM	EE	EC	EM	EE	MLC	MLM	MLE	EC	EM	EE
Tensile																	
10.5	11.1	11.4	10.0	10.9	11.4	9.1	9.1	9.4	9.6	10.2	10.9	9.2	10.3	11.0	8.9	8.1	8.8
±2.0	±0.5	±0.6	±0.7	±0.7	±0.6	±0.9	±0.6	±0.6	±0.7	±0.8	±0.6	±0.8	±0.7	±0.9	±1.1	±1.4	±0.9
Compressive																	
44.7	43.9	45.7	41.7	44.8	45.5	41.7	40.3	40.7	42.2	41.1	42.5	40.2	41.8	43.3	40.2	39.1	38.3
±0.9	±2.8	±1.6	±2.2	±2.0	±1.9	±0.8	±1.9	±2.1	±2.7	±2.8	±1.5	±2.2	±1.5	±1.7	±1.4	±1.1	±1.8

TABLE 11-10

TENSILE PROPERTIES OF PGX GRAPHITE

LOT NO. AD5-3 SPEC. DIA. 12.8 MM
LOG NO. 6484-112 SPEC. LENGTH 63. MM
LOG DENSITY 1.78 MG/M**3

SPECIMEN NUMBER	ORIENTATION	LOCATION	DENSITY (MG/M**3)	YOUNGS MODULUS (GPA)	PERMANENT SET (PCT)	FRACTURE STRAIN (PCT)	TENSILE STRENGTH (MPA)
1AC-E- 10A	AX	EC	1.784	6.2	.020	.205	10.6
- 12A	AX	EC	1.787	6.5	.027	.213	10.5
- 22A	AX	EC	1.786	7.1	.024	.163	9.2
- 24A	AX	EC	1.785	6.5	.030	.212	10.3
- 06A	AX	EC					11.9
- 08A	AX	EC					12.0
- 10B	AX	EC					11.4
- 12B	AX	EC					11.0
- 18A	AX	EC					9.9
- 20B	AX	EC					10.6
- 22B	AX	EC					7.3
- 24B	AX	EC					12.0
1BC-E-106B	AX	EC	1.777	6.4	.025	.219	10.6
-108B	AX	EC	1.778				3.3
- 94B	AX	EC	1.776	6.3	.020	.216	10.8
- 96B	AX	EC	1.774	6.3	.022	.218	11.7
-102A	AX	EC					7.2
-104B	AX	EC					11.8
-106A	AX	EC					11.9
-108A	AX	EC					11.3
1BC-E- 90A	AX	EC					12.0
- 92B	AX	EC					11.5
- 94A	AX	EC					11.6
- 96A	AX	EC					12.0
	MEAN		1.781	6.5 (.94 MPSI)	.024	.207	10.5 (1525.PSI)
	STD. DEV.		.005	.3 (.04 MPSI)	.004	.020	2.0 (296.PSI)

TABLE 11-10 (Continued)

TENSILE PROPERTIES OF PGX GRAPHITE

LOT NO. RDS-3 SPEC. DIA. 12.8 MM
LOG NO. 6484-112 SPEC. LENGTH 63. MM
LOG DENSITY 1.78 MG/M**3

SPECIMEN NUMBER	ORIENTATION	LOCATION	DENSITY (MG/M**3)	YOUNGS MODULUS (GPA)	PERMANENT SET (PCT)	FRACTURE STRAIN (PCT)	TENSILE STRENGTH (MPA)
12AC-B- 10B	AX	EC	1.786	6.0	.025	.188	8.8
- 12B	AX	EC	1.777	5.7	.031	.197	8.8
- 22B	AX	EC	1.771	7.3	.022	.152	8.7
- 24B	AX	EC	1.775	5.8	.030	.209	9.0
- 06A	AX	EC					9.7
- 08B	AX	EC					8.2
- 10A	AX	EC					10.0
- 12A	AX	EC					9.7
- 18A	AX	EC					10.0
- 20B	AX	EC					9.0
- 22A	AX	EC					9.0
- 24A	AX	EC					10.1
12BC-B- 94B	AX	EC	1.791	6.3	.031	.171	8.3
- 96B	AX	EC	1.795	6.6	.026	.188	9.1
-106B	AX	EC	1.789	6.1	.019	.170	8.5
-108B	AX	EC	1.777	5.9	.030	.203	9.0
12HC-B- 96A	AX	EC					10.2
- 90A	AX	EC					10.2
- 92B	AX	EC					7.6
- 94A	AX	EC					9.6
-102A	AX	EC					6.5
-104B	AX	EC					9.0
-106A	AX	EC					9.2
-108A	AX	EC					9.8
MEAN			1.783	6.2 (.90 MPSI)	.027	.185	9.1 (1317.PSI)
STD. DEV.			.009	.5 (.08 MPSI)	.005	.019	.9 (127.PSI)

TABLE 11-10 (Continued)

TENSILE PROPERTIES OF PGX GRAPHITE

LOT NO. 8D5-3 SPEC. DIA. 12.8 MM
LOG NO. 6484-112 SPEC. LENGTH 63. MM
LOG DENSITY 1.78 MG/M**3

SPECIMEN NUMBER	ORIENTATION	LOCATION	DENSITY (MG/M**3)	YOUNGS MODULUS (GPA)	PERMANENT SET (PCT)	FRACTURE STRAIN (PCT)	TENSILE STRENGTH (MPA)
1AC-E-31	RAD	EC	1.779	6.7	.019	.174	9.5
-27	RAD	EC	1.779	7.0	.017	.160	9.3
-11	RAD	EC	1.779	6.9	.021	.180	10.2
-07	RAD	EC	1.784			.174	9.7
-05	RAD	EC		6.7	.023	.187	9.8
-09	RAD	EC					9.3
-23	RAD	EC					9.9
-25	RAD	EC					7.8
-29	RAD	EC					8.3
-03	RAD	EC					9.6
1BC-E-113	RAD	EC	1.770	6.5	.025	.185	9.6
-117	RAD	EC	1.772	6.5	.021	.192	10.0
-133	RAD	EC	1.772	6.8	.020	.175	9.6
-137	RAD	EC	1.769	6.6	.022	.153	10.6
-111	RAD	EC					9.5
-115	RAD	EC					10.1
1BC-E-119	RAD	EC					9.6
-131	RAD	EC					8.4
-135	RAD	EC					10.3
-139	RAD	EC					10.2
	MEAN		1.776	6.7 (.97 MPSI)	.021	.176	9.6 (1389.PSI)
	STD. DEV.		.006	.2 (.03 MPSI)	.002	.013	.7 (102.PSI)

TABLE 11-10 (Continued)

TENSILE PROPERTIES OF PGX GRAPHITE

LOT NO. 8D5-3 SPEC. DIA. 12.8 MM
LOG NO. 6484-112 SPEC. LENGTH 63. MM
LOG DENSITY 1.78 MG/M**3

SPECIMEN NUMBER	ORIENTATION	LOCATION	DENSITY (MG/M**3)	YOUNGS MODULUS (GPA)	PERMANENT SET (PCT)	FRACTURE STRAIN (PCT)	TENSILE STRENGTH (MPA)
12AC-B- 05	RAD	EC	1.769	7.0	.026	.186	9.7
- 09	RAD	EC	1.782	7.4	.020	.152	8.7
- 27	RAD	EC	1.778	7.1	.023	.150	8.3
- 03	RAD	EC					9.9
- 07	RAD	EC					9.5
- 11	RAD	EC					7.4
- 21	RAD	EC					8.8
- 25	RAD	EC					8.6
- 29	RAD	EC					8.5
12BC-B-111	RAD	EC					9.1
-115	RAD	EC					10.4
12BC-B-119	RAD	EC					8.7
-129	RAD	EC					6.3
-133	RAD	EC					9.3
-137	RAD	EC					7.5
12HC-B-113	RAD	EC	1.780	7.0	.021	.149	8.4
-117	RAD	EC	1.779	7.6	.021	.160	9.0
-131	RAD	EC	1.776	7.6	.023	.187	10.3
-135	RAD	EC	1.774	7.7	.019	.180	10.6
	MEAN		1.777	7.4 (1.07 MPSI)	.022	.166	8.9 (1292.PSI)
	STD. DEV.		.004	.3 (.05 MPSI)	.002	.017	1.1 (159.PSI)

TABLE 11-10 (Continued)

TENSILE PROPERTIES OF PGX GRAPHITE

LOT NO. RD5-3 SPEC. DIA. 12.8 MM
LOG NO. 6484-112 SPEC. LENGTH 63. MM
LOG DENSITY 1.78 MG/M**3

SPECIMEN NUMBER	ORIENTATION	LOCATION	DENSITY (MG/M**3)	YOUNGS MODULUS (GPA)	PERMANENT SET (PCT)	FRACTURE STRAIN (PCT)	TENSILE STRENGTH (MPA)
1AY-E-30B	AX	EM	1.771	6.2	.025	.237	11.3
-34A	AX	EM	1.772	6.4	.029	.223	10.6
-46B	AX	EM	1.774	6.0	.026	.222	10.3
-54A	AX	EM	1.769	6.0	.023	.231	10.6
-30A	AX	EM					11.0
-34B	AX	EM					11.0
-42A	AX	EM					10.7
-42B	AX	EM					11.4
-46A	AX	EM					11.0
-54B	AX	EM					11.4
1BY-E-114B	AX	EM	1.773	6.3	.020	.239	11.7
-118A	AX	EM	1.773	6.4	.019	.239	11.7
-130B	AX	EM	1.778	6.3	.025	.226	11.0
-138A	AX	EM	1.779	6.4	.025	.227	11.0
-114A	AX	EM					11.6
-118B	AX	EM					10.5
1BY-E-126A	AX	EM					10.3
-126B	AX	EM					12.3
-130A	AX	EM					11.3
-138B	AX	EM					12.0
	MEAN		1.774	6.2 (.91 MPSI)	.024	.230	11.1 (1614.PSI)
	STD. DEV.		.003	.2 (.03 MPSI)	.003	.007	.5 (79.PSI)

TABLE 11-10 (Continued)

TENSILE PROPERTIES OF PGX GRAPHITE

LOT NO. 805-3 SPEC. DIA. 12.8 MM
LOG NO. 6484-112 SPEC. LENGTH 63. MM
LOG DENSITY 1.78 MG/M**3

SPECIMEN NUMBER	ORIENTATION	LOCATION	DENSITY (MG/M**3)	YOUNGS MODULUS (GPA)	PERMANENT SET (PCT)	FRACTURE STRAIN (PCT)	TENSILE STRENGTH (MPA)
12AY-B- 30B	AX	EM	1.770	5.7	.032	.231	9.3
- 34A	AX	EM	1.767	6.0	.031	.189	8.7
- 46B	AX	EM	1.776	5.8	.027	.212	9.1
- 54A	AX	EM	1.769	5.8	.030	.186	8.4
- 30A	AX	EM					9.3
- 34B	AX	EM					8.8
- 42A	AX	EM					9.4
- 42B	AX	EM					9.2
- 46A	AX	EM					9.6
- 54B	AX	EM					9.3
12BY-B-114B	AX	EM	1.771	5.9	.028	.210	9.2
-118A	AX	EM	1.771	6.1	.029	.224	9.9
-130B	AX	EM	1.775				6.8
-138A	AX	EM	1.782	6.4	.030	.184	8.8
-114A	AX	EM					9.0
-118B	AX	EM					9.3
12HY-B-126A	AX	EM					9.5
-126B	AX	EM					9.8
-130A	AX	EM					9.1
-138B	AX	EM					9.1
MEAN			1.773	6.0 (.87 MPSI)	.030	.205	9.1 (1316. PSI)
STD. DEV.			.005	.2 (.03 MPSI)	.002	.019	.6 (93. PSI)

TABLE 11-10 (Continued)

TENSILE PROPERTIES OF PGX GRAPHITE

LOT NO. HD5-3 SPEC. DIA. 12.8 MM
LOG NO. 6484-112 SPEC. LENGTH 63. MM
LOG DENSITY 1.78 MG/M**3

SPECIMEN NUMBER	ORIENTATION	LOCATION	DENSITY (MG/M**3)	YOUNGS MODULUS (GPA)	PERMANENT SET (PCT)	FRACTURE STRAIN (PCT)	TENSILE STRENGTH (MPA)
1AY-F- 45	RAD	EM	1.772	6.3	.018	.193	9.8
- 49	RAD	EM	1.772	6.5	.021	.186	9.7
- 63	RAD	EM	1.775	7.2	.016	.130	10.6
- 67	RAD	EM	1.776	7.0	.015	.201	11.3
- 43	RAD	EM					9.3
- 47	RAD	EM					9.3
- 51	RAD	EM					8.3
- 61	RAD	EM					10.3
- 65	RAD	EM					11.0
- 69	RAD	EM					10.0
1BY-F-153	RAD	EM	1.774	7.1	.018	.159	9.2
-157	RAD	EM	1.773	7.0	.021	.209	11.3
-171	RAD	EM	1.776	6.8	.018	.191	10.5
-175	RAD	EM	1.775	6.8	.020	.184	10.1
-151	RAD	EM					11.0
-155	RAD	EM					11.0
1BY-E-159	RAD	EM					10.2
-169	RAD	EM					10.9
-173	RAD	EM					9.9
-177	RAD	EM					9.7
	MEAN		1.774	6.8 (.99 MPSI)	.018	.182	10.2 (1475.PSI)
	STD. DEV.		.002	.3 (.04 MPSI)	.002	.025	.8 (115.PSI)

TABLE 11-10 (Continued)

TENSILE PROPERTIES OF PGX GRAPHITE

LOT NO. 805-3 SPEC. DIA. 12.6 MM
LOG NO. 6484-112 SPEC. LENGTH 63. MM
LOG DENSITY 1.78 MG/M**3

SPECIMEN NUMBER	ORIENTATION	LOCATION	DENSITY (MG/M**3)	YOUNGS MODULUS (GPA)	PERMANENT SET (PCT)	FRACTURE STRAIN (PCT)	TENSILE STRENGTH (MPA)
12AY-B- 45	RAD	EM	1.776	6.8	.026	.179	9.1
- 49	RAD	EM	1.776	6.6	.026	.150	7.9
- 63	RAD	EM	1.774	6.9	.020	.168	8.7
- 67	RAD	EM	1.773	6.9	.022	.159	8.4
- 43	RAD	EM					7.1
- 47	RAD	EM					7.8
- 51	RAD	EM					8.1
- 61	RAD	EM					9.3
- 65	RAD	EM					8.0
- 69	RAD	EM					8.9
12BY-B-153	RAD	EM	1.775				6.1
-157	RAD	EM	1.772	7.0	.019	.180	9.5
-171	RAD	EM	1.788	7.2	.024	.147	8.0
-175	RAD	EM	1.782	7.2	.020	.147	8.3
-151	RAD	EM					9.5
-155	RAD	EM					7.0
12BY-B-159	RAD	EM					9.0
-169	RAD	EM					3.6
-173	RAD	EM					9.3
-177	RAD	EM					9.0
	MEAN		1.777	6.9 (1.01 MPSI)	.022	.161	8.1 (1181.PSI)
	STD. DEV.		.005	.2 (.03 MPSI)	.003	.014	1.4 (202.PSI)

TABLE 11-10 (Continued)

TENSILE PROPERTIES OF PGX GRAPHITE

LOT NO. AD5-3 SPEC. DIA. 12.8 MM
LOG NO. 6484-112 SPEC. LENGTH 63. MM
LOG DENSITY 1.78 MG/M**3

SPECIMEN NUMBER	ORIENTATION	LOCATION	DENSITY (MG/M**3)	YOUNGS MODULUS (GPA)	PERMANENT SET (PCT)	FRACTURE STRAIN (PCT)	TENSILE STRENGTH (MPA)
1AE-E- 60B	AX	EE	1.773	6.1	.028	.250	11.4
- 64A	AX	EE	1.795	6.3	.020	.223	11.0
- 76B	AX	EE	1.782	6.1	.020	.219	10.8
- 84A	AX	EE	1.786	6.3	.022	.219	10.7
- 60A	AX	EE					11.3
- 64B	AX	EE					10.3
- 72A	AX	EE					11.8
- 72B	AX	EE					11.0
- 76A	AX	EE					12.0
- 84B	AX	EE					10.7
1BE-E-144B	AX	EE	1.785	6.4	.020	.259	12.3
-148A	AX	EE	1.825	6.8	.024	.240	12.2
-160B	AX	EE	1.792	6.4	.027	.254	11.9
-168A	AX	EE	1.781	6.2	.027	.247	11.5
-144A	AX	EE					12.0
-148B	AX	EE					11.9
1BE-E-156A	AX	EE					11.7
-156B	AX	EE					11.0
-160A	AX	EE					10.7
-168B	AX	EE					11.6
MEAN			1.790	6.3 (.91 MPSI)	.023	.239	11.4 (1654.PSI)
STD. DEV.			.016	.2 (.03 MPSI)	.003	.016	.6 (85.PSI)

TABLE 11-10 (Continued)

TENSILE PROPERTIES OF PGX GRAPHITE

LOT NO. 805-3 SPEC. DIA. 12.8 MM
LOG NO. 6484-112 SPEC. LENGTH 63. MM
LOG DENSITY 1.78 MG/M**3

SPECIMEN NUMBER	ORIENTATION	LOCATION	DENSITY (MG/M**3)	YOUNGS MODULUS (GPA)	PERMANENT SET (PCT)	FRACTURE STRAIN (PCT)	TENSILE STRENGTH (MPA)
12AE-B- 60B	AX	EE	1.764	5.6	.040	.205	8.4
- 64A	AX	EE	1.776	5.9	.025	.211	9.4
- 76B	AX	EE	1.796	6.1	.029	.200	9.0
- 84A	AX	EE	1.785	6.0	.026	.214	9.8
- 60A	AX	EE					9.5
- 64B	AX	EE					8.7
- 72A	AX	EE					9.3
- 72B	AX	EE					9.6
- 76A	AX	EE					9.1
- 84B	AX	EE					7.9
12BE-B-144B	AX	EE	1.769	5.9	.025	.217	9.6
-148A	AX	EE	1.786	6.1	.028	.192	9.0
-160B	AX	EE	1.785	6.4	.024	.206	9.7
-168A	AX	EE	1.780	6.3	.030	.231	10.0
-144A	AX	EE					9.5
-148B	AX	EE					10.2
12BE-B-156A	AX	EE					10.3
-156B	AX	EE					9.5
-160A	AX	EE					10.0
-168B	AX	EE					10.0
MEAN			1.780	6.1 (.88 MPSI)	.028	.209	9.4 (1367.PSI)
STD. DEV.			.010	.2 (.04 MPSI)	.005	.012	.6 (88.PSI)

TABLE 11-10 (Continued)

TENSILE PROPERTIES OF PGX GRAPHITE

LOT NO. 805-3 SPEC. DIA. 12.8 MM
LOG NO. 6484-112 SPEC. LENGTH 63. MM
LOG DENSITY 1.78 MG/M**3

SPECIMEN NUMBER	ORIENTATION	LOCATION	DENSITY (MG/M**3)	YOUNGS MODULUS (GPA)	PERMANENT SET (PCT)	FRACTURE STRAIN (PCT)	TENSILE STRENGTH (MPA)
1AE-F-85	RAD	EE	1.787	7.2	.018	.197	11.3
-81	RAD	EE	1.787	7.3	.021	.198	11.3
-99	RAD	EE	1.789	7.4	.012	.175	10.9
-103	RAD	EE	1.788	7.5	.022	.196	11.4
-79	RAD	EE					10.9
-83	RAD	EE					11.0
-87	RAD	EE					10.8
-97	RAD	EE					10.4
-101	RAD	EE					10.9
-105	RAD	EE					11.5
1BE-E-189	RAD	EE	1.794	7.2	.021	.201	11.3
-193	RAD	EE	1.792	7.3	.015	.176	10.7
-207	RAD	EE	1.789	6.7	.020	.180	10.0
-211	RAD	EE	1.789	7.2	.020	.195	11.0
-187	RAD	EE					11.9
-191	RAD	EE					11.9
1HE-F-195	RAD	EE					10.4
-205	RAD	EE					9.4
-209	RAD	EE					11.1
-213	RAD	EE					10.6
	MEAN		1.790	7.2 (1.05 MPSI)	.019	.190	10.9 (1586.PSI)
	STD. DEV.		.002	.2 (.03 MPSI)	.003	.011	.6 (88.PSI)

TABLE 11-10 (Continued)

TENSILE PROPERTIES OF PGX GRAPHITE

LOT NO. 805-3 SPEC. DIA. 12.8 MM
LOG NO. 6484-112 SPEC. LENGTH 63. MM
LOG DENSITY 1.78 MG/M**3

SPECIMEN NUMBER	ORIENTATION	LOCATION	DENSITY (MG/M**3)	YOUNGS MODULUS (GPA)	PERMANENT SET (PCT)	FRACTURE STRAIN (PCT)	TENSILE STRENGTH (MPA)
12AE-B- 81	RAD	EE	1.771	6.8	.029	.203	10.0
- 85	RAD	EE	1.776	6.8	.029	.150	7.9
- 90	RAD	EE	1.778	7.3	.026	.177	9.1
-103	RAD	EE	1.778	7.0	.015	.179	9.7
- 79	RAD	EE					9.6
- 83	RAD	EE					9.3
- 87	RAD	EE					9.0
- 97	RAD	EE					8.2
-101	RAD	EE					9.5
-105	RAD	EE					9.2
12BE-B-189	RAD	EE	1.773	6.7	.024	.135	7.3
-193	RAD	EE	1.773	6.6	.021	.131	7.3
-207	RAD	EE	1.776	7.3	.024	.180	9.4
-211	RAD	EE	1.774	6.8	.025	.131	7.2
-187	RAD	EE					8.7
-191	RAD	EE					9.3
12BE-B-195	RAD	EE					7.9
-205	RAD	EE					9.3
-209	RAD	EE					8.9
-213	RAD	EE					8.5
	MEAN		1.775	6.9 (1.00 MPSI)	.024	.161	8.8 (1270. PSI)
	STD. DEV.		.003	.3 (.04 MPSI)	.005	.028	.9 (124. PSI)

TABLE 11-10 (Continued)

TENSILE PROPERTIES OF PGX GRAPHITE

LOT NO. AD5-3 SPEC. DIA. 12.8 MM
LOG NO. 6484-112 SPEC. LENGTH 63. MM
LOG DENSITY 1.78 MG/M**3

SPECIMEN NUMBER	ORIENTATION	LOCATION	DENSITY (MG/M**3)	YOUNGS MODULUS (GPA)	PERMANENT SET (PCT)	FRACTURE STRAIN (PCT)	TENSILE STRENGTH (MPA)
8AC-M- 10B	AX	MLC	1.785	6.3	.019	.181	9.4
- 12B	AX	MLC	1.781	6.1	.024	.227	10.8
- 22A	AX	MLC	1.792	6.3	.024	.192	9.8
- 24A	AX	MLC	1.784	6.5	.021	.174	9.1
- 10A	AX	MLC					10.7
- 08B	AX	MLC					9.9
- 06B	AX	MLC					9.9
- 12A	AX	MLC					9.7
- 18A	AX	MLC					9.2
- 20A	AX	MLC					10.1
- 22B	AX	MLC					11.2
- 24B	AX	MLC					9.9
6BC-M- 94B	AX	MLC	1.769	6.0	.023	.215	10.3
- 96A	AX	MLC	1.771	5.8	.017	.204	10.1
- 98A	AX	MLC	1.780	6.3	.019	.220	10.9
6BC-M-104B	AX	MLC					9.5
-106B	AX	MLC	1.770	6.0	.022	.218	10.6
- 92A	AX	MLC					11.0
- 94A	AX	MLC					9.4
- 96B	AX	MLC					10.0
- 98B	AX	MLC					10.1
-106A	AX	MLC					8.5
MEAN			1.779	6.2 (.90 MPSI)	.021	.204	10.0 (1451.PSI)
STD. DEV.			.008	.2 (.03 MPSI)	.003	.020	.7 (98.PSI)

TABLE 11-10 (Continued)

TENSILE PROPERTIES OF PGX GRAPHITE

LOT NO. 805-3 SPEC. DIA. 12.8 MM
LOG NO. 6484-112 SPEC. LENGTH 63. MM
LOG DENSITY 1.78 MG/M**3

SPECIMEN NUMBER	ORIENTATION	LOCATION	DENSITY (MG/M**3)	YOUNGS MODULUS (GPA)	PERMANENT SET (PCT)	FRACTURE STRAIN (PCT)	TENSILE STRENGTH (MPA)
6AC-M- 07	RAD	MLC	1.782	7.0	.021	.146	8.6
- 11	RAD	MLC	1.784	6.9	.020	.141	8.2
- 25	RAD	MLC	1.781	7.5	.021	.162	9.7
- 29	RAD	MLC	1.779	7.3	.019	.130	8.1
- 05	RAD	MLC					10.1
- 09	RAD	MLC					8.8
- 13	RAD	MLC					8.7
- 23	RAD	MLC					9.2
- 27	RAD	MLC					7.6
- 31	RAD	MLC					9.9
6BC-M-115	RAD	MLC	1.779	7.1	.020	.144	8.4
-119	RAD	MLC	1.771	7.2	.024	.156	8.9
6BC-M-133	RAD	MLC	1.775	7.0	.017	.177	10.0
-137	RAD	MLC	1.773	7.0	.017	.190	10.7
-113	RAD	MLC					9.3
-117	RAD	MLC					8.4
-121	RAD	MLC					9.7
-131	RAD	MLC					9.5
-135	RAD	MLC					10.1
-139	RAD	MLC					9.3
	MEAN		1.778	7.1 (1.03 MPSI)	.020	.156	9.2 (1329.PSI)
	STD. DEV.		.005	.2 (.03 MPSI)	.002	.020	.8 (116.PSI)

TABLE 11-10 (Continued)

TENSILE PROPERTIES OF PGX GRAPHITE

LOT NO. AD5-3 SPEC. DIA. 12.8 MM
LOG NO. 6484-112 SPEC. LENGTH 63. MM
LOG DENSITY 1.78 MG/M**3

SPECIMEN NUMBER	ORIENTATION	LOCATION	DENSITY (MG/M**3)	YOUNGS MODULUS (GPA)	PERMANENT SET (PCT)	FRACTURE STRAIN (PCT)	TENSILE STRENGTH (MPA)
6AY-M- 30H	AX	MLM	1.782	6.4	.021	.200	10.4
- 34A	AX	MLM	1.783	6.3	.025	.225	10.8
- 46B	AX	MLM	1.778	6.4	.022	.211	10.8
- 52A	AX	MLM	1.775	6.3	.021	.224	11.3
- 30A	AX	MLM					11.1
- 34B	AX	MLM					12.0
- 42A	AX	MLM					10.6
- 42B	AX	MLM					11.9
- 46A	AX	MLM					11.2
- 52B	AX	MLM					10.3
6BY-M-112B	AX	MLM	1.781	6.7	.026	.208	10.7
-116A	AX	MLM	1.782	6.5	.021	.216	10.8
6BY-M-128B	AX	MLM	1.781	6.5	.026	.242	11.7
-134A	AX	MLM	1.779	6.7	.022	.207	10.5
-124A	AX	MLM					9.4
-124B	AX	MLM					12.0
6BY-M-128A	AX	MLM					10.5
-134B	AX	MLM					11.0
MEAN			1.780	6.5 (.94 MPSI)	.023	.217	10.9 (1587.PSI)
STD. DEV.			.003	.2 (.02 MPSI)	.002	.013	.7 (99.PSI)

TABLE 11-10 (Continued)

TENSILE PROPERTIES OF PGX GRAPHITE

LOT NO. 805-3 SPEC. DIA. 12.8 MM
LOG NO. 6484-112 SPEC. LENGTH 63. MM
LOG DENSITY 1.78 MG/M**3

SPECIMEN NUMBER	ORIENTATION	LOCATION	DENSITY (MG/M**3)	YOUNGS MODULUS (GPA)	PERMANENT SET (PCT)	FRACTURE STRAIN (PCT)	TENSILE STRENGTH (MPA)
6AY-M- 45	RAD	MLM	1.789	7.8	.021	.151	9.3
- 49	RAD	MLM	1.787	7.2	.020	.162	9.4
- 63	RAD	MLM	1.783	7.2	.021	.161	9.7
- 67	RAD	MLM	1.785	7.2	.020	.159	9.5
- 43	RAD	MLM					9.9
- 47	RAD	MLM					10.3
- 51	RAD	MLM					10.4
- 61	RAD	MLM					10.1
- 65	RAD	MLM					9.9
- 69	RAD	MLM					10.3
6BY-M-153	RAD	MLM	1.780	7.0	.020	.216	11.7
-157	RAD	MLM	1.778	7.4	.019	.217	11.5
-171	RAD	MLM	1.783	7.3	.020	.186	10.7
-175	RAD	MLM	1.781	7.2	.021	.184	10.5
-151	RAD	MLM					9.6
-155	RAD	MLM					11.3
6BY-M-159	RAD	MLM					10.3
-169	RAD	MLM					10.5
-173	RAD	MLM					11.1
-177	RAD	MLM					10.7
	MEAN		1.783	7.3 (1.06 MPSI)	.020	.179	10.3 (1500.PSI)
	STD. DEV.		.004	.2 (.03 MPSI)	.001	.026	.7 (98.PSI)

TABLE 11-10 (Continued)

TENSILE PROPERTIES OF PGX GRAPHITE

LOT NO. 805-3 SPEC. DIA. 12.8 MM
LOG NO. 6484-112 SPEC. LENGTH 63. MM
LOG DENSITY 1.78 MG/M**3

SPECIMEN NUMBER	ORIENTATION	LOCATION	DENSITY (MG/M**3)	YOUNGS MODULUS (GPA)	PERMANENT SET (PCT)	FRACTURE STRAIN (PCT)	TENSILE STRENGTH (MPA)
6AE-M-60B	AX	MLE	1.790	6.5	.020	.241	11.9
-64A	AX	MLE	1.792	6.6	.013	.208	11.3
-76B	AX	MLE	1.792	6.7	.022	.206	10.8
-84A	AX	MLE	1.789	6.6	.020	.204	10.6
-60A	AX	MLE					11.5
-64B	AX	MLE					10.3
-72A	AX	MLE					11.3
-72B	AX	MLE					11.7
-76A	AX	MLE					11.3
-84B	AX	MLE					11.6
6HE-M-142B	AX	MLE	1.792	6.7	.020	.241	12.0
-146A	AX	MLE	1.787	6.7	.024	.258	12.8
-158B	AX	MLE	1.798	6.5	.019	.198	10.7
-164A	AX	MLE	1.784	6.4	.024	.254	12.0
-142A	AX	MLE					11.6
-146B	AX	MLE					11.8
6BE-M-154A	AX	MLE					11.0
-154B	AX	MLE					11.3
-158A	AX	MLE					11.1
-164B	AX	MLE					11.7
MEAN			1.790	6.6 (.96 MPSI)	.020	.226	11.4 (1656. PSI)
STD. DEV.			.004	.1 (.02 MPSI)	.003	.025	.6 (84. PSI)

TABLE 11-10 (Continued)

TENSILE PROPERTIES OF PGX GRAPHITE

LOT NO. 805-3 SPEC. DIA. 12.8 MM
LOG NO. 6484-112 SPEC. LENGTH 63. MM
LOG DENSITY 1.78 MG/M**3

SPECIMEN NUMBER	ORIENTATION	LOCATION	DENSITY (MG/M**3)	YOUNGS MODULUS (GPA)	PERMANENT SET (PCT)	FRACTURE STRAIN (PCT)	TENSILE STRENGTH (MPA)
6AE-M- 81	RAD	MLE	1.794	7.6	.016	.149	8.9
- 85	RAD	MLE	1.789	7.7	.020	.201	12.1
- 99	RAD	MLE	1.790	7.5	.018	.168	10.3
-103	RAD	MLE	1.790	7.7	.011	.184	11.5
- 79	RAD	MLE					11.0
- 83	RAD	MLE					10.6
- 87	RAD	MLE					10.8
- 97	RAD	MLE					10.7
-101	RAD	MLE					11.6
-105	RAD	MLE					11.4
6BE-M-189	RAD	MLE	1.791	7.9	.013	.145	10.0
-193	RAD	MLE	1.789	7.7	.016	.198	12.0
-207	RAD	MLE	1.791	7.8	.015	.189	11.7
-211	RAD	MLE	1.793	7.6	.020	.197	11.8
-187	RAD	MLE					11.6
-191	RAD	MLE					9.2
6BE-M-195	RAD	MLE					11.4
-205	RAD	MLE					10.3
-209	RAD	MLE					12.0
-213	RAD	MLE					11.4
	MEAN		1.791	7.7 (1.12 MPSI)	.016	.179	11.0 (1598.PSI)
	STD. DEV.		.002	.2 (.02 MPSI)	.003	.022	.9 (131.PSI)

TABLE 11-11

COMPRESSIVE PROPERTIES OF PGX GRAPHITE

LOT NO. 805-3 SPEC. DIA. 12.6 MM
LOG NO. 6484-112 SPEC. LENGTH 25. MM
LOG DENSITY 1.78 MG/M**3

SPECIMEN NUMBER	ORIENTATION	LOCATION	DENSITY (MG/M**3)	YOUNGS MODULUS (GPA)	PERMANENT SET (PCT)	FRACTURE STRAIN (PCT)	COMPR. STRENGTH (MPA)
1AC	E 6C	AX	EC	5.4	.171	2.030	45.0
	E 8C	AX	EC	5.3	.191	1.986	44.0
	E10C	AX	EC	5.5	.171	1.933	44.8
	E12C	AX	EC	5.8	.151	1.936	46.0
1BC	E102C	AX	EC	5.5	.160	1.855	45.1
	E104C	AX	EC	5.6	.171	1.939	45.4
	E106C	AX	FC	6.0	.161	1.709	43.2
	E108C	AX	EC	5.3	.171	2.002	43.9
	MEAN			5.6 (.81 MPSI)	.168	1.924	44.7 (6479.PSI)
	STD. DEV.			.2 (.03 MPSI)	.012	.102	.9 (130.PSI)
12AC	B 6C	AX	EC	4.8	.175	1.853	40.6
	B 8C	AX	FC	4.7	.180	1.987	41.7
	B10C	AX	FC	4.6	.200	2.192	42.3
	B12C	AX	EC	4.8	.215	2.170	42.7
12BC	B90C	AX	EC	5.0	.180	2.024	42.6
	B92C	AX	EC	5.3	.180	1.864	41.8
	B94C	AX	EC	5.1	.185	1.897	41.0
	B96C	AX	EC	4.9	.180	1.850	41.0
	MEAN			4.9 (.71 MPSI)	.187	1.980	41.7 (6050.PSI)
	STD. DEV.			.2 (.04 MPSI)	.014	.140	.8 (113.PSI)

TABLE 11-11 (Continued)

COMPRESSIVE PROPERTIES OF PGX GRAPHITE

LOT NO. AD5-3 SPEC. DIA. 12.8 MM
LOG NO. 6484-112 SPEC. LENGTH 25. MM
LOG DENSITY 1.78 MG/M***3

SPECIMEN NUMBER	ORIENTATION	LOCATION	DENSITY (MG/M***3)	YOUNGS MODULUS (GPA)	PERMANENT SET (PCT)	FRACTURE STRAIN (PCT)	COMPR. STRENGTH (MPA)
1AC	E 3B	RAD	EC	5.7	.151	1.355	37.7
	E 7B	RAD	EC	5.8	.151	1.941	44.8
	E11B	RAD	EC	5.4	.171	1.888	41.6
	E23B	RAD	EC	5.6	.181	2.056	46.7
1BC	E111B	RAD	EC	5.4	.151	1.792	42.1
	E115B	RAD	EC	4.8	.161	2.060	42.8
	E119B	RAD	EC	5.2	.161	1.860	40.8
	E131B	RAD	EC	5.2	.181	1.982	41.5
	MEAN			5.4	.163	1.867	42.2
				(.78 MPSI)			(6126.PSI)
	STD. DEV.			.3	.013	.227	2.7
				(.05 MPSI)			(390.PSI)
12AC	B 3B	RAD	EC	5.2	.185	1.795	40.6
	B 7B	RAD	EC	5.8	.150	1.779	42.7
	B11B	RAD	EC	5.5	.160	1.668	39.3
	B21B	RAD	EC	5.7	.180	1.819	41.4
12BC	B111B	RAD	EC	6.3	.150	1.515	40.3
	B115B	RAD	EC	5.7	.130	1.604	40.4
	B119B	RAD	EC	6.2	.169	1.393	38.3
	B129B	RAD	EC	5.7	.150	1.578	38.7
	MEAN			5.8	.159	1.644	40.2
				(.84 MPSI)			(5831.PSI)
	STD. DEV.			.4	.018	.150	1.4
				(.05 MPSI)			(207.PSI)

TABLE 11-11 (Continued)

COMPRESSIVE PROPERTIES OF PGX GRAPHITE

LOT NO. RDS-3 SPEC. DIA. 12.6 MM
LOG NO. 6484-112 SPEC. LENGTH 25. MM
LOG DENSITY 1.78 MG/M**3

SPECIMEN NUMBER	ORIENTATION	LOCATION	DENSITY (MG/M**3)	YOUNGS MODULUS (GPA)	PERMANENT SET (PCT)	FRACTURE STRAIN (PCT)	COMPR. STRENGTH (MPA)
1AY	E30C	AX	EM	5.2	.181	2.144	44.7
	E34C	AX	EM	5.1	.171	1.925	42.6
	E42C	AX	EM	5.0	.201	1.780	40.1
	E46C	AX	EM	4.8	.181	1.736	39.7
1BY	E114C	AX	EM	5.4	.171	2.175	46.5
	E118C	AX	EM	5.2	.171	2.044	45.4
	E126C	AX	EM	5.4	.171	2.092	45.4
	E130C	AX	EM	5.8	.181	2.164	46.8
	MEAN			5.2	.178	2.008	43.9
				(.76 MPSI)			(6368.PSI)
	STD. DEV.			.3	.010	.174	2.8
				(.05 MPSI)			(404.PSI)
12AY	B30C	AX	EM	4.9	.180	2.140	43.9
	B34C	AX	EM	4.3	.211	1.853	38.4
	B42C	AX	EM	4.3	.150	2.004	39.0
	B46C	AX	EM	4.4	.200	1.887	39.3
12BY	B114C	AX	EM	4.6	.200	1.967	39.8
	B118C	AX	EM	4.5	.180	1.881	38.8
	B126C	AX	EM	4.5	.202	2.188	41.7
	B130C	AX	EM	4.6	.200	1.948	41.2
	MEAN			4.5	.190	1.983	40.3
				(.65 MPSI)			(5838.PSI)
	STD. DEV.			.2	.020	.122	1.9
				(.03 MPSI)			(271.PSI)

TABLE 11-11 (Continued)

COMPRESSIVE PROPERTIES OF PGX GRAPHITE

LOT NO. AD5-3 SPEC. DIA. 12.8 MM
LOG NO. 6484-112 SPEC. LENGTH 25. MM
LOG DENSITY 1.78 MG/M**3

SPECIMEN NUMBER	ORIENTATION	LOCATION	DENSITY (MG/M**3)	YOUNGS MODULUS (GPA)	PERMANENT SET (PCT)	FRACTURE STRAIN (PCT)	COMPR. STRENGTH (MPA)
1AY	F43B	RAD	EM	4.8	.191	1.814	38.3
	F47B	RAD	EM	4.8	.171	1.625	37.5
	F51B	RAD	EM	4.8	.171	1.619	38.0
	F61B	RAD	EM	6.0	.151	1.779	44.3
1BY	E151B	RAD	EM	5.5	.181	2.017	44.3
	E155B	RAD	EM	5.8	.180	1.763	42.4
	E159B	RAD	EM	5.3	.171	1.841	42.1
	E169B	RAD	EM	5.5	.181	1.697	42.2
	MEAN			5.3 (.77 MPSI)	.174	1.794	41.1 (5966.PSI)
	STD. DEV.			.5 (.07 MPSI)	.012	.133	2.8 (407.PSI)
12AY	B43B	RAD	EM	5.3	.199	1.626	37.4
	B47B	RAD	EM	5.3	.189	1.748	39.4
	B51B	RAD	EM	5.4	.190	1.702	39.2
	B61B	RAD	EM	5.5	.180	1.792	40.6
12BY	B151B	RAD	EM	5.5	.180	1.741	39.8
	B155B	RAD	EM	5.3	.180	1.557	37.5
	B159B	RAD	EM	5.4	.180	1.726	38.8
	B169B	RAD	EM	6.2	.170	1.634	40.5
	MEAN			5.5 (.79 MPSI)	.183	1.691	39.1 (5667.PSI)
	STD. DEV.			.3 (.04 MPSI)	.009	.078	1.1 (163.PSI)

TABLE 11-11 (Continued)

COMPRESSIVE PROPERTIES OF PGX GRAPHITE

LOT NO. 805-3 SPEC. DIA. 12.6 MM
LOG NO. 6484-112 SPEC. LENGTH 25. MM
LOG DENSITY 1.78 MG/M**3

SPECIMEN NUMBER	ORIENTATION	LOCATION	DENSITY (MG/M**3)	YOUNGS MODULUS (GPA)	PERMANENT SET (PCT)	FRACTURE STRAIN (PCT)	COMPR. STRENGTH (MPA)
1AE	E60C	AX	EE	5.3	.181	2.136	46.1
	E64C	AX	EE	5.5	.201	2.101	45.1
	E72C	AX	EE	5.3	.181	1.973	43.4
	E76C	AX	EE	5.3	.171	2.146	44.1
1BE	E144C	AX	EE	5.5	.140	2.079	46.8
	E148C	AX	EE	6.0	.151	2.004	48.1
	E156C	AX	EE	5.4	.171	2.269	47.0
	E160C	AX	EE	5.0	.191	2.226	44.7
	MEAN			5.4 (.78 MPSI)	.173	2.117	45.7 (6624.PSI)
	STD. DEV.			.3 (.04 MPSI)	.020	.101	1.6 (232.PSI)
12AE	B60C	AX	EE	4.9	.190	2.171	44.3
	B64C	AX	EE	4.3	.180	1.928	39.2
	B72C	AX	EE	4.7	.269	2.170	41.3
	B76C	AX	EE	5.0	.201	2.001	41.2
12BE	B144C	AX	EE	4.6	.192	1.851	40.6
	B148C	AX	EE	4.7	.182	1.839	38.7
	B156C	AX	EE	5.0	.190	1.812	38.0
	B160C	AX	EE	4.7	.210	2.031	42.3
	MEAN			4.7 (.69 MPSI)	.202	1.975	40.7 (5904.PSI)
	STD. DEV.			.2 (.03 MPSI)	.029	.143	2.1 (301.PSI)

TABLE 11-11 (Continued)

COMPRESSIVE PROPERTIES OF PGX GRAPHITE

LOT NO. AU5-3 SPEC. DIA. 12.8 MM
LOG NO. 6484-112 SPEC. LENGTH 25. MM
LOG DENSITY 1.78 MG/M**3

SPECIMEN NUMBER	ORIENTATION	LOCATION	DENSITY (MG/M**3)	YOUNGS MODULUS (GPA)	PERMANENT SET (PCT)	FRACTURE STRAIN (PCT)	COMPR. STRENGTH (MPA)
1AE	F79B	RAD	EE	5.4	.181	1.867	40.9
	E83B	RAD	EF	5.4	.161	1.567	40.1
	F87B	RAD	EE	5.4	.161	1.767	41.7
	E97B	RAD	EF	5.8	.161	1.883	43.0
1BE	B187B	RAD	FE	5.9	.161	1.981	44.7
	B191B	RAD	EE	5.4	.181	1.832	42.6
	B195B	RAD	EF	5.2	.151	1.890	43.6
	B205B	RAD	EE	5.0	.181	2.003	43.2
	MEAN			5.4	.167	1.849	42.5
				(.79 MPSI)			(6160.PSI)
	STD. DEV.			.3	.012	.137	1.5
				(.04 MPSI)			(219.PSI)
12AE	B79B	RAD	EE	5.1	.180	1.572	35.7
	B83B	RAD	EE	5.1	.179	1.824	38.9
	B87B	RAD	EE	5.2	.180	1.841	39.9
	B97B	RAD	EE	5.2	.170	1.482	36.4
12BE	B187B	RAD	FE	5.5	.180	1.635	38.2
	B191B	RAD	EE	5.2	.160	1.590	37.9
	B195B	RAD	EE	5.4	.160	1.615	38.3
	B205B	RAD	EE	5.4	.150	1.889	41.3
	MEAN			5.3	.170	1.681	38.3
				(.76 MPSI)			(5559.PSI)
	STD. DEV.			.1	.012	.149	1.8
				(.02 MPSI)			(258.PSI)

TABLE 11-11 (Continued)

COMPRESSIVE PROPERTIES OF PGX GRAPHITE

LOT NO. AD5-3 SPEC. DIA. 12.8 MM
LOG NO. 6484-112 SPEC. LENGTH 25. MM
LOG DENSITY 1.78 MG/M**3

SPECIMEN NUMBER	ORIENTATION	LOCATION	DENSITY (MG/M**3)	YOUNGS MODULUS (GPA)	PERMANENT SET (PCT)	FRACTURE STRAIN (PCT)	COMPR. STRENGTH (MPA)
6AC	M10C	AX	MLC	5.3	.170	1.580	39.5
	M 8C	AX	MLC	5.1	.170	1.599	37.7
	M12C	AX	MLC	5.4	.180	1.746	41.1
	M18C	AX	MLC	4.9	.200	1.875	41.9
6BC	M92C	AX	MLC	4.4	.200	2.184	43.2
	M94C	AX	MLC	5.0	.200	1.952	41.9
	M96C	AX	MLC	5.0	.190	2.199	44.2
	M98C	AX	MLC	5.2	.190	2.152	43.9
	MEAN			5.0	.187	1.911	41.7
				(.73 MPSI)			(6046.PSI)
	STD. DEV.			.3	.013	.254	2.2
				(.04 MPSI)			(322.PSI)
6AC	M 5B	RAD	MLC	6.3	.150	1.511	40.2
	M 9B	RAD	MLC	5.5	.150	1.268	35.0
	M13B	RAD	MLC	6.0	.150	1.619	41.0
	M23B	RAD	MLC	6.0	.140	1.540	41.5
6BC	M113B	RAD	MLC	7.5	.189	1.600	40.7
	M117B	RAD	MLC	5.4	.140	1.763	41.3
	M121B	RAD	MLC	5.9	.150	1.563	39.8
	M131B	RAD	MLC	5.2	.170	1.801	41.9
	MEAN			6.0	.155	1.585	40.2
				(.87 MPSI)			(5827.PSI)
	STD. DEV.			.7	.017	.164	2.2
				(.10 MPSI)			(320.PSI)

TABLE 11-11 (Continued)

COMPRESSIVE PROPERTIES OF PGX GRAPHITE

LOT NO. 805-3 SPEC. DIA. 12.8 MM
LOG NO. 6484-112 SPEC. LENGTH 25. MM
LOG DENSITY 1.78 MG/M**3

SPECIMEN NUMBER	ORIENTATION	LOCATION	DENSITY (MG/M**3)	YOUNGS MODULUS (GPA)	PERMANENT SET (PCT)	FRACTURE STRAIN (PCT)	COMPR. STRENGTH (MPA)
6AY	M30C	AX	MLM	5.5	.200	1.865	43.4
	M34C	AX	MLM	5.5	.180	2.164	46.0
	M42C	AX	MLM	5.4	.190	1.767	41.7
	M46C	AX	MLM	5.2	.190	2.119	45.0
6BY	M112C	AX	MLM	5.4	.149	2.157	47.2
	M116C	AX	MLM	5.5	.184	2.175	45.7
	M124C	AX	MLM	5.3	.200	2.271	46.7
	M128C	AX	MLM	5.3	.160	1.790	42.6
	MEAN			5.4	.181	2.038	44.8
				(.78 MPSI)			(6498.PSI)
	STD. DEV.			.1	.018	.198	2.0
				(.01 MPSI)			(292.PSI)
6AE	M60C	AX	MLE	5.2	.170	2.165	46.8
	M64C	AX	MLE	4.7	.200	1.962	42.9
	M72C	AX	MLE	5.6	.190	1.886	43.1
	M76C	AX	MLE	5.5	.180	1.952	44.2
6BE	M142C	AX	MLE	5.7	.170	2.196	47.7
	M146C	AX	MLE	5.5	.199	2.071	46.6
	M154C	AX	MLE	6.0	.170	2.017	45.6
	M158C	AX	MLE	5.7	.190	2.096	47.2
	MEAN			5.5	.184	2.043	45.5
				(.80 MPSI)			(6601.PSI)
	STD. DEV.			.4	.013	.107	1.9
				(.05 MPSI)			(274.PSI)

TABLE 11-11 (Continued)

COMPRESSIVE PROPERTIES OF PGX GRAPHITE

LOT NO. AD5-3 SPEC. DIA. 12.8 MM
LUG NO. 6484-112 SPEC. LENGTH 25. MM
LUG DENSITY 1.78 MG/M**3

SPECIMEN NUMBER	ORIENTATION	LOCATION	DENSITY (MG/M**3)	YOUNGS MODULUS (GPA)	PERMANENT SET (PCT)	FRACTURE STRAIN (PCT)	COMPR. STRENGTH (MPA)
6AY	M43M	RAD	MLM	6.1	.170	1.587	40.4
	M47M	RAD	MLM	6.0	.150	1.723	42.6
	M51M	RAD	MLM	6.4	.150	1.727	43.9
	M61M	RAD	MLM	5.8	.181	1.911	44.0
6BY	M151M	RAD	MLM	5.7	.180	1.797	41.0
	M155M	RAD	MLM	5.5	.170	1.745	41.6
	M159M	RAD	MLM	5.6	.170	1.657	40.9
	M160M	RAD	MLM	5.8	.180	1.786	40.3
	MEAN			5.9	.169	1.742	41.8
				(.85 MPSI)			(6069.PSI)
	STD. DEV.			.3	.013	.097	1.5
				(.04 MPSI)			(214.PSI)
6AE	M79B	RAD	MLE	6.6	.170	1.798	44.6
	M83B	RAD	MLE	6.4	.170	1.518	41.8
	M87B	RAD	MLE	6.4	.150	1.569	43.1
	M97B	RAD	MLE	6.3	.150	1.876	46.1
6BE	M187B	RAD	MLE	6.4	.170	1.614	43.1
	M191B	RAD	MLE	6.2	.170	1.584	41.7
	M195B	RAD	MLE	6.3	.150	1.590	41.5
	M205B	RAD	MLE	6.4	.150	1.723	44.6
	MEAN			6.4	.160	1.659	43.3
				(.92 MPSI)			(6281.PSI)
	STD. DEV.			.1	.011	.126	1.7
				(.02 MPSI)			(242.PSI)

TABLE 11-12
MEAN STRENGTH VALUES OF GRADE 2020 GRAPHITE
(LOG 6484-110)
(MPa)

Axial		Radial	
Slab 1	Slab 6	Slab 1	Slab 6
Tensile			
14.1 ±1.9	15.8 ±2.4	15.8 ±1.4	18.9 ±1.5
Flexural			
25.0 ±2.4	27.4 ±0.9	25.2 ±0.8	27.2 ±0.8
Compressive			
Slab 2 78.6 ±3.1		Slab 2 78.5 ±1.5	

TABLE 11-13

TENSILE PROPERTIES OF 2020 GRAPHITE

LOT NO. 728 SPEC. DIA. 12.8 MM
LOG NO. 6494-110 SPEC. LENGTH 70. MM
LOG DENSITY 1.803 MG/M**3

SPECIMEN NUMBER	ORIENTATION	LOCATION	DENSITY (KG/M**3)	YOUNGS MODULUS (GPA)	PERMANENT SET (PCT)	FRACTURE STRAIN (PCT)	TENSILE STRENGTH (MPA)
1A-L6A	AX	END	1.787	7.3	.012	.242	15.2
-L8A	AX	END	1.781	7.3	.015	.231	14.1
-L10A	AX	END	1.776	7.1	.015	.175	10.7
-L14A	AX	END	1.792	7.4	.012	.198	12.6
-L20A	AX	END	1.784	7.3	.015	.207	12.5
-L22A	AX	END	1.783	7.0	.010	.176	11.3
1A-L30A	AX	END	1.791	7.9	.010	.157	11.0
-L34A	AX	END	1.784	7.5	.012	.179	11.7
-L36A	AX	END	1.782	7.3	.011	.219	13.9
-L38A	AX	END	1.793	7.3	.011	.228	14.0
-L44A	AX	END	1.795	7.4	.010	.214	13.7
-L46A	AX	END	1.792	7.4	.012	.230	15.0
1A- L6A	AX	END					13.0
- L8A	AX	END					16.7
-L12A	AX	END					14.4
-L12A	AX	END					14.0
-L14A	AX	END					14.0
-L18A	AX	END					14.5
-L18A	AX	END					15.0
-L20A	AX	END					14.4
-L22A	AX	END					12.1
-L24A	AX	END					15.7
-L24A	AX	END					14.7
1A-L30A	AX	END					12.4
-L32A	AX	END					11.0
-L32A	AX	END					13.7
-L36A	AX	END					15.3
-L38A	AX	END					15.8
-L42A	AX	END					13.7
-L42A	AX	END					15.5
-L44A	AX	END					17.2
-L46A	AX	END					14.4
-L48A	AX	END					16.4
-L48A	AX	END					19.7
	MEAN		1.787	7.3 (1.06 MPSI)	.012	.205	14.1 (2051.PSI)
	STD. DEV.		.006	.2 (.03 MPSI)	.002	.028	1.9 (279.PSI)

TABLE 11-13 (Continued)

TENSILE PROPERTIES OF 2020 GRAPHITE

LOT NO. 728 SPEC. DIA. 12.8 MM
LOG NO. 6484-110 SPEC. LENGTH 70. MM
LOG DENSITY 1.803 MG/M**3

SPECIMEN NUMBER	ORIENTATION	LOCATION	DENSITY (KG/M**3)	YOUNGS MODULUS (GPA)	PERMANENT SET (PCT)	FRACTURE STRAIN (PCT)	TENSILE STRENGTH (MPA)
1A- L7	RAD	END	1.786	7.7	.010	.238	15.7
- L11	RAD	END	1.788	7.5	.013	.241	15.6
- L25	RAD	END	1.788	8.1	.010	.241	16.2
- L29	RAD	END	1.789	8.0	.010	.184	13.6
1B- L43	RAD	END	1.791	7.8	.010	.235	16.1
- L47	RAD	END	1.789	8.0	.007	.214	15.1
1B- L61	RAD	END	1.792	8.0	.008	.260	17.8
- L65	RAD	END	1.791	8.0	.011	.269	18.0
1A- L5	RAD	END					16.1
- L9	RAD	END					17.0
1A- L13	RAD	END					15.3
- L23	RAD	END					16.8
- L27	RAD	END					17.1
- L31	RAD	END					15.1
1B- L41	RAD	END					12.7
- L45	RAD	END					15.7
- L49	RAD	END					17.2
1B- L59	RAD	END					15.4
- L63	RAD	END					16.9
- L67	RAD	END					15.1
	MEAN		1.789	7.9 (1.15 MPSI)	.010	.235	15.8 (2295.PSI)
	STD. DEV.		.002	.2 (.03 MPSI)	.002	.026	1.4 (210.PSI)

TABLE 11-13 (Continued)

TENSILE PROPERTIES OF 2020 GRAPHITE

LOT NO. 72A — SPEC. DIA. 12.8 MM
LOG NO. 6484-110 — SPEC. LENGTH 70. MM
LOG DENSITY 1.803 MG/M**3

SPECIMEN NUMBER	ORIENTATION	LOCATION	DENSITY (KG/M**3)	YOUNGS MODULUS (GPA)	PERMANENT SET (PCT)	FRACTURE STRAIN (PCT)	TENSILE STRENGTH (MPA)
0A-L54A	AX	ML	1.795	7.0	.014	.206	12.7
-L56A	AX	ML	1.779	6.9	.010	.239	14.1
-L58A	AX	ML	1.775	6.8	.011	.260	15.1
-L62A	AX	ML	1.794	7.2	.013	.204	12.9
-L64A	AX	ML	1.793	7.2	.010	.209	13.0
-L70A	AX	ML	1.792	7.2	.010	.236	14.8
0A-L78A	AX	ML	1.795	7.4	.014	.226	14.3
-L82A	AX	ML	1.781	6.8	.012	.239	14.2
-L84A	AX	ML	1.781	6.9	.010	.217	13.3
-L86A	AX	ML	1.794	7.4	.012	.145	9.7
-L92A	AX	ML	1.803	7.2	.010	.250	15.2
-L94A	AX	ML	1.798	7.3	.011	.224	14.1
0A-L50A	AX	ML					13.5
-L50A	AX	ML					17.0
-L54A	AX	ML					15.5
-L56A	AX	ML					13.0
-L60A	AX	ML					17.4
-L60A	AX	ML					17.8
-L66A	AX	ML					15.4
-L66A	AX	ML					18.3
-L68A	AX	ML					16.6
-L70A	AX	ML					15.4
-L72A	AX	ML					18.9
-L72A	AX	ML					19.2
0B-L74A	AX	ML					18.3
-L74A	AX	ML					20.2
-L78B	AX	ML					16.1
-L80A	AX	ML					17.1
-L80A	AX	ML					18.4
-L84A	AX	ML					14.2
-L86A	AX	ML					15.4
-L90A	AX	ML					17.2
-L90A	AX	ML					19.1
-L92A	AX	ML					12.3
-L94A	AX	ML					19.6
-L96A	AX	ML					16.5
-L96A	AX	ML					18.1
	MEAN		1.790	7.1 (1.03 MPSI)	.011	.221	15.8 (2288.PSI)
	STD. DEV.		.009	.2 (.03 MPSI)	.002	.030	2.4 (354.PSI)

TABLE 11-13 (Continued)

TENSILE PROPERTIES OF 2020 GRAPHITE

LOT NO. 728 SPEC. DIA. 12.8 MM
LOG NO. 6484-110 SPEC. LENGTH 70. MM
LOG DENSITY 1.803 MG/M**3

SPECIMEN NUMBER	ORIENTATION	LOCATION	DENSITY (KG/M**3)	YOUNGS MODULUS (GPA)	PERMANENT SET (PCT)	FRACTURE STRAIN (PCT)	TENSILE STRENGTH (MPA)
6A-L79	RAD	ML	1.795	7.6	.011	.254	16.5
-L83	RAD	ML	1.793	7.4	.012	.300	18.6
-L97	RAD	ML	1.795	7.5	.014	.284	18.0
6A-L101	RAD	ML	1.794	7.5	.011	.301	19.2
6B-L115	RAD	ML	1.796	7.6	.011	.285	18.2
-L119	RAD	ML	1.797	7.5	.012	.274	17.5
-L133	RAD	ML	1.799	7.8	.012	.256	16.9
-L137	RAD	ML	1.796	7.6	.015	.271	17.2
6A-L77	RAD	ML					18.3
-L81	RAD	ML					19.2
-L85	RAD	ML					18.2
6A-L95	RAD	ML					21.0
-L99	RAD	ML					18.8
-L103	RAD	ML					19.1
6B-L113	RAD	ML					20.3
-L117	RAD	ML					17.2
6B-L121	RAD	ML					21.3
-L131	RAD	ML					20.7
-L135	RAD	ML					21.3
-L139	RAD	ML					19.7
	MEAN		1.796	7.6 (1.10 MPSI)	.012	.278	18.9 (2735.PSI)
	STD. DEV.		.002	.1 (.02 MPSI)	.001	.018	1.5 (214.PSI)

TABLE 11-14

FLEXURAL PROPERTIES OF 2020 GRAPHITE

LOT NO. 72A — SPEC. DIA. 6.4 MM
LOG NO. 6484-110 SPEC. LENGTH 51. MM
LOG DENSITY 1.803 MG/M**3

SPECIMEN NUMBER	ORIENTATION	LOCATION	DENSITY (KG/M**3)	MODULUS OF RUPTURE (MPA) (UNCORRECTED)	FLEXURAL STRENGTH (MPA) (CORRECTED)
1A	2A	AX END		34.3	25.7
	2B	AX END		36.2	26.4
	4A	AX END		34.5	25.8
	4B	AX END		35.0	26.0
	6A	AX END		35.7	26.2
	6B	AX END		31.7	24.7
	10A	AX END		35.8	26.3
	10B	AX END		33.5	25.4
	12A	AX END		13.5	12.5
	12B	AX END		22.2	19.1
	14A	AX END		33.9	25.6
	14B	AX END		27.3	22.3
	18A	AX END		32.1	24.8
	18B	AX END		36.0	26.3
	20A	AX END		35.4	26.1
	20B	AX END		31.6	24.6
	22A	AX END		33.0	25.2
	22B	AX END		34.2	25.7
	30A	AX END		32.0	24.8
1A	30B	AX END		33.2	25.3
	32A	AX END		32.0	24.8
	32B	AX END		38.4	26.9
1B	34A	AX END		32.0	24.8
	34B	AX END		33.9	25.6
	36A	AX END		34.5	25.8
	36B	AX END		35.2	26.1
	40A	AX END		31.4	24.5
	40B	AX END		32.3	24.9
	42A	AX END		32.2	24.9
	42B	AX END		33.0	25.2
	44A	AX END		34.8	25.9
	44B	AX END		32.9	25.2
	50A	AX END		32.7	25.1
	50B	AX END		35.5	26.1
	52A	AX END		34.4	25.8
	52B	AX END		35.2	26.1
	56A	AX END		36.7	26.5
	56B	AX END		34.3	25.7
1B	58A	AX END		29.0	23.3
	58B	AX END		39.3	27.1
	60A	AX END		39.3	27.1
	60B	AX END		33.9	25.6
	MEAN			33.2 MPA (4814. PSI)	25.0 MPA (3632. PSI)
	STD. DEV.			4.3 MPA (622. PSI)	2.4 MPA (348. PSI)

TABLE 11-14 (Continued)

FLEXURAL PROPERTIES OF 2020 GRAPHITE

LOT NO. 728 SPEC. DIA. 6.4 MM
LOG NO. 6484-110 SPEC. LENGTH 51. MM
LOG DENSITY 1.803 MG/M**3

SPECIMEN NUMBER	ORIENTATION	LOCATION	DENSITY (KG/M**3)	MODULUS OF RUPTURE (MPA) (UNCORRECTED)	FLEXURAL STRENGTH (MPA) (CORRECTED)
1A	7 RAD	END		32.0	25.6
	9 RAD	END		35.9	27.4
	13 RAD	END		35.0	27.0
	15 RAD	END		38.0	28.2
	19 RAD	END		34.2	26.7
	33 RAD	END		33.8	26.5
	35 RAD	END		35.2	27.1
	39 RAD	END		35.3	27.1
	41 RAD	END		35.0	27.0
	45 RAD	END		33.8	26.5
1B	59 RAD	END		39.3	28.6
	61 RAD	END		38.4	28.4
	65 RAD	END		38.3	28.3
	67 RAD	END		33.2	26.2
	71 RAD	END		35.8	27.4
	85 RAD	END		38.1	28.2
	87 RAD	END		39.6	28.7
	91 RAD	END		34.7	26.9
	93 RAD	END		36.8	27.8
1B	97 RAD	END		39.5	28.7
	MEAN			36.1 MPA (5235. PSI)	27.4 MPA (3975. PSI)
	STD. DEV.			2.3 MPA (329. PSI)	.9 MPA (132. PSI)

TABLE 11-14 (Continued)

FLEXURAL PROPERTIES OF 2020 GRAPHITE

LOT NO. 728 SPEC. DIA. 6.4 MM
LOG NO. 6484-110 SPEC. LENGTH 51. MM
LOG DENSITY 1.803 MG/M**3

SPECIMEN NUMBER	ORIENTATION	LOCATION	DENSITY (KG/M**3)	MODULUS OF RUPTURE (MPA) (UNCORRECTED)	FLEXURAL STRENGTH (MPA) (CORRECTED)
6A	66A AX	ML		33.8	25.2
	66B AX	ML		37.0	26.1
	68A AX	ML		34.5	25.4
	68B AX	ML		32.2	24.6
	70A AX	ML		35.8	25.8
	70B AX	ML		34.0	25.3
	74A AX	ML		34.8	25.5
	74B AX	ML		34.3	25.3
	76A AX	ML		31.7	24.4
	76B AX	ML		32.7	24.8
	78A AX	ML		34.5	25.4
	78B AX	ML		35.1	25.8
	82A AX	ML		32.7	24.8
	82B AX	ML		34.2	25.3
	84A AX	ML		32.9	24.8
6A	84B AX	ML		34.7	25.5
	86A AX	ML		30.0	23.6
	86B AX	ML		33.6	25.1
	92A AX	ML		31.8	24.4
	92B AX	ML		29.2	23.2
	94A AX	ML		33.0	24.9
	94B AX	ML		35.7	25.8
6B	98A AX	ML		34.8	25.5
	98B AX	ML		34.2	25.3
	100A AX	ML		35.3	25.7
	100B AX	ML		29.3	23.2
	104A AX	ML		37.0	26.1
	104B AX	ML		37.2	26.1
	106A AX	ML		32.7	24.8
	106B AX	ML		34.0	25.3
	108A AX	ML		32.6	24.7
	108B AX	ML		33.6	25.1
	114A AX	ML		31.7	24.3
	114B AX	ML		31.3	24.2
6B	116A AX	ML		38.6	26.4
	116B AX	ML		41.4	26.8
	120A AX	ML		34.6	25.5
	120B AX	ML		36.9	26.1
	122A AX	ML		34.0	25.3
	122B AX	ML		36.2	25.9
	128A AX	ML		38.1	26.3
	128B AX	ML		34.3	25.3
	MEAN			34.2 MPA (4960. PSI)	25.2 MPA (3655. PSI)
	STD. DEV.			2.4 MPA (353. PSI)	.8 MPA (115. PSI)

TABLE 11-14 (Continued)

FLEXURAL PROPERTIES OF 2020 GRAPHITE

LOT NO. 728 SPEC. DIA. 6.4 MM
LOG NO. 6484-110 SPEC. LENGTH 51. MM
LOG DENSITY 1.803 MG/M**3

SPECIMEN NUMBER	ORIENTATION	LOCATION	DENSITY (KG/M**3)	MODULUS OF RUPTURE (MPA) (UNCORRECTED)	FLEXURAL STRENGTH (MPA) (CORRECTED)
6A	111 RAD	ML		38.8	27.7
	113 RAD	ML		39.6	27.9
	117 RAD	ML		39.5	27.9
	119 RAD	ML		39.7	27.9
	123 RAD	ML		40.6	28.1
	137 RAD	ML		37.3	27.1
	139 RAD	ML		35.2	26.6
	143 RAD	ML		33.2	25.7
	145 RAD	ML		35.3	26.6
	149 RAD	ML		37.0	27.2
6B	163 RAD	ML		34.8	26.4
	165 RAD	ML		40.6	28.1
	169 RAD	ML		37.3	27.3
	171 RAD	ML		36.9	27.2
	175 RAD	ML		35.0	26.5
	189 RAD	ML		36.1	26.9
	191 RAD	ML		39.7	27.9
	195 RAD	ML		39.5	27.9
6B	197 RAD	ML		37.6	27.4
	201 RAD	ML		31.6	25.0
	MEAN			37.3 MPA (5404. PSI)	27.2 MPA (3939. PSI)
	STD. DEV.			2.5 MPA (367. PSI)	.8 MPA (122. PSI)

TABLE 11-15

COMPRESSIVE PROPERTIES OF 2020 GRAPHITE

LOT NO. 728 SPEC. DIA. 12.8 MM
LOG NO. 6484-110 SPEC. LENGTH 25. MM
LOG DENSITY 1.803 MG/M**3

SPECIMEN NUMBER	ORIENTATION	LOCATION	DENSITY (MG/M**3)	YOUNGS MODULUS (GPA)	PERMANENT SET (PCT)	FRACTURE STRAIN (PCT)	COMPR. STRENGTH (MPA)
2A	L02C AX	END		9.2	.050	1.621	76.3
	L12C AX	END		10.1	.060	1.800	76.3
2B	L32C AX	END		10.6	.060	1.847	78.7
	L42C AX	END		10.1	.070	2.084	83.0
	MEAN			10.0 (1.45 MPSI)	.060	1.838	78.6 (11396.PSI)
	STD. DEV.			.6 (.09 MPSI)	.008	.191	3.1 (455.PSI)
2A	L01B RAD	END		10.2	.060	1.819	77.4
	L19B RAD	END		8.6	.070	1.969	78.8
2B	L37B RAD	END		10.8	.050	1.602	77.2
	L55B RAD	END		10.2	.070	1.922	80.5
	MEAN			9.9 (1.44 MPSI)	.062	1.828	78.5 (11383.PSI)
	STD. DEV.			.9 (.13 MPSI)	.010	.163	1.5 (223.PSI)

TABLE 11-16

THERMAL CONDUCTIVITY OF 2020 GRAPHITE

LOT NUMBER: -- LOG NUMBER: 6484-110

ORIENTATION	LOCATION	SPECIMEN NUMBER	THERMAL CONDUCTIVITY (W/M-K) AT: 295K (22C)	473K (200C)	673K (400C)	873K (600C)	1073K (800C)
AXIAL	MLE	6-L88A	61.3	64.2	52.3	42.4	39.4
		6-L88B	69.4	61.0	51.7	43.3	37.9
		6-L88C	59.2	66.5	56.3	49.8	43.8
		6-L88D	64.9	61.4	55.4	43.8	41.5
		6-L88E	59.7	60.6	49.4	40.9	38.2
		6-L88F	61.2	65.9	56.0	48.3	45.3
		6-L88F	66.0	64.2	55.4	48.0	41.0
		6-L88H	62.6	65.5	52.9	45.1	39.6
		MEAN:	63.0	63.7	53.7	45.2	40.8
		STD. DEV:	3.5	2.4	2.5	3.2	2.6

TABLE 11-17

FATIGUE TESTS ON PGX GRAPHITE

LOT NO: ** LOG NO: 6484-74
ORIENTATION: RADIAL LOCATION: END-ONE THIRD RADIUS

STRESS RATIO, R (MIN. STRESS / MAX. STRESS): =1.0

SPECIMEN NO.	DENSITY (MG/M**3)	MAX. STRESS (MPA)	MIN. STRESS (MPA)	CYCLES TO FAILURE
9C	1.759	5.6	-5.6	>143100 (RUNOUT)
57D	1.758	5.6	-5.6	>114200 (RUNOUT)
47A	1.761	5.6	-5.6	>106200 (RUNOUT)
41B	1.760	5.6	-5.6	>110300 (RUNOUT)
35C	1.767	5.6	-5.6	>109500 (RUNOUT)
29D	1.758	5.6	-5.6	>106600 (RUNOUT)
13B	1.757	5.6	-5.6	>123600 (RUNOUT)
21A	1.760	5.6	-5.6	>107500 (RUNOUT)
3D	1.764	5.6	-5.6	>155800 (RUNOUT)
63C	1.773	5.6	-5.6	>105400 (RUNOUT)
9B	1.763	6.8	-6.8	1300
57C	1.750	6.8	-6.8	27800
45A	1.768	6.8	-6.8	>127300 (RUNOUT)
37B	1.758	6.8	-6.8	2100
31C	1.760	6.8	-6.8	4000
25D	1.761	6.8	-6.8	>132200 (RUNOUT)
15A	1.764	6.8	-6.8	>100200 (RUNOUT)
5C	1.768	6.8	-6.8	>105800 (RUNOUT)
65B	1.770	6.8	-6.8	350
51D	1.772	6.8	-6.8	6700
11A	1.766	8.0	-8.0	32
57B	1.760	8.0	-8.0	4300
5B	1.768	8.0	-8.0	86
45D	1.757	8.0	-8.0	1052
37A	1.765	8.0	-8.0	6516
31B	1.764	8.0	-8.0	764
25C	1.762	8.0	-8.0	2987
19D	1.766	8.0	-8.0	1362
63A	1.764	8.1	-8.1	346
51C	1.772	8.1	-8.1	764
59A	1.758	8.8	-8.8	4
13D	1.765	8.8	-8.8	< 1 (FIRST CYCLE)
9A	1.758	8.8	-8.8	110
47C	1.754	8.8	-8.8	78
25B	1.761	8.8	-8.8	351
41D	1.759	8.8	-8.8	52
31A	1.767	8.8	-8.8	10
19C	1.761	8.8	-8.8	< 1 (FIRST CYCLE)
67D	1.767	8.9	-8.9	101
53B	1.771	8.9	-8.9	42

TABLE 11-18

FATIGUE TESTS ON PGX GRAPHITE

LOT NO: --
ORIENTATION: AX
LOG NO: 6484-74
LOCATION: END-ONE THIRD RADIUS

CONTROL TENSILE TESTS

SPECIMEN NO.	DENSITY (MG/M**3)	DIA. (MM)	FRACTURE LOAD (KN)	TENSILE STRENGTH (MPA)
2A	1.739	12.71	.88	6.9
4B	1.768	12.70	1.01	7.9
6C	1.762	12.70	.96	7.5
10A	1.733	12.70	.96	7.5
12B	1.750	12.70	.90	7.1
14C	1.701	12.70	.93	7.3
18A	1.722	12.71	.98	7.7
20B	1.723	12.70	.93	7.3
22C	1.762	12.71	1.06	8.3
26A	1.759	12.71	.87	6.8
28B	1.763	12.71	1.01	7.9
30C	1.750	12.71	.90	7.1
34A	1.747	12.71	.98	7.7
36B	1.760	12.71	1.01	7.9
38C	1.766	12.71	1.01	7.9
42A	1.769	12.71	1.08	8.5
44B	1.761	12.71	1.03	8.1
46C	1.763	12.71	.96	7.5
50A	1.765	12.70	1.06	8.3
52B	1.761	12.71	1.01	7.9
54C	1.760	12.70	.90	7.1
58A	1.752	12.70	1.01	7.9
60B	1.938	12.70	.98	7.7
62C	1.762	12.70	.96	7.5
66A	1.754	12.70	1.01	7.9
68B	1.761	12.70	.93	7.3
70C	1.761	12.70	.98	7.7
74A	1.749	12.70	.96	7.5
76B	1.755	12.70	.93	7.3
78C	1.762	12.70	.96	7.5
82A	1.745	12.70	1.01	7.9
84B	1.747	12.70	1.01	7.9
86C	1.763	12.69	.88	7.0
90A	1.768	12.69	.85	6.8
MEAN:	1.759		MEAN:	7.6 MPA (1105.PSI)
STD. DEV:	.035		STD. DEV:	.4 MPA (63.PSI)

TABLE 11-19

FATIGUE TESTS ON PGX GRAPHITE

LOT NO: -- LOG NO: 6484-74
ORIENTATION: AX LOCATION: END-ONE THIRD RADIUS

STRESS RATIO, R (MIN. STRESS / MAX. STRESS): .0

SPECIMEN NO.	DENSITY (MG/M**3)	MAX. STRESS (MPA)	MIN. STRESS (MPA)	CYCLES TO FAILURE
42B	1.765	5.1	.0	>122800 (RUNOUT)
16B	1.761	5.1	.0	>108800 (RUNOUT)
24A	1.764	5.1	.0	>111000 (RUNOUT)
52A	1.764	5.1	.0	>114700 (RUNOUT)
32C	1.762	5.1	.0	>159240 (RUNOUT)
58C	1.764	5.1	.0	>114400 (RUNOUT)
4C	1.762	5.1	.0	>120300 (RUNOUT)
70B	1.762	5.1	.0	>104500 (RUNOUT)
84C	1.759	5.1	.0	>121900 (RUNOUT)
78A	1.764	5.1	.0	>104100 (RUNOUT)
38B	1.758	5.9	.0	>
26C	1.765	5.9	.0	643
46A	1.760	5.9	.0	>105800 (RUNOUT)
52C	1.763	5.9	.0	305
72A	1.763	5.9	.0	11000
10B	1.745	5.9	.0	822
80C	1.766	5.9	.0	>117100 (RUNOUT)
64B	1.767	5.9	.0	92
20A	1.762	5.9	.0	572
90B	1.769	5.9	.0	572
56A	1.763	5.9	.0	< 1 (FIRST CYCLE)
40A	1.768	6.3	.0	91000
48C	1.761	6.3	.0	656
32B	1.764	6.3	.0	12226
14A	1.756	6.3	.0	451
58B	1.764	6.3	.0	79
6B	1.759	6.3	.0	1998
68A	1.763	6.3	.0	415
86B	1.759	6.3	.0	977
74C	1.763	6.3	.0	642
20C	1.758	6.3	.0	15672
22B	1.759	6.3	.0	< 1 (FIRST CYCLE)
68C	1.771	6.7	.0	49
80B	1.764	6.7	.0	11
88A	1.767	6.7	.0	85
36A	1.755	6.7	.0	4
42C	1.757	6.7	.0	2
26B	1.764	6.7	.0	6
16C	1.755	6.7	.0	< 1 (FIRST CYCLE)
8A	1.748	6.7	.0	< 1 (FIRST CYCLE)
54B	1.766	6.7	.0	25
62A	1.764	6.7	.0	129
30A	1.765	6.9	.0	< 1 (FIRST CYCLE)
48B	1.768	7.1	.0	< 1 (FIRST CYCLE)
36C	1.765	7.1	.0	< 1 (FIRST CYCLE)
10C	1.749	7.1	.0	< 1 (FIRST CYCLE)
64C	1.765	7.5	.0	15
4A	1.764	7.9	.0	< 1 (FIRST CYCLE)

TABLE 11-20
FLUENCE, TEMPERATURE, AND STRESS DATA FOR FTE-3, -4, -5, AND -6 AT EOL

Element	Axial Position	Fluence (10^{25} n/m^2)	Temperature (K)		Axial Stress (MPa)		Hoop Stress (MPa)		
			10[a]	297[a]	20[a]	297[a]	20[a]	288[a]	359[a]
FTE-3	5	0.428	991	1189	6.6	-3.2	6.1	-3.6	8.8
	15	0.547	1181	1395	11.4	-6.5	8.3	-4.8	11.9
	25	0.352	1159	1280	5.2	-2.9	4.1	-2.4	5.9
FTE-4	7	1.625	1040	1274	15.1	-8.2	11.0	-6.4	15.8
	13	1.9	1175	1423	15.7	-9.6	10.2	-5.9	14.8
	23	1.587	1249	1457	12.6	-7.6	8.6	-5.0	12.5
FTE-5	5	2.756	831	961	8.4	-3.7	6.1	-3.5	8.8
	15	3.705	838	1079	10.1	-6.1	4.2	-2.4	6.2
	25	2.77	1009	1133	9.7	-5.5	5.3	-2.4	7.7
FTE-6	5	2.08	877	1182	14.0	-7.2	10.0	-5.7	14.3
	15	2.83	1179	1393	13.3	-8.3	7.6	-4.4	11.0
	25	2.21	1056	1505	11.9	-7.3	7.7	-4.5	11.2

[a] Finite element number (see Fig. 11-4).

TABLE 11-21
COMPARISON OF ANALYTICAL AND EXPERIMENTAL RESULTS FOR STRIP CUTTING AND RING CUTTING EXPERIMENTS

Element	Position	Change of Diameter During Irradiation, $\Delta D/D$ (%)		Change of Diameter After Cutting, $\Delta D_1/D_1$ (%)		Change of Groove Distance After Cutting, $\Delta G/G$ (%)		Bow of Strip 1, B_1 (mm)		Bow of Strip 2, B_2 (mm)	
		Analysis	Experiment	Analysis	Experiment	Analysis	Experiment	Analysis	Experiment	Analysis	Experiment
3	5	-0.038	-0.04	-0.145	-0.05	-1.26	-0.929	--	--	--	--
	15	-0.096	-0.04	--	--	--	--	1.61	0.28	2.15	0.88
	25	-0.058	0	-0.085	-0.036	-0.8	-0.78	--	--	--	--
4	7	-0.197	-0.09	-0.055	-0.102	-0.7	-1.31	--	--	--	--
	13	-0.304	-0.217	--	--	--	--	2.49	-0.22	2.9	0.51
	23	-0.30	-0.188	-0.066	-0.069	-0.74	-1.21	--	--	--	--
5	5	--	--	--	--	--	--	--	--	--	--
	15	--	--	--	--	--	--	1.79	-2.54	2.16	-0.74
	25	--	--	--	--	--	--	1.48	0.06	1.85	0.35
6	5	--	--	--	--	--	--	1.69	0.22	2.54	0.76
	15	--	--	--	--	--	--	2.43	-1.24	2.76	0.39
	25	--	--	--	--	--	--	2.26	-0.82	2.62	0.22

APPENDIX
TOPICAL REPORTS PUBLISHED DURING THE QUARTER

Engle, G. B., and W. R. Johnson, "Properties of Unirradiated Fuel Element Graphites H-451 and SO818," ERDA Report Ga-A14068, General Atomic Company, October 8, 1976

Scott, C. B., D. P. Harmon, and J. F. Holzgraf, "Postirradiation Examination of Capsules P13R and P13S," ERDA Report Ga-A13827, General Atomic Company, October 8, 1976.

Johnson, W. R., "Comparison of Dimensional Changes in LHTGR Graphites by Irradiation in the HFIR (Capsules HT-20, HT-21, HT-22, and HT-23)," ERDA Report GA-A14028, General Atomic Company, November 1976.